A HIGHLY DISTORTED TURBULENT FREE SHEAR LAYER

by

I.P. CASTRO, M.A., M.Sc.

Department of Aeronautics,

Imperial College of Science and Technology

A Thesis Submitted for the Doctor of Philosophy Degree of the University of London, February 1973.

SUMMARY

Present-day calculation methods for turbulent boundary layers and other thin shear layers are often inapplicable to the more complex flows met with in engineering practice. Sometimes the thin-shear-layer approximation itself (a purely mathematical approximation having nothing to do with the physics of turbulence) is violated: more frequently still, the turbulence structure ceases to obey the empirical rules which describe its behaviour in simple flows.

To develop suitable calculation methods, more experimental information about these complex flows is required. This Thesis presents the results of an experimental investigation of a highly curved, two-dimensional mixing layer. The results are compared with the more familiar plane self-preserving mixing layer and an attempt is made to explain some of the interesting physical phenomena caused by the distortion, with a view to assisting in the development of suitable calculation procedures.

The curvature is of a stabilising nature, so that the turbulent intensity is considerably reduced and on removal of the curvature this intensity, instead of increasing monotonically to its original level, overshoots and then reduces monotonically. It seems that the turbulent diffusion is suppressed relatively more than the other terms in the Reynolds transport equations, resulting in a 'surfeit' of energy production.

ACKNOWLEDGEMENTS

The work described in this volume could not have been undertaken without the help of a great many people and I would like to thank all those (whether mentioned below or not) who have been in any way involved.

I have been indebted to the members of the Donald Campbell Memorial Trust who, by their financial support, made it all possible. Professor P.R. Owen and his staff have been a vital source of inspiration: I should like in particular to thank Mr. P. Bradshaw for his continual guidance and encouragement as supervisor of most of the work reported herein, and Mr. B.J. Belcher and Mr. C. Mott, for their patient instruction in electronic 'know-how'.

The experimental work would have been impossible without the skilled assistance of Mr. W.H. Davies and his workshop staff, especially Messrs. J. Coles and C.P. McAra, who are probably grateful that it is all over.

Finally I must thank my wife, Lucilla, for moral support during the inevitable times of mental anguish associated with a work of this nature.

LIST OF CONTENTS

		Page No.
SUMMARY		i
ACKNOWLEDGEMENTS		ii
TABLE OF CONTENTS		iii
LIST OF FIGURES		vii
LIST OF SYMBOLS		xi
CHAPTER 1	INTRODUCTION	1
	1.1 INTRODUCTORY REMARKS	1
	1.2 GENERAL EFFECTS OF FLOW CURVATURE	3
	1.3 THE PRESENT EXPERIMENT	6
CHAPTER 2	THE EXPERIMENTAL ARRANGEMENTS AND INSTRUMENTATION	8
	2.1 THE WIND TUNNEL	8
	2.2 TRAVERSE GEAR	9
	2.3 PITOT TUBES AND MANOMETERS	10
	2.4 HOT WIRE TECHNIQUES	11
	2.4.1 Hot Wires and Calibration Procedures	11
	2.4.2 Yaw Response Calibrations	12
	2.5 ANALOGUE AND DIGITAL RECORDING	14
	2.6 ANALYSIS OF DIGITAL DATA	16
	2.7 OTHER INSTRUMENTATION	18
CHAPTER 3	TRANSPORT EQUATIONS AND NOTATION	20
	3.1 THE TRANSPORT EQUATIONS IN CARTESIAN AXES	20
	3.2 THE TRANSPORT EQUATIONS IN CURVILINEAR CO-ORDINATES	21
	3.3 NOTATION	25

CHAPTER 4 THE PLANE MIXING LAYER 28

4.1 THE SCOPE OF THE TESTS 28

4.2 THE MEAN FLOW 29

4.2.1 Mean Velocity Measurements 29

4.2.2 Calculation of the Transverse Mean Velocity Component 30

4.3 THE TURBULENCE 32

4.3.1 Turbulent Intensities 32

4.3.2 The Turbulent Shear Stress 33

4.3.3 The Triple Products and Flatness Factor 35

4.3.4 U-Component Spectra 36

4.4 THE TURBULENT ENERGY BALANCE 37

4.4.1 The Dissipation Term 37

4.4.2 The Production Term and Overall Balance 39

4.5 THE SHEAR STRESS BALANCE 41

4.6 THE INTERMITTENCY 41

4.6.1 The Problem 41

4.6.2 The Method Adopted 44

CHAPTER 5 THE DISTORTED MIXING LAYER 47

5.1 THE MEAN FLOW 47

5.1.1 Setting-Up and Flow Visualisation 47

5.1.2 Initial Total Pressure Measurements 48

5.1.3 Checks of Two-Dimensionality 49

5.1.4 Measurements of The 'Bounding Streamline' 51

5.1.5 Hot-Wire Velocity Profiles 53

5.1.6 Reduction of Mean Flow Data 56

5.1.6.1 The Mixing Layer Growth Rate 56

5.1.6.2 Mean Vorticity and Rates of Strain 57

5.2 THE TURBULENCE 59

5.2.1 Initial Analogue Measurements 59

5.2.2 The Crossed Hot-Wire Traverses and U-Component Spectra 59

5.2.3 The Direction of the Mixing Layer 62

5.2.4 Turbulent Energy and Shear Stress 63

5.2.5 Turbulent Energy Balances 65

5.2.5.1 Centre Line Balance 66

5.2.5.2 Cross-Layer Balances 70

5.2.6 Shear Stress Balances 72

5.2.6.1 Cross-Layer Balances 73

5.2.7 The Mean Momentum Equation - Turbulent Terms 74

CHAPTER 6 FURTHER RESULTS AND DISCUSSION 77

6.1 THE PHENOMENA 77

6.1.1 The Stabilising Nature of the Curvature 77

6.1.2 The 'Overshoot' on Removal of the Curvature 79

6.1.3 Deductions from the Cross-Layer Balances 81

6.1.4 The Intermittency 82

6.2 'TOWARDS A CALCULATION METHOD' 84

6.2.1 The Equivalent Shear Layer Assumption 84

6.2.2 Probable Requirements of a Calculation Procedure 86

6.3 CONCLUSIONS AND SUGGESTIONS FOR FURTHER WORK 90

REFERENCES 93

APPENDIX I A PULSED-WIRE TECHNIQUE FOR VELOCITY MEASUREMENTS IN HIGHLY TURBULENT FLOWS II

APPENDIX II SOME COMMENTS ON HEAT-TRANSFER LAWS FOR FINE WIRES XXXVIII

APPENDIX III ANALYSIS OF CROSSED HOT-WIRE DATA XLVIII

APPENDIX IV STATISTICS OF THE INSTANTANEOUS VELOCITY VELOCITY VECTOR AND THE CONSEQUENT ERRORS IN HOT-WIRE MEASUREMENTS LI

IV.1 THE PROBLEM LI

IV.2 THE FLOW-ANGLE PROBABILITY DISTRIBUTION LII

IV.2.1 Analytic Solutions LII

IV.2.2 Results of Numerical Integration of Equation AIV.1 LVII

IV.3 COMPARISON WITH MEASUREMENTS LIX

APPENDIX V THE MEAN FLOW PROGRAMS LXIV

V.1 THE NUMERICAL SCHEME LXIV

V.2 THE TEST CASE LXVI

V.3 INPUT DATA FOR THE REAL CASE LXVIII

V.4 THE PROGRAM FOR THE VERTICAL PORTION LXXX

LIST OF FIGURES

2.1 Pitot Tube Yaw Response

2.2 Typical Crossed Hot-Wire Calibration

2.3 Typical Crossed Hot-Wire Yaw Response

2.4 Cumulative $\overline{u^2}$ (after every 5000 points)

2.5 Cumulative $\overline{v^3}$ (after every 5000 points)

4.1 The Plane Mixing Layer

4.2 Spread of Mixing Layer

4.3 Mean Velocity Variation

4.4 Mean Velocity (V-component)

4.5 Longitudinal Turbulent Intensity

4.6 Transverse and Lateral Turbulent Intensities

4.7 Turbulent Shear Stress

4.8 Shear Correlation Coefficient

4.9a Triple Products

4.9b Triple Products

4.10 Flatness Factor

4.11 U-Component Spectra

4.12 Energy and Dissipation Spectra

4.13 Comparison of Spectra with Grant's Universal Curve

4.14 Energy Balance (measured values)

4.15 Comparison Between Triple Velocity Diffusion' and Total Diffusion Obtained by Difference

4.16 Shear Stress Balance

4.17 Variation of Intermittency with Threshold Values

4.18 The Intermittency Function

4.19 Variation of Intermittency with Sample Length

5.1 Sketch of Possible Traverse Movements

5.2a The Curved Mixing Layer (curved portion)

5.2b The Curved Mixing Layer (vertical portion)

5.3 Wake Excess Temperature

5.4 Flow Divergence

5.5a Temperature Profiles in Wake of Heated Source

5.5b Temperature Profiles

5.6 Temperature Along Bounding Streamline

5.7 Mean Velocity Along Bounding Streamline

5.8 Mean Velocity Profiles (curved portion)

5.8 Mean Velocity Profiles (curved portion)

5.9 Mean Velocity Profiles (curved portion)

5.10 Mean Velocity Profiles (vertical portion)

5.11 Mean Velocity Profiles (vertical portion)

5.12 Mean Velocity Profiles (vertical portion)

5.13 Mixing Layer Growth Rate

5.14a Mean Vorticity and Rates of Strain

5.14b Mean Vorticity and Principal Rate of Strain

5.15 Streamline Direction

5.16a-f Turbulent Energy and Shear Stress

5.17 Triple Products

5.18 U-Component Spectra

5.19 U-Component Spectra

5.20 U-Component Spectra

5.21 U-Component Spectra

5.22 Direction of Curved Mixing Layer

5.23 Maximum Turbulent Energy and Shear Stress

5.24a Maximum Triple Products

5.24b Maximum Triple Products

5.25 Principal Turbulent Stress and Mean Rate of Strain

5.26 Direction of Principal Stress and Strain

5.27 Energy Balance Round the Centre Line

5.28 The Energy Production Terms

5.29 Accuracy Checks (streamwise energy gradient)

5.30 Triple Velocity Diffusion Round the Centre Line

5.31 Typical $\overline{q^2u'}$ vs. x_j' for Estimation of Longitudinal Gradients

5.32 Energy Balance S = 34.4, J = 11

5.33 Energy Balance S = 38.8, J = 13

5.34 Energy Balance S = 81.5, J = 27

5.35 Triple-Velocity Diffusion

5.36 Mixing Layer Curvature

5.37 Shear Stress Balance Round the Centre Line

5.38 The Shear Stress Production Terms

5.39 Shear Stress Balance J = 5, S = 21.1

5.40 Shear Stress Balance J = 9, S = 29.9

5.41 Shear Stress Balance J = 13, S = 38.8

5.42 Shear Stress Balance J = 23, S = 61.1

5.43 Terms in the Normal Momentum Equation

5.44 Turbulent Terms in the Streamwise Momentum Equation

5.45 Turbulent Terms in the Streamwise Momentum Equation

6.1 Direction of Principal Stress Along the Line $\frac{p}{p_r} = 0.64$

6.2 Direction of Principal Stress Along J = 9

6.3 Relative Reduction in Terms in Energy Transport Equation

6.4 Relative Large-Eddy Strength

6.5a Dissipation Length and Microscale

6.5b Dissipation Length and Microscale

6.6 The Intermittency

6.7 Contributions to Total Production of Energy and Shear Stress

6.8 Variation of Mixing Length Around the Centre-Line

6.9 Richardson Number and its Relation to the Dissipation Length Scale

6.10 Eddy Diffusivity

AIV.1 Solution of Equation AIV.3

AIV.2 Solution of Equation AIV.4

AIV.3 Results of Numerical Integration of Equation AIV.1 for Typical Case

AIV.4 The Effect of a Non-Zero Correlation Coefficient

AIV.5 Probability Density of $\tan^{-1}(\frac{v}{u})$, $\eta = -0.0687$

AIV.6 Probability Density of $\tan^{-1}(\frac{v}{u})$, $\eta = -0.0144$

AIV.7 Probability Density of $\tan^{-1}(\frac{v}{u})$, $\eta = +0.0757$

AIV.8 Probability Density of $\tan^{-1}(\frac{v}{u})$, $\eta = +0.112$

AV.1 Numerical Program Test Case

AV.2 Test Case - Errors in Vorticity Calculation

AV.3 $\frac{V'}{U'}$ Around Bounding Streamline

AV.4a Accuracy Checks (see Table AV.1)

AV.4b Accuracy Checks and Table AV.1

LIST OF SYMBOLS

$A \equiv \frac{\partial U}{\partial y} + \frac{\partial V}{\partial x}$	Mean rate of strain
B	Constant in hot-wire response equation
d	Distance from backplate
d′	Distance around line joining measurement points in the two-dimensional checks (Section 5.1.3)
E	Anemometer output voltage
E(k)	Wavenumber magnitude spectrum
F	Cumulative integrated probability function
$h \equiv 1 + nS(\kappa)$	Curvature parameter
i,j (= J)	Notation for mesh points and radial traverse lines (see Section 3.3 and Appendix V)
$L \equiv \frac{(\tau)^{3/2}}{\epsilon}$	Dissipation length scale
l	Length scale, usually the mixing length
N	Nusselt number
n	Line normal to local direction of s
P	Probability or total pressure
p or ps, p′	Mean and fluctuating static pressure respectively
$\overline{q^2} = \overline{u^2} + \overline{v^2} + \overline{w^2}$	Turbulent energy
R	Reynolds number or radius of curvature
Ri, R_f	Richardson numbers, defined in Chapter 1 and Section 6.2.2 respectively
r_{12}	Shear stress correlation coefficient
r_j	Radius of curvature (i.e. distance along 'j-line' from rotating traverse axis)
s	Any line, in the x-y plane (of curvature κ) but usually the distance around the curved mixing layer centre-line (S is used in the latter case)

S_b	Distance around bounding streamline
$S_c \equiv U\kappa / \frac{\partial U}{\partial n}$	Curvature parameter
T	Temperature
U,V,W	Mean velocities in the x, y, z directions respectively. U, V also refer to mean velocities in the x´, y´ or s´, n´ directions, see Section 3.3
U_r	Reference velocity at contraction exit
$\tilde{U} \equiv \left[U^2 + V^2\right]^{\frac{1}{2}}$	Total mean velocity ($W \equiv 0$)
u,v,w	Fluctuating velocities in the x, y, z (or x´, y´, z and s´, n´, z) directions.
$\overline{uv} \equiv \tau$	Turbulent shear stress
x,y,z	Cartesian axes; for full definitions of these and other axis notation refer to Section 3.3
α_u, α_v α_w	r.m.s. turbulent intensities in the x, y, z directions respectively
α_1, α_2	Directions of principal rate of strain and principal turbulent stress, respectively
α	Constant in universal equilibrium theory
β	Direction of curved mixing layer, fully defined in Section 5.2.3
γ	Intermittency
δ	Shear layer thickness
δ_2	Momentum thickness
ε_{ed}, ε_{sd}	Energy and shear stress eddy diffusivities, respectively
ε	Energy dissipation rate
$\eta \equiv \frac{y}{x}$	Lateral position in plane mixing layer
η	Kolmogorov length scale
θ	Temperature, or angle in degrees
κ	Curvature

λ	Turbulent microscale
ν	Kinematic viscosity
ν_T	Effective turbulent viscosity
ρ	Density
$\tau = \overline{uv}$	Turbulent shear stress
$\phi(k)$, $\phi_{11}(k)$	True and measured one dimensional energy spectrum function respectively. $\int_0^\infty \phi(k)dk = 1$
ψ_e	Hot-wire effective angle
ψ	Stream function
$\omega \equiv 2\pi f$	Circular frequency
$\Omega \equiv \frac{\partial V}{\partial x} - \frac{\partial U}{\partial y}$	Mean vorticity

1. INTRODUCTION

1.1 INTRODUCTORY REMARKS

In recent years, particularly since the widespread introduction of electronic measuring equipment, there has been a considerable improvement in the understanding of many fluid motion phenomena. Perhaps the most notable example is the advance in our knowledge of the random, eddying motions of turbulent flow, but most workers would agree that it remains "the chief outstanding difficulty of our subject" as Lamb[1] called it over fifty years ago. Not only is this most complicated kind of fluid motion the most interesting to a scientific research worker but it is also the most important to an engineer because of the great variety of practical situations in which turbulent phenomena are important and in which their effects must be quantitatively predicted. Much of the power required to propel aircraft, ships, or high speed vehicles, or to pump fluid through large pipes and channels, is expended in overcoming the large frictional forces generated by turbulence, which are many times larger than they would be if steady, laminar flow could be maintained. Turbulence is also the most important agent in mixing two different fluids, from milk in a cup of tea to pollutants in the atmosphere or ocean.

Turbulent velocity fluctuations are at their most intense and frictional forces and mixing rates at their largest in 'shear layers', fairly thin sheets parallel to the flow direction across which the speed of flow changes significantly: the turbulence maintains itself by extracting energy from the mean shear. The most common example is the boundary layer next to a solid surface, in which the speed of flow increases rapidly from zero at the surface

to a more nearly constant value in the external stream: most shear layers far from a solid surface are descended from boundary layers which have separated from the surface, either at a sharp edge or in a region of rapidly decelerating flow.

A large amount of data has been accumulated relating to turbulent shear flows, especially boundary layers, and this has led to better understanding of the physics and consequent significant improvements in calculation methods. Of necessity most of the work, until very recently, has concentrated on relatively simple turbulent shear flows, usually those in which the 'thin-shear-layer approximation', originally developed by Prandtl[2], can be applied. A thin layer is an obvious starting point from the fluid mechanic point of view, but also the immediate requirements of the engineer, in particular the aircraft designer, have no doubt played their part. There are, however, many practical flow situations even around an aircraft in which the above approximation cannot be applied because the shear layers are not 'thin' and slowly growing. This does not necessarily imply that such flows are radically different from Prandtl's thin shear layers; simply that because of the extra interactions, accelerations or distortions involved present day calculation methods are usually inapplicable.

Because of the great lack of experimental data relating to such complex flows there are two outstanding requirements which need to be met before it becomes feasible to construct useful calculation procedures. Firstly and obviously, more data are needed and any experiments should be oriented towards particular physical phenomena. Secondly, it is important to understand, in principle at least, the basic physical processes occurring. It is dangerous (though possible) to relate calculation methods to experimental data without such understanding. The work described in this Thesis is an attempt to satisfy, in part, these

two requirements in the case of turbulent shear flows subject to large curvature. Such flows are typical of a number of engineering situations, especially the flow around 'partly streamlined' bodies, whose shapes are constrained by non-aerodynamic considerations. High speed vehicles are the most prominent example of bodies whose air resistance is important but which cannot be as well streamlined as an aircraft. In view of Donald Campbell's life-long association with high speed cars and boats it was felt that this would be a suitable line of investigation during the author's tenure of the first Donald Campbell Fellowship.

Since the long-term aim is to assist in the evolution of calculation methods which are able to cope with such complex flow situations, an experiment on an idealised flow is clearly a more profitable approach than, say, the ad hoc investigation of a particular practical problem. The latter would perhaps be of more immediate use but we aim to gain understanding of basic phenomena in order to provide useful data for calculation methods. The former has certainly been achieved and it is felt that progress has been made towards the latter, although, particularly as some of the results were totally unexpected, our understanding is still far from complete.

The following sections of Chapter 1 briefly review the literature and introduce the present experiment.

1.2 GENERAL EFFECTS OF FLOW CURVATURE

Rayleigh[3] was perhaps the first to consider the influence of curvature on the stability of fluid flow. His analysis, which was explained in some detail by Wattendorf[4], indicated that the motion of an ideal fluid with mean tangential velocity U at a distance R from the centre of curvature of the streamline is stable if the radial gradient of the angular momentum UR is positive and unstable

if it is negative. The truth of this general criterion in turbulent flows has been amply demonstrated. Wattendorf and, more recently, Eskinazi & Yeh[5] and co-workers have made measurements of the turbulent flow in curved ducts. Eskinazi & Yeh found that the production of turbulence is larger near the outer concave wall and smaller near the inner convex wall than the corresponding values in a straight channel, in agreement with Rayleigh's stability criterion.

Stratford, Jawor & Golesworthy[6], Sawyer[7], Guitton[8] and others have shown that a wall jet on a convex surface grows more rapidly (and that on a concave surface less rapidly) than a jet on a flat surface which, again, is to be expected from Rayleigh's criterion. In the convex wall jet there is a large outer region where the momentum gradient is negative so that the turbulence is amplified with a consequent increase in entrainment and jet spreading rate. Conversely, measurements made in boundary layers developing on a convex wall by Patel[9], Schmidbauer[10] and Schubauer & Klebanoff[11] suggest indirectly that in this case convex curvature reduces the turbulence level. So & Mellor[12], in addition to confirming these findings, measured the turbulent energy and shear stress directly and found that, as expected, convex curvature tends to reduce the production of turbulence. These authors also investigated the system of longitudinal vortices, similar to Taylor-Görtler vortices, existing at the concave wall (unstable curvature effects) whose existence had previously been recognised by a number of authors: Patel[13] for example.

Because of the turbomachinery and geophysical applications there is considerable interest in the effects of rotation on shear flow turbulence. Rotating flows, particularly those rotating about an axis perpendicular to the plane of mean shear, are directly analogous

to flows with longitudinal streamline curvature. (In fact most of the basic differences result from the different co-ordinate systems usually employed for the two cases). Johnston[14] and Halleen & Johnston[15] have studied the effects of rotation on the boundary layers in turbo-machines and on flow in a rectangular duct. They found that rotation suppresses turbulence production in regions where simple stability analysis (similar to Rayleigh's analysis for curved flows) indicates that it should. Indeed, at sufficiently high rotation, complete relaminarisation of the trailing (stable) side wall layers was observed. Hughes[16] has made measurements in the boundary layers on the centre body (stationary and rotating) of an annular diffuser and found similar general effects. Although Schmidbauer's 1936 experiment clearly indicated the importance of curvature effects in boundary layers, Thompson[17] was perhaps the first author to indicate the necessity of incorporating a curvature parameter in calculation methods. He found that for small flow curvature, as was present in the aerofoil experiments of Schubauer & Klebanoff for example, the effect of the streamline curvature on the turbulent motions and the entrainment of free stream fluid was much more important than the extra terms in the mean motion equation. Such effects can be appreciable even for quite small mean flow curvature. In fact, as Bradshaw[18] has pointed out, the fractional change in apparent mixing length is typically of the order of ten times the ratio of the extra rate of strain caused by curvature ($\frac{U}{R}$) to the usual strain rate, $\frac{\partial U}{\partial y}$ say. For small curvature Bradshaw was able to modify the calculation method of Bradshaw, Ferriss & Atwell[19] by considering the meteorological analogue (buoyancy) of streamline curvature. If the transport terms are negligible he deduced a 'Richardson' number for curved flow

$$Ri = \frac{2U}{R} \Big/ \frac{(\overline{uv}/\rho)^{\frac{1}{2}}}{L}$$

where L is the dissipation length parameter used in Bradshaw et al. By replacing L by

$$L \,/(1 + 7(\frac{2U}{R} L \,/(\frac{\tau}{\rho})^{\frac{1}{2}}))$$

he obtained a significant improvement in the agreement between calculation and the data of Schubauer & Klebanoff and Schmidbauer.

Simple linear corrections such as this will obviously fail in cases where streamline curvature is large. Indeed, as Bradshaw[18] pointed out, the curvature in the experiments of Eskinazi & Yeh[5] was so large that the curved-flow analogue of free convection appeared (UR ~ constant). In these cases the flow was grossly altered and clearly any calculation method may well need to take into account the extra Reynolds stress gradients in the equations of mean motion as well as the dynamic effects on eddy structure. A first requirement therefore, as indicated in Section 1.1, is information on how the turbulence in general and the Reynolds stresses in particular react to the disturbing effect of large extra rates of strain caused by flow curvature.

1.3 THE PRESENT EXPERIMENT

The basis of the present work is, as the title suggests, an experimental investigation of a highly curved mixing layer. It was decided that a fairly simple distortion of one of the well-documented plane shear flows would provide more useful information than an investigation into a more complex flow situation. One of the latter that was considered was the flow down a backward facing step but this is a considerably more complicated flow. Because of the separation there is a basic change of 'species' of thin shear layer, from

boundary layer to free mixing layer and back to boundary layer, so that effects other than those caused by curvature or pressure gradients will be apparent.

It is fairly simple to produce a plane self-preserving mixing layer and this flow has the advantage of a relatively large scale (compared with the usual laboratory boundary layer, for example): it is generally easier to make measurements in a large scale flow. Accordingly it was decided to generate a plane mixing layer and then apply a large distortion by deflecting it through 90° (Figure 5.1 and Plate 3). This is half an impinging jet - a flow of practical interest. The latter will presumably eventually recover to its usual self-preserving state and particular interest is focused on the region of distortion itself and the recovery region that follows it.

A disadvantage of the free shear layer is the presence of high percentage turbulent intensities at the low velocity edge; instrument accuracy is usually less in such regions. This no doubt is partly responsible for the scatter in the published measurements of self-preserving shear layers. It was therefore decided to perform a baseline experiment by measuring all the relevant quantities in the self-preserving layer, so that useful comparisons between these and the results in the distorted layer were possible.

Chapter 2 describes the basic experimental arrangements and the instrumentation, whilst Chapter 3 introduces the various axis systems used and sets out the Reynolds-stress transport equations in these various co-ordinates. Chapter 4 presents the self-preserving layer results and Chapter 5, which contains the bulk of the work, describes the results of measurements in the curved mixing layer. The main results are discussed and some subsidiary measurements presented in Chapter 6.

2. THE EXPERIMENTAL ARRANGEMENTS AND INSTRUMENTATION

2.1 THE WIND TUNNEL

The experimental programme was carried out in the 30" x 5" No. 1 open circuit boundary layer tunnel of the Department of Aeronautics (fully described in IC Aero Report 72-10). This tunnel is driven by a 12½ kW centrifugal blower, has a contraction ratio of 9 and a maximum speed of about 45 m/s. The working section which is used for boundary layer work is in two separate lengths of 1.45 m and has an adjustable roof. In the present investigation, however, this working section was used only for measurements in the plane self-preserving mixing layer, when the roof was removed and the side walls extended. A special rig for reproducing a mixing layer which is turned through 90° was designed and built in the departmental workshop. Plates 1 and 2 show the rig in position at the exit of the contraction. The position of the backplate could be adjusted longitudinally to select the width of the shear layer in the region of deflection and also vertically in order to vary the quantity of air bled from the base for boundary layer control. Once a suitable and stable flow had been obtained (as detailed in Section 5.1.1) the backplate was kept in the same position throughout the complete experimental programme.

The dynamic pressure in the contraction exit was found by Wong[20] to be uniform to within 0.2% of $\frac{1}{2}\rho U^2$ at about 30 m/s and the turbulent intensity $\frac{\sqrt{u^2}}{U}$ (with the backplate in position) measured with an unlinearised hot wire and corrected for electronic noise was about 0.08% at 15 m/s rising to about 0.12%.at 30 m/s. This was somewhat higher than the values obtained with the normal working section in position but was still two to three orders of magnitude below typical turbulence levels in the shear flow under investigation. From rough

$\overline{u^2}$ spectra measured in the exit there appeared to be no dominant frequency.

The contraction exit velocity was monitored by a Betz manometer, measuring the difference between the settling chamber total pressure and the exit static pressure. For practically all the experiments described in Chapters 4 and 5 the exit velocity was kept at about 30.3 m/s.

2.2 TRAVERSE GEAR

A number of the wind tunnel working sections in the Aeronautics Department are fitted with 3½" brass discs which plug into brass rings inserted into the tunnel floor. These discs can be fitted with various types of traverse gear and for convenience similar arrangements were made for the present work. The curved layer rig was fitted with mounting rings spaced at intervals along the centre line of the floor and the backplate. Exclusive use was made of a Disa traverse gear type 55H01 which was adapted to enable it to be attached to one of the brass discs (Plate 2 shows the complete assembly mounted on the backplate). The traverse gear could be fitted with pitot tubes, hot wires or thermocouples as required.

For making measurements in the curved part of the distorted shear layer a somewhat different arrangement was required as it was necessary to align the probes along or close to the local mean streamline and to traverse normal to it. Chapter 5 describes how the actual position of the curved flow was first determined and once this had been done a rotating traverse mechanism was designed and built. This consisted basically of a rectangular section bar spanning the gap between the two side walls at a position corresponding to the approximate centre of curvature of the curved layer (Plate 3). The bar, which could be

rotated about its own axis in steps of $2\frac{1}{2}^{o}$, carried the Disa traverse gear which was usually mounted at the centre but could be moved laterally along the bar to enable checks of spanwise consistency to be made. A further mechanism was constructed which enabled the hot wire probes to be rotated in pitch to an accuracy of $\frac{1}{2}^{o}$. Movements of this pitch mechanism altered the spatial position of the probe so that careful calibration was necessary to determine the Disa traverse rod movement necessary to compensate for this. The traverse gear had a ten-turn potentiometer attached so that probe position could be measured simply by the potentiometer output voltage. The complete arrangement of rotating traverse, Disa traverse gear and pitch mechanism is shown in Plate 2 and the sketch in Figure 5.1 shows the various movements possible.

The Disa traverse gear was calibrated (using slip gauges) to give 10.00 volts for 10.00 cms of movement with an accuracy of 0.1% of full scale. Actual spatial position of the probe was of course only known to the accuracy of measurement of the initial zero position which was about ± ¼ mm. Traverses which involved movement of all three mechanisms (pitch, rotation and radial movements of the traverse arm in the pitch plane) were a little less accurate; careful checks showed that once the probe had been set in an initial zero position it could be moved to any desired position in the flow (subject to the limits of the system) to an accuracy of ± ½ mm. Most traverses in fact only required movement of one or two of the mechanisms and since the shear layer width was, at the very least, 50 mm over the range of interest the positional accuracy was considered satisfactory.

2.3 PITOT TUBES AND MANOMETERS

Total-pressure measurements were made using three pitot tubes (Plate 4) manufactured in the Departmental workshop. Because of the

initial uncertainty of the mean flow direction in the curved mixing layer it was important to have as good a pitch (or yaw) response as possible. The probes were calibrated for yaw in the small 20" octagonal closed circuit wind tunnel in the Aeronautics Department and found to have a flat response to within 0.1% of $\frac{U}{U_{max}}$ over $\pm 12\frac{1}{2}^{o}$ and to within 1% over $\pm 20^{o}$ (Figure 2.1).

For most of the pressure measurements an Airflow Developments Mk. 5 manometer was used. This instrument has a single inclined tube which could be rotated in a vertical plane so that the full scale reading corresponded to ½", 1", 2" or 10" of water. The four scales gave internally consistent readings over most of the overlap regions to within 1% on pressure (½% of velocity): they were calibrated against the Betz manometer used for monitoring tunnel speed and found to differ by less than 1% on total pressure over the whole range.

2.4 HOT WIRE TECHNIQUES

2.4.1 Hot Wires and Calibration Procedures

Disa single and crossed hot wires, types 55F01 and 55A38 respectively, with type 55D01 constant temperature anemometers and associated equipment including a type 55D30 r.m.s. meter, were used for all the turbulence measurements and for mean flow profiles in regions where the static pressure varied rapidly (i.e. the 'corner' region of the curved mixing layer). In an investigation of heat transfer laws for long, fine wires Bradbury & Castro[21] (Appendix I) found that the relationship suggested by Collis & Williams[22] for the wire Reynolds number range $0.02 < R < 44$, given by

$$N_m \left(\frac{\Theta_m}{\Theta_a}\right)^{-0.17} = 0.24 + 0.56\, R_m^{0.45}$$

was accurate to within about 10% for $2 < \frac{\Theta_w}{\Theta_a} < 30$, where Θ_w refers to the wire temperature. N, Θ, R are the Nusselt number, temperature and

Reynolds number respectively and the subscripts, m and a, refer to wire properties evaluated at the mean temperature (θ_m) and the ambient temperature (θ_a) respectively. The wire aspect ratios for which a correction was applied varied between about 1000 and 2000, but some tests were made on shorter wires to ensure that there were no large aspect-ratio effects.

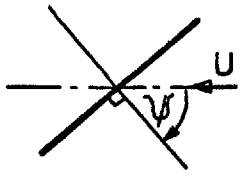
In common with many other workers, therefore, the relation

$$E^2 = E_o^2 + BU^{0.45} \qquad 2.1$$

was used for all hot wire calibrations and this was found to give a good fit to the data in the speed range $3 < U < 30$ m/s (even though the aspect ratio of a typical Disa hot wire is about 200) provided that the wire was not very old or dirty. E_o^2 was found by plotting E^2 against $U^{0.45}$ and extrapolating back to zero velocity - it is therefore not the value of E^2 actually measured in still air. Each wire was calibrated immediately before and after every traverse to ensure that drift was negligible and if variations of more than 2% on E^2 at a given velocity occurred the traverse was rejected. Figure 2.2 shows a typical crossed-wire probe calibration.

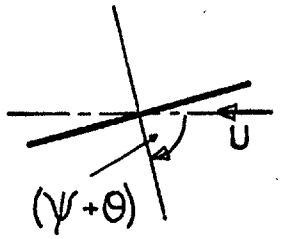
2.4.2 Yaw Response Calibrations

Consider a wire at an angle $(90 - \psi)^o$ to the x-axis (see sketch below). The simplest assumption for the yaw response is that the wire responds only to the component of velocity normal to its axis, so if $V = 0$ the effective velocity is $U\cos\psi$. However the 'effective' (or apparent) angle ψ_e may not be exactly equal to the geometrical angle ψ, which is anyway difficult to measure accurately, and it is therefore better to calibrate the wire for yaw. This was performed by mounting the crossed-wire probe in a free stream of constant velocity and measuring the anemometer output voltages for various yaw angles.



For a yaw angle of θ (see sketch) and assuming an effective cosine law (2.1) becomes

$$E_\theta^2 = E_o^2 + B(U\cos\overline{\psi_e + \theta})^{0.45} \quad .$$



Using the corresponding equation for $\theta = 0$ it follows that

$$\sin\theta\tan\psi_e = \cos\theta - \left\{\frac{E_\theta^2 - E_o^2}{E_{\theta=0}^2 - E_o^2}\right\}^{1/0.45} \quad .$$

The right-hand side is plotted against $\sin\theta$ and a straight line drawn through the points; its slope is therefore $\tan\psi_e$. This procedure amounts to a curve fit, the cosine curve being chosen to touch the real calibration when the flow is along the probe axis. Any deviation of the points from a straight line is (after allowing for any experimental errors) a measure of the error caused by assuming an 'effective' cosine law response. Figure 2.3 shows a typical yaw calibration from which it can be seen that the effective cosine law was quite adequate up to at least $\pm 15^\circ$ to the $\theta = 0^\circ$ line, or in other words down to at least 30° to the wire axis. The work described in Appendix V (mentioned below) suggests that the effective cosine law is adequate for even larger angles. The effective angle ψ_e drifted very little with time and often did not change significantly over a period of one to two weeks of continuous running.

It is possible to adopt more complicated formulae for the yaw response, most of which involve the velocity component tangential to the wire. Some authors (Rodi[23] for example) go as far as calibrating the wire in pitch and yaw right up to angles almost coincident with the wire-axis and then claim greater accuracy at high turbulence levels. But at high turbulence levels the instantaneous velocity vector will often be approaching the wire from behind (particularly a wire inclined

at 45° to the x-axis) and whatever one does it is impossible to correct for the consequent 'rectifying' effect of the wire. In Appendix V this problem is investigated more closely: the conclusion is that any increase in accuracy attainable by using complicated yaw-response calibration procedures does not warrant the extra effort and time required. It seems that there are so many other uncertainties in hot-wire operation that such increase in accuracy is lost in the 'background scatter' observable in the general run of published hot-wire measurements, particularly in such high-intensity flows as the one under investigation here. However, in many cases it is possibly worth using the relatively simple Champagne et al.[24] tangential cooling method, but since only comparative results were sought, even this was not considered worthwhile in the present experiments.

2.5 ANALOGUE AND DIGITAL RECORDING

Apart from mean flow measurements, a few exploratory intensity measurements and U-component spectra, all the turbulence data were obtained by recording the hot-wire signals on analogue magnetic tape and subsequently digitising and recording on digital magnetic tape for reduction on the CDC 6400 computer at Imperial College. If only mean squares and cross-products (i.e. $\overline{u^2}$, $\overline{v^2}$, $\overline{w^2}$ and $\overline{uv}$) had been required this would have been a somewhat expensive, though probably more accurate, method compared with using analogue equipment, but since triple-products were required and the necessary recording and digitising equipment was readily available it was felt to be well worthwhile. Storing the data on magnetic tape also provided the opportunity for further information, such as the intermittency, to be found at a later date if required.

As little electronic equipment as possible was used between the anemometers and the tape recorder so as to reduce electronic noise, drift of zero levels and the like. Each anemometer output signal was passed through a high-pass filter to remove the d.c. and then through one of the modular operational amplifiers ("PHI system") developed in the Department by Mr. B.J. Belcher and manufactured by Servicon Dynamics Ltd. These were arranged to have a variable gain to bring the signal to a suitable level for recording on an Ampex FR1300 analogue tape recorder. The gain was measured using a calibrated signal from a sine-wave generator. All recordings were made at a tape speed of 60 ins/s and at this speed the tape recorder had a frequency response of 20 kHz.

Digital recording was performed using a small PDP-8/L computer controlling an AD08B analogue to digital converter and an Ampex TM16 digital tape transport. The input requirements of the AD converter were not compatible with the analogue recorder output voltage levels, so the signals were passed through a further series of modular, operational amplifiers with fixed gains and summing d.c. voltage lines. The system had a total digital sampling rate of 20,000 per second (although the analogue tape speed could be varied if required to alter the effective digitising rate) on 1 to 4 input channels (5,000 samples per second per channel for 4 channel recording) and a quantisation level corresponding to 10 binary bits or 1 part in 1024. For crossed-wire work only two channels were required so the effective sampling rate was 10,000 per second.

The operation of the complete system is described fully by Bradshaw[25].

2.6 ANALYSIS OF DIGITAL DATA

During the course of the present investigation there were a number of workers in the Department using the analogue-to-digital (AD) conversion system described briefly in Section 2.5, so that much of the necessary computer programming had been done. In particular, Dr. A. Brandt had written the subroutines required to read in and de-multiplex the 12-bit (PDP) words from the digital tape and store them in the CDC 6400. This involved putting them in 60-bit (CDC) words and then sorting them into arrays, for each of the original channels (two in this case). These routines are described in detail in Brandt & Bradshaw[26]. It was left to the individual user to deal with the resulting data as desired.

In this case two programs were used. Each included a routine to convert the data into suitable physical form (u- and v-component signals) by linearising and combining the two original signals. The equations used for this, derived from the hot-wire response equations, are laid out in Appendix III. Program DIGAN then computed all the powers and cross-products required.

It was not necessary to analyse every single datum point as the sampling rate was effectively 10 kHz (having been chosen with the requirements of conditional sampling in mind) so that adjacent samples were highly correlated. Checks showed that the resulting time lag between points on different channels was small enough for the errors caused by assuming the points to be sampled instantaneously to be insignificant, but sequential sampling did prevent the possibility of large reductions in the analogue tape speed to lower the effective sampling rate and computer central processor (CP) time required. Instead only every 40th pair of datum points were linearised and used for the running averages. For a typical sample of 20 seconds

(real time) duration this amounted to using 5000 almost random datum points, which was quite adequate (see for example Mandel[48]) and reduced the CP time by at least a factor of 2.

About 12 20 second samples could be recorded on a single digital tape, so the usual procedure was to record a complete traverse (8 - 12 stations) on one digital magtape. Program DIGAN included a subroutine (FIND) which could search for any particular recording but the usual scheme was for DIGAN to operate on each recording sequentially and hence output the results for a complete traverse.

Development of DIGAN included checking on the sample length required to obtain steady ("converged") averages of the various turbulence quantities. Tests for convergence were made using two typical signals, one recorded in the centre of the mixing layer where the turbulent intensity was high and the intermittency low and the other in a region of low intensity and high intermittency. It was expected that a longer sample would be required to get good, steady values in the intermittent region. Figure 2.4 is a plot of the running average of $\frac{\overline{u^2}}{U_r^2}$ computed after every 5000 points ($\frac{1}{2}$ second real time since for this test <u>every</u> datum point was used) up to 200,000 (20 seconds real time) for these two signals. Figure 2.5 is a similar plot for one of the triple products ($\frac{\overline{v^3}}{U_r^3}$). It is clear that convergence takes longer for the highly intermittent signal. However, the actual, absolute value of the turbulence parameter is usually considerably less in the highly intermittent region of the flow (except for quantities like $\overline{u^4}$) so that the accuracy of the result expressed as a percentage of its final value need not be so high. For example, the 'waviness' of the $\frac{\overline{u^2}}{U_r^2}$ signal in the high intensity region between 10 and 20 seconds is no more than about 1% of its final value whereas for the intermittent signal it is more than 2%,

but the actual value of $\frac{\overline{u^2}}{U_r^2}$ for the latter signal is an order of magnitude less than the high intensity value. 20 seconds was chosen as the length of sample used for all the turbulence computations. This would perhaps be a little excessive if only second order products were required, but as higher order quantities were needed and since one would usually use integrating times of at least 20 seconds if analogue instruments were used, this was felt to be a suitable compromise.

In contrast to the conditional sampling programs the de-multiplexing subroutines were responsible for most of the CP time. For the 20 second sample, the total CP time was about 60 seconds of CDC 6400 time, of which only about 10% was attributable to the linearisation and calculation of the turbulence quantities.

For the intermittency measurements program CS4A (described in reference 26) was modified. Setting up the intermittency criteria is described in Section 4.6 and since no conditional averages were required most of the running average routines were removed to save CP time. The resulting program (CS4C) had a run-time of about 600 seconds of CDC 6400 time/20 seconds of real time data, which was about half the time required for the full CS4A program (reference 26).

2.7 OTHER INSTRUMENTATION

Initial work to set up the best position of the backplate in the curved layer rig involved flow visualisation. The standard oil-flow technique, using a mixture of kerosene and "Dayglo" fluorescent powder was used to investigate the general flow pattern on the floor and the backplate and a paraffin smoke generator was used to investigate the general behaviour and position of the curved mixing layer.

To check for possible three-dimensionality (lateral convergence or divergence) of the flow and for the measurement of a mean flow streamline in the potential flow region at the high-velocity edge of the mixing layer, the heated-wake technique was used. A Nichrome wire stretched between the side walls was heated to almost red heat using a 2 kW Variac and temperature profiles in the wake were measured with a Comark thermocouple system and digital voltmeter. Some zero drift problems were encountered but by using a second thermocouple as a reference in the Comark differential thermocouple system it was possible to detect temperature differences as low as $0.1^{\circ}C$, which was quite adequate for the purposes mentioned above.

At the beginning of the investigation, while the wind tunnel was being built and while awaiting the d.c. motor and thyristor drive, some time was spent in developing the pulsed hot wire anemometer (Appendix II). It was felt that this instrument might well be used at a later stage for measurements in regions of the flow where hot-wires would be too inaccurate. In the event time did not permit this work but the apparatus is now being used for deflected jet studies by another worker in the Department.

PLATE 1. Rig for the curved mixing layer experiment.



PLATE 2. Rotating traverse arrangements.

(See also fig. 5.1)

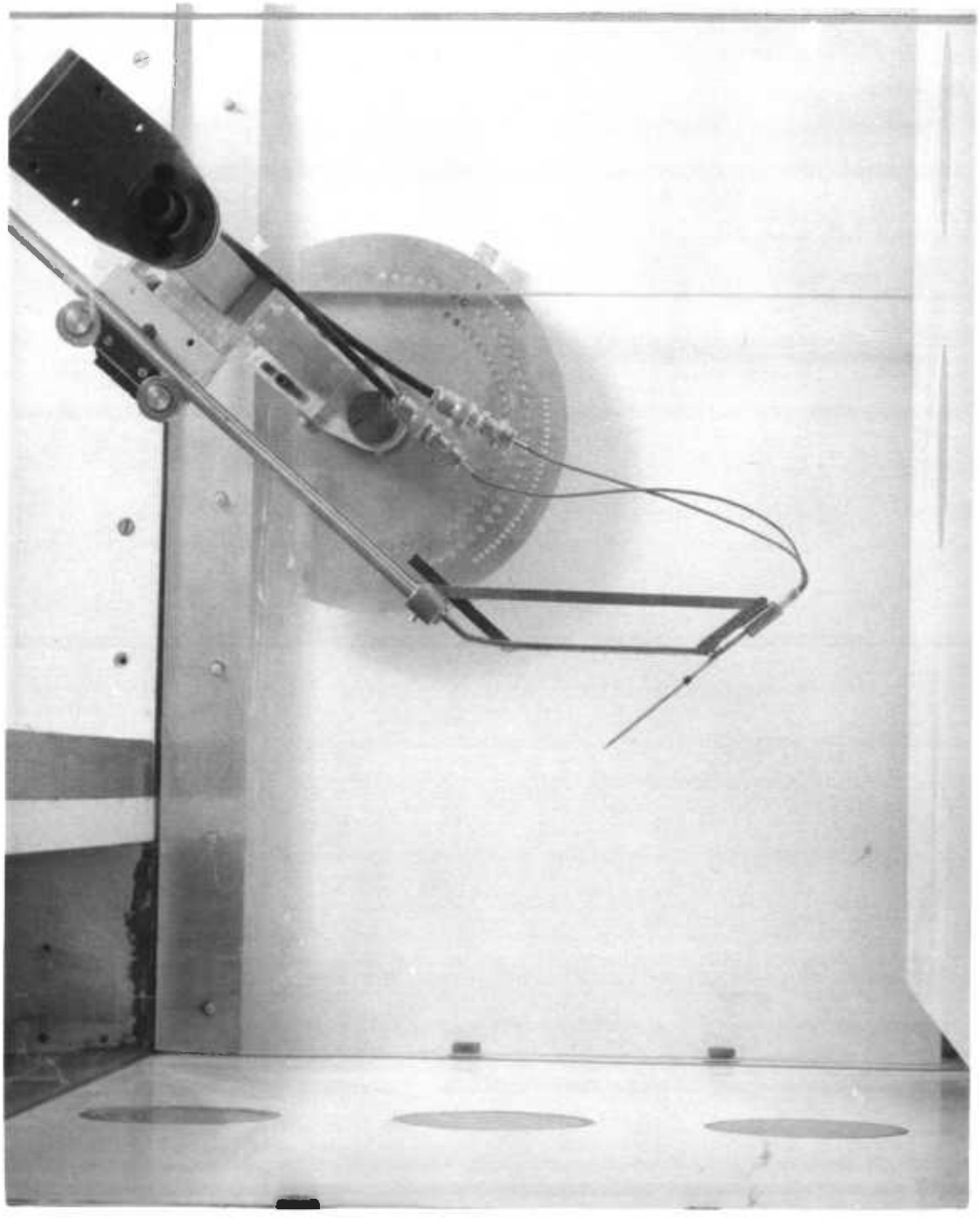
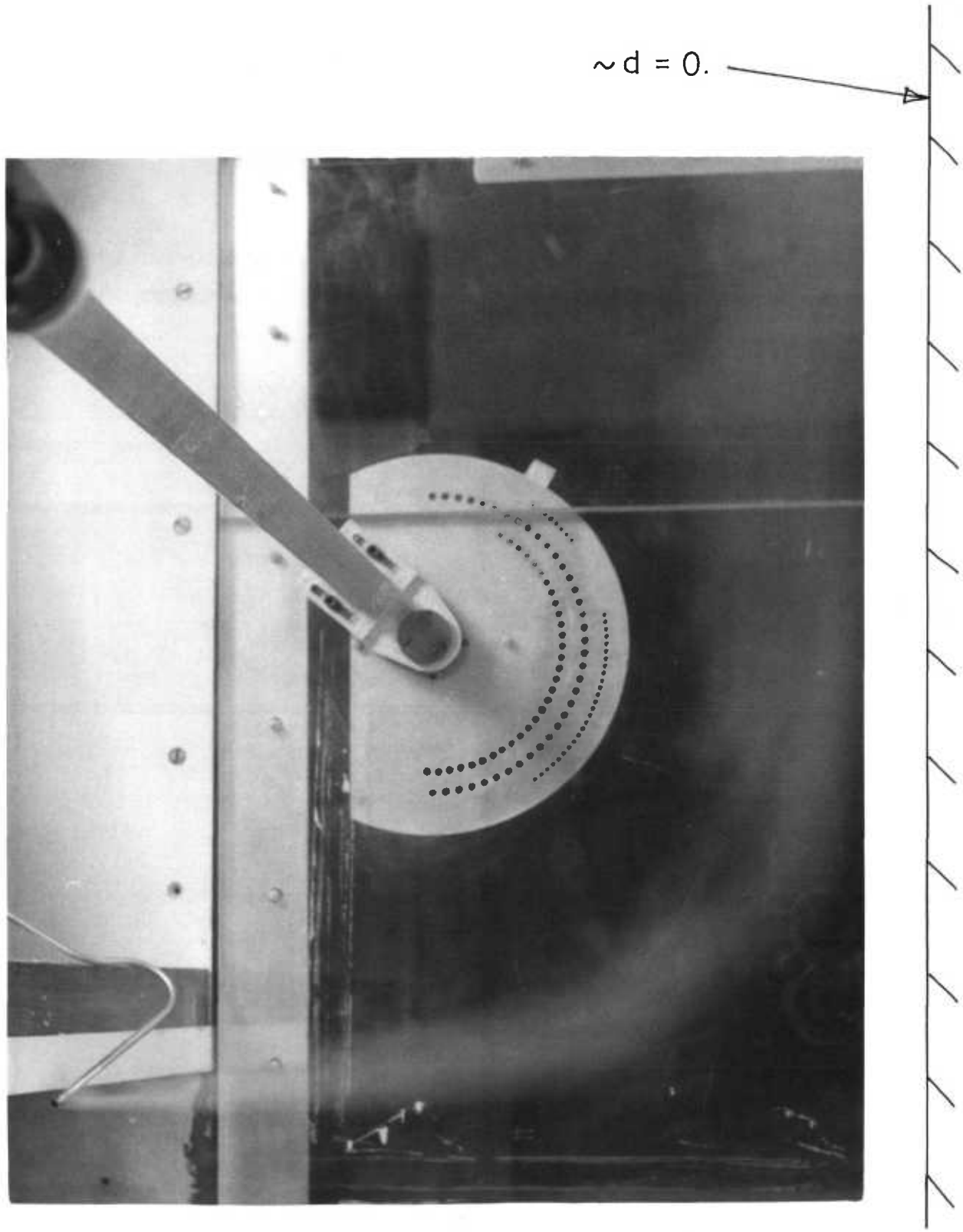


PLATE 3. Flow visualisation showing approximate position of curved mixing layer.



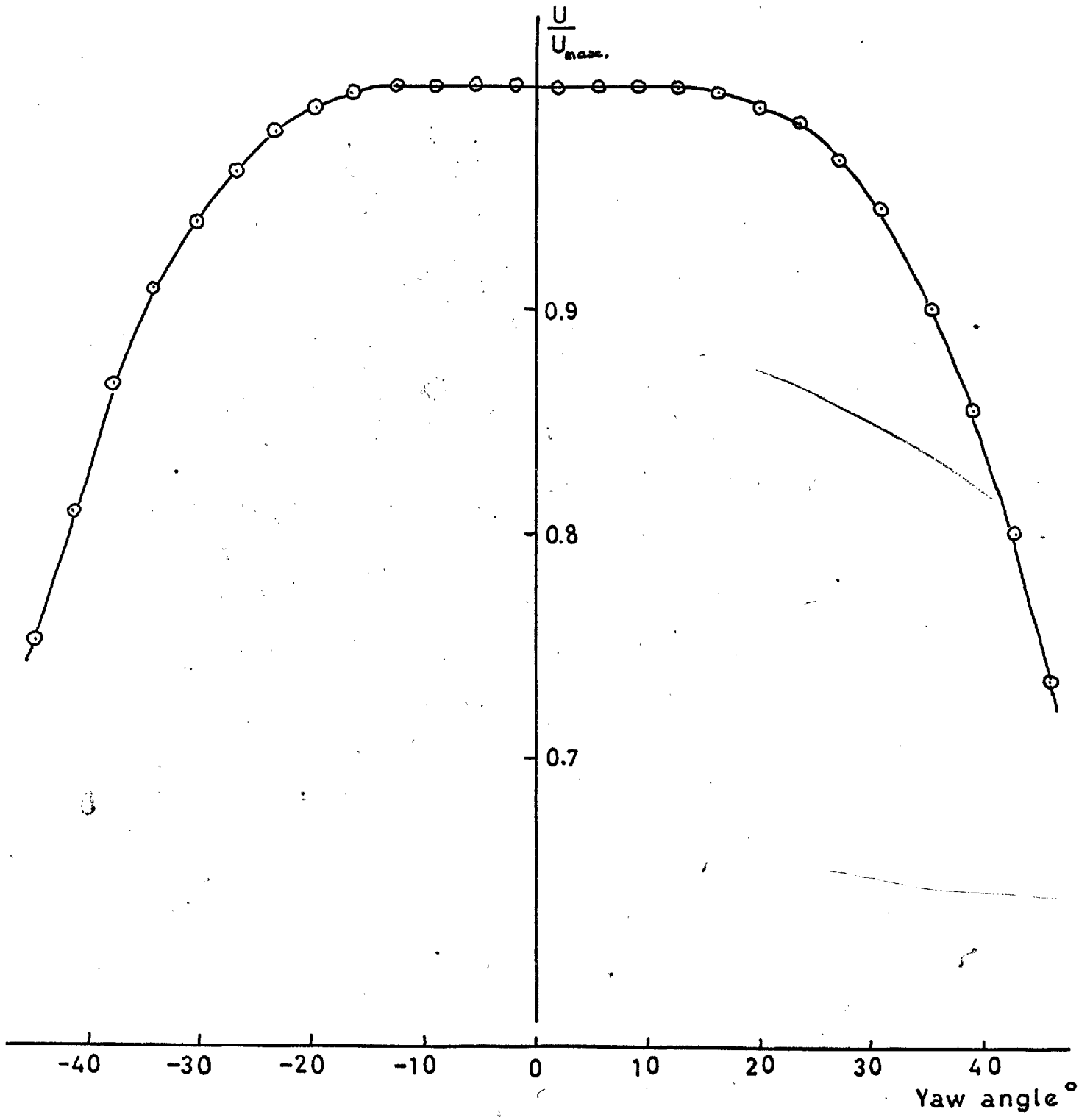


FIG. 2.1. Pitot tube yaw response.

FIG. 2.2 Typical crossed hot wire calibration.

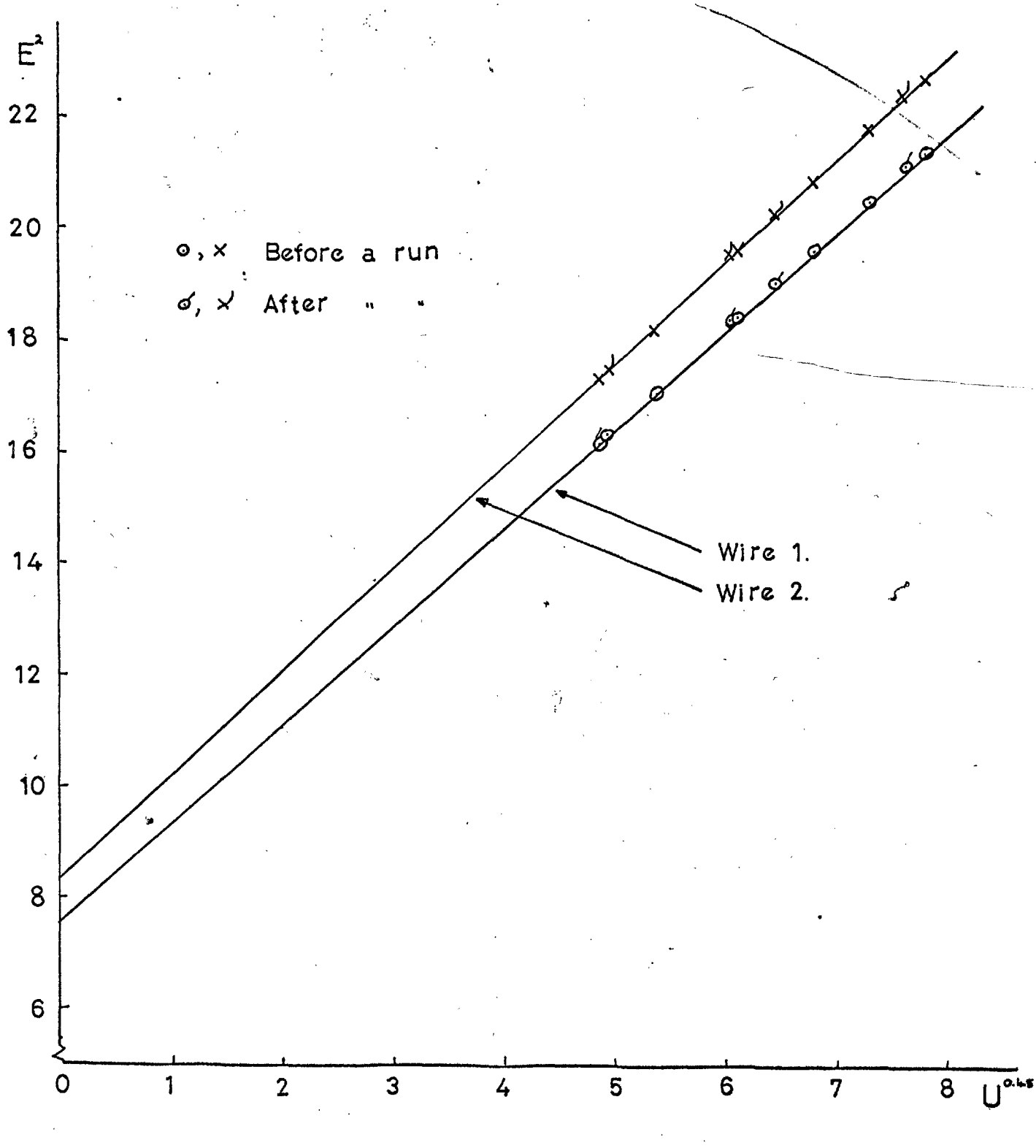
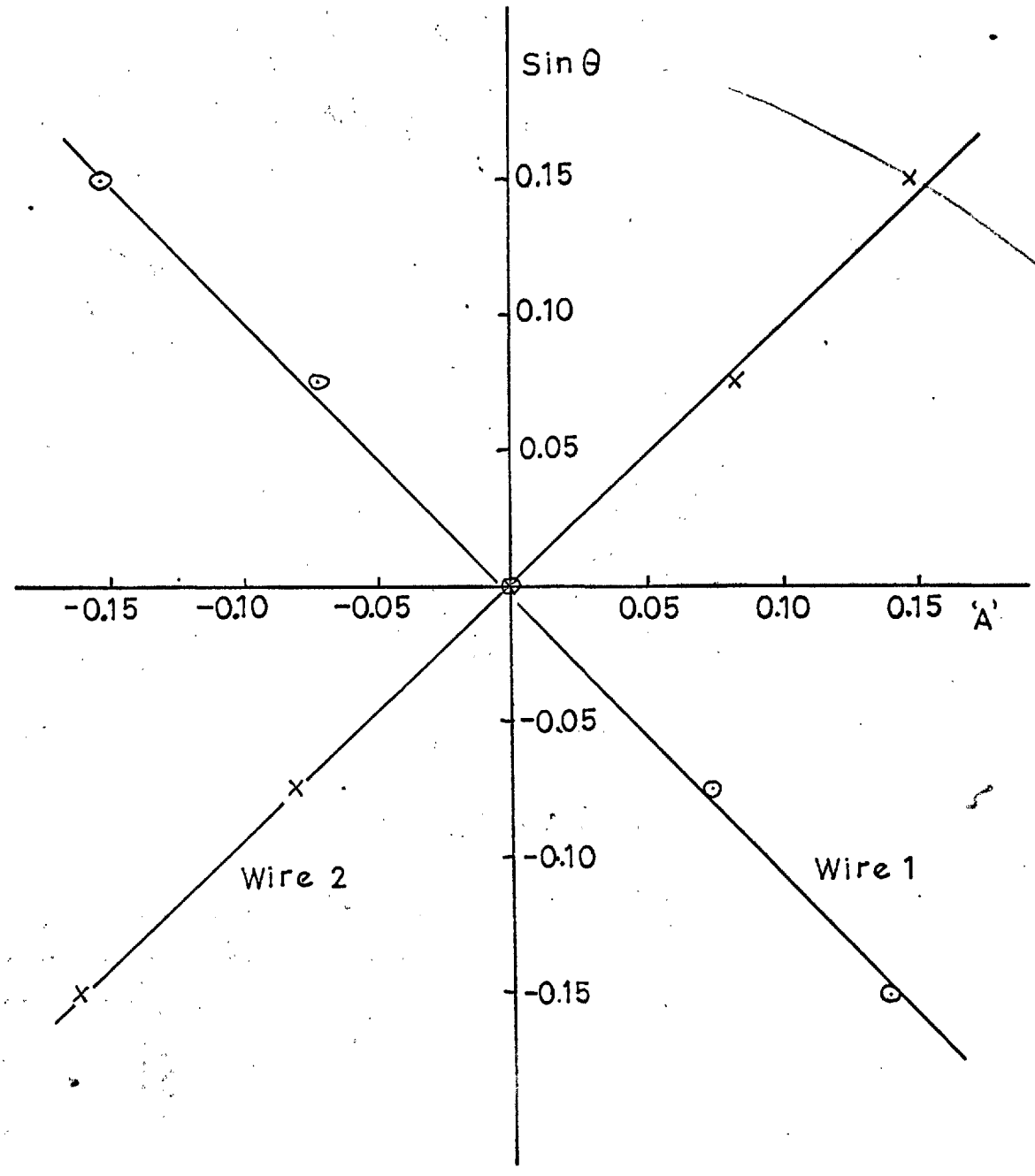


FIG. 2.3 Typical crossed hot wire yaw response.



$$'A' = \cos\Theta - \left[\frac{E_{\theta}^2 - E_o^2}{E_{\theta=0}^2 - E_o^2}\right]^{1/0.45}$$

FIG. 2.4. Cumulative $\overline{u^2}$ (after every 5000 points.)

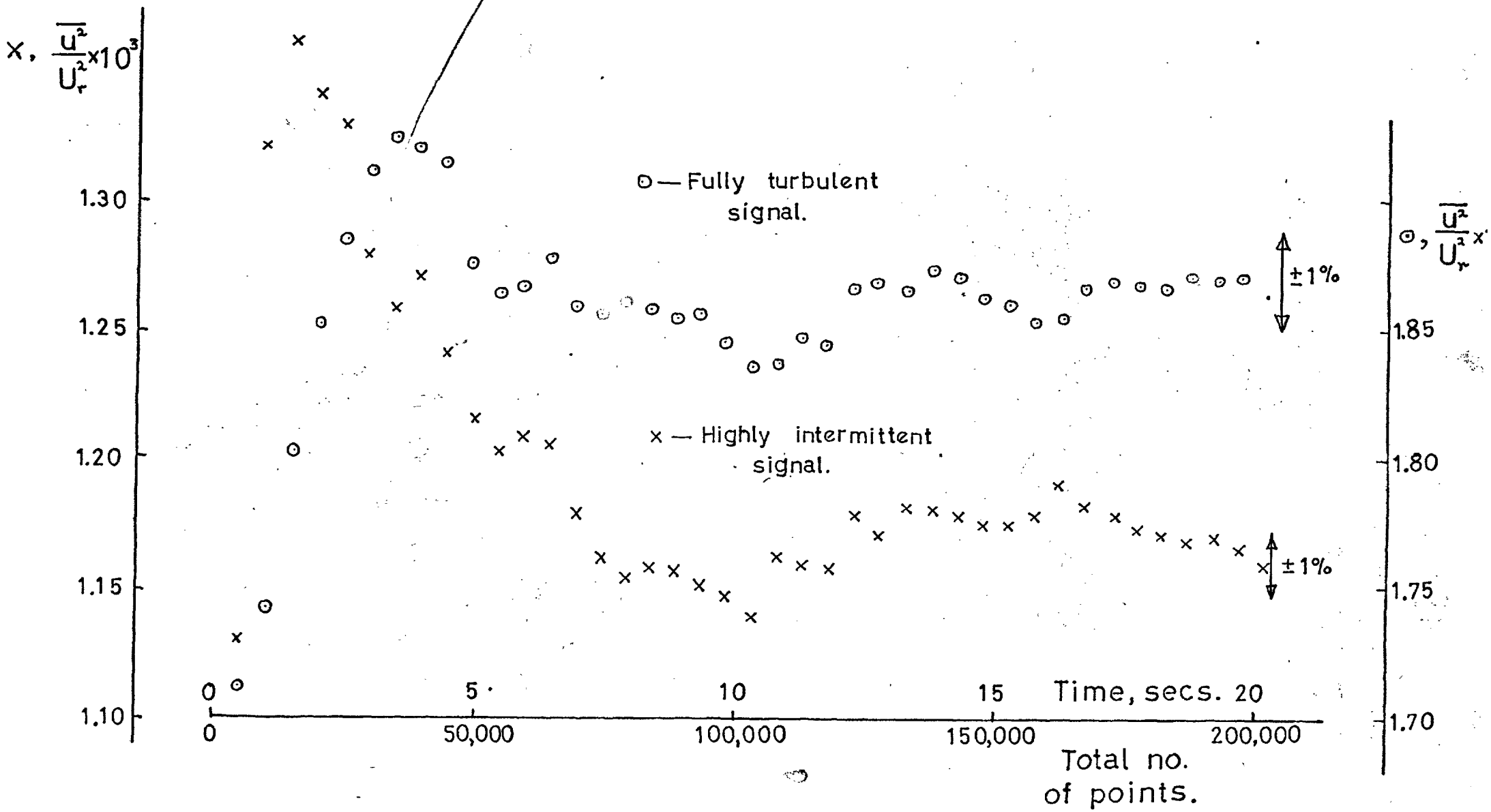
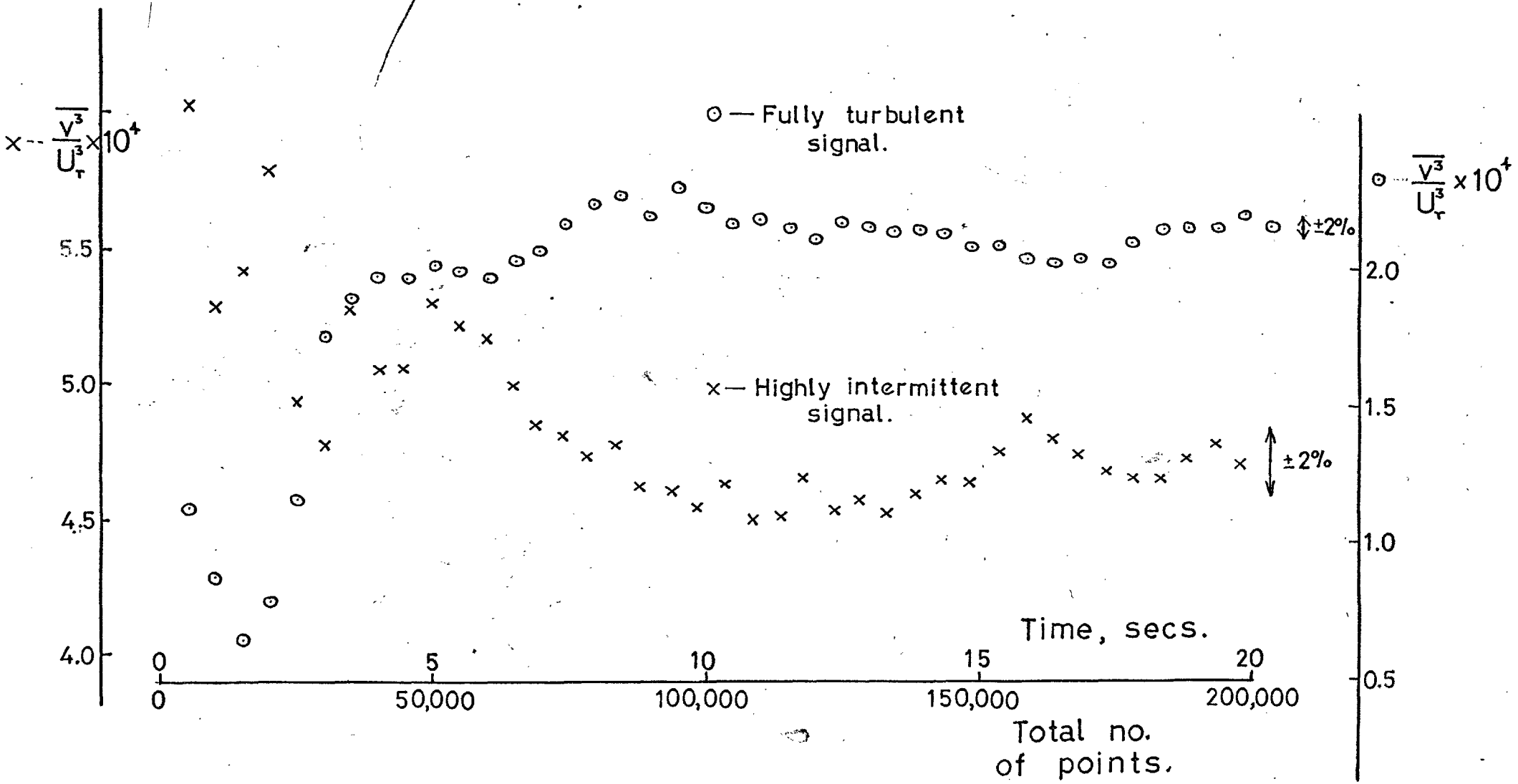


FIG. 2.5 Cumulative $\overline{v^3}$ (after every 5000 points)



3. TRANSPORT EQUATIONS AND NOTATION

3.1 THE TRANSPORT EQUATIONS IN CARTESIAN AXES

The exact transport equation for the Reynolds stresses $\overline{u_i u_j}$ is (see for example Hanjalic & Launder[27])

$$\frac{D}{Dt}(\overline{u_i u_j}) = -\left[\overline{u_j u_k}\frac{\partial U_i}{\partial x_k} + \overline{u_i u_k}\frac{\partial U_j}{\partial x_k}\right] - 2\nu\,\overline{\frac{\partial u_i}{\partial x_k}\cdot\frac{\partial u_j}{\partial x_k}}$$
$$+ \overline{\frac{p'}{\rho}\left(\frac{\partial u_i}{\partial x_j} + \frac{\partial u_j}{\partial x_k}\right)} - \frac{\partial}{\partial x_k}\left[\overline{u_i u_j u_k} - \nu\frac{\partial \overline{u_i u_j}}{\partial x_k}\right]$$
$$- \left[\frac{\partial}{\partial x_i}\overline{pu_j} + \frac{\partial}{\partial x_j}(\overline{pu_i})\right] \qquad (3.1)$$

with the usual suffix notation. The equation for the turbulent energy transport can be obtained by equating i and j and summing, writing $\overline{q^2}$ for $\overline{u_i^2}$. Neglecting the viscous diffusion term $\left(\nu\frac{\partial}{\partial x_k^2}(\overline{u_i u_j})\right)$ and noting that the first pressure term disappears for i = j we obtain, in x-y-z axes

$$\frac{D}{Dt}(\tfrac{1}{2}\overline{q^2}) \equiv U\frac{\partial \frac{1}{2}\overline{q^2}}{\partial x} + V\frac{\partial \frac{1}{2}\overline{q^2}}{\partial y} = -\overline{uv}\left(\frac{\partial U}{\partial y} + \frac{\partial V}{\partial x}\right) - \overline{u^2}\frac{\partial U}{\partial x} - \overline{v^2}\frac{\partial V}{\partial y}$$
$$- \frac{\partial}{\partial x}\left(\tfrac{1}{2}\overline{q^2 u} + \frac{\overline{pu}}{\rho}\right) - \frac{\partial}{\partial y}\left(\tfrac{1}{2}\overline{q^2 v} + \frac{\overline{pv}}{\rho}\right) - \varepsilon \qquad (3.2)$$

for a steady, two-dimensional flow and assuming isotropy of the dissipating eddies so that the dissipation rate is given by

$$\varepsilon = \nu\,\overline{\left(\frac{\partial u_i}{\partial x_j}\right)^2} \quad .$$

Similarly the shear stress transport equation follows directly from equation 3.1 for $i \neq j$. Making the same assumptions, this can be written

$$\frac{D}{Dt}(\overline{uv}) \equiv U\frac{\partial}{\partial x}(\overline{uv}) + V\frac{\partial}{\partial y}(\overline{uv}) = -\overline{v^2}\frac{\partial U}{\partial y} - \overline{u^2}\frac{\partial V}{\partial x}$$

$$+ \overline{\frac{p}{\rho}\left(\frac{\partial u}{\partial y} + \frac{\partial v}{\partial x}\right)} - \frac{\partial}{\partial x}\left(\overline{u^2 v} + \overline{\frac{pv}{\rho}}\right) - \frac{\partial}{\partial y}\left(\overline{v^2 u} + \overline{\frac{pu}{\rho}}\right) \qquad 3.3$$

(The viscous term disappears completely if the small eddies are isotropic).

In the plane mixing layer it is usual to employ the dimensionless self-preserving forms of equations 3.2 and 3.3:

$$\left[\frac{V}{U_r} - \eta\frac{U}{U_r}\right]\frac{d}{d\eta}\left(\frac{\overline{\frac{1}{2}q^2}}{U_r^2}\right) = -\left[\frac{\overline{uv}}{U_r^2} - \eta\frac{\overline{(u^2 - v^2)}}{U_r^2}\right]\frac{d}{d\eta}\left(\frac{U}{U_r}\right)$$

$$- \frac{d}{d\eta}\left(\frac{\overline{\frac{1}{2}q^2 v}}{U_r^3}\right) + \eta\frac{d}{d\eta}\left(\frac{\overline{\frac{1}{2}q^2 u}}{U_r^3}\right) - \frac{\varepsilon x}{U_r^3} \qquad 3.4$$

and

$$\left[\frac{V}{U_r} - \eta\frac{U}{U_r}\right]\frac{d}{d\eta}\left(\frac{\overline{uv}}{U_r^2}\right) = -\left[\frac{\overline{v^2}}{U_r^2} + \eta\frac{\overline{u^2}}{U_r^2}\right]\frac{d}{d\eta}\left(\frac{U}{U_r}\right)$$

$$+ \eta\frac{d}{d\eta}\left(\frac{\overline{u^2 v}}{U_r^3}\right) - \frac{d}{d\eta}\left(\frac{\overline{v^2 u}}{U_r^3}\right) + x\cdot\overline{\frac{p}{\rho U_r^2}\left[\frac{\partial}{\partial y}\left(\frac{u}{U_r}\right) + \frac{\partial}{\partial x}\left(\frac{v}{U_r}\right)\right]} \qquad 3.5$$

where the pressure transport terms (and the term $\frac{\overline{uv}}{U_r^2}\eta\frac{d}{d\eta}\left(\frac{V}{U_r}\right)$ in the energy equation) have been omitted. U_r is any convenient reference velocity and $\eta = \frac{y}{x}$.

3.2 THE TRANSPORT EQUATIONS IN CURVILINEAR CO-ORDINATES

Since the turbulent energy equation (3.2) expresses the rate of change of a scalar quantity the various terms will be unaffected by the particular choice of co-ordinate system. For example, the total production term which in cartesian axes is given by $\left(U\frac{\partial\overline{\frac{1}{2}q^2}}{\partial x} + V\frac{\partial\overline{\frac{1}{2}q^2}}{\partial y}\right)$ will not change in magnitude if it were derived in, say, polar co-ordinates, although the individual contributions to the

total production will differ. However, the turbulent shear stress is a vector quantity and therefore the various terms in its transport equation will in general depend on the particular axis system used. So to present shear stress balances whose individual terms have the same physical significance as those in the usual equation for plane flows (equation 3.3) requires particular care in the case of a flow with large curvature effects.

The instantaneous equations of motion including all the longitudinal curvature terms can be written (e.g. Van Dyke[28])

$$\frac{\partial u}{\partial s} + h\frac{\partial v}{\partial n} + v\kappa = 0,$$

$$\frac{\partial u}{\partial t} + u\frac{\partial v}{\partial s} + hv\frac{\partial u}{\partial n} + uv\kappa = -\frac{1}{\rho}\frac{\partial p}{\partial s} + \nu h\frac{\partial}{\partial n}\left\{\frac{1}{h}\left[h\frac{\partial u}{\partial n} - u\kappa - \frac{\partial v}{\partial s}\right]\right\},$$

$$\frac{\partial v}{\partial t} + u\frac{\partial v}{\partial s} + hv\frac{\partial v}{\partial n} - \kappa u^2 = -\frac{1}{\rho}h\frac{\partial p}{\partial n} + \nu h\frac{\partial}{\partial s}\left\{\frac{1}{h}\left[h\frac{\partial u}{\partial n} - u\kappa - \frac{\partial v}{\partial s}\right]\right\}$$

and

$$\frac{\partial w}{\partial t} + u\frac{\partial w}{\partial s} + hv\frac{\partial w}{\partial n} - \qquad = -\frac{1}{\rho}\frac{\partial p}{\partial z} + \nu\nabla^2 w$$

where $h = 1 + n\kappa(s)$.

u, v and w are here defined as the total velocities, s is any surface of curvature $\kappa(s)$ and n is a line normal to it. κ is positive if n increases away from the centre of curvature. Using these equations, the turbulent energy and shear stress transport equations can be derived in the usual way.

The energy equation is

$$U\frac{\partial \overline{\tfrac{1}{2}q^2}}{\partial s} + hV\frac{\partial \overline{\tfrac{1}{2}q^2}}{\partial n} = -\overline{u^2}\left(\frac{\partial U}{\partial s} + V\kappa\right) - h\overline{v^2}\frac{\partial V}{\partial n}$$

$$- \overline{uv}\left(\frac{\partial V}{\partial s} + h\frac{\partial U}{\partial n} - U\kappa\right) - \frac{\partial}{\partial s}\left(\overline{\tfrac{1}{2}q^2 u} + \overline{\frac{pu}{\rho}}\right)$$

$$- h\frac{\partial}{\partial n}\left(\overline{\tfrac{1}{2}q^2 v} + \overline{\frac{pv}{\rho}}\right) - \kappa\left(\overline{\tfrac{1}{2}q^2 v} + \overline{\frac{pv}{\rho}}\right) - \varepsilon \qquad 3.6$$

and the shear stress equation is

$$U\frac{\partial \overline{uv}}{\partial s} + Vh\frac{\partial \overline{uv}}{\partial n} = -\overline{u^2}\left(\frac{\partial V}{\partial s} - U\kappa\right) - \overline{v^2}h\frac{\partial U}{\partial n} + U\kappa\left(\overline{u^2} - \overline{v^2}\right)$$

$$- \frac{\partial}{\partial s}\left(\overline{u^2 v} + \overline{\frac{pv}{\rho}}\right) - h\frac{\partial}{\partial n}\left(\overline{uv^2} + \overline{\frac{pu}{\rho}}\right) - \kappa\left(2\overline{v^2 u} - \overline{u^3}\right)$$

$$+ \overline{\frac{p}{\rho}\left(\frac{\partial v}{\partial s} + h\frac{\partial u}{\partial n}\right)} \qquad 3.7$$

with the standard notation. In common with Section 3.1 the viscous diffusion terms are omitted.

It is particularly convenient here to choose the surface, s, to be a streamline and to define the origin of co-ordinates to be at the particular position of interest, with n <u>decreasing</u> away from the centre of curvature so that at $n = 0$, $h = 1$, $V = 0$ and κ is negative. We now define rectilinear Cartesian axes x', y' which coincide at their origin with the s,n axes at a given point $s = s_o$, $n = n_o$. The transport equations in the two systems are compared in Table 1.

The equations emphasise the stabilising character of the curvature. Both κ and $\frac{\partial U}{\partial n}$ are negative so that the curvature parts of the energy and shear stress production terms reduce the magnitude of the total production. Note that it is only because we have chosen the Cartesian axes

TABLE 1

The Energy Equation

TERM	CO-ORDINATES	
	STREAMLINE (s, n)	CARTESIAN (x′, y′)
ADVECTION	$U \frac{\partial \frac{1}{2}\overline{q^2}}{\partial s} + \left[V \frac{\partial \frac{1}{2}\overline{q^2}}{\partial n} \right] \equiv 0$	$U \frac{\partial \frac{1}{2}\overline{q^2}}{\partial x'} + \left[V \frac{\partial \frac{1}{2}\overline{q^2}}{\partial n} \right] \equiv 0$
PRODUCTION	$\overline{u^2} \frac{\partial U}{\partial s} + \overline{v^2} \frac{\partial V}{\partial n} + \overline{uv} \left(\frac{\partial U}{\partial n} - U\kappa\right)$	$\overline{u^2} \frac{\partial U}{\partial x'} + \overline{v^2} \frac{\partial V}{\partial y'} + \overline{uv} \left(\frac{\partial U}{\partial y'} + \frac{\partial V}{\partial x'}\right)$
DIFFUSION	$\frac{\partial}{\partial s} \left(\frac{1}{2}\overline{q^2 u}\right) + \frac{\overline{pu}}{\rho} + \frac{\partial}{\partial n} \left(\frac{1}{2}\overline{q^2 v} + \frac{\overline{pv}}{\rho}\right) + \frac{\kappa}{2} \overline{q^2 v} + \kappa \frac{\overline{pv}}{\rho}$	$\frac{\partial}{\partial x'} \left(\frac{1}{2}\overline{q^2 u} + \frac{\overline{pu}}{\rho}\right) + \frac{\partial}{\partial y'} \left(\frac{1}{2}\overline{q^2 v} + \frac{\overline{pv}}{\rho}\right)$

The Shear Stress Equation

ADVECTION	$U \frac{\partial \overline{uv}}{\partial s} + \left[V \frac{\partial \overline{uv}}{\partial n} \right] \equiv 0$	$U \frac{\partial \overline{uv}}{\partial x'} + \left[V \frac{\partial \overline{uv}}{\partial y'} \right] \equiv 0$
PRODUCTION	$\overline{u^2} \left(\left[\frac{\partial V}{\partial s} \right] \equiv 0 - U\kappa \right) + \overline{v^2} \frac{\partial U}{\partial n}$	$\overline{u^2} \frac{\partial V}{\partial x'} + \overline{v^2} \frac{\partial U}{\partial y'}$
CURVATURE (i)	$- U\kappa \left(\overline{u^2} - \overline{v^2}\right)$	-
DIFFUSION	$\frac{\partial}{\partial s} \left(\overline{u^2 v} + \frac{\overline{pv}}{\rho}\right) + \frac{\partial}{\partial n} \left(\overline{uv^2} + \frac{\overline{pu}}{\rho}\right)$	$\frac{\partial}{\partial x'} \left(\overline{u^2 v} + \frac{\overline{pv}}{\rho}\right) + \frac{\partial}{\partial y'} \left(\overline{uv^2} + \frac{\overline{pu}}{\rho}\right)$
CURVATURE (ii)	$\kappa \left(2\overline{v^2 u} - \overline{u^3}\right)$	-
PRESSURE STRAIN	$\overline{p \left(\frac{\partial u}{\partial n} + \frac{\partial v}{\partial s}\right)}$	$\overline{p \left(\frac{\partial u}{\partial y'} + \frac{\partial v}{\partial x'}\right)}$

to coincide with the local streamline direction that the individual terms in each set in the energy equation are identical: for example, not only is the total production the same in both cases (of necessity) but the contribution made by the shear stress production is also identical:

$$\overline{uv}\ (\frac{\partial U}{\partial n} - U\kappa) \equiv \overline{uv}\ (\frac{\partial U}{\partial y'} + \frac{\partial V}{\partial x'}) \quad .$$

As it happens this is also true for the production term in the shear stress equation because $\frac{\partial V}{\partial s} \equiv 0$, although there is an additional term, $U\kappa\ (\overline{u^2} - \overline{v^2})$, which might be thought of as a 'curvature production' term. However the shear stress advection is clearly different in the two axis systems. uv, unlike $\overline{q^2}$, is affected by rotation of the axes and therefore $U\ \frac{\partial \overline{uv}}{\partial s}$ is different from $U\ \frac{\partial \overline{uv}}{\partial x'}$ because the s axis has rotated through an angle ds/R in the distance ds. Now we shall see that if s,n coordinates are used, with a suitable choice for the s axis, even this sharply-curved shear layer behaves approximately like a plane shear layer in the sense that the largest Reynolds-stress gradient is $\frac{\partial \overline{uv}}{\partial n}$, normal-stress gradients being much smaller. In analysing the experimental results we therefore use the (s,n) system described in the next section, with the s-axis aligned with the 'effective direction' of the shear layer. The transport equations in (s,n) coordinates contain extra 'curvature' terms which are small compared with the other terms, as will be seen in Chapter 5.

3.3 NOTATION

Because of the geometrical complexity of the curved mixing layer, various co-ordinate systems are used and to avoid later confusion these are now defined. Figure 5.2 anticipates later results but conveniently defines most of the co-ordinates used.

The origin of the usual linear Cartesian co-ordinates, x, y is taken as the shear layer separation point (the upper lip of the contraction exit) for both the plane and the curved mixing layers. The z-wise line defined by x = 12.6, y = 25.1 (distances are in cms unless otherwise stated) is the axis of the rotating traverse described in Section 2.2 and radial lines inclined at θ^o to the x-axis are defined as 'j-lines'. j (or J) = 1 corresponds to $\theta = 90^o$, j = 2 to $\theta = 85^o$ and so on in steps of 5^o to j = 19 at $\theta = 0^o$.

Section 5.1 describes the measurement of what is termed 'the bounding streamline'; rather than to use true polar co-ordinates (r, θ) it was convenient in the experimental work to define subsidiary rectangular Cartesian co-ordinates x_j', y_j' for each j-line (Figure 5.2a). y_j' is measured along a j-line from its intersection with the bounding streamline and is taken positive towards the centre of curvature (the low velocity side of the layer); x_j' is measured from the same point, positive downstream. R_j is the distance from the rotation axis to the bounding streamline, so that $y_j' = R_j - r_j$ (Figure 5.2a). All dashed quantities, U', V' or $\overline{u'v'}$ for example are measured with respect to the local x_j', y_j' co-ordinates: note that these co-ordinates are not necessarily aligned with the mean flow direction.

For the main part of the data analysis rectangular, Cartesian co-ordinates x', y', and curvilinear co-ordinates s', n' are used. It is shown in Section 5.2.3 that the local direction of the curved mixing layer can be identified and s' is measured from the separation point along the line of maximum turbulent energy (close to $\eta = 0$ in the plane layer and also close to the 'effective' $\eta = 0$ in the curved layer - Section 5.2.3): n' is measured along straight lines normal

to this line. S is used (instead of s′) to denote downstream traverse locations. It should be noted that in general s′ is <u>not</u> a streamline, although it is close to being one. The curved mixing layer centre line is defined throughout this Thesis, unless stated otherwise, as the line of maximum $\overline{q^2}$ ($n' \equiv 0$) in the curved portion of the flow ($y < 25$) and the line $d = 10$ in the vertical portion. This latter line is close to the line of maximum $\overline{q^2}$ (in fact it lies between $\overline{q^2}_{max}$ and $\frac{U}{U_r} = 0.67$ - see Figure 5.2a) and was chosen simply for convenience. The co-ordinates x′, y′ <u>locally</u> have the same orientation as s′, n′ but since they are rectangular Cartesians the tranposrt equations in x′, y′ contain no curvature terms, whereas those using s′, n′ do.

Undashed quantities (U, V or $\overline{uv}$ for example) relate to both x′, y′ and s′, n′ co-ordinates remembering that, for example, $\frac{\partial \overline{uv}}{\partial x'} \neq \frac{\partial \overline{uv}}{\partial s'}$ since for measurement of the latter $\overline{uv}$ must be rotated. As no velocities are associated with the reference axis system x, y in the curved layer case, this should involve no confusion.

All mean and turbulent quantities throughout the rest of the text are, if not actually written as such, understood to be non-dimensionalised by the tunnel reference velocity, U_r. Other symbols and notation are listed in the appropriate section.

4. THE PLANE MIXING LAYER

4.1 THE SCOPE OF THE TESTS

There has been a number of apparently careful investigations of the plane self-preserving mixing layer. For example Liepmann & Laufer (see Townsend[29]) made detailed measurements of the turbulent intensities, scales and dissipation. More recently Wygnanski & Fiedler[30] undertook a comprehensive range of measurements including conditionally-averaged quantities and Bradshaw & Ferriss[31] and Bradshaw, Ferriss & Johnston[32] investigated an axi-symmetric mixing layer. Rodi & Spalding[33] have also measured some of the more basic turbulence quantities. There are a number of differences in the results, some of which are undoubtedly due to differing measurement techniques and others may be caused by different initial conditions upstream of separation: Bradshaw[34] has shown how various upstream boundary layers affect the development of the mixing layer. It therefore seemed worthwhile to make a further fairly careful study of this basic flow if only to serve as a baseline for comparison with the distorted mixing layer. Measured differences between these two flows could then be attributed to fluid-mechanic phenomena irrespective of uncertainties about previous workers' results since the general measurement techniques would be identical.

The usual mean flow and turbulent quantities were measured, including all the triple product terms (with the exception of the pressure transport and the pressure-strain term) occurring in the energy and shear stress transport equations (Chapter 3). Some spectra of the longitudinal component of the turbulent fluctuations were also measured, enabling the dissipation to be estimated by a $-\frac{5}{3}$ law fit, and the intermittency was measured using the digital programs

mentioned in Section 2.6; see Section 4.6 for details of the criteria.

4.2 THE MEAN FLOW

4.2.1 Mean Velocity Measurements

Initial pitot tube traverses across the shear layer were made at a number of stations downstream from the contraction exit to determine the approximate distance required for the flow to achieve self-preservation and to find the virtual origin of the flow. Figure 4.1 defines the axis system (see also Section 3.3).

As indicated by Bradshaw[34] the only affect of Reynolds number (if it is high enough) on a free turbulent flow will be on the initial conditions, so that for a mixing layer the velocity profiles in the self-preserving region will take the form

$$\frac{U}{U_r} = f\left(\frac{y}{x - x_o}\right)$$

where x_o is the virtual origin of the flow and may vary with Reynolds number. Exploratory traverses at various free-stream speeds (U_r) showed that this was indeed the case and, as was stated in Section 2.1, all the main work was done at a free stream speed of about 30.30 m/s, which ensured reasonable instrument accuracy over most of the flow. To find the virtual origin, the points at which the mean velocity was 0.90 and 0.25 of the free stream value (U_r) were plotted against x (Figure 4.2). The spreading rate, defined rather arbitrarily as $\frac{\delta}{(x - x_o)}$, where δ is the distance between the two lines of constant $\frac{U}{U_r}$ defined above, was 0.112 and was constant after about 15 cms downstream. This is very close to the value found by Liepmann & Laufer (0.11) and by Bradshaw & Ferriss (0.116) but is substantially less than the 0.154 measured by Wygnanski & Fiedler.

From mean flow profiles of the laminar boundary layer just upstream of separation from a rearward facing step on the lower surface of the tunnel exit, Wong[20] found that the momentum thickness, δ_2, was about 0.3 mm ($\frac{U_r \delta_2}{\nu} \sim 600$). The boundary layer on the upper surface (without the step) is unlikely to be very different from this. Bradshaw found that the distance to self-preservation after separation was about $\frac{7 \times 10^5 \nu}{U_r}$ for laminar upstream boundary layers with a Reynolds number of $500 < \frac{U_r \delta_2}{\nu} < 1000$. This implies that in this particular flow self-preservation may not be complete until about 35 cms downstream of separation. In fact checks showed that self-preservation was achieved a littler earlier than this but all the main turbulence measurements were made at a station about 53 cms downstream: this was certainly well within the self-preserving region of the flow.

The mean flow profiles plotted as $\frac{U}{U_r}$ against η where $\eta = \frac{y}{x - x_o}$ are shown in Figure 4.3. x_o was taken as - 2.4 cms: the value found from Figure 4.2 and collapse is seen to be very good. Unlinearised hot wires were also used to measure the mean flow profile at x = 53 and the results were found to agree very well with the pitot tube profiles, though this must be a little fortuitous at the extreme low velocity edge of the flow as the response of both instruments in this region is somewhat uncertain.

4.2.2 Calculation of the Transverse Mean Velocity Component

The transverse mean velocity component, V, was required for the calculation of momentum and energy balances. If the flow is exactly self-preserving U and V are functions only of η so that the continuity equation can be written as

$$- \eta \frac{dU}{d\eta} + \frac{dV}{d\eta} = 0$$

and hence

$$V_\eta = \int_1^\eta \eta dU \qquad 4.1$$

provided that V = 0 at the lower limit of integration denoted by 1 and where V_η is the value of V at η.

At sufficiently large negative values of η (the high velocity edge), V will be zero and inspection of Figure 4.3 shows that at $\eta = -0.10$, $\frac{U}{U_r} = 1$ and $\frac{dU}{d\eta}$ is very nearly zero so this seems a reasonable location to assume a zero V. The lower limit of integration is therefore taken at $\eta = -0.10$ and equation 4.1 can be rewritten

$$V_\eta = \eta U_\eta + 0.1 - \int_1^\eta U d\eta \qquad 4.2$$

where U_η is the value of U at η. The distribution of V across the layer follows simply by graphical integration of the U profile.

Later work on the curved mixing layer involved development of a computer program to find the mean streamlines. This consisted basically of using the continuity equation with measured profiles of resultant mean velocity ($(U^2 + V^2)^{\frac{1}{2}}$) - from hot-wires - to find U and V everywhere in the flow. To obtain an idea of the sort of program required, a similar procedure was used for the plane self-preserving flow. This is discussed in Section 5.1.6 and Appendix V and the only point of interest here is that, although the numerical integration (for the plane layer) started considerably further out in the potential flow ($\eta = -0.40$), the transverse velocity component did not change significantly from zero until $\eta = -0.10$, so that the assumption of zero V at $\eta = -0.1$ for the graphical integration is seen to be quite satisfactory. Figure 4.4 shows the resulting V-velocity variation from both techniques. The graphical integration (using equation 4.2) is expected to be a little less accurate at the

extreme low velocity side of the flow, because the measured U-profile is really a $(U^2 + V^2)^{\frac{1}{2}}$ profile and U is very low in this region - the numerical integration takes this into account. Both methods of course depend on the accuracy of the measured mean flow profile which in any case is somewhat poorer at the low velocity, high intensity edge of the flow.

Also plotted in Figure 4.4 are the values of V measured using a linearised cross-wire probe. This was not the aim of the cross-wire traverses but the data were available and it is surprising, in view of the inherent inaccuracies of a crossed hot-wire, that the values of V measured in this way are so close to the calculated profile.

4.3 THE TURBULENCE

4.3.1 Turbulent Intensities

Crossed hot-wire traverses were made at x = 52.2 cms with the wires in four different planes. For determination of $\overline{u^2}$, $\overline{v^2}$, $\overline{w^2}$ and $\overline{uv}$ and the corresponding triple products, recordings were made at 13 stations with the hot wires first in the x-y and then the x-z planes. To obtain the non-zero triple product in the y-z plane ($\overline{vw^2}$) the wires were placed in a plane at 45° to the x-y and x-z planes and the measurements repeated with the wires at -45°. This not only gives a better-conditioned measure of $\overline{vw^2}$ but also provides a number of cross-checks. For instance, both $\overline{u^2}$ and $\overline{u^4}$ are measured with the wires in all four configurations and $\overline{u^2v}$ can be deduced from the two 45° sets of measurements and compared with the results obtained in the usual way from wires in the x-y plane. Comparisons of this sort give at least some idea of the reliability of the cross-wire measurements.

Figure 4.5 shows the variation of $\overline{u^2}$ across the layer; there is

encouragingly little scatter between the four sets of measurements. Figure 4.6 gives the variation of the lateral components of turbulent intensity and also plotted is the sum, $\overline{v^2} + \overline{w^2}$, deduced from the two 45^o traverses. The difference between this and the sum obtained from the conventional traverses is less than 10% at every point and this is a good indication of the consistency of the results. Table 2 gives the maximum values of $\overline{u^2}$, $\overline{v^2}$, $\overline{w^2}$ and $\overline{uv}$ (discussed in Section 4.3.2) compared with those found by other workers.

TABLE 2

SOURCE	$\overline{u^2}$	$\overline{v^2}$	$\overline{w^2}$	$\overline{uv}_m$	$\overline{uv}_c$
Present Work	0.0264	0.0130	0.0163	0.0085	0.0098
Liepmann & Laufer[29]	0.0220	0.0105	-	0.0088	0.0092
Bradshaw et al.[32]	0.0210	0.0170	0.0190	0.0100	0.0100
Wygnanski & Fiedler[30]	0.0290	0.0174	0.0228	0.0095	0.0092
Rodi & Spalding[33]	0.0280	0.0121	0.0120	0.0100	0.0105

$\overline{uv}_m$ and $\overline{uv}_c$ are the measured and calculated shear stress, respectively.

Wygnanski & Fiedler's results seem in general somewhat high and the only other comment worth making, apart from the obvious remark that there is considerable scatter between the different sets of data, is that the spread of intensities, or to put it another way $\frac{\overline{u^2}}{\overline{v^2}}$, measured by Bradshaw et al. is considerably lower than all the other investigations suggest.

4.3.2 The Turbulent Shear Stress

The shear stress measured in the usual way and also deduced from the measurements made in the 45^o planes is shown in Figure 4.7. The

maximum value of about 0.0085 is compared with other workers' results in Table 2 and is seen to be a little lower than the average. Correction for tangential cooling of the hot wire (which in fact both Wygnanski & Fiedler and Rodi & Spalding applied) would tend to raise the measured $\overline{uv}$ but for the reasons discussed in Section 2.4 and Appendix IV this was not done in the present experiments.

The shear stress distribution was also calculated using the mean momentum equation and the mean flow profiles. Following Townsend[29] the momentum equation can be written

$$U \frac{\partial U}{\partial x} + V \frac{\partial U}{\partial y} + \frac{\partial}{\partial x} (\overline{u^2} - \overline{v^2}) + \frac{\partial \overline{uv}}{\partial y} = \nu \frac{\partial^2 U}{\partial y^2} \quad . \qquad 4.3$$

Replacing U, $\overline{u^2}$ and $\overline{v^2}$ by their self-preserving forms $f(\eta)$, $g_1(\eta)$ and $g_2(\eta)$ respectively equation 4.3 can be rewritten, neglecting the viscous term, and making use of the continuity equation (equation 4.1). The integrated form is

$$\overline{uv} = f_\eta \int_1^\eta f d\eta - \int_1^\eta f^2 d\eta + f_\eta (\eta f)_1 - (\eta f^2)_1 + \int_1^\eta \eta d(g_1 - g_2) \qquad 4.4$$

As for the integration of the continuity equation, the lower limit was taken at the point $\eta = 0.10$ where the measurements indicate that $\overline{uv}$ is close to zero. The last term is important only at the low velocity edge of the flow where, for example at $\eta = 0.10$, the normal stress term reduces the calculated shear stress by about 20%. The resulting distribution of $\overline{uv}$ is also plotted in Figure 4.7 and the maximum value is seen to reach about 0.010 which, as Table 2 indicates, is quite close to the value calculated by other workers. This is merely a reflection of the agreement attained in the mean velocity profiles, although it is curious that despite Wygnanski and Fiedler's very

different mean velocity profile their calculated shear stress is also very similar. This may be a reflection on their calculation procedure.

The shear stress correlation coefficient, $\frac{\overline{uv}}{\sqrt{\overline{u^2}}\sqrt{\overline{v^2}}}$, where $\overline{uv}$ was taken as the calculated value because of the rather low measured value, is plotted in Figure 4.8. The maximum value of about 0.53 agrees quite well with other workers, except Wygnanski and Fiedler's rather low value of 0.41 which is caused by their relatively high turbulence intensities.

4.3.3 The Triple Products and Flatness Factor

The various non-zero triple products are shown in Figure 4.9. The results are very similar in form to those obtained by Bradshaw et al. and Wynanski & Fiedler although somewhat lower in magnitude than the latter. Figure 4.9a shows $\overline{u^3}$ measured with the wires in all four configurations and $\overline{u^2v}$ measured in the usual x-y plane and deduced from the 45^o measurements. The scatter is no more than one would expect and in fact the terms $\overline{u^2w}$, $\overline{w^3}$ and $\overline{uvw}$ which, in a fully two-dimensional flow should be identically zero, are on the whole less than 1×10^4 which is a factor of 20 less than the maximum $\overline{u^3}$. However, the smallest non-zero term, $\overline{vw^2}$, only reaches a maximum of about 3×10^4 so that the relative accuracy of this term must be somewhat less than that of the larger triple products. It is interesting that $\overline{vw^2}$ is not the same in magnitude as $\overline{v^3}$ as was assumed by Bradshaw et al.[32] in their calculation of the energy balance diffusion term but is only a little more than half $\overline{v^3}$. Wygnanski and Fiedler found a similar result.

The flatness factor of the u-component of velocity is plotted in Figure 4.10 and again the scatter is not excessive. The region of flow for which the flatness factor is less than the Gaussian value

of 3 is not so extensive as the measurements of Bradshaw et al. indicate mainly because of the faster rise on the low velocity side of the flow. There seems to be no obvious reason for this difference but since the present results agree with those of Wygnanski & Fiedler (at least on the basis of the value of $\frac{\overline{u^4}}{(\overline{u^2})^2}$ at a given value of U) it may be caused by the inherent axi-symmetry of Bradshaw's flow.

4.3.4 U-Component Spectra

U-component spectra were measured at x = 20, 30 and 52 cms and $\eta = 0$ using a normal unlinearised hot wire and a Bruel and Kjaer spectrum analyser. Figure 4.11 shows the resulting spectra plotted in non-dimensional form as ϕ_{11} vs. $\frac{\omega x}{U_r}$ where $\phi_{11} = \frac{\overline{u^2(f)}}{\overline{u^2}_{total} \cdot \Delta f} \cdot \frac{U_r}{2\pi x}$ and $\omega = 2\pi f$. $\overline{u^2(f)}$ is the u-component energy in a frequency band centred on f and of width Δf; since the $\frac{1}{3}$ octave filters were used throughout, Δf was 0.231f.

The plane mixing layer is one of the few laboratory flows in which one might expect to find an extensive inertial frequency range where the dissipation is negligible and the turbulence is isotropic. Bradshaw[31] points out that Batchelor's[35] condition for universal equilibrium of the dissipation part of the spectrum can be written $(\frac{\nu_\varepsilon}{\nu})^{\frac{3}{4}} >> 1$ where ν_ε is $-\overline{uv}/\frac{\partial U}{\partial y}$. In the present case, at x = 50 cms, $(\frac{\nu_\varepsilon}{\nu})^{\frac{3}{4}}$ is about 250. Further $2(\frac{\nu_\varepsilon}{\nu})^{\frac{3}{8}}$, which should also be much greater than unity for an appreciable inertial sub-range to exist, is about 32, so not only can one expect isotropy of the dissipating eddies, but it is likely that there will be an inertial sub-range. In fact, Figure 4.12, which shows $k\phi_{11}(k)$ and $k^3\phi_{11}(k)$, the one-dimensional energy spectrum function and the dissipation spectrum (multiplied by the wave number k so that the areas under the curves represent the total energy and the rate of decay of energy

respectively) indicates that there is almost a decade of wavenumber where the contribution to both spectra is a small part of the total. The spectra in Figure 4.11 certainly indicate a region of about a decade over which the $-\frac{5}{3}$ power law seems to hold.

Further discussion of the spectra and confirmation of the presence of an inertial sub-range is deferred to Section 4.4.1.

4.4 THE TURBULENT ENERGY BALANCE

4.4.1 The Dissipation Term

The Kolmogorov hypothesis leads to the well known result

$$E(k) = \varepsilon^{2/3} k^{-5/3} F(\frac{k}{k_s}) \qquad 4.5$$

where $k_s = (\frac{\varepsilon}{\nu^3})^{\frac{1}{4}}$ and $E(k)$ is the wavenumber magnitude spectrum function. If the hypothesis holds for a range of wavenumbers upon which viscosity has little effect (the inertial sub-range) then $E(k)$ must be independent of k_s so that $F(\frac{k}{k_s}) = \alpha$ where α is a constant.

Various authors have quoted values for α; perhaps the most convincing measurements are those of Grant et al.[36] in a tidal channel and they find $\alpha = 1.437$. Using this value and the isotropic relation between $E(k)$ and $\phi(k)$, i.e.

$$2E(k) = k^2 \frac{\partial^2 \phi(k)}{\partial k^2} - k \frac{\partial \phi(k)}{\partial k} \quad ,$$

equation 4.5 can be written

$$\frac{\phi(k)}{\nu U_r} = 0.481 D^{8/3} (\frac{k\nu}{U_r})^{-5/3} \qquad 4.6$$

where D is a non-dimensional dissipation rate $(\frac{\varepsilon \nu}{U_r^4})^{\frac{1}{4}}$. An obvious check on the presence of an inertial sub-range in a laboratory flow is to replot Grant's data as $\frac{\phi}{\nu U_r}$ vs. $\log(\frac{k\nu}{U_r})$ for various values of D and compare the resulting 'universal' curve (which is probably reasonably

accurate even in the dissipation range) with the laboratory spectra. This technique is analogous to the "Clauser chart" principle for determining skin friction in a boundary layer. Figure 4.13 shows the plane layer spectra (Section 4.3.4) plotted in this way and it is clear that only at the high frequency end, where the hot-wire's spatial resolution is inadequate, do the spectra deviate from the true 'universal' spectra. This fit immediately allows a value of D to be interpolated and is of course a valid procedure even if no $-\frac{5}{3}$ region exists, provided that there <u>is</u> a region of fit in the dissipation range of wavenumbers. Inadequate spatial resolution will often prevent this so it seemed worthwhile to make some length corrections. Wyngaard[37] has demonstrated how this can be done and has shown that, typically, for a 1 mm hot-wire in a region where the Kolmogonoff length scale, η_e, is 0.04 mm, the spectrum function is underestimated by about 40% at $\frac{k\nu}{U_r} = 1 \times 10^{-3}$. Figure 4.13 includes the corrected values of ϕ (using Wyngaard's results) for the spectrum measured at x = 30 cms, and this clearly increases the range of agreement with the universal curve, although a faster fall-off still occurs at $\frac{k\nu}{U_r}$ values corresponding to frequencies greater than about 25 - 30 kHz because of the hot-wire anemometer's limited frequency response.

For the centre-line spectra the convection velocity, U_c, ($k = \frac{2\pi f}{U_c}$) was taken as the local mean velocity. This is a reasonable value where the flow is almost fully turbulent and in fact $(U + \frac{\overline{q^2 u}}{\overline{q^2}})$, which is perhaps the 'next best guess' for the convection velocity, only differs from U by about 1% at the centre of the mixing layer. In the intermittent region some other definition of U_c is required: we return to this problem in Section 5.2.5 where spectra measured away from the centre-line are discussed.

The complete procedure outlined above yields a value of 0.0452 for the non-dimensional dissipation term, $\frac{\varepsilon x}{U_r^3}$. However checks showed that the area under the spectrum curve plotted as $\phi_{11}\omega$ vs. $\log\omega$ exceeds the correct value of unity by, on average, 8%, indicating inaccuracies in the frequency analyser filters. This leads to a 16% error in the dissipation and the results (including those in the curved layer) were reduced accordingly. The resulting value of 0.039 compares quite favourably with the 0.036 given by Bradshaw[31]. His value was simply the original measurement of Liepmann and Laufer factored suitably so that the lateral diffusion term (of the energy balance) obtained by difference integrated to zero. However, D can only be estimated from plots like Figure 4.13 to within about 3% and this produces changes of about 12% in ε, so that it is probably fair to say that the dissipation rate can only be estimated from frequency spectra to within about 15 - 20%.

Bradshaw also found that the dissipation across the shear layer was very nearly proportional to $(\overline{q^2})^{3/2}$: the dissipation curve in the present energy balance was obtained by assuming this to be the case and using the above value of 0.039 at $\eta = 0$.

At $x = 50$ and $\eta = 0$ the values of the dissipation length scale, L, the microscale, λ, and the Kolmogoroff length scale, η_e, defined below, were 1.01, 0.152 and 0.0035 cms respectively.

$$L \doteq \frac{(\overline{uv})^{3/2}}{\varepsilon}, \quad \varepsilon = \frac{15\nu\overline{u^2}}{\lambda^2}, \quad \eta_e = \left(\frac{\nu^3}{\varepsilon}\right)^{1/4}.$$

At this station δ (the distance between $\frac{U}{U_r} = 0.9$ and $\frac{U}{U_r} = 0.25$) is 5.6 cms. The turbulence Reynolds number, $R_e = \frac{\sqrt{u^2}\lambda}{\nu}$ was about 500.

4.4.2 The Production Term and Overall Balance

The production was calculated using both the measured and the calculated values of the shear stress. Using the measured values

the lateral diffusion term obtained by difference fails to integrate to zero by about 14% of the area under the production curve and if the calculated shear stress is used the difference term again fails to integrate to zero, this time by about - 10% of the same production area. In the latter case the diffusion term is quite close to the measured values and to that obtained by Bradshaw[31]. Since, in the curved layer, calculation of the shear stress from the momentum equation was very inaccurate it seemed best to use the measured values, so for the purposes of comparison this was done for the production curve shown in the energy balance of Figure 4.14. Figure 4.15 shows the diffusion by difference compared with the measured $\frac{\partial}{\partial y}(\overline{q^2 v})$. Taking the difference term obtained by using the calculated shear stress $(\overline{uv}_c)$ for the production as likely to be the more accurate, this indicates that the pressure diffusion, $\frac{\partial}{\partial y}(\overline{pv})$, may well be small compared with the triple-correlation diffusion - a result also found by Bradshaw[31], whereas Wygnanski & Fiedler[30] found a high value of the pressure diffusion particularly at the high velocity edge of the flow.

Only measured values of diffusion are presented in Figure 4.14 and the resulting 'out-of-balance' term is also shown. The errors are highest in the central region of the flow and are probably no greater than one would expect, although they would be considerably reduced if the calculated shear stress were used for the production term and it seemed pointless attempting to achieve a better balance, particularly in view of the uncertainties in the dissipation term (Section 4.4.1).

It is also worth noting that the normal-stress production term contributes less than 5% to the total except at the outer edge of the flow where the total is small anyway; similarly the longitudinal

diffusion is negligible except at the outer edge where it becomes of the same order as the advection and the lateral diffusion.

4.5 THE SHEAR STRESS BALANCE

The production, advection and triple velocity diffusion terms of the shear stress transport equation (3.3) were calculated and the resulting balance is shown in Figure 4.16. The pressure-strain term was obtained by difference, assuming that the pressure transport terms are negligible. It is reasonable to suppose that the pressure diffusion will be no larger and probably smaller than the equivalent pressure transport of energy, which, as shown in Section 4.4, is itself quite small.

Longitudinal diffusion of shear stress is exceedingly small - even at the outer edge of the flow it is little more than 10% of the total, and the $\overline{u^2}\,\frac{\partial V}{\partial x}$ production term is also very small, being less than 5% of $\overline{v^2}\,\frac{\partial U}{\partial y}$ over most of the flow. The advection and diffusion terms are noticeably smaller ~~with~~ than the production, compared with the corresponding terms in the energy balance. Using the computed shear stress distribution the advection term would be some 15 - 20% larger but this would make very little difference to the pressure-strain term.

4.6 THE INTERMITTENCY

4.6.1 The Problem

There is a variety of opinion about the best way to measure the intermittency at a point in a turbulent shear flow. The earliest method, by necessity, was to take a film or make a chart recording of the signal from a hot-wire placed in the flow and to estimate the intermittency by marking the regions of turbulent and non-turbulent activity. This somewhat crude method, employed by Bradshaw[49] for

example, is obviously rather subjective, but the results seemed sensible. More recently, Wygnanski & Fiedler[38] used the u-component signal from a hot-wire and if the function $\frac{\partial^2 u}{\partial t^2} + \frac{\partial u}{\partial t}$ exceeded a certain threshold value, the flow was deemed turbulent. They used analogue equipment for the differentiations and adjusted the threshold level until the resulting intermittency signal (zero for non-turbulent and 1 V, say, for turbulent flow) 'looked right' when displayed with the u-signal on an oscilloscope. This technique removes the tedium of having to analyse long lengths of film or chart recordings but the subjectiveness is certainly not removed.

Kovasznay, Kibens & Blackwelder[39] argued that it would be better to use, ideally, the fluctuating vorticity signal, since this should be identically zero in the irrotational regions. Using two hot-wires spaced a small distance apart they measured $\frac{\partial u}{\partial y}$ as a first approximation to the vorticity and, again using analogue equipment, produced $\frac{\partial^2 u}{\partial t . \partial y}$ and $\frac{\partial}{\partial t}\left(\frac{\partial^2 u}{\partial t . \partial y}\right)$. From these two signals they deduced a characteristic time scale of the turbulence and if $\frac{\partial^2 u}{\partial t \partial y}$ exceeded a certain threshold value for longer than a time related to this time scale, the flow was defined as turbulent. This method goes some way towards overcoming what seem to be two basic problems involved in intermittency measurements.

Although no definite conclusions will be reached it is worth making some general remarks about these problems since interest in the intermittent structure of the turbulent shear flow is increasing and unless one is aware of the difficulties, it is easy to produce results to order without understanding the physics.

The first problem is "what signal should be used?" It is clearly best to use a signal, like the vorticity, which should be zero in the potential flow regions rather than, say, the u- or

v-component of velocity, which take significantly non-zero values in irrotational regions. However, despite the very different methods used by different workers there is reasonable agreement between the intermittency results in 'standard' turbulent shear flows. This is probably because every worker tends to inspect his intermittency signal and adjust the criteria until it 'looks right'. The human eye is admirably consistent, although it may not interpret the data correctly.

This is linked with the second problem - "how do we treat the very short bursts?" (both turbulent and irrotational) which inevitably occur in the intermittency signal. The present work highlighted this problem, probably because we were operating on digitised signals in a computer. There was therefore no inherent 'delay time' in forming the necessary quantities and comparing them with threshold levels, as there is if analogue equipment is used. The necessary presence of this delay was noticed by Thomas [40] who nevertheless implicitly assumed that there were no turbulent bursts shorter than the delay time. If only the overall intermittency or averages taken in the turbulent and non-turbulent regions are wanted this may not be important since there are usually as many short upward as downward-going spikes in the intermittency signal. However, if one is interested in quantities such as average burst lengths, or the eddy statistics in general, there is a real problem.

At the present state of knowledge about turbulence and the small scale structure in particular, I feel that what one does about the very short bursts is conditioned simply by what one believes about the turbulence. If it is felt that a vorticity sheet whose thickness is of the order of the Kolmogorov length scale can exist in isolation, then every burst of duration equal or greater than that length scale,

divided by a suitable convection speed, could be accepted. On the other hand if it is believed that such a vorticity sheet could only exist embedded in a larger eddy, then one would have to define the smallest size of 'larger eddy' and cut out all bursts of a time scale smaller than such an eddy. This, in effect, is what Kovasznay et al. did by defining a characteristic time scale and cutting out all shorter bursts. The resulting intermittency signal would certainly 'look' better, but may not of course be correct. The eye tends to look at the overall picture rather than the small detail. Kovasznay in fact states the problem succinctly: "In order to define the interface, one faces the same type of difficulties as in defining the shore line of the sea; it always depends on the magnification, if you like, on the coarseness of the method of detection. The shore line, on the one hand, may be considered relatively smooth, or, on the other hand, full of small inlets and islands, depending upon how small details are taken into account".

4.6.2 The Method Adopted

The basic digital program written by Dr. A. Brandt (described in detail in reference 26) was modified for use in the present work. Various criteria were tested and it was finally decided to define the signal as turbulent if either $\left|\frac{\partial(uv)}{\partial t}\right|$ or $\left|\frac{\partial^2(uv)}{\partial t^2}\right|$ exceeded certain threshold values. The uv product is usually a far better signal to use than the u- or v-component velocity because, as inspection of each signal showed, the fluctuations of uv in the irrotational regions are far less (when expressed as a fraction of the fluctuation levels in the turbulent zones) than in the corresponding velocity signals. On average of course, the shear stress is close to zero in the irrotational flow, although Stewart[41] has shown that in general its instantaneous value is not zero and that even its mean value need not be exactly zero.

Ideally one would like to be able to vary the threshold levels over a region around the 'correct' values with no resultant change in the intermittency, γ. No such region could be found: Figure 4.17 shows the variation of γ with the threshold values for $\frac{\partial(uv)}{\partial t}$ and $\frac{\partial^2(uv)}{\partial t^2}$. Inspection of the intermittency signals indicated no obvious 'correct' values for k_1 and k_2 (defined in Figure 4.17) and, after many records had been studied, it was decided to use $k_1 = 0.10$ and $k_2 = 0.15$. These values gave the variation of intermittency in the plane layer shown in Figure 4.18. The measurements of Bradshaw et al.[32] in an axisymmetric mixing layer indicate a slightly broader profile on the low velocity side (correlating with their flatness factor results mention in Section 4.4.3) but the general agreement is considered satisfactory. The comparisons are based on the value of γ at particular values of $\frac{U}{U_r}$; Wygnanski & Fiedler's[30] results agree with the present measurements when plotted on this basis but not when plotted against η.

Since only the overall intermittency was required, the short burst problem was not important. Any burst containing two or more datum points (i.e. a sample of length $\frac{2}{20 \times 10^3}$ s at least) was retained but cutting out single spikes was not based on any physical reasoning. It simply produced a signal which 'looked' better. In fact, close inspection revealed that if two-point bursts had also been eliminated, a much cleaner intermittency signal would result - looking more like the sort of signal one usually associates with analogue intermittency meters. Two-datum-point bursts correspond to a frequency of 10 kHz and a burst thickness of about 2 mm: the latter is between one and two orders of magnitude greater than the Kolmogonov length (based on the dissipation rate at x = 50 measured as in Section 4.4.1) so it is conceivable that bursts shorter than

this could occur. One inevitable result of the short bursts is that the intermittency never quite reaches unity in the mixing layer. Probably the only way to determine the maximum intermittency is by careful scrutiny of smoke pictures: irrotational fluid must sometimes reach the centre of any shear layer so in logic γ_{max} must be less than one.

To economise on computer time, only five seconds of real time data were used for the intermittency measurements; Figure 4.19 shows that this is an adequate time. The small scatter in Figure 4.18 is an even better witness.

At a later date some chart recordings of the hot-wire anemometer output signals were produced and the intermittency estimated from these in the usual way. The results are also shown in Figure 4.18 and despite the very short sample lengths used (less than ½ s in most cases) and the uncertainties discussed above, there is reasonable agreement between the two methods.

The intermittency factor can also be estimated from the flatness factor, as shown by Townsend[29], and the resulting γ defined as

$$\gamma = \left| \frac{\overline{u^4}}{(\overline{u^2})^2} \right| \Big/ \left| \frac{\overline{u^4}}{(\overline{u^2})^2} \right|_T$$

where the denominator is the flatness factor in the fully turbulent central region of the flow (approximately 2.7, see Figure 4.10) is also plotted in Figure 4.18. The agreement is surprisingly good in view of the fact that the u-component velocity fluctuations cannot be expected to be zero in the potential regions.

FIG. 4.1 THE PLANE MIXING LAYER

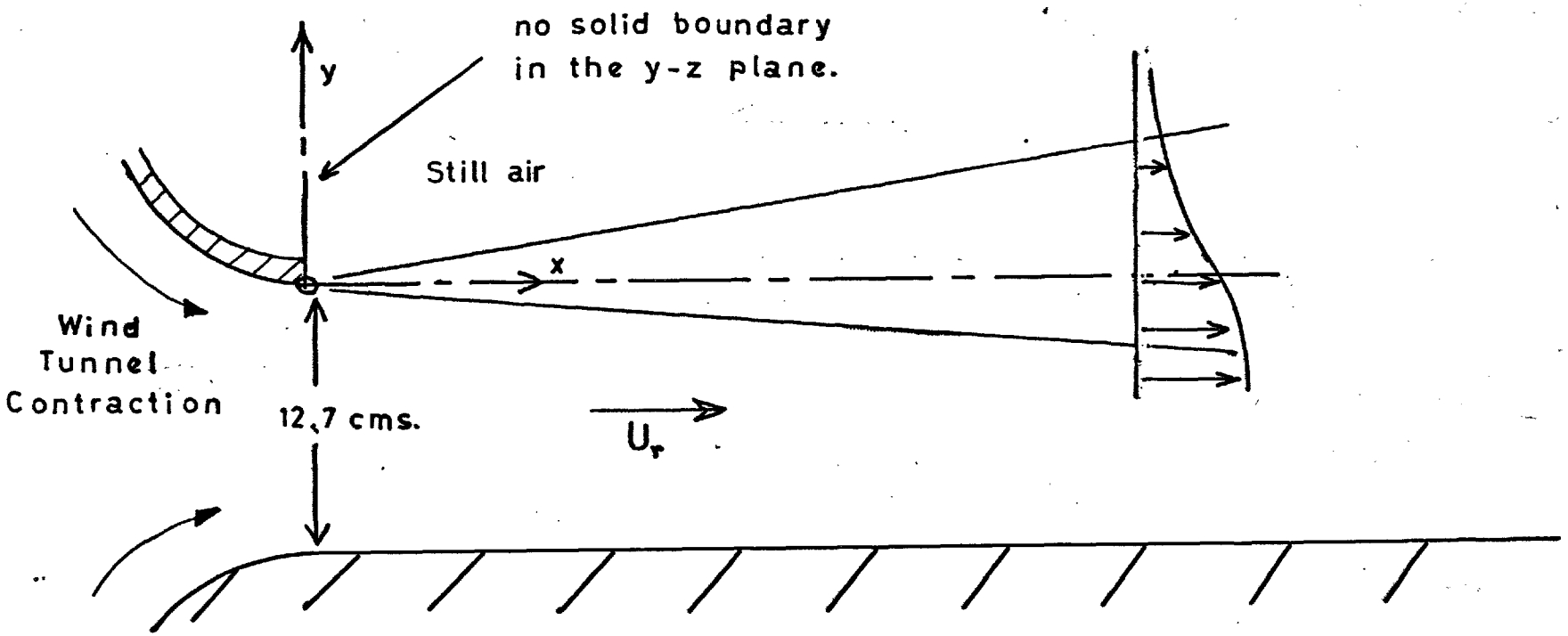


FIG. 4.2. Spread of mixing layer

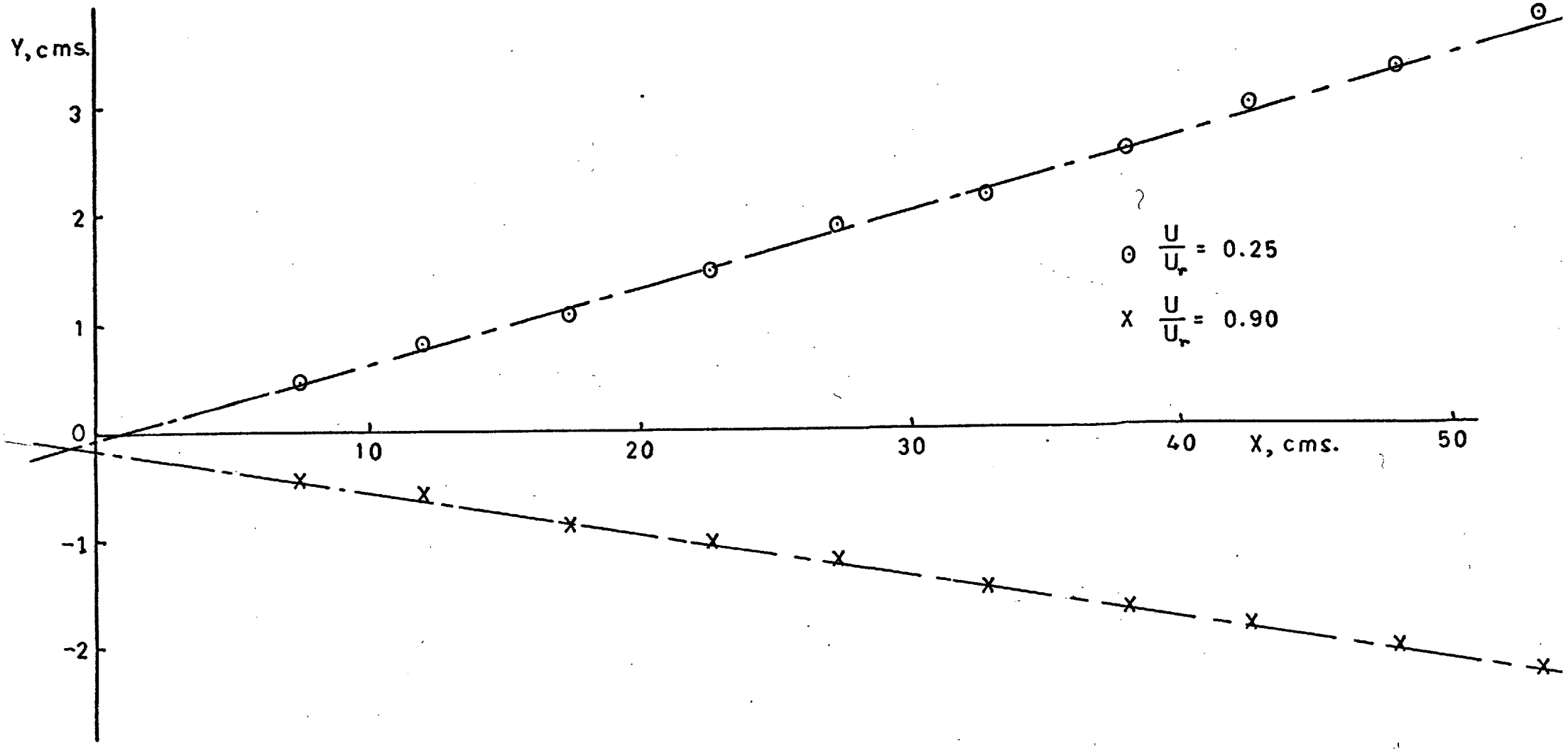
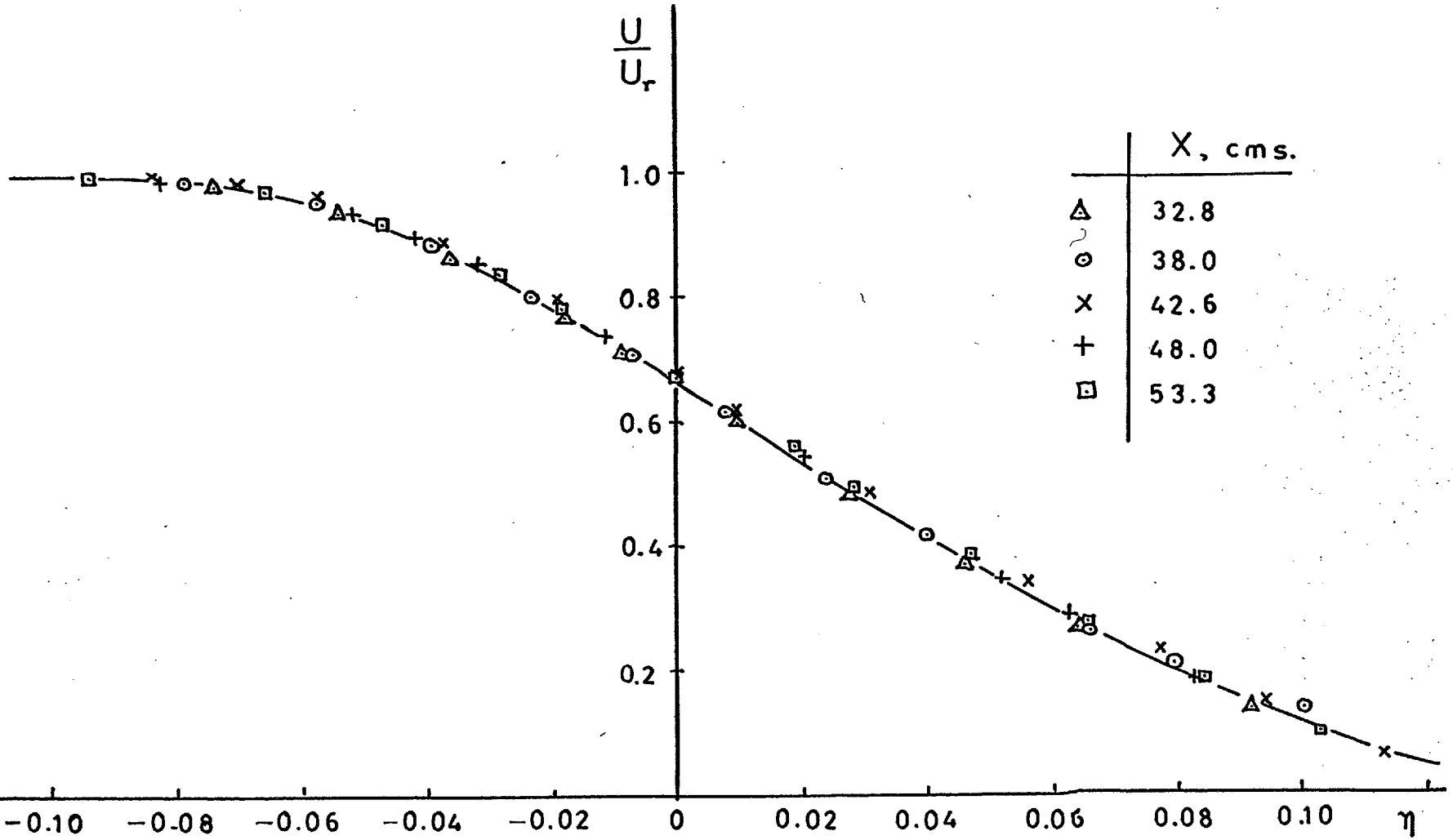
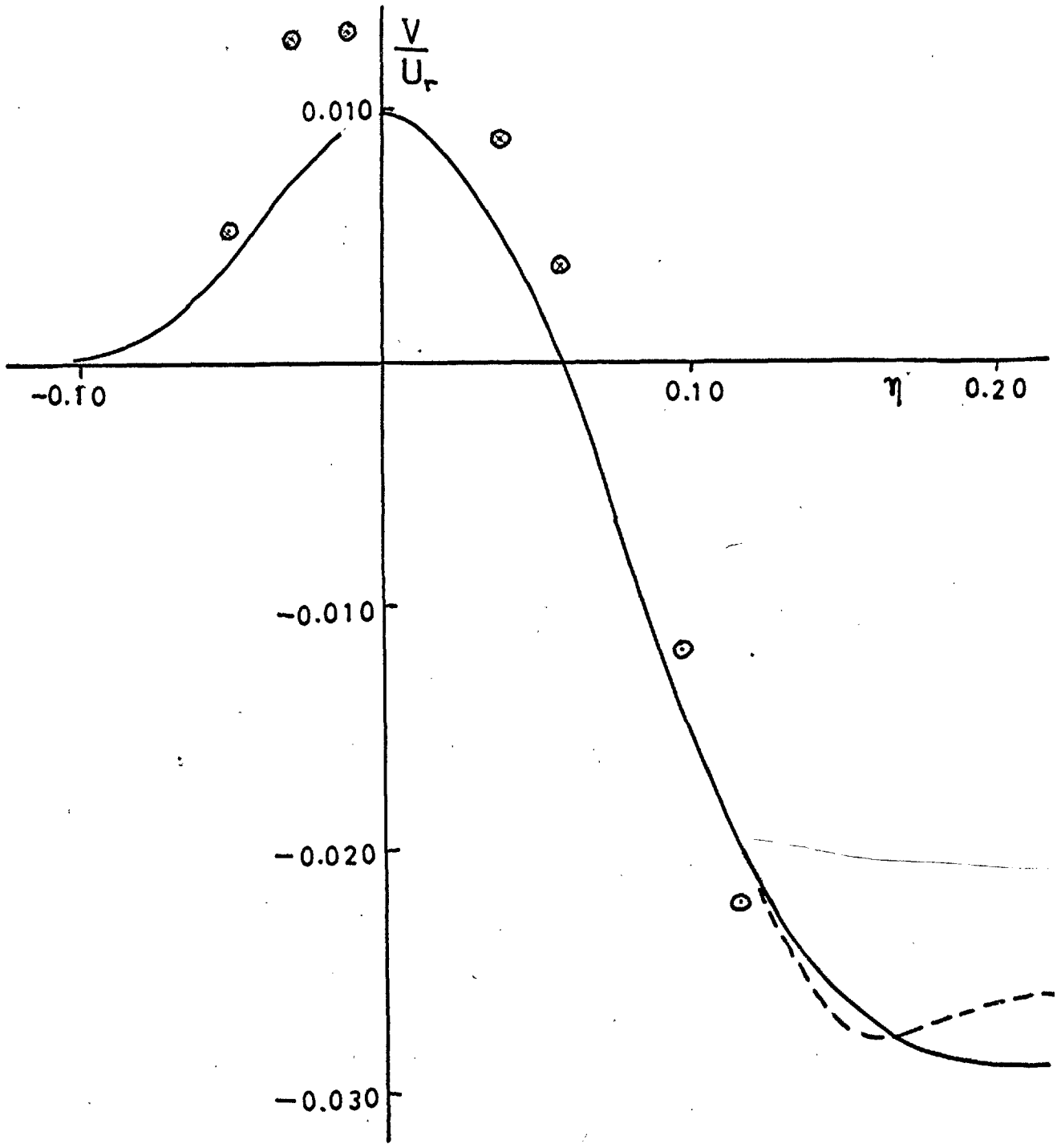


FIG. 4.3 Mean velocity variation.





——— numerical integration

– – – graphical "

⊙ from crossed hot wires

FIG. 4.4 Mean velocity (V-component)

FIG.4.5 Longitudinal turbulent intensity

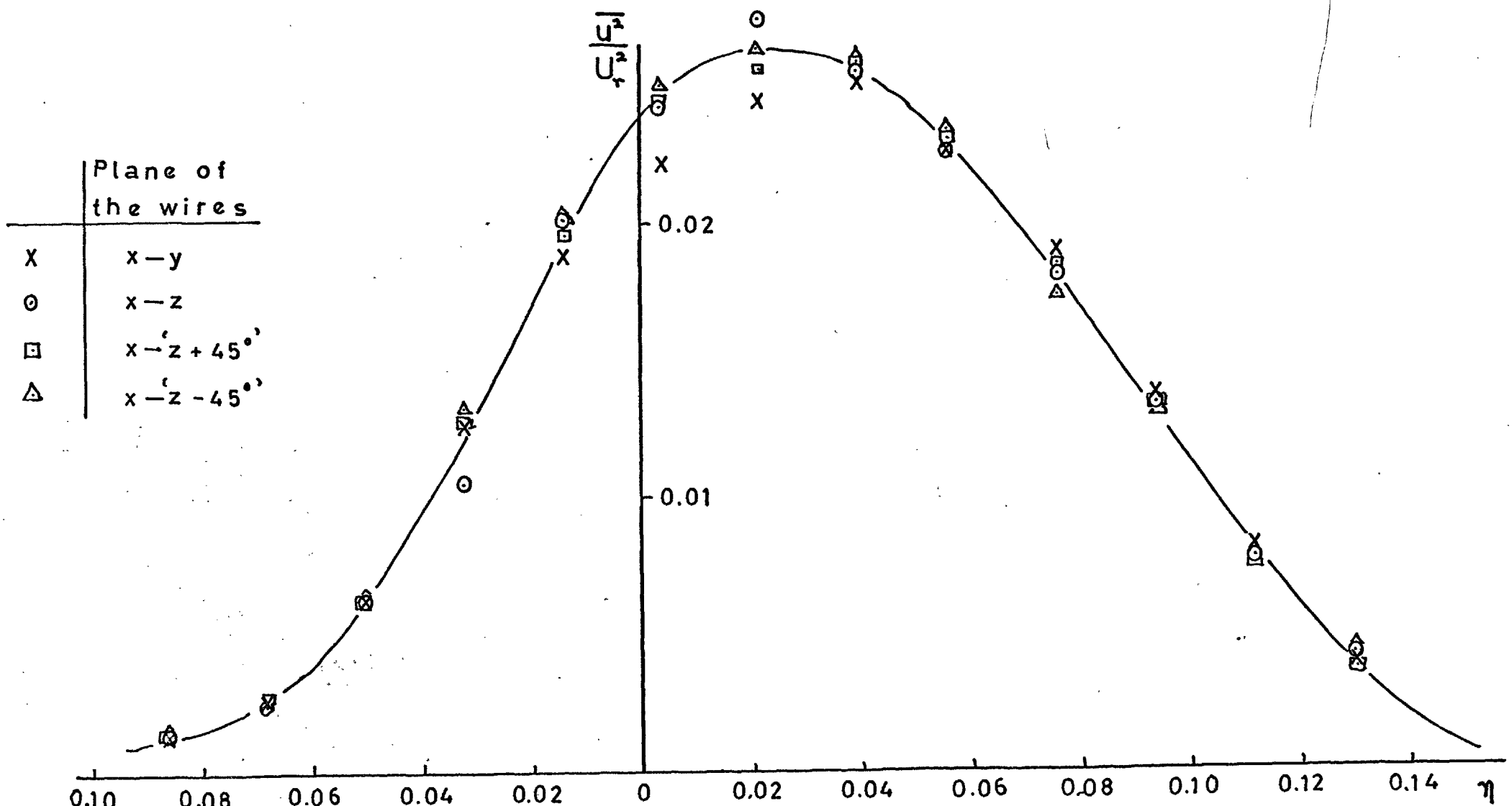


FIG. 4.6 Transverse & lateral turbulent intensities.

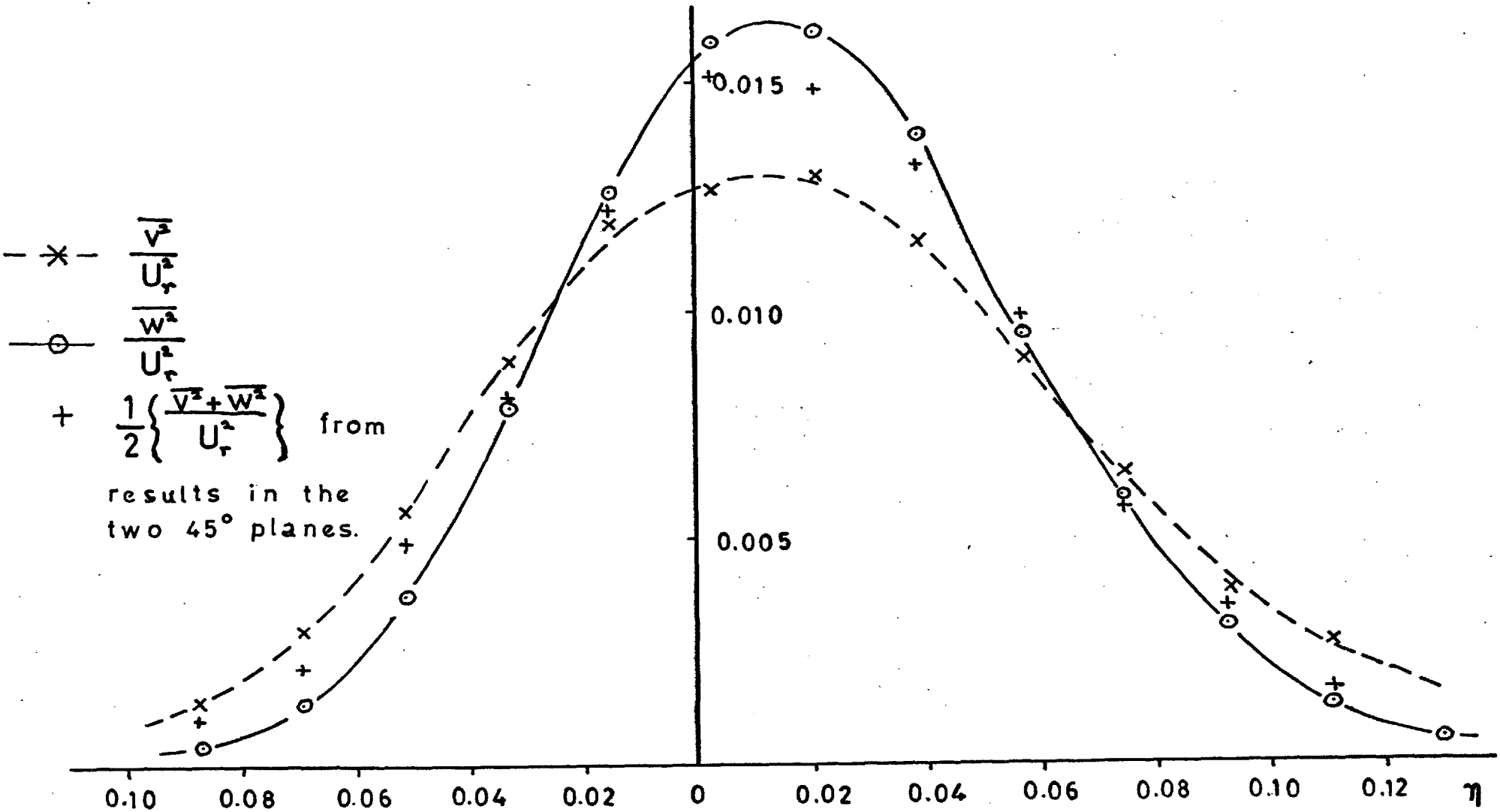


FIG. 4.7 Turbulent shear stress

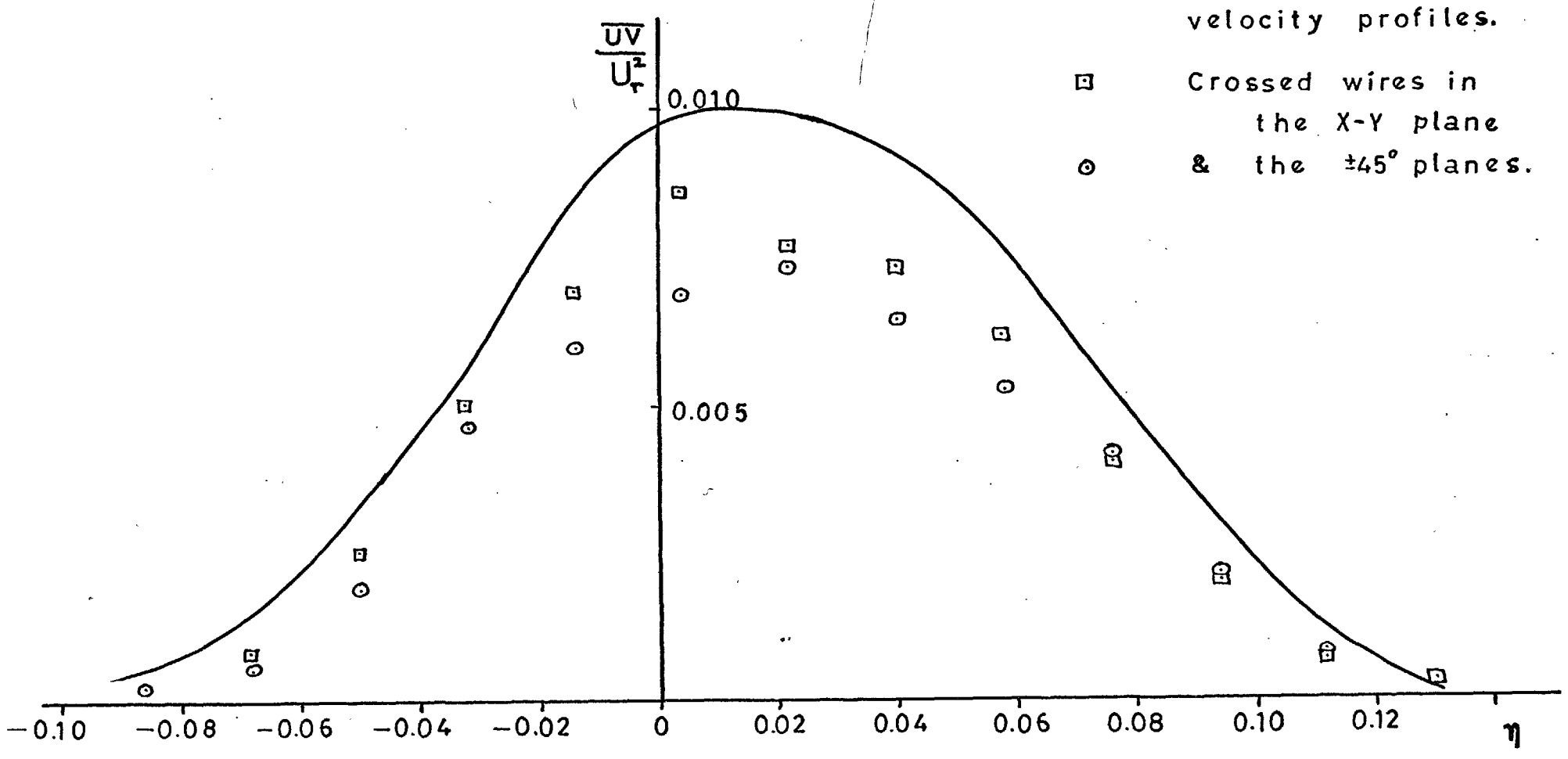


FIG. 4.8 Shear correlation coefficient (calculated $\overline{uv}$ used).

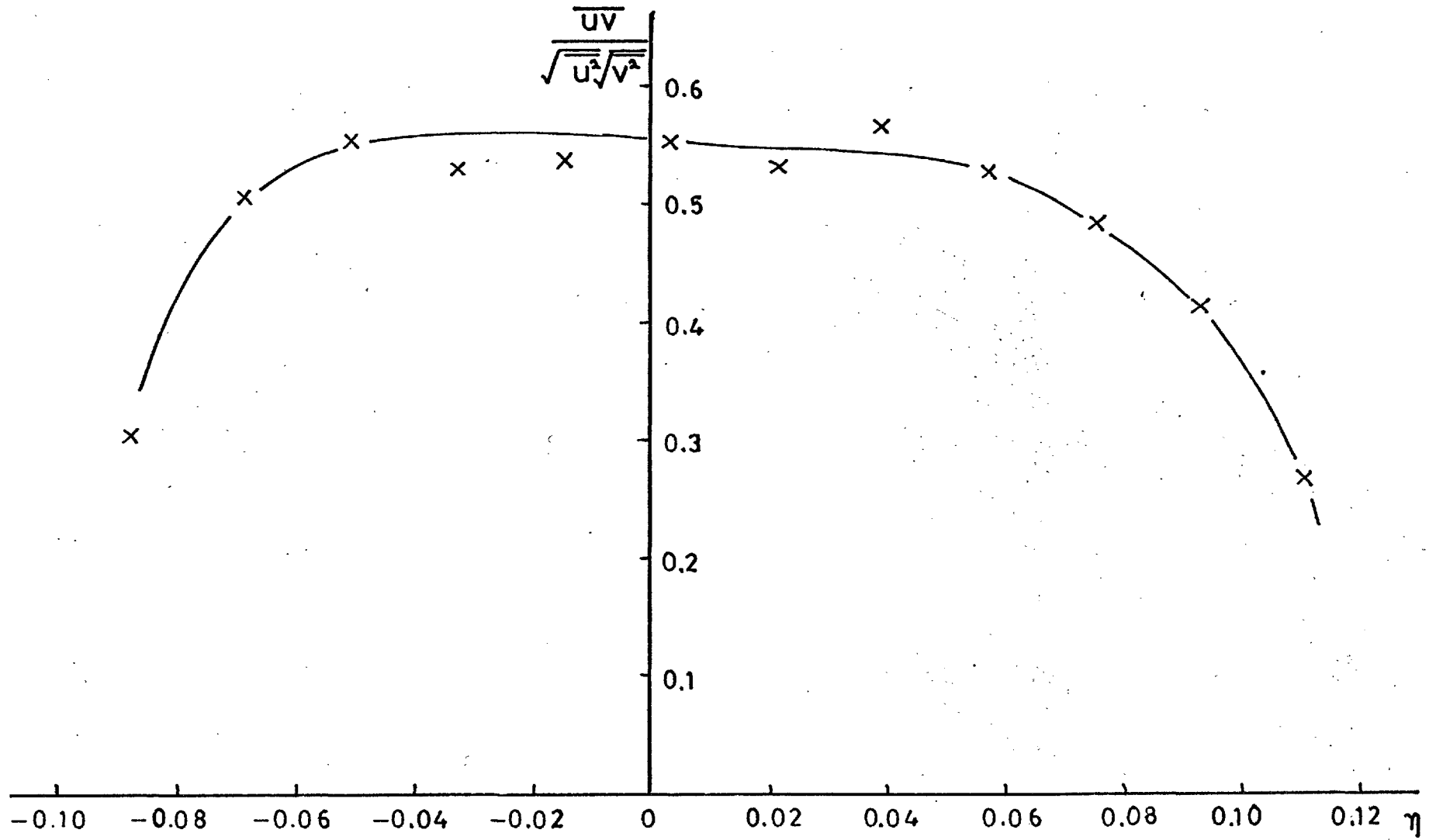
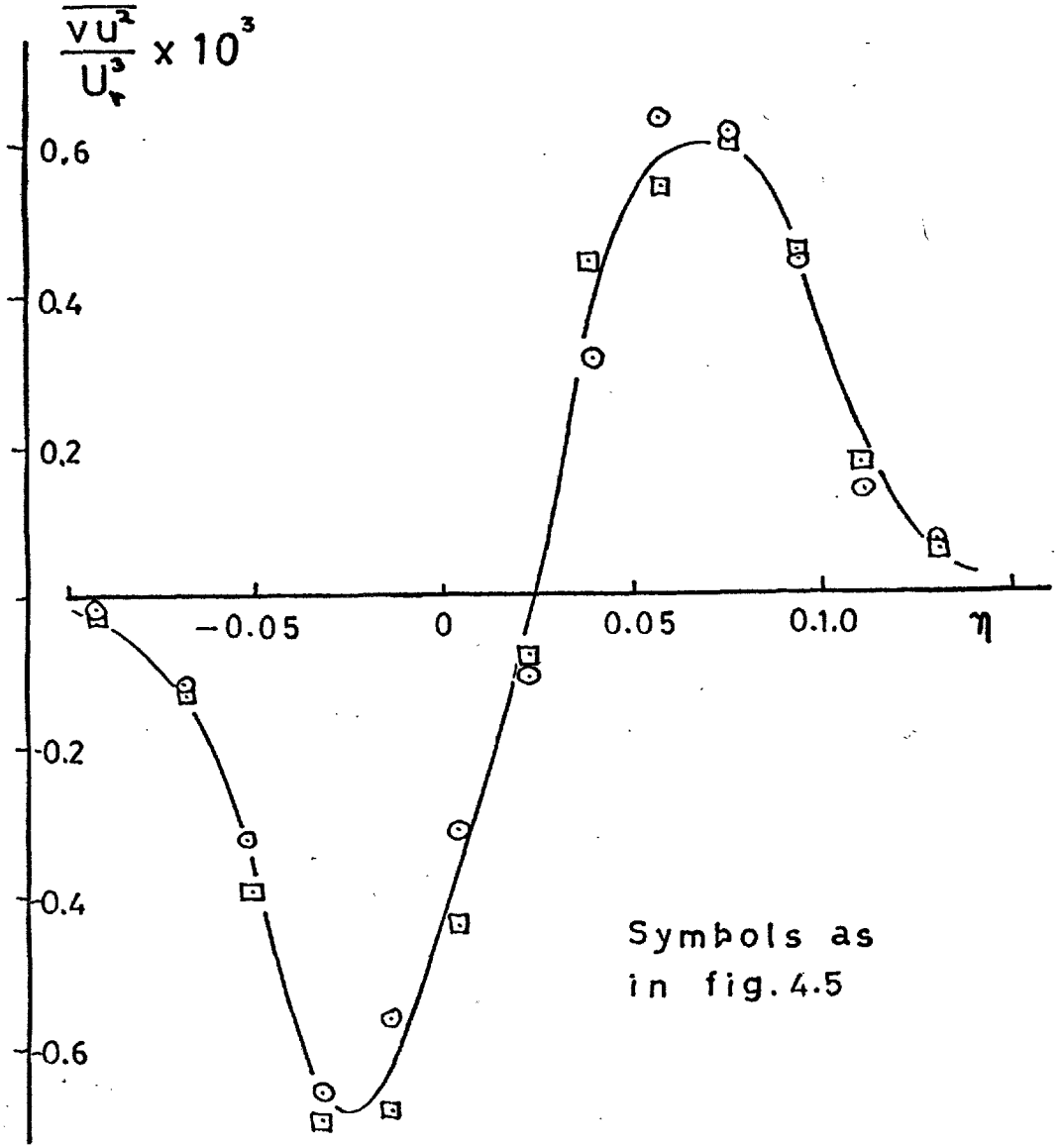
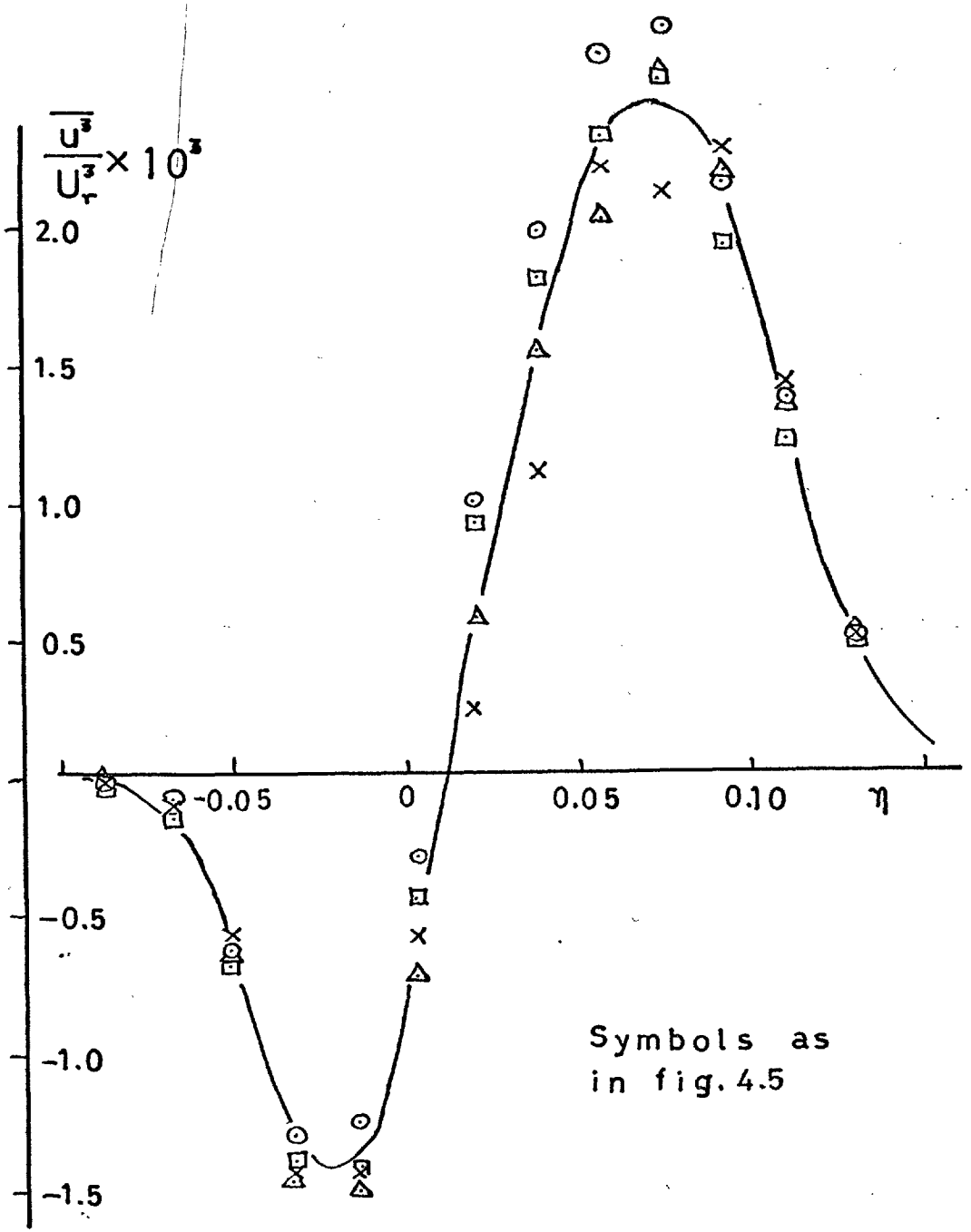


FIG. 4.9a Triple products.

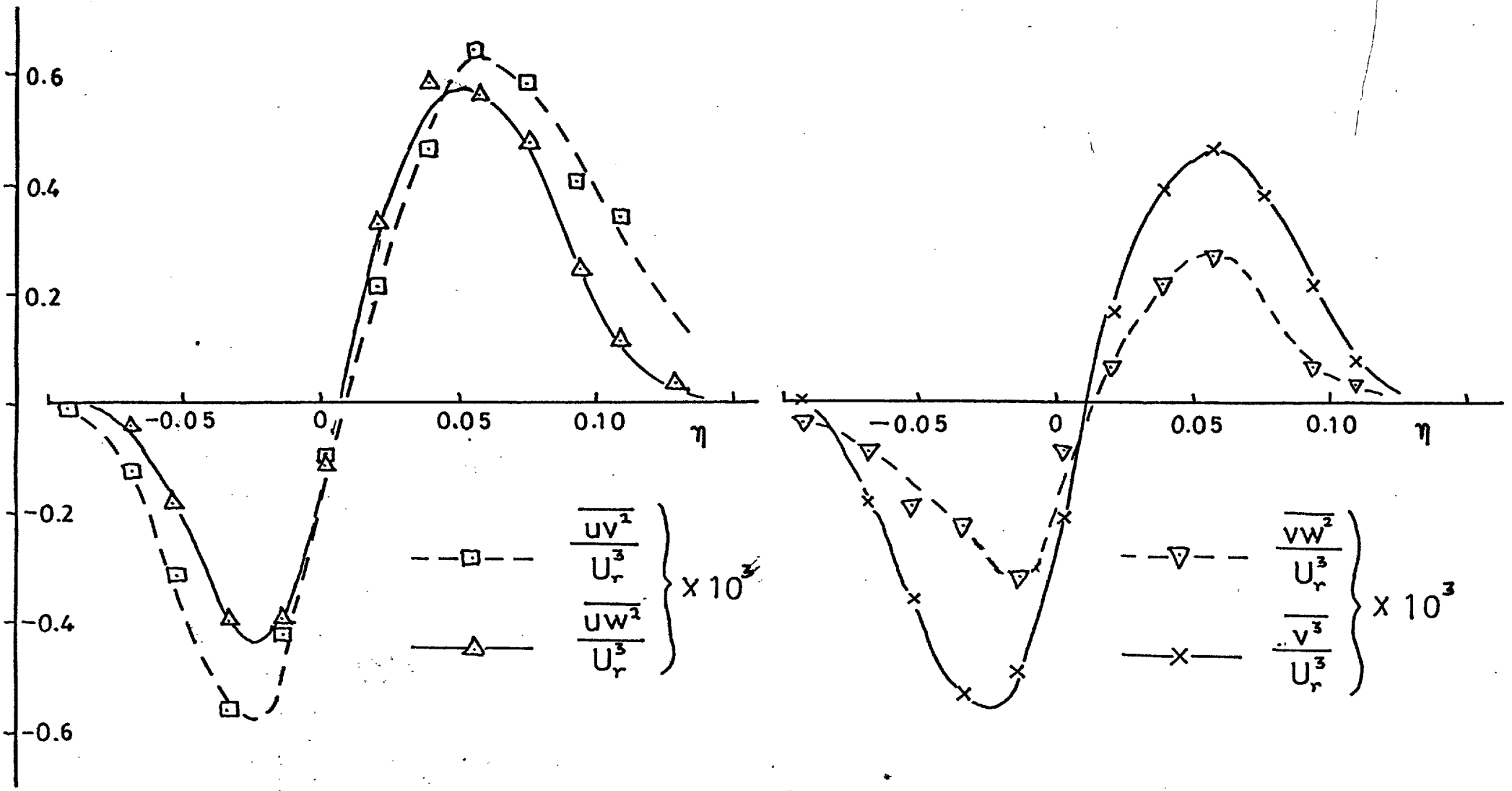


Symbols as in fig. 4.5



Symbols as in fig. 4.5

FIG. 4.9b Triple products.



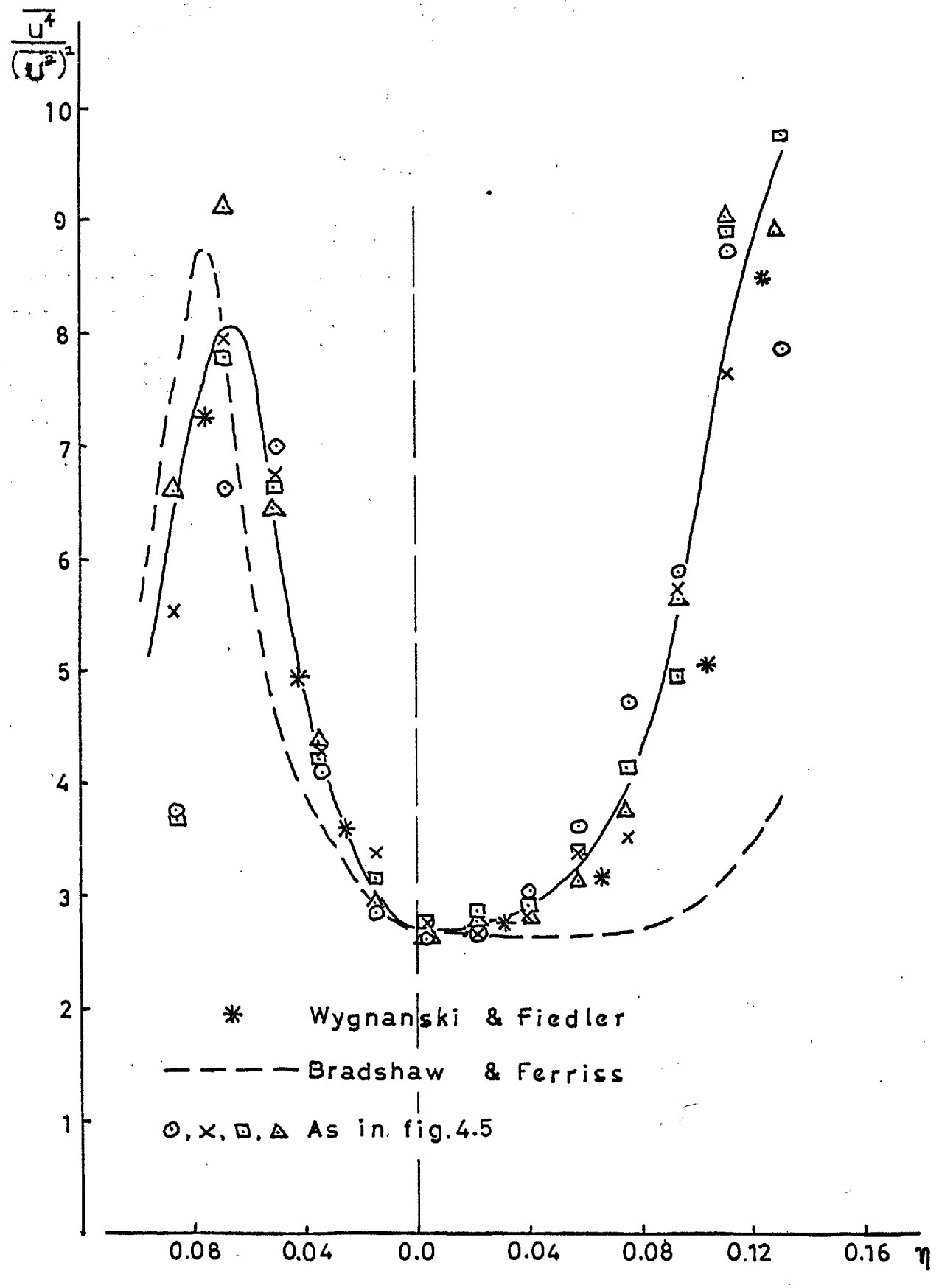


FIG. 4.10 Flatness factor.

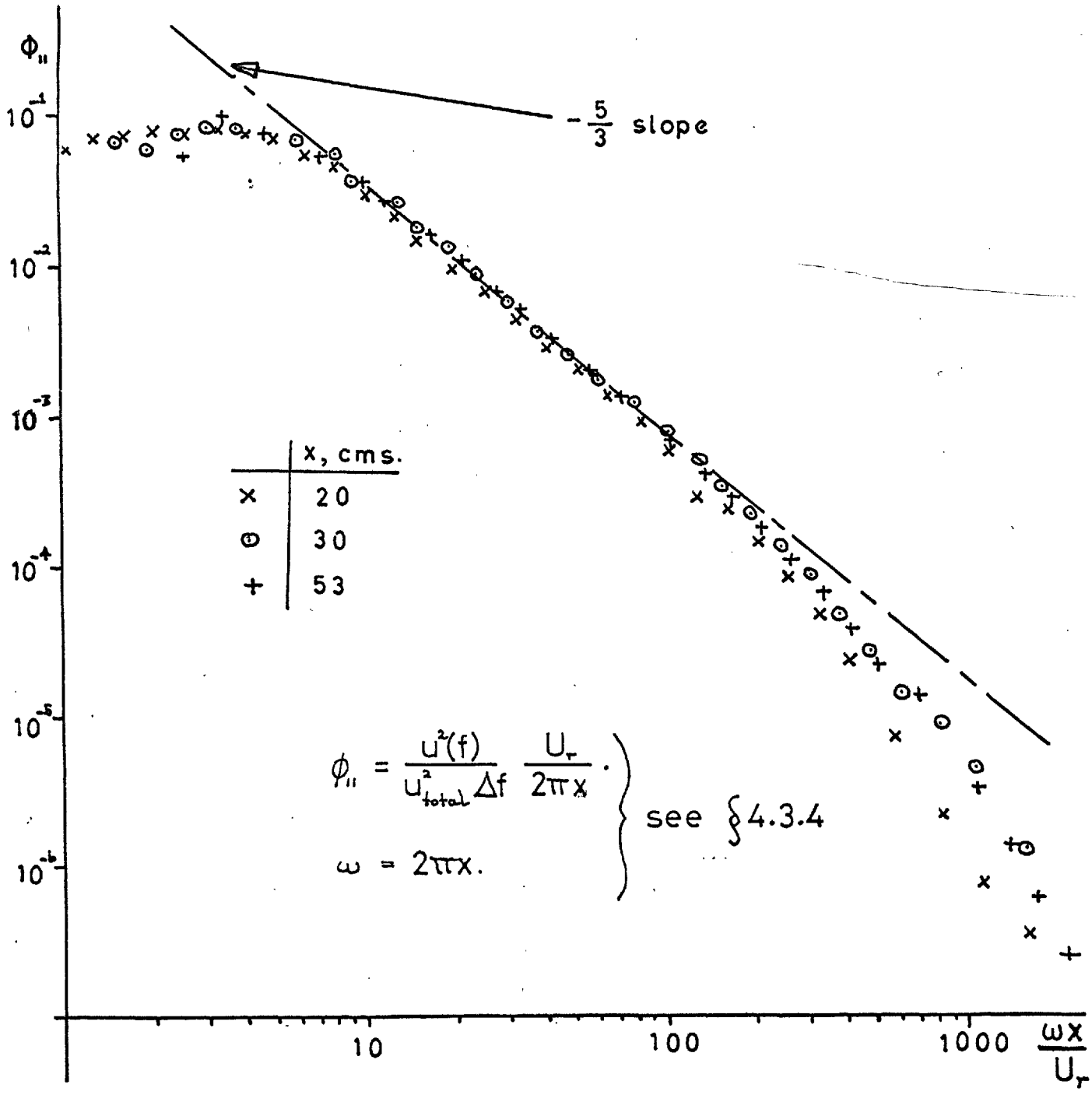


FIG. 4.11 u-component spectra at $\eta = 0$.

FIG. 4.12 Energy and dissipation spectra

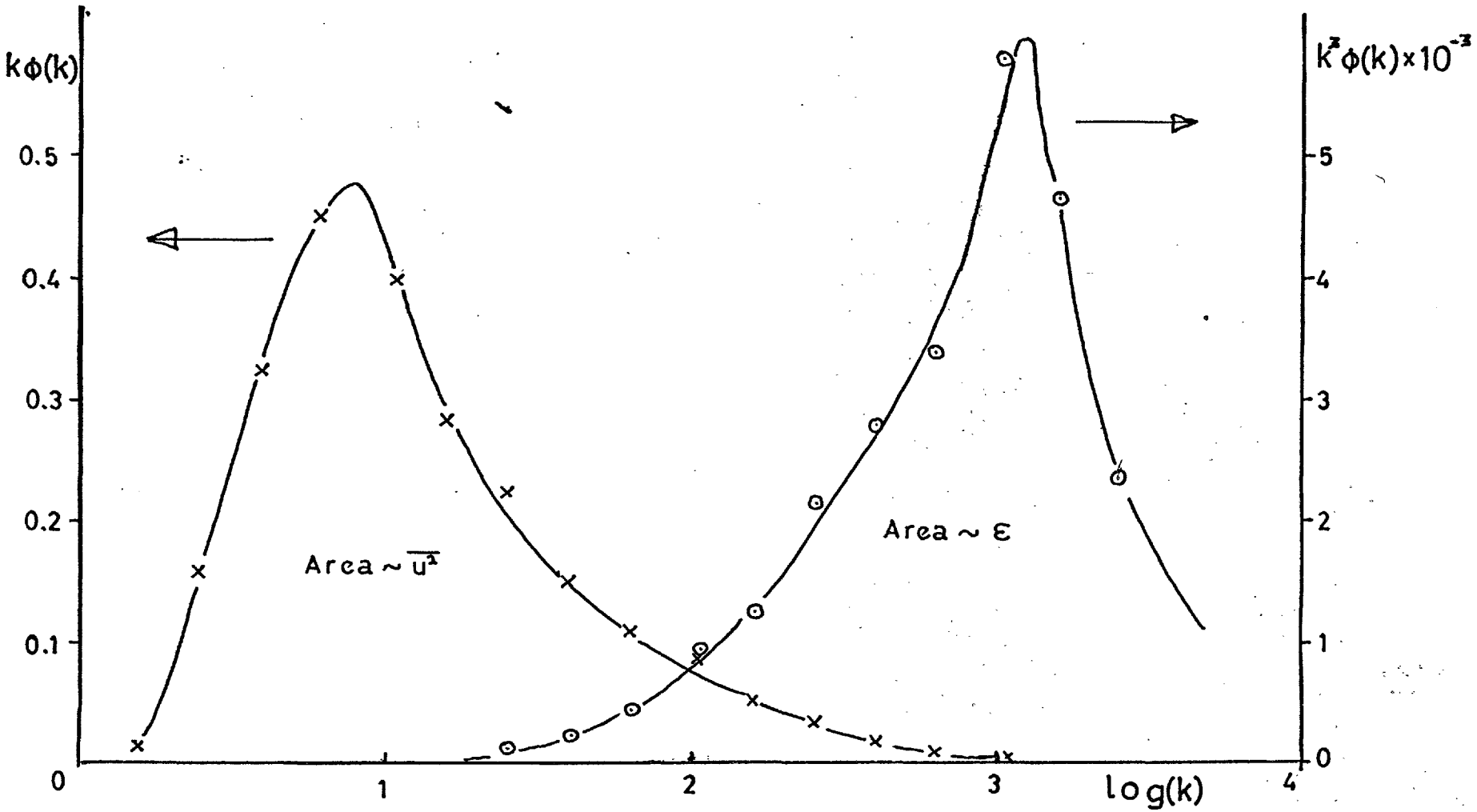


FIG. 4.13 Comparison of spectra with Grant's universal curve.

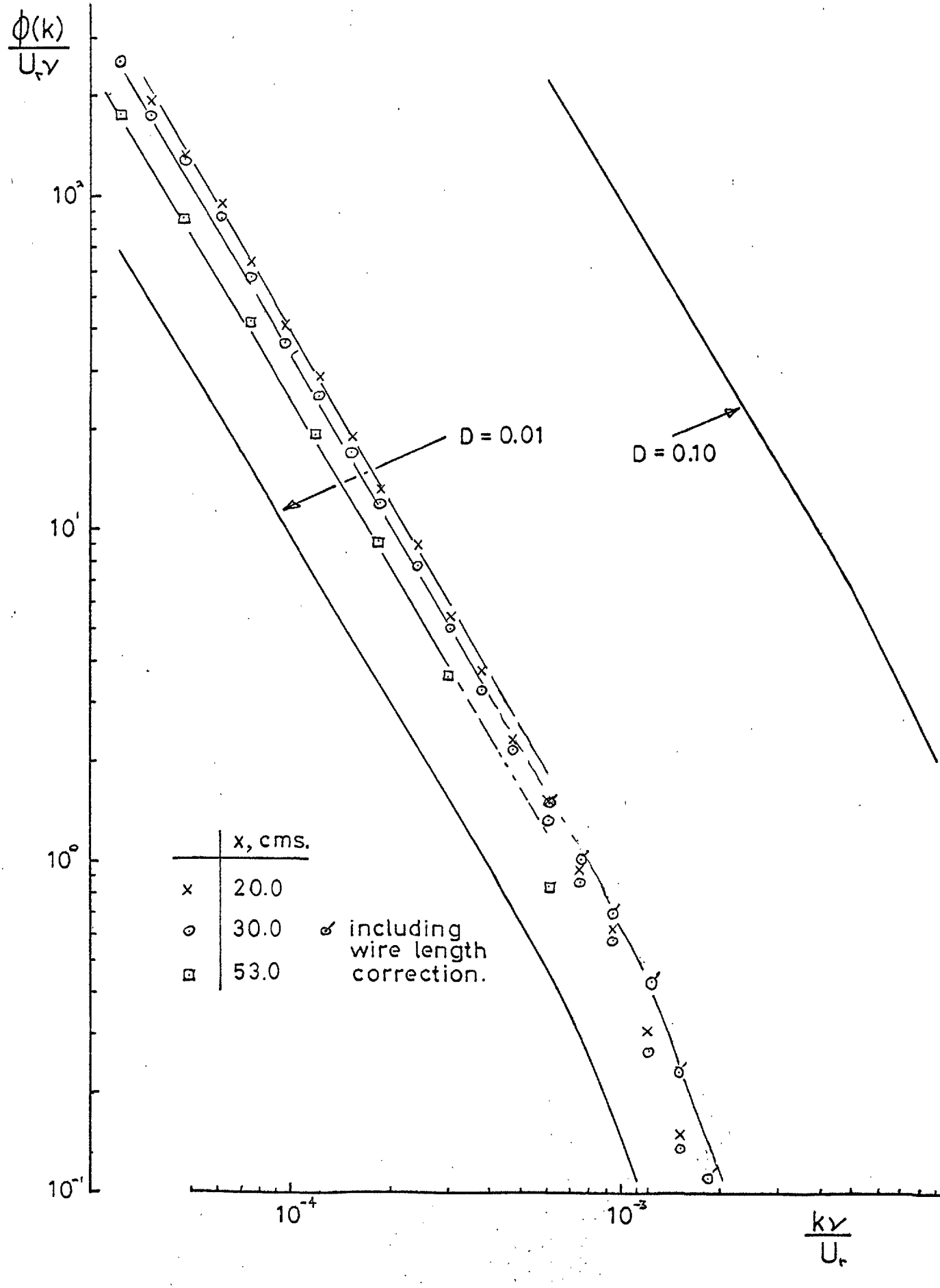


FIG. 4.14 Energy balance (measured values)

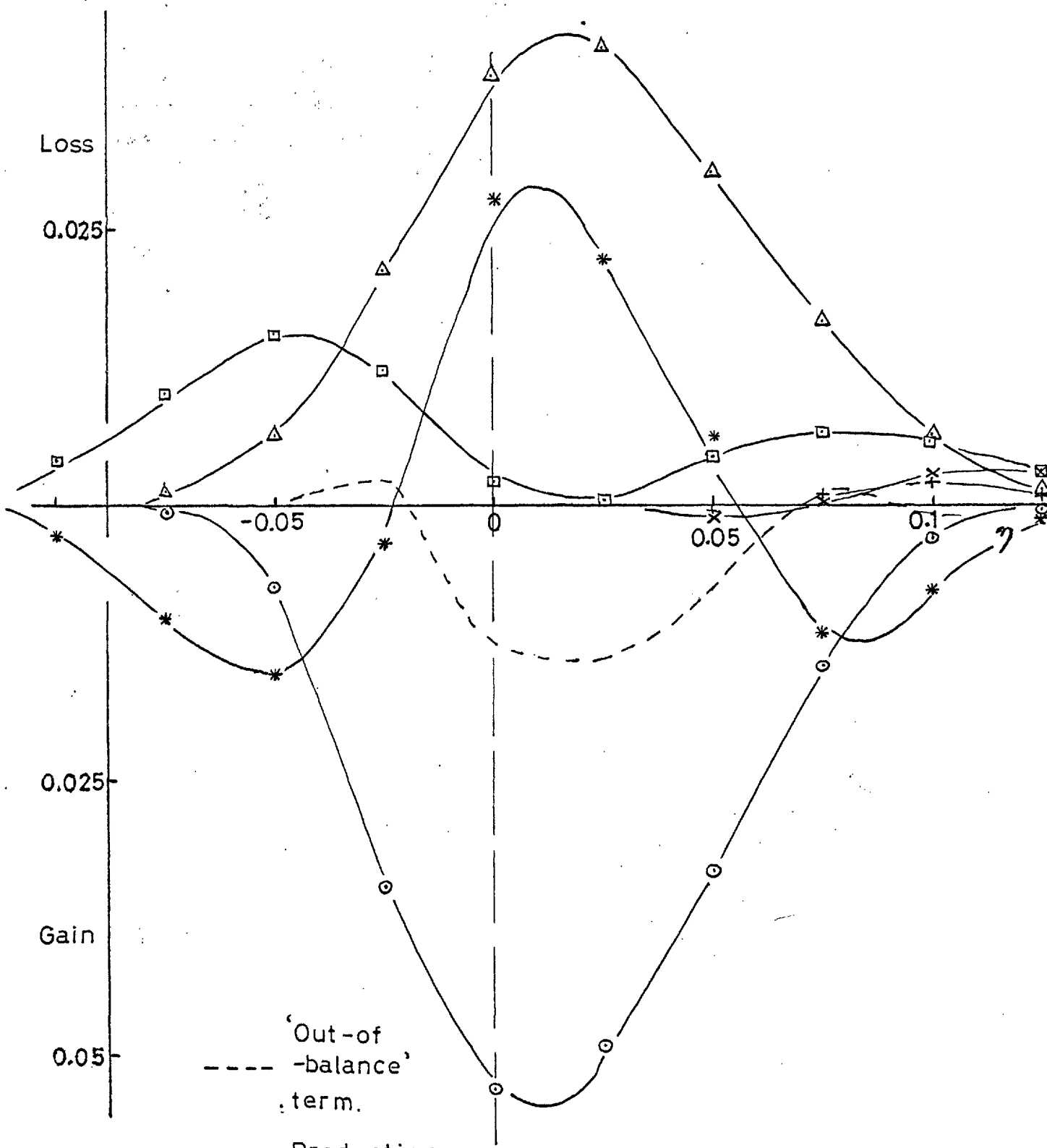


FIG. 4.15 Comparison between triple velocity diffusion and total diffusion obtained by difference.

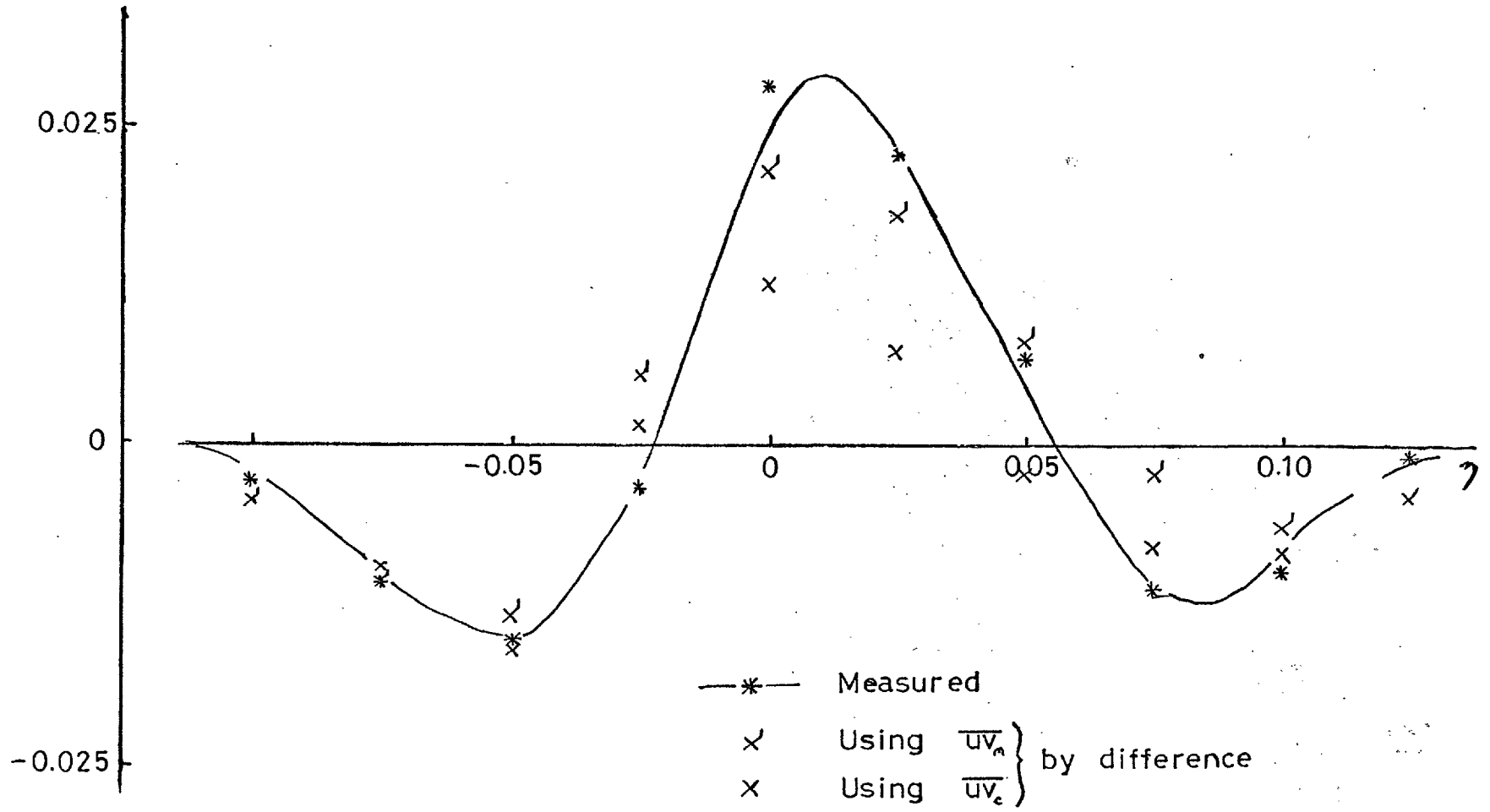


FIG. 4.16 Shear stress balance.

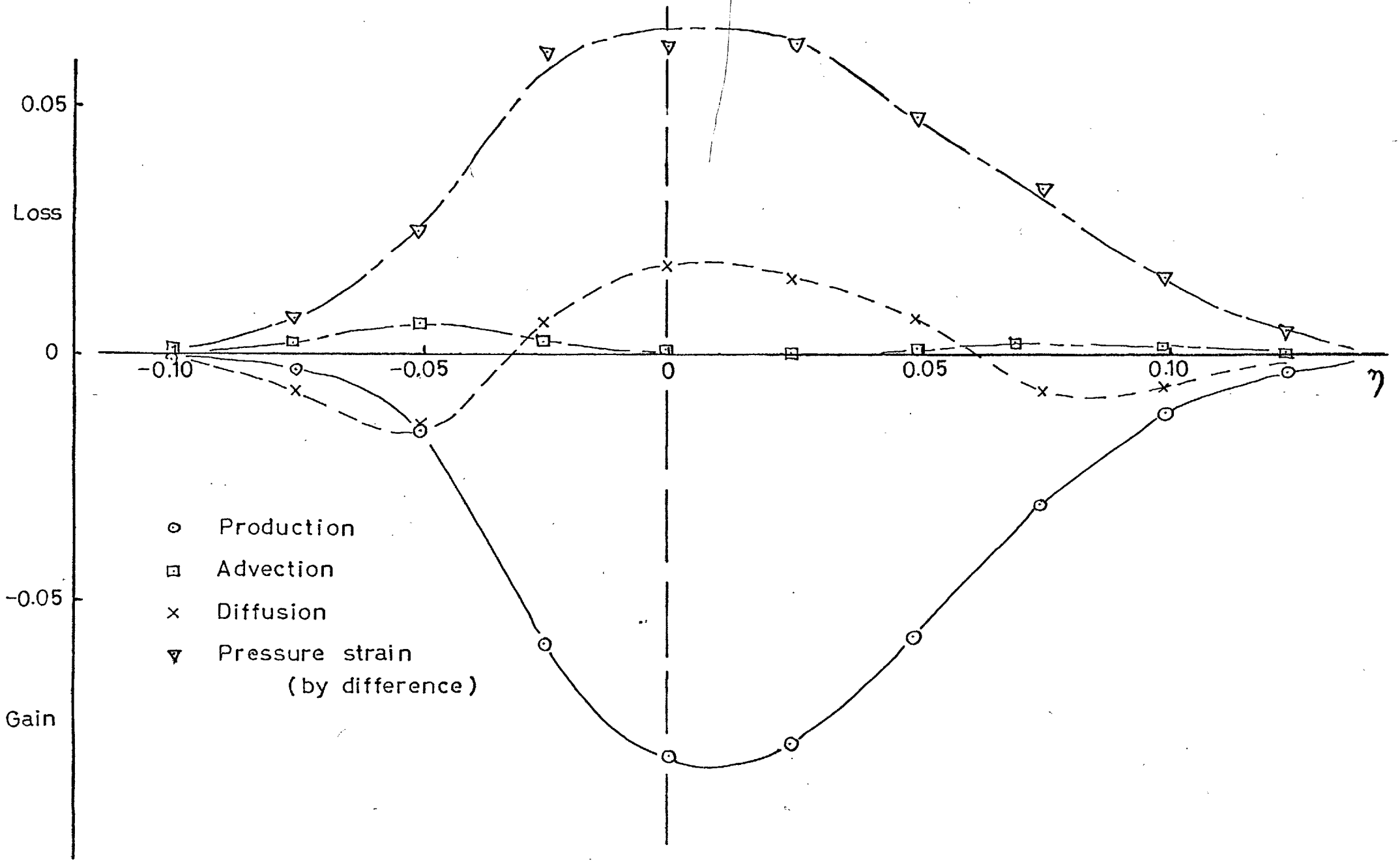
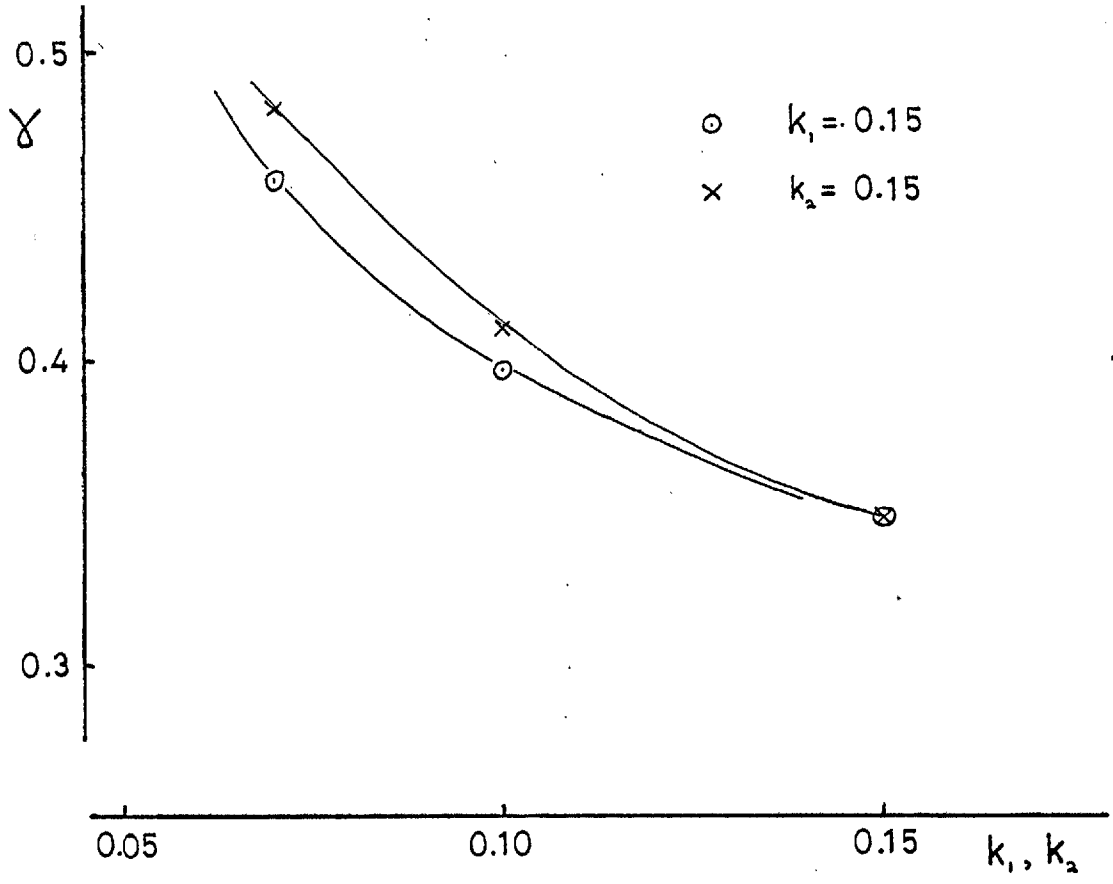


FIG. 4.17. Variation of intermittency with threshold levels.



$$k_1 = \left(\frac{\partial uv}{\partial t}\right) \Big/ \left[\overline{\left(\frac{\partial uv}{\partial t}\right)^2}_T\right]^{1/2}$$

$$k_2 = \left(\frac{\partial^2 uv}{\partial t^2}\right) \Big/ \left[\overline{\left(\frac{\partial^2 uv}{\partial t^2}\right)^2}_T\right]^{1/2}$$

Suffix T denotes an average over the turbulent region only.

(Plane mixing layer, $\eta = -0.05$)

FIG. 4.18 The intermittency function.

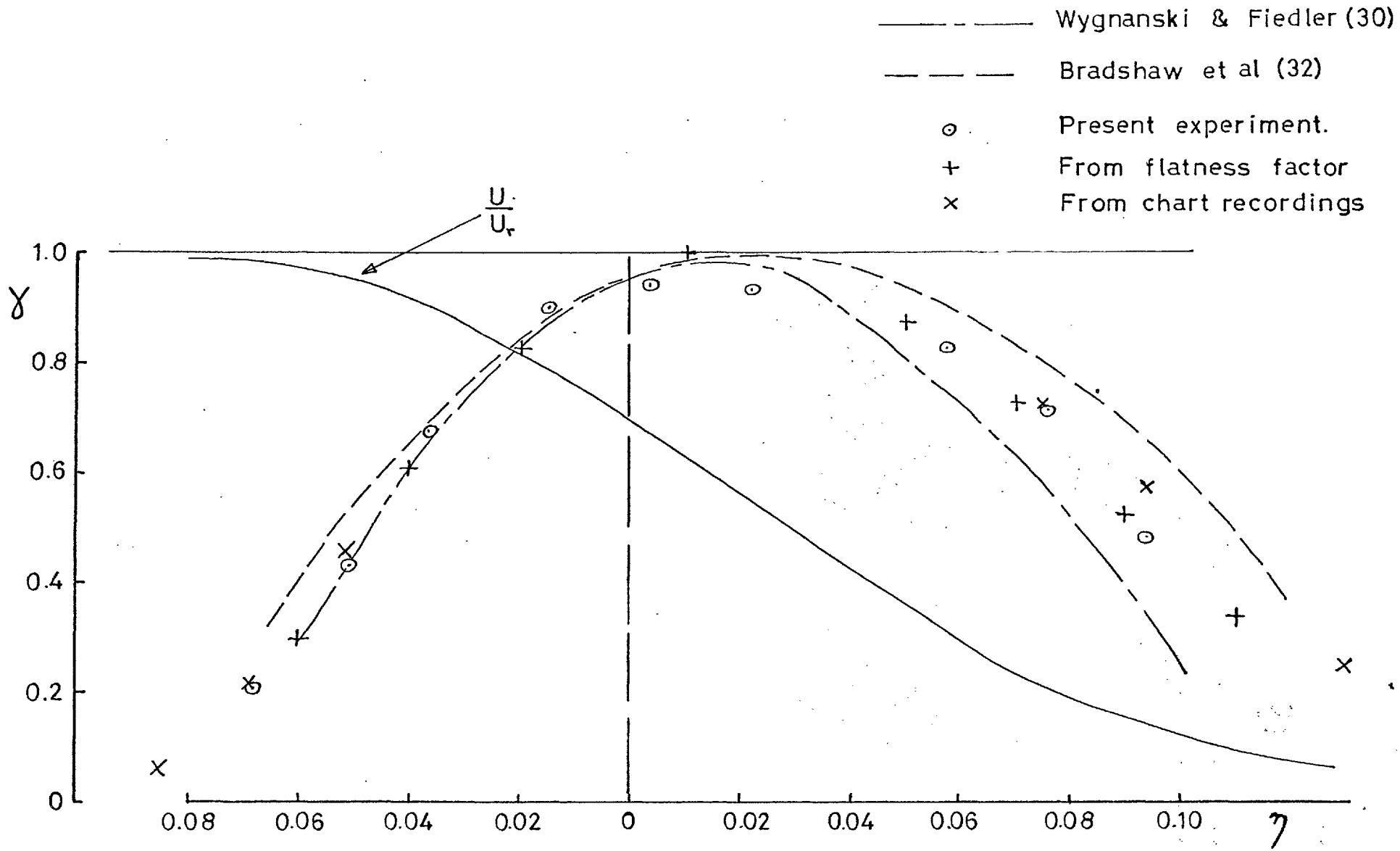
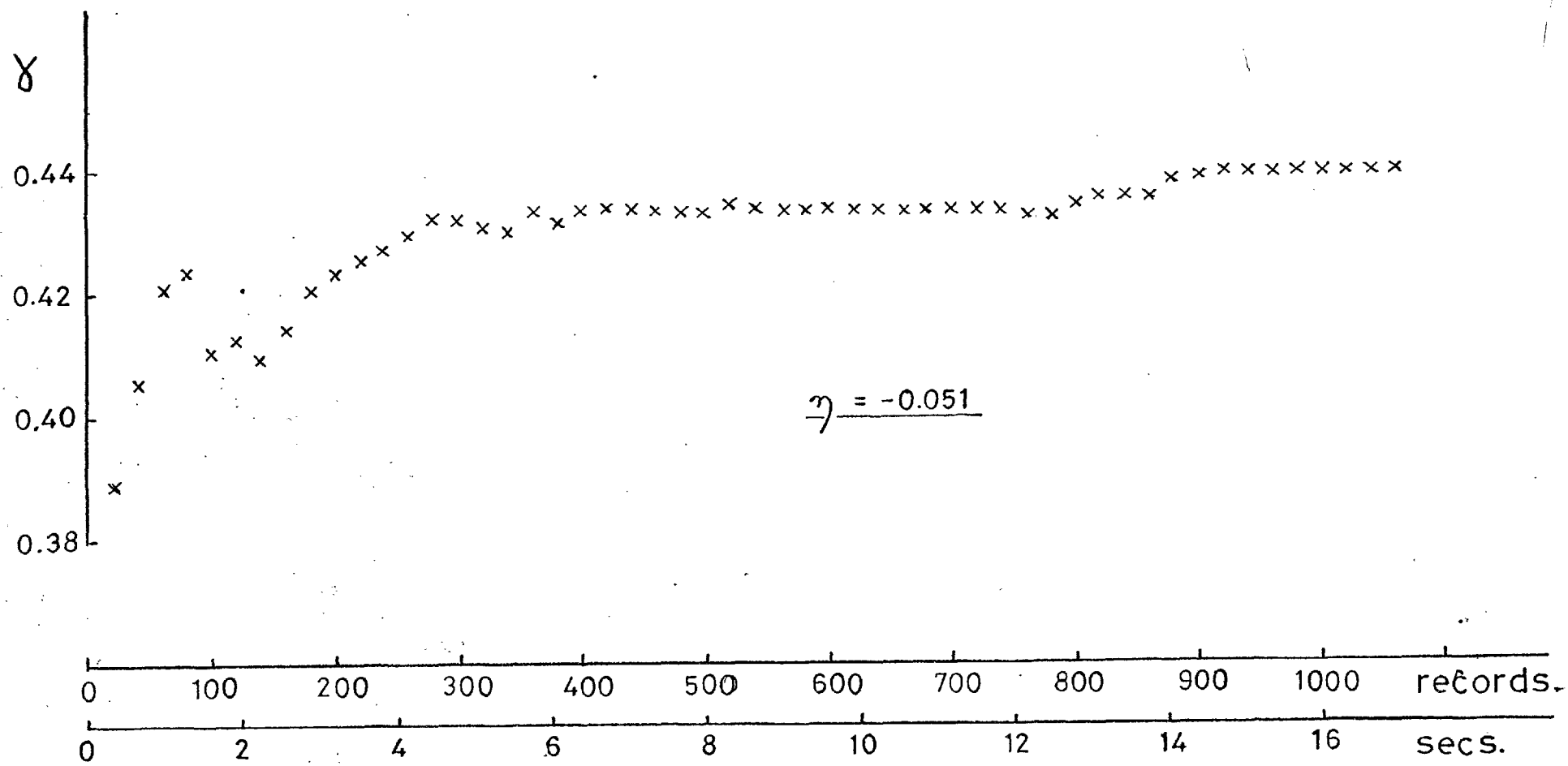


FIG. 4.19. Variation of intermittency with sample length.



5. THE DISTORTED MIXING LAYER

5.1 THE MEAN FLOW

5.1.1 Setting up and Flow Visualisation

The curved mixing layer was produced by placing a barrier in the lateral (y-z) plane between the side walls so as to turn the plane shear layer through 90^{o}. Figure 5.1 depicts the arrangement and includes a rough sketch of the resulting mixing layer. Plates 1 and 2 (see Chapter 2) are photographs of the actual rig in position at the contraction exit.

The ratio of the distance to the backplate to the contraction exit height determines both the ratio of shear layer thickness to radius of curvature and the ratio of the thickness of the potential flow layer to that of the shear layer. It was desirable to make the former ratio as large as possible while ensuring that some potential flow remained between the growing shear layer and the backplate at least up to the end of the region of interest. However, it was also necessary to bleed off the boundary layer - and some of the potential flow - to prevent separation at the 90^{o} corner. Paraffin vapour 'smoke' injected into the mixing layer near the contraction exit was used to check the extent of the shear layer and a mixture of 'Dayglo' powder paint and ker osene was used to check for separation on the floor and the side-walls near the corner. The backplate distance was gradually increased, adjusting the bleed width to the minimum that would prevent separation, until the point at which the shear layer had spread to the backplate had moved as far upstream as was acceptable.

Plate 3 is a typical smoke photograph of the final set-up; with the bleed width set at 5 cms and the backplate set at 44.7 cms

the mixing layer did not meet the backplate boundary layer until about 80 cm up the backplate and this was considered satisfactory.

The flow visualisation also checked, as far as is possible with such a technique, that there was no large scale 'flapping' of the mixing layer.

5.1.2 Initial Total Pressure Measurements

All the work presented here and in later sections was undertaken at a contraction exit velocity of 30.3 m/s, as in the plane mixing layer experiment.

Once a satisfactory flow had been obtained the next task was to find the actual path of the mixing layer with respect to the floor and the backplate. This was done by performing total pressure traverses across the shear layer at positions corresponding to the discs set into the floor and backplate as described in Section 2.2. Traverses using the floor discs near the contraction exit and the backplate discs beyond y = 25 cms were quite straightforward as the mean flow curvature in these regions was small. However, traverses in the curved portion required considerable care to ensure that the readings were not affected by inadequate pitch response of the pitot tube. The procedure was as follows. Once the former traverses had been made, a reasonable guess at the 'average' mean streamline direction on an intended traverse line in the corner region was made, and a pitot probe similar to the ones shown in Plate 2 was bent so that it would face in this guessed direction. A set of nine traverses (five vertical and four horizontal) was taken in this way and since the pitot tube pitch response was flat to within 0.2% of dynamic pressure for pitch angles less than $12\frac{1}{2}^{o}$ (see Figure 2.1) only one of these traverses had to be repeated with a slight change in the probe angle.

Figure 5.2a shows three lines of constant total pressure. Since in the plane mixing layer $\frac{U}{U_r}$ was found to be 0.67 at $\eta = 0$, the line $\frac{P}{P_r} = 0.67^2 = 0.45$ is plotted, where the total pressure P is measured with respect to the atmospheric pressure. The lines $\frac{P}{P_r} = 0.81$ and $\frac{P}{P_r} = 0.0625$ are also shown. Because of the static pressure variation in the corner region these lines are not expected to coincide, necessarily, with the lines $\frac{U}{U_r} = 0.90$ and $\frac{U}{U_r} = 0.25$. This is discussed further in Section 5.1.5. Figure 5.2b shows the continuation of these lines in the vertical portion of the mixing layer.

A measure of the accuracy of these traverses, which are not plotted individually since the final velocity measurements were made with hot-wires, is given in Figure 5.2a. There were three points where horizontal and vertical traverses crossed and the points marked as stars (*) on the Figure are points at which $\frac{P}{P_r}$ in the horizontal traverse was equal to $\frac{P}{P_r}$ at the relevant y-position in the vertical traverse. The error is always equivalent to less than 1 mm in spatial position.

The initial total pressure traverses across the vertical position of the mixing layer (Figure 5.2b) extended only to y = 47 cms but in view of later findings, the rig was extended vertically and all later work included measurements up to $y \simeq 75$ cms.

Although the streamlines in the curved portion are not, of course, exact circular arcs, inspection of Figure 5.2a showed that they were quite closely approximated by circular arcs with the centre at x = 12.6, y = 25, which was therefore chosen as the pivot position for the rotating traverse mechanism.

5.1.3 Checks of Two-Dimensionality

The work described in this Section (and Section 5.1.4) involved the use of the heated wire technique described in Section 2.7. Before

proceeding further with the mean flow work it was felt advisable to check that three-dimensionality of the flow, caused by variations in the thickness of the side wall boundary layers, was not important. This was done by stringing a heated nichrome wire vertically across the contraction exit at $x \simeq 2$ cms and at two positions either side of the centre line, $z = \pm 23$ cms. The mean temperature variation with z in the wake of the heated wire was measured at three fixed positions in the x-y plane and the results are shown in Figure 5.3. The reference thermometer was placed at some convenient location outside the wake of the heated wire, so that Figure 5.3 shows the excess temperature in the wake, ΔT, non-dimensionalised by its maximum value, plotted against z' where $z' = z \pm 23$. Even at the location furthest from the heat source ΔT_{max} was about $\frac{1}{2}^{o}C$ and was easily detectable.

Figure 5.4 shows the points of maximum excess temperature (which were assumed to coincide with the wake centre-line) plotted against the distance, d', from the source; bars on each point denote the possible error in position of ΔT_{max}. d' was taken as the distance measured around the $\frac{P}{P_r} = 0.45$ line (plotted in Figure 5.2a) which was quite close to the three wake traverse locations which were at (x,y) co-ordinates given by (25,4), (34.7,37) and (34.7,50).

Because of the complicated static pressure variations, particularly near the side walls in the corner region, it would be difficult to predict the behaviour of the side wall boundary layers. However, from Figure 5.4, it is clear that the curved position of the flow diverges slightly. It is most unlikely that this divergence is linear, but even drawing the steepest possible straight line through the four points (the fourth being the actual location of the heat source) yields an apparent origin of the flow at about 2000 cms upstream. The effect

of lateral divergence on the shear layer growth rate (or the momentum balance) will be a term of order $\frac{\delta}{2(S - S_o)}$ where δ is the thickness and S is measured along the shear layer centre line, additional to a term of order $\frac{d\delta}{dS}$ or $\frac{\delta}{S}$. So the error caused by neglecting the divergence is of order $\frac{S}{2(S - S_o)}$. S_o is - 2000 cms and S never exceeds 100 cms so the maximum error will be only about 3% and usually considerably less. Since this is almost within the expected measurement accuracy of the turbulence quantities it seemed pointless to apply any corrections.

5.1.4 Measurement of 'The Bounding Streamline'

These measurements, using the heated wire technique described in Section 5.1.3, were made after the hot-wire measurements described in Section 5.1.5 but form a convenient introduction to the latter.

In order to derive the mean streamlines from the measured velocity magnitude, $\tilde{U}$, ($\tilde{U} \equiv (U^2 + V^2)^{\frac{1}{2}}$) by integrating the continuity equation (see Section 5.1.6) we need to know the path of a single reference streamline and the velocity variation along it to provide a boundary condition. Since the floor streamline cannot be used because of the bleed, the most convenient choice is a streamline somewhere in the potential flow on the high velocity side of the mixing layer. A heated nichrome wire was stretched across the contraction exit along the line y = - 4 cms and temperature traverses made across its wake at 12 intervals of $\theta = 10^o$ between - 20^o and 90^o inclusive. Three further traverses in the vertical portion were made at y = 40.6, 48.6 and 61.2 but these were not used as it was not possible to determine the wake centre-line position to better than about 1½ mm at such large distances downstream. In fact the calculations described in Section 5.1.6 used a separate program for the vertical portion in which the bounding streamline required as

input was taken as the backplate surface streamline, so that determination of a free streamline in the potential flow was not necessary in this region.

The results of the traverses in the curved portion are shown in Figure 5.5 where ΔT has the same meaning as in Section 5.1.3. It is noticeable (Figure 5.5b) that there is a temperature gradient across the shear layer itself; the reference thermometer was in the potential flow and it was found that the laboratory air (at the low velocity side of the shear layer - small r_j) was actually $1^{\circ}C$ below the temperature of the free stream air. This was undoubtedly not attributable to the heating caused by the wind tunnel blower but it did not affect the accuracy of the determination of the wake centre line: even at $\theta = 20^{\circ}$ (Figure 5.5b) the maximum ΔT was still in the pure potential flow region.

The positions of maximum ΔT taken from these plots are plotted in Figure 5.2. The resulting smooth curve drawn through the points is hereafter referred to as the bounding streamline and, as indicated in Section 3.3, later results of cross shear layer traverses are plotted against y_j' where y_j' is the distance from this bounding streamline (Figure 5.2).

As a check on the relative accuracy of each wake traverse, the thermocouple was also traversed around the bounding streamline and Figure 5.6 shows the resulting ΔT plotted against S_b (where S_b is simply the distance between each measurement point) and compared with the individual values of ΔT_{max} taken from Figure 5.5. The difference is seen to be very small confirming the good repeatability of the measurements. Assuming that the position of the maximum temperature was a good measure of the wake centre-line the error in the resulting mean streamline position was probably no more than $\frac{1}{2}$ mm.

It is worth noting that we cannot expect ΔT_{max} to fall off approximately as $s_b^{-\frac{1}{2}}$ (as it might for a self-preserving wake) because of the large rates of strain imposed by the pressure gradients. Figure 5.6 shows that ΔT falls off somewhat faster than $s_b^{-\frac{1}{2}}$.

The mean velocity variation along the bounding streamline, measured using an unlinearised hot-wire with its axis in the z-direction, is shown in Figure 5.7, plotted as $\frac{\tilde{U}}{U_r}$ against θ. Using this velocity variation and the known bounding streamline direction it was possible to find U and V independently; discussion of this is deferred until Section 5.1.6. Figure 5.7 also gives an indication of the static pressure in the corner region; $\frac{\tilde{U}}{U_r}$ reaches a minimum of about 0.75 so that at this point, since the total pressure is constant along the streamline, $\frac{P_s}{\frac{1}{2}\rho U_r^2} = \{1 - (0.75)^2\}\ 0.44$ where P_s is measured with respect to atmospheric pressure.

5.1.5 Hot-Wire Velocity Profiles

Because of the static pressure gradient across the flow in the curved portion and since it is difficult to measure mean static pressure directly in a highly turbulent flow, the mean velocity field was measured using a normal unlinearised hot-wire (unlinearised because at the time the author felt that the increase in accuracy obtainable by linearisation, which anyway would only be noticeable - typically 3% - near the outer low velocity edge of the flow, did not warrant the use of further electronic apparatus). The wire was aligned with its axis in the z-direction so that it nominally responded to the total velocity vector $\tilde{U}$.

Ten traverses of mean velocity were made in the curved portion and a further eight in the vertical portion. The complete results are shown in Figures 5.8 - 5.12; traverses in the curved portion extended in some cases beyond the bounding streamline ($y_j' < 0$) and

in particular the traverse at $\theta = 0$ ($j = 19$) included a quick check of the backplate boundary layer which, as the inset to Figure 5.10 shows, was less than 1 mm thick at this position. $\frac{\tilde{U}}{U_r}$ values at the bounding streamline taken from these plots are also shown in Figure 5.7; the difference between these and the values measured in the streamline traverse is seen to be usually less than 1% of U_r. A further check, actually within the turbulent flow, was made by setting the hot-wire up at the $\frac{\tilde{U}}{U_r} = 0.67$ point on $j = 19$ ($\theta = 0^o$) and traversing around the shear layer, adjusting the probe position to obtain the same anemometer output voltage at each θ. The resulting positions of the $\frac{\tilde{U}}{U_r} = 0.67$ points are shown on Figures 5.8 - 5.10; the repeatability is very satifactory.

The velocity traverses in the vertical portion (Figures 5.11 and 5.12) are plotted against d, where d is the distance from the backplate, and are compared where possible with pitot tube traverses. The static pressure in this region had recovered to atmospheric and since it was quite close to atmospheric in the contraction exit there should be good agreement between the two methods. However, there is a noticeable difference between the pitot tube and hot-wire measurements on the low velocity side of the shear layer. The later calculations showed that the transverse mean velocity component (V) was small compared with U at the $\frac{U}{U_r} = 0.25$ point, so that this difference cannot be attributed to large mean pitch angles of the streamlines. Later work showed that the turbulent intensities were somewhat larger in this region than in the plane layer, so it is possible that some of the errors may have been due to a combination of inadequate pitot probe yaw response (which would tend to <u>decrease</u> the measured dynamic pressure) and hot-wire inaccuracies (large intensities tending to <u>increase</u> the measured mean velocity). However,

it is difficult to attribute all the difference to these effects, so there remains some doubt. The hot-wire profile certainly 'looks' more plausible (very similar to the plane layer results in fact): it is assumed that the pitot results are in error in this region, so that the true $\frac{P}{P_r} = 0.0625$ line is co-incident with the $\frac{U}{U_r} = 0.25$ line.

The points on each velocity profile at which $\frac{\tilde{U}}{U_r} = 0.9$, 0.67 and 0.25 are shown in Figure 5.2. There is a considerable difference for $70^o > \theta > 10^o$ between the lines $\frac{P}{P_r} = 0.81$ and $\frac{U}{U_r} = 0.90$; this is merely a reflection of the large static pressure in this region. The normal mean momentum equation can be written

$$U \frac{\partial V}{\partial x'} \equiv \frac{U^2}{R} = - \frac{\partial \overline{uv}}{\partial x'} - \frac{\partial v^2}{\partial y'} - \frac{1}{\rho} \frac{\partial p}{\partial y'} \quad .$$

Neglecting the turbulent contributions (and checks showed this to be justified, see Section 5.2.7) we can write

$$\frac{p - p_{b.s}}{\rho U_r^2} = \frac{1}{U_r^2} \int_{b.s} U \frac{\partial V}{\partial x'} \cdot dy'$$

where b.s. denotes the bounding streamline. The results of the mean flow calculation described in Section 5.1.6 enabled a rough variation of $U \frac{\partial V}{\partial x'}$ against y' to be determined and it was evident from this that at the point where the local velocity $\frac{\tilde{U}}{U_r}$ was 0.67, the difference between local static pressure and atmospheric was only about 0.1 of its value at the bounding streamline. Even in the region of maximum static pressure ($\theta = 40^o$, say) this implies that at $\frac{\tilde{U}}{U_r} = 0.67$ the static pressure was different from atmospheric by only about 1% of the reference velocity. It is therefore not surprising that the lines $\frac{P}{P_r} = 0.45$ and $\frac{\tilde{U}}{U_r} = 0.67$ shown in Figure 5.2 collapse well even in the corner region. See Section 5.2.7 and Figure 5.43 for further details.

5.1.6 Reduction of Mean Flow Data and Some Results

If it were not for the rather complicated geometry of the curved mixing layer, calculation of the transverse mean velocity, V, (or, to put it another way, determination of the mean streamlines) using the continuity equation and the measured total velocity $\tilde{U}$ would be a trivial problem. In fact, as stated in Section 4.2.2, a very simple numerical program was written for the self-preserving mixing layer as a guide to the sort of program required for the curved layer. The results are not presented apart from the transverse mean velocity profile, Figure 4.4, discussed in Section 4.2.2.

Computation of the curved flow was broken into two separate programs, the first and more complex solving the curved portion of the flow ($\Theta = 0^{o} - 90^{o}$) and the second the vertical portion ($y > 25.0$) The essential details of these programs, including a description of the preparation of input data and accuracy checks using test cases, are given in Appendix V. No attempt is made to present the complete results as this would involve a large number of plots and tables most of which would add nothing of immediate relevance: complete program outputs are obtainable from Mr. P. Bradshaw of the Department of Aeronautics. Instead, some of the more interesting and pertinent aspects of the results are presented here and further results are explained in later chapters.

5.1.6.1 The mixing layer growth rate In the case of the self-preserving mixing layer (Section 4.2) the shear layer thickness, δ, was defined as the distance between two lines of constant $\frac{U}{U_r}$ ($\frac{U}{U_r} = 0.90$ and 0.25 being chosen for convenience). Figure 5.2 enables a similarly defined shear layer thickness to be determined, δ being measured along a line normal to the local direction of the $\frac{\tilde{U}}{U_r} = 0.67$ line. Figure 5.13 is a plot of δ defined both on constant velocity

(δ_u) and constant total pressure (δ_p) lines, against S, compared with the variation of δ in the plane mixing layer (deduced from Figure 4.2 or 4.3). In the corner region the mixing layer clearly grows less rapidly than the self-preserving flow. As indicated in Section 2.2 the streamline curvature will tend to stabilise the flow in this region so we would expect a decrease in turbulent mixing and therefore in shear layer growth rate: this expectation is confirmed.

What is more surprising is that once the curvature has ceased (beyond S ~ 50) the mixing layer grows a little faster than the self-preserving flow. In the light of the previous investigations mentioned in Section 1.2 we might have expected that after the distortion there would be a very slow monotonic return of the mean flow (and turbulence) to the asymptotic self-preserving condition. It appears that there is an initial 'overshoot' so that $\delta S/dx$ is asymptoting from above rather than below its final value. This overshoot implies an increase in the turbulent shear stress beyond the self-preserving value and indicates that the response of the flow to the extra rates of strain caused by the curvature is not without interest. The high velocity side is relatively thicker and the low velocity side relatively thinner than in the plane mixing layer: Figure 5.2b indicates that the ratio of the distance between the $\frac{U}{U_r} = 0.90$ and 0.67 lines to that between the $\frac{U}{U_r} = 0.67$ and 0.25 lines is considerably greater than 0.6, which is about the corresponding plane layer value (Figures 4.2 and 4.3). Possible reasons for this are discussed in Chapter 6.

5.1.6.2 Mean Vorticity and Rates of Strain To give an indication of the extra rates of strain imposed by the distortion, Figure 5.14 shows the principal rate of strain and the vorticity

(both independent of the axes) around the mixing layer centre line. The principal rate of strain is given by

$$\pm \left[4 \left(\frac{\partial U'}{\partial x_j}\right)^2 + \left(\frac{\partial U'}{\partial y_j} + \frac{\partial V'}{\partial x_j}\right)^2 \right]^{\frac{1}{2}}$$

and the vorticity is $\frac{\partial U'}{\partial y_j} - \frac{\partial V'}{\partial x_j}$. In the plane mixing layer both $\frac{\partial U}{\partial x}$ and $\frac{\partial V}{\partial x}$ are small so that the principal and shear rates of strain and the vorticity are all numerically equal to $\frac{\partial U}{\partial y}$. At the very start of the distortion $\frac{\partial V'}{\partial x_j} \equiv \frac{U'}{R}$ (where R is the streamline curvature) is the term which dominates the change in strain rate, so that the vorticity and the principal rate of strain should lie at equal distances above and below (respectively) the ordinary mixing layer value (Figure 5.14a). The fact that this is not exactly true is a reflection of the program errors in this region which tend to increase the calculated vorticity (see Appendix V) and lower the calculated strain rate. It is clear from Figure 5.14a that the longitudinal normal strain, $\frac{\partial U'}{\partial x_j}$ only becomes significant compared with the shear strain $\left(\frac{\partial U'}{\partial y_j} + \frac{\partial V'}{\partial x_j}\right)$ after $S \approx 30$ so that the change in vorticity and principal strain up to this point is due largely to changes in $\frac{\partial V'}{\partial x_j}$ caused by the rotation.

After the sudden increase in the magnitude of the principal strain rate at about S = 35, due to gradual reduction in magnitude of $\frac{\partial V'}{\partial x_j}$ and a relatively significant increase in $\frac{\partial U'}{\partial x_j}$, both vorticity and the principal strain rate appear to asymptote to the values calculated by assuming that the flow has recovered to a self-preserving state. In fact, despite the overshoot evident in Figures 5.13 and 5.14b, the growth rate does seem to be roughly constant in this region and the virtual origin of the flow was found simply by extrapolating this line backwards to the S-axis (Figures 5.13 and 5.14b).

It is the response of the turbulence to these strains that will be of particular interest and further discussion of them and of the direction of the principal strain rate is deferred until Section 5.2.

5.2 THE TURBULENCE

5.2.1 Initial Analogue Measurements

In the course of the hot-wire mean velocity measurements some analogue measurements of the streamwise, $\overline{u^2}$, component of turbulence intensity were made and subsequently a crossed hot-wire was used to measure $\overline{u^2}$, $\overline{v^2}$, $\overline{w^2}$ and $\overline{uv}$ around the centre line of the mixing layer (defined in this case as the $\frac{\tilde{U}}{U_r} = 0.67$ line). The crossed wire was not linearised and the measurements are not presented here as their accuracy was not considered to be as good as the later complete series of crossed wire traverses. However, the work did serve to acquaint the author with the many problems and pitfalls invariably encountered in hot-wire work and the resulting decisions regarding calibration procedures have been described in Section 2.4. One result of this work that is worth mentioning because it inspired much of the later work was the substantial overshoot in turbulent energy ($\overline{q^2} = \overline{u^2} + \overline{v^2} + \overline{w^2}$) and shear stress ($\overline{uv}$) after the end of the distortion (Figure 5.23). It was felt that the turbulent structure should be investigated in somewhat more detail than originally intended.

5.2.2 The Crossed Hot-Wire Traverses and U-Component Spectra

Crossed hot-wire traverses in the curved portion of the mixing layer were made using the rotating traverse arrangement described in Section 2.2. The probe was traversed along lines of constant Θ (Figure 5.1) between $\Theta = 0$ and 90° in intervals of 10° and by using the pitch mechanism described in Section 2.2, the probe was aligned

in the local free stream direction previously determined by the numerical mean flow program (Appendix V). This was intended to minimise errors caused by the probe's uncertain yaw response at large angles of yaw and in fact provided an interesting comparison between the computed mean flow direction and that measured by the crossed wire. A typical example is shown in Figure 5.15 where the mean flow direction determined in these two ways is compared for $j = 13$ ($\theta = 30^{o}$). Only at the outer edge of the flow, where the errors in the computed mean flow direction and also in the crossed wire measurements are bound to be largest, does the difference exceed one degree. This was particularly satisfying (although perhaps a little fortuitous!) because the crossed wire is not recognised as an accurate mean flow instrument.

In the vertical portion, where the mean flow curvature was small, the crossed wire was aligned in the usual way with the probe axis parallel to the backplate and traverses were made at six stations using the disc-mounted traverse gear as described in Section 2.2.

In both the curved and vertical portions each traverse consisted of between eight and twelve measuring stations, which for convenience were chosen to coincide with mesh points as defined in the mean flow program (Appendix V). Analogue tape recordings of the two anemometer voltage signals were made at each station with the wires in both the x_j'-y_j' and the x_j'-z planes (x-y and y-z in the vertical portion) and these recordings were later digitised and analysed as described in Sections 2.5 and 2.6. For this work the crossed wire recordings were linearised digitally; this made extra analogue apparatus unnecessary and merely involved two extra program statements, with a consequent increase in central processor time (about 4% of the total program

time since only a proportion of the total number of digitised samples was used - Section 2.6) so that it was felt to be worthwhile.

The program output had all the usual quantities i.e. $\overline{u^2}$, $\overline{v^2}$, $\overline{uv}$, $\overline{u^3}$, $\overline{u^2v}$, $\overline{v^2u}$, $\overline{v^3}$ and $\overline{u^4}$ (and the corresponding quantities measured in the x-z plane) non-dimensionalised by the contraction exit velocity U_r. Typical sets of results (along the J-lines used for energy and shear stress balances) are presented in Figures 5.16 and 5.17 where each quantity has been rotated so that it is measured with respect to x_j', y_j' co-ordinates. This seems the most consistent way to present the results, although to obtain, for instance, shear stress balances, different axes are required (Chapter 3). Only the triple products along J = 11 are shown as an example; complete tabulations of these and the other turbulence quantities are available from Mr. P. Bradshaw.

As a check on the consistency of the results, a traverse around the streamline $\psi = 40.0$, where ψ (used in the mean flow program, see Appendix V) is defined as $\int_{b.s.} U dy_j'$ where subscript b.s. denotes the bounding streamline at which $\psi \equiv 0$, was made with the wires in the $x_j' - y_j'$ and the $x_j' - z$ planes. The resulting measurements on the J = 11 line (which are typical) are included in Figures 5.16c and 5.17 where it is seen that the differences are quite small, even in the case of the triple products. This was particularly encouraging and no attempt was made to smooth the raw data by cross-plotting.

The normal diffusion term in the energy balance $(\frac{\partial}{\partial y} \overline{q^2 v})$ requires knowledge of $\overline{vw^2}$. Extra traverses along J = 19 ($\Theta = 0^\circ$) with the wires in planes at $\pm 45^\circ$ to the $x_j' - y_j'$ and $x_j' - z$ planes showed no difference in the relative behaviour of $\overline{vw^2}$ and $\overline{v^3}$ compared with the plane layer. Since measurement of $\overline{vw^2}$ over the whole mixing layer would have almost doubled the amount of recorded data it was assumed that $\overline{vw^2} = \frac{1}{2}\overline{v^3}$ everywhere.

U-component spectra were measured in the same way as for the plane mixing layer. The frequency range of the Bruel and Kjaer analyser was scanned at a number of positions around the maximum $\overline{q^2}$ line (or, in some cases, on the $\frac{U}{U_r} = 0.67$ line) of the curved layer and across the layer at S = 60. The results plotted in the usual way are shown in Figures 5.18 - 5.21 and are discussed further when the energy balances are presented (Section 5.2.5). It is worth noting here that there seems to be no extensive $^{-5}/_{3}$ region in spectra measured away from the (almost) fully turbulent central region of the mixing layer (Figure 5.21); this may be caused by the highly intermittent nature of the flow. Discussion of the spectral measurements is deferred to Section 5.2.5 when the energy balances are considered.

5.2.3 The Direction of the Mixing Layer

One of the interesting features of any distorted shear layer is the behaviour of the shear stress. However, as stated in Chapter 3, the shear stress depends on the co-ordinate axes: in a thin shear layer the x-axis is always taken in the direction of the layer but in a highly curved layer like the present one it is not immediately certain whether any meaningful choice can be made for the 'direction' of the layer. Preferably the several definitions of the direction which are valid in a plane layer should also coincide in the distorted layer. If not, it is necessary to abandon the concept of a shear layer and to treat the flow as sui generis by discussing principal stresses and rates of strain.

The most obvious definition of shear layer direction in the curved layer is simply the direction of the 'effective' $\eta = 0$ line defined in Section 5.1.as the line along which $\frac{U}{U_r} = 0.67$. Other possible definitions are

(i) the direction, β_1, of the line dividing the distance between the $\frac{P}{P_r} = 0.81$ and 0.0625 lines in the same ratio as the $\frac{P}{P_r} = 0.45$ line in the plane layer.

(ii) The direction, β_2, of the line of maximum $\overline{q^2}$ minus about 1^o (since $\overline{q^2}_{max}$ in the plane layer is at $\eta \sim 0.017$).

(iii) The direction, β_3, of the mean streamline at $\frac{U}{U_r} = 0.67$ minus about 0.6^o (since $\frac{V}{U_r}$ at $\eta = 0$ in the plane layer is about 0.01).

(iv) The direction, β_4, of the line having the same inclination to the expansive rate of strain as does the $\eta = 0$ line in the plane layer.

The shear layer direction was determined in each of these ways and is plotted in Figure 5.22, in which β is measured with respect to the local J-line. (The 'effective' $\eta = 0$ line was found to coincide exactly with (i) in the curved portion of the layer). Within the experimental accuracy of measuring directions of curved lines, say ± 1 degree, the four definitions are seen to give similar results; (β_3 and β_4 are subject to larger errors near J = 1 and 19 due to mean flow program inaccuracies, see Appendix V). At the centre of the plane layer a change in axes of 1 degree produces less than a 3% change in shear stress; it was therefore felt that the smooth curve drawn through the points plotted in Figure 5.22 could justifiably be defined as the variation of the local direction of the mixing layer.

5.2.4 Turbulent Energy and Shear Stress

The variations of maximum turbulent energy, $\overline{q^2}$, and maximum shear stress, $\overline{uv}_m$, around the shear layer centre-line are shown in Figure 5.23 where $\overline{uv}_m$ is measured with respect to both the ordinary

x_j', y_j' co-ordinates and the curved co-ordinates s', n' defined in Section 5.3. The anticipated initial stabilising effect of the curvature is obvious; the shear stress is reduced relatively more than the turbulent energy. As mentioned in Section 5.2.1 the distinctive feature of this plot is the large overshoot in energy and shear stress when the curvature is removed. The behaviour of the maximum and minimum values of the triple velocity products appearing in the transport equations is similar (Figure 5.24). Discussion of possible reasons for this extra turbulent activity is deferred until Chapter 6. However, it is worth noting that the maximum value of $\overline{q^2v'}$ on the high velocity side (Figure 5.24b) drops far more than the other turbulence quantities in Figures 5.23 and 5.24. $\overline{q^2v'}$ is related to the entrainment so this is an indication that the entrainment is reduced far more on the high than on the low velocity side of the mixing layer and that the turbulent diffusion probably drops relatively more than the other terms in the energy transport equation. The latter statement is proven in Section 5.2.5 and both points are discussed more fully in Chapter 6.

It will also be noticed on Figure 5.24 that all the triple products on the high velocity side begin to decrease beyond about S = 80. This is undoubtedly caused by the presence of the backplate: there is a corresponding decrease in $\frac{\overline{v^2}}{u^2}$ along the line of minimum triple products, indicating that the solid boundary is tending to 'flatten' the large eddies. This is what one would expect but it is interesting that $\overline{q^2v}$ decreases as much as $\overline{q^2u}$. Clearly $\overline{q^2v}$, as well as $\overline{q^2u}$ comes mainly from the large eddies. In view of this effect, the energy and shear stress balances in the vertical portion were derived at cross-sections upstream of S = 80.

Figure 5.25 shows the variation of the maximum principal

turbulent stress around the centre line compared with the principal rate of strain, non-dimensionalised by the shear layer thickness, δ. Both are divided by the corresponding plane shear layer quantity and the use of δ_p as the non-dimensionalising quantity (for the principal rate of strain) rather than S, avoids the problem of a changing virtual origin. As expected, the response of the turbulence lags behind, and is somewhat more vigorous than, the mean flow behaviour.

The direction of the principal rate of strain is given by

$$\alpha_1 = \tfrac{1}{2} \tan^{-1} \left(\frac{\frac{\partial U}{\partial y'} + \frac{\partial V}{\partial x'}}{2 \frac{\partial U}{\partial x'}} \right) ,$$

and the direction of the principal turbulent stress is

$$\alpha_2 = \tfrac{1}{2} \tan^{-1} \left(\frac{2\overline{uv}}{\overline{u^2} - \overline{v^2}} \right) .$$

Figure 5.26 shows how the two directions vary around the mixing layer centre line. If the shear layer were to rotate with no change in the almost zero value of $\frac{\partial U'}{\partial x}$ in the plane layer, α_1 would follow the dotted line. However the pressure gradients cause a substantial variation of longitudinal velocity around the centre line (similar to that around the bounding streamline, Figure 5.7) so that $\frac{\partial U}{\partial x'}$ takes significant negative (for $S < 35$) and then positive (for $S \geq 35$) values, causing the variation of α_1 as shown in Figure 5.26.

5.2.5 Turbulent Energy Balances

Energy and shear stress balances have been derived around the mixing layer centre line and at various cross-sections of the flow. This and the following section outline the procedure adopted for deriving each term in the relevant transport equation, indicate the sources of error and likely accuracy and present the resulting balances. Discussion of the physical significance of the results is deferred to

5.2.5.1 Centre Line Balance. Figure 5.27 In view of the vast amount of labour required to obtain the balances from the raw experimental data, particularly to calculate the terms involving longitudinal gradients of turbulence quantities, the 'centre-line' is re-defined for the purposes of these sections as the line joining the mesh points, i, j, (used in the mean flow program) nearest to the line of maximum turbulent energy (q^2). Although not coincident with it this is very close to the centre-line defined in Section 3.3 and resulted in a significant reduction in the amount of interpolation of experimental data required.

(i) The Production Term

$$- \overline{u'v'}\left(\frac{\partial U'}{\partial y_j} + \frac{\partial V'}{\partial x_j}\right) - \left(\overline{u'^2} - \overline{v'^2}\right) \frac{\partial U'}{\partial x_j} \quad .$$

This is relatively straightforward. The mean rates of strain are output directly by the mean flow program (Section 5.1.7) so that, using the measured turbulence quantities, the production follows directly. Shear stress measurements in the plane layer (Section 4.3.2) were 15 - 20% lower than the calculated shear stress. For the sake of consistency no attempt is made to use a calculated shear stress in the curved layer (this would anyway not be a particularly accurate calculation) so that the production term in Figure 5.27 is expected to be somewhat low. Near j = 1 (S = 12) the calculated rates of strain are too low because of program errors in this region (Appendix V).

Figure 5.28 shows the contributions of the shear and normal stress production to the total. In this case of

course the terms need to be measured in co-ordinates (x', y') aligned with the direction of the shear layer - Chapter 3.

(ii) The Advection Term

$$- \tfrac{1}{2}U' \frac{\partial \overline{q^2}}{\partial y_j'} - \tfrac{1}{2}V' \frac{\partial \overline{q^2}}{\partial x_j'} \quad .$$

This can also be written as

$$- \tfrac{1}{2}\tilde{U} \frac{\partial \overline{q^2}}{\partial s}$$

(where s is measured along a streamline) and this form is preferred as it reduces the labour and increases the accuracy. The path of the streamline through the point of interest (i, j) was found from the mean flow output data, and $\overline{q^2}$ at the relevant y_j' position in the J-4, J-2, J+2 and J+4 lines was interpolated from the $\overline{q^2}$ plots (e.g. Figure 5.16). $\frac{\partial \overline{q^2}}{\partial s}$ was then found by plotting $\overline{q^2}$ against s, smoothing as necessary and measuring the gradient. Very little smoothing was actually required and as a check on the accuracy, $\frac{\partial \overline{q^2}}{\partial s}$ was plotted against S and the resulting $\int_{S_1}^{S_2} \frac{\partial}{\partial s} (\overline{q^2})\, dS$ compared with $\overline{q^2}_{S_2} - \overline{q^2}_{S_1}$. This is a reasonable check since the centre line defined above is quite close to the streamline $\psi = 40$ (see Section 5.2.2 for definition of ψ) so that s can be taken to be identical with S. The result of this check is shown in Figure 5.29 and Table 3. $\frac{\partial \overline{q^2}}{\partial S}$ taken from Figure 5.23 is also shown, confirming that s can be taken as S: in fact it would clearly have been simpler to use these values directly for the advection term, but since for the cross-layer balances at positions away

from the centre line this was not possible, the procedure described above was used throughout. Table 3 shows that $\int_{S_1}^{S_2} \frac{\partial}{\partial s} (\overline{q^2})\, dS$ differed from $\overline{q^2}_{S_2} - \overline{q^2}_{S_1}$ by less than about 6% of their mean, which was considered very satisfactory.

(iii) The Diffusion Term

$$- \frac{\partial}{\partial y_j'} \left(\frac{\overline{q^2 v'}}{2}\right) - \frac{\partial}{\partial x_j'} \left(\frac{\overline{q^2 u'}}{2}\right) .$$

The first term was measured directly from the plots of $\overline{q^2 v'}$ against y_j' (e.g. Figure 5.17) and $\frac{\partial}{\partial x_j}(\overline{q^2 u'})$ was obtained in a similar way to the advection term. Figure 5.30 shows the two parts of the triple velocity diffusion in the curved portion of the flow (in the vertical portion $\frac{\partial}{\partial x} (\overline{q^2 u'})$ reduces to zero). The accuracy of the longitudinal term was not expected to be very high, particularly on the centre-line where $\frac{\partial}{\partial y_j} (\overline{q^2 u'})$ is at its greatest but, as Figure 5.31 shows, it was possible to draw plausible smooth curves through the experimental data. The examples shown are typical of the results in the regions where $\frac{\partial}{\partial x_j} (\overline{q^2 u'})$ was negative ($S > 30$) and positive ($S < 30$) and it is clear that the negative gradients are probably more accurate than the positive ones because of the difficulty of deciding which line to draw through the points in the latter region. The only way to improve this situation would have been to increase the number of cross layer traverses: this was not considered worthwhile.

Because both the lateral and longitudinal terms are of

the same order but of opposite sign in the region $S = 40$, the total triple velocity turbulent diffusion becomes extremely small in this region. This is discussed further in Chapter 6.

(iv) The Dissipation Term

The dissipation $\frac{\epsilon S}{U_r^3}$ was calculated in exactly the same way as for the plane layer (Section 4.4.1). The universal spectra are not presented: they were similar to the plane layer case (Figure 4.13). All the corrections described in Section 4.4.1 were applied, although it was noticeable that at large values of S the length correction was not sufficient to maintain a good fit in the dissipation range. Since the Kolmogorov length scale was about 0.04 mm throughout (it only varies as $x^{\frac{1}{4}}$ in the plane layer) this was difficult to explain, but did not prevent sensible estimations of the dissipation since there was still an extensive inertial sub-range. The accuracy of the dissipation results is not expected to be any higher than that estimated for the plane layer, i.e. between 15 - 20% (Section 4.4.1) although since the results lie on a reasonably smooth curve (Figure 5.27) they do seem to be consistent. Discussion of the dissipation length parameter derived from these results is deferred until Chapter 6.

(v) The Overall Balance

Each term is made dimensionless by multiplying by the distance, S, around the centre-line. Since the virtual origin varies with S, at least up to $S \sim 80$ (Figures 5.13 and 5.14b) it is difficult to plot the equivalent

plane shear layer values of each term, except for very small S and for S ~ 80 where the virtual origin S_o is roughly constant (Figures 5.13 and 5.14b) and the plane layer values therefore must be increased in the ratio $\frac{S}{S - S_o}$.

The 'out-of-balance' term is plotted in Figure 5.27. It is somewhat larger than the plane-layer centre-line value (Figure 4.14) in the region S = 80, but this is where the turbulent energy $\frac{\overline{q^2}}{U_r^2}$ is considerably greater than the plane layer value (although the mean velocity is the same). It is reasonable to suppose that the error in measured shear stress will be correspondingly greater. In the vertical portion, of course, the shear stress can easily be calculated from the mean momentum equation (Section 4.3.2) and a quick check at S = 73 indicated a larger difference between the calculated and measured shear stress than was apparent in the plane layer. The errors in the measurement of the other terms in the energy balance in the vertical portion of the curved mixing layer are unlikely to be very different from those in the plane layer, so it certainly seems that it is errors in the production term which cause the larger out-of-balance term in this region.

Similar arguments could explain the relatively small error around S = 40.

5.2.5.2 Cross-Layer Balances Energy balances were constructed at three flow cross-sections corresponding to S = 34.3 (J = 11), S = 38.8 (J = 13) and S = 81.5 (J = 27) and they are shown in Figures

5.32 - 5.34. Except for the dissipation the method of deriving each term, described above, was used over the whole of each cross-section. Figure 5.35 shows the contributions to the total triple-velocity diffusion made by the lateral and longitudinal terms in the two cases where the latter is significant. The errors are probably no worse than those associated with the centre-line balance; indeed the lateral diffusion term integrates quite closely to zero and the errors in the longitudinal term will be smaller away from the centre line (since the lateral gradients are lower). The diffusion term plotted in the balances (Figures 5.32 and 5.33) is the sum of the smoothed curves shown in Figure 5.35.

Figure 5.21, which is typical of any cross shear layer traverse, shows that the u-component spectra measured at positions away from the centre-line do not contain a significant region of $-\frac{5}{3}$ slope, when plotted in the usual way. Attempts were made to construct universal spectrum in the way described in Section 4.4.1, making allowance for the intermittency of the flow. This was assumed to have a variation similar to that in the plane layer (later found to be correct at this location - S = 73) and the dissipation was assumed to occur entirely within the turbulent regions. As stated in Section 4.4.1 the convection velocity could not be taken as simply the local mean velocity and it was defined as $U_c = U + \frac{\overline{q^2 u}}{\overline{q^2}}$. This differed from U by less than 10% on the high velocity side but exceeded U by over 100% on the extreme low velocity side. The resulting values of the dissipation were reasonable on the high velocity side but were clearly grossly in error on the low velocity side, being typically a factor of three higher than the centre-line value. Even significant variations of U_c and/or γ did not produce much change. Sensible reasons for this behaviour were not obvious and in view of the difficulty the

dissipation was derived in the same way for the plane layer, by assuming it to vary as $(q^2)^{3/2}$.

The out of balance term, indicated in Figures 5.32 - 5.34, is in general similar to the corresponding result in the plane layer (see for example Figure 4.14). The exceptions are the somewhat larger value at S = 81.5 (Figure 5.34) which was plausibly explained in the previous section and the large values at the high velocity edge at S = 34.3 and 38.8 (Figures 5.32 and 5.33). In the plane mixing layer the out-of-balance term, usually attributed to a mixture of experimental inaccuracies and the pressure diffusion, was very small at the high velocity edge (Figure 4.14). It is most unlikely that the large out-of-balance is caused by errors in say, the advection term and the only possible conclusion is that the pressure diffusion, usually thought to be quite small, is significant in this region. This is discussed further in Chapter 6.

It will be noticed that in the balances along J = 11 and 13 the production term has a small negative 'loop' at the high velocity edge. This is caused by the change in sign of both the mean velocity gradient (Figure 5.9) and the shear stress (Figure 5.16) and is also discussed in Chapter 6.

5.2.6 Shear Stress Balances

For the reasons given in Chapter 3 the shear stress balance around the centre-line was measured with respect to curved co-ordinates (s', n') and to evaluate the curvature terms the curvature, κ was required. This was taken as the curvature of the mixing layer centre-line defined in the usual way (Section 3.3). Figure 5.36 shows the measured κ plotted against S ($\equiv s'$). This provided a convenient check on accuracy since

$$\int_{S_1}^{S_2} \kappa dS = \Theta_{S_2} - \Theta_{S_1} \quad .$$

The smooth curve drawn through the points gives a value of the integral (between S = 12.6 (J = 1) and 51.2 (J = 19)) of 1.56, which is encouragingly close to $\frac{\pi}{2}$, the angle through which the shear layer turns between J = 1 and J = 19.

Each term in the transport equation was derived in a similar way to the corresponding energy transport terms, remembering of course that streamwise gradients ($\frac{\partial Q}{\partial s}$) require Q to be measured with respect to s' and not x', the local direction of s'. The curvature term $\kappa(2\overline{v^2}u - \overline{u^3})$ was extremely small so has been neglected throughout. It could only be significant compared with the term $U\kappa(\overline{u^2} - \overline{v^2})$ at the extreme low velocity edge of the flow where $\frac{\overline{u^2}}{U^2} = O(1)$, and in this region U is small so that $U\kappa(\overline{u^2} - \overline{v^2})$ is itself small.

The resulting shear stress balance is shown in Figure 5.37, where the pressure strain term has been obtained by difference and the contributions made by $\overline{v^2}\frac{\partial U}{\partial n}$ and $-\overline{u^2}U\kappa$ to the total production are shown in Figure 5.38.

5.2.6.1 Cross Layer Balances Restating the conclusion of Section 3.3, it is clearly better to use the relevant curved co-ordinates to derive the various terms in the transport equation of a vector quantity (like $\overline{uv}$) so that each term has the same physical meaning as in the plane layer. All the cross-shear layer balances were derived before this conclusion had been reached and were measured with respect to the axes (x', y') aligned with the local direction of the mixing layer. However it will be shown that the resulting pressure strain term is not very sensitive to this difference of axes, so that in view of the amount of work required to produce a

single balance, they have not been recalculated.

Figures 5.39 - 5.42 show the four resulting balances, measured at representative positions in the mixing layer. The accuracy of each term is similar to that for the corresponding terms in the energy balance. In fact the longitudinal diffusion was found to be small compared with the lateral diffusion, so that the total diffusion term is probably somewhat more accurate than the energy diffusion measurements.

Comparison of Figures 5.39 - 5.42 and Figure 5.37 shows that the advection terms on the centre-line are of opposite sign: a result of the different axis systems used. To check that the pressure-strain term is not too dependent on the axes, the shear stress balance at S = 29.9 (J = 9) was also calculated with respect to curved co-ordinates in the same way as the centre-line balance. The rotation term ($U\kappa(\overline{u^2} - \overline{v^2})$) was about twice the advection (and of opposite sign) which itself was of the same order as shown in Figure 5.40 but of opposite sign. Since the velocity diffusion was almost identical, the resulting pressure-strain term was not very different from that found in ($x'y'$) co-ordinates. Figure 5.40 includes this 'correct' pressure-strain term and also the production term, measured in curved co-ordinates.

There is nothing inherently 'wrong' about the balances measured in x', y' axes, but care has to be exercised in any deductions that are made about the physical phenomena relating to each term.

5.2.7 The Mean Momentum Equation-Turbulent Terms

Using the equation of motion written in curved co-ordinates (Section 3.2) the mean momentum equations can be derived. In the usual s', n' co-ordinates (s' being measured along the mixing layer centre-line) they are

$$U \frac{\partial U}{\partial s'} + hV \frac{\partial U}{\partial n'} + h \frac{\partial \overline{uv}}{\partial n'} + \frac{\partial \overline{u^2}}{\partial s} + UV\kappa + 2\overline{uv}\kappa = - \frac{\partial p}{\partial s'}$$

and

$$U \frac{\partial V}{\partial s'} + hV \frac{\partial V}{\partial n'} + \frac{\partial \overline{uv}}{\partial s'} + h \frac{\partial \overline{v^2}}{\partial n'} - \kappa U^2 - \kappa(\overline{u^2} - \overline{v^2}) = - h \frac{\partial p}{\partial n'} \quad .$$

$$(h = 1 + n'\kappa(s')) \quad .$$

Using the continuity equation it can be shown that

$$U \frac{\partial V}{\partial s'} + hV \frac{\partial V}{\partial n'} \equiv U \frac{\partial V}{\partial s'} - V \frac{\partial U}{\partial s'} - \kappa V^2$$

and this is always extremely small compared with κU^2 - indeed if s' were a streamline it would be identically zero. The lateral momentum equation can therefore be written, since the data indicate that the only significant turbulent term is $h \frac{\partial \overline{v^2}}{\partial n'}$,

$$- \kappa U^2 + h \frac{\partial \overline{v^2}}{\partial n'} = - h \frac{\partial p}{\partial n'} \quad .$$

The terms on the left hand side are plotted, for J = 9 - the region of maximum curvature, in Figure 5.43. κ is taken as constant across the layer and equal to the centre-line value. Clearly $\frac{\partial \overline{v^2}}{\partial n'}$ is only significant at the extreme low velocity edge of the flow and both $\frac{\partial \overline{uv}}{\partial s'}$ and $\kappa(\overline{u^2} - \overline{v^2})$ are an order of magnitude smaller.

More interesting of course is the behaviour of the streamwise momentum equation. It is very difficult to measure the various terms along a line across the mixing layer. The simplest way is to use co-ordinates along and normal to the mixing layer direction (x', y') so that the curvature terms disappear. Comparisons of $\frac{\partial \overline{uv}}{\partial y'}$ and $\frac{\partial \overline{u^2}}{\partial x'}$ are shown in Figure 5.44 and clearly in the region of minimum turbulent energy and shear stress (S ~ 35) the two terms are of the same order. However it would be more meaningful, as explained previously, to use s', n' co-ordinates so that $\overline{u^2}$ retains its usual significance away from the J-line of interest. The curvature terms,

$(UV + 2\overline{uv})\kappa$, must be retained and it is particularly difficult to estimate the size of the terms involving mean velocities (and their gradients) <u>across</u> the mixing layer. To get some indication of the relative size of the two terms $\frac{\partial \overline{uv}}{\partial n}$ and $\frac{\partial \overline{u^2}}{\partial s}$ ($2\overline{uv}\kappa$ being negligible) Figure 5.45 shows the maximum shear stress gradient (on the high velocity side of the layer) and the streamwise gradient of $\overline{u^2}$ along the centre line, plotted against $S.\frac{\partial \overline{u^2}}{\partial s}$ is roughly at its maximum on the centre line, so we deduce that $\frac{\partial \overline{uv}}{\partial n}$ is the dominant term over most of the mixing layer.

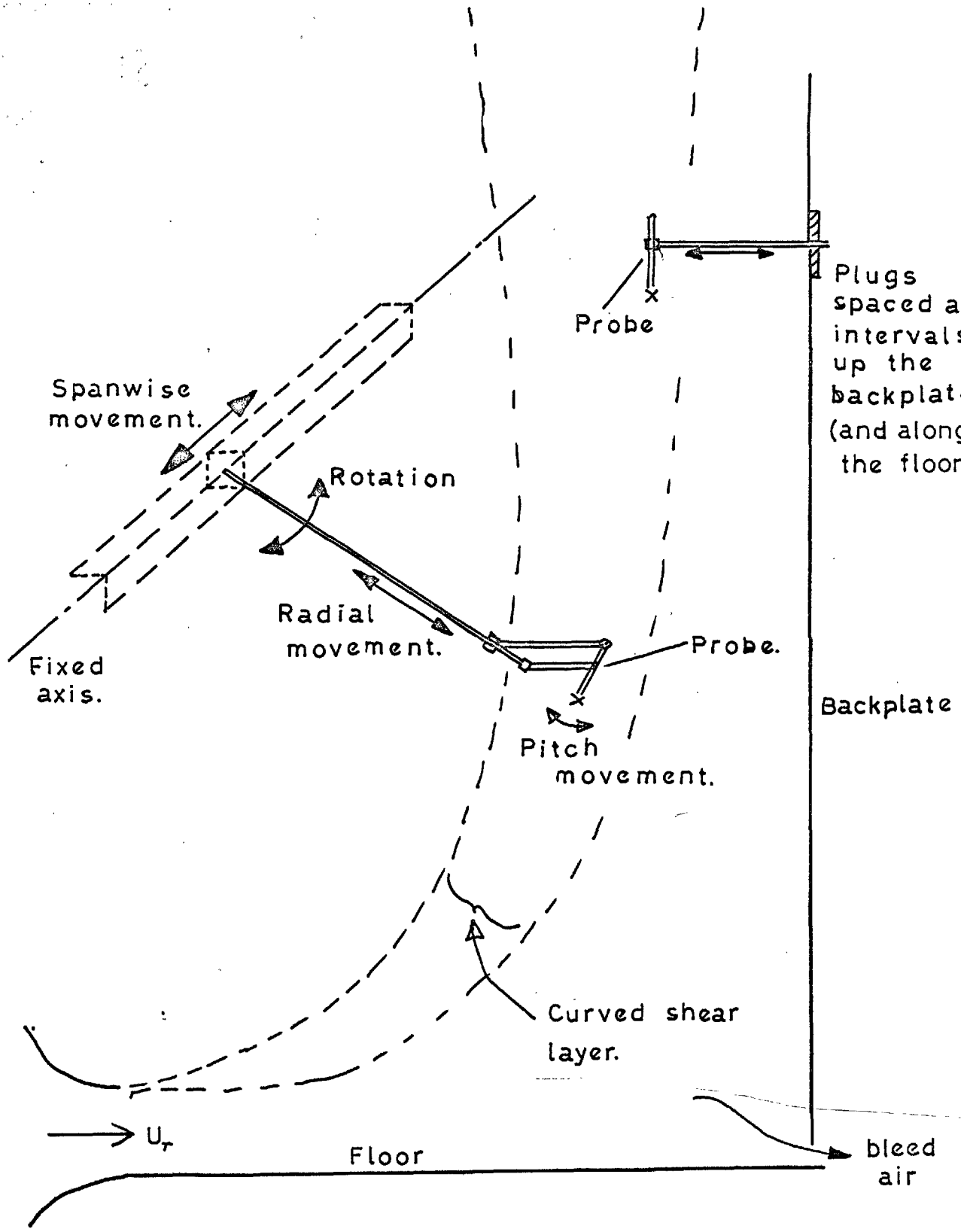
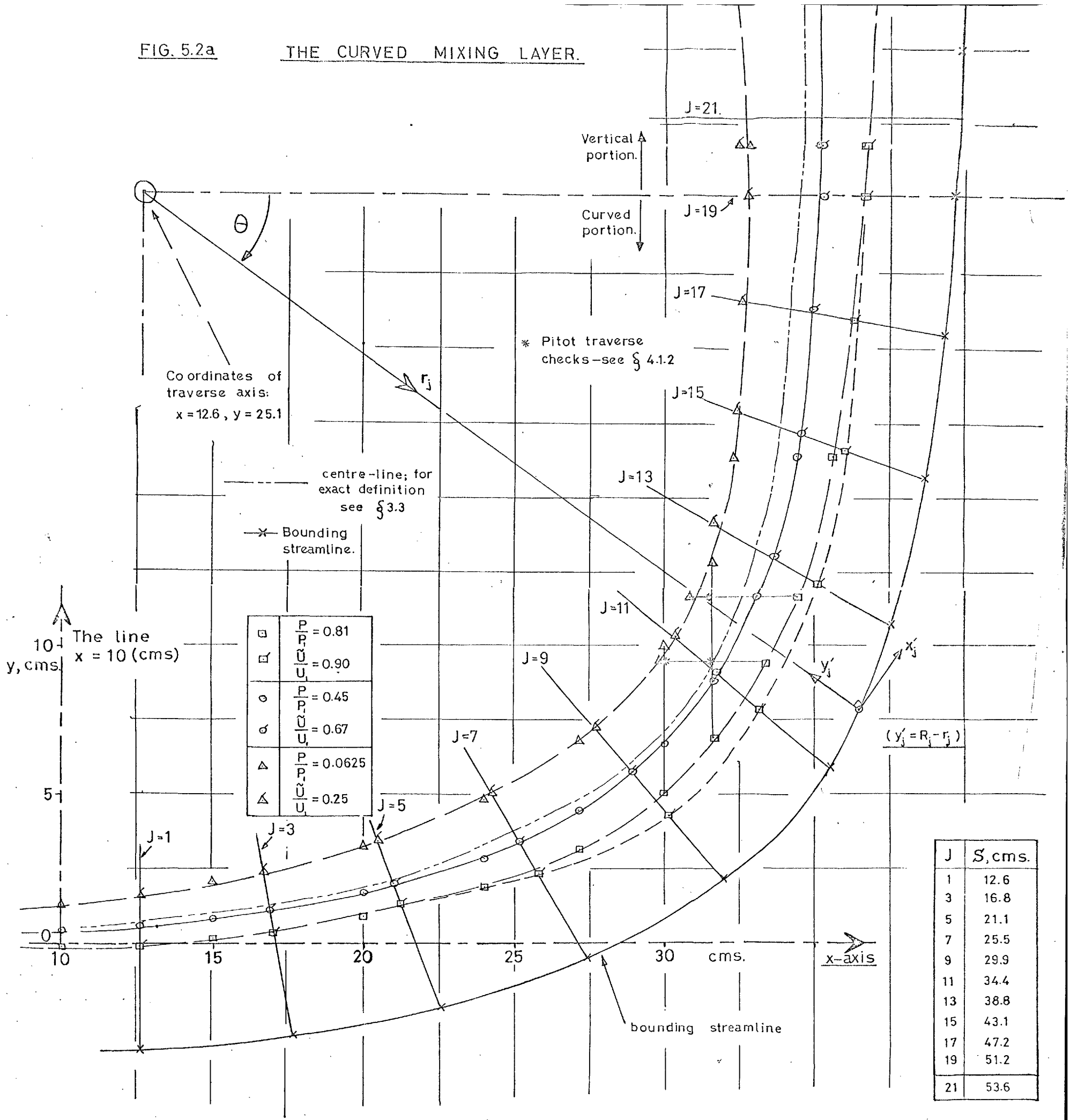


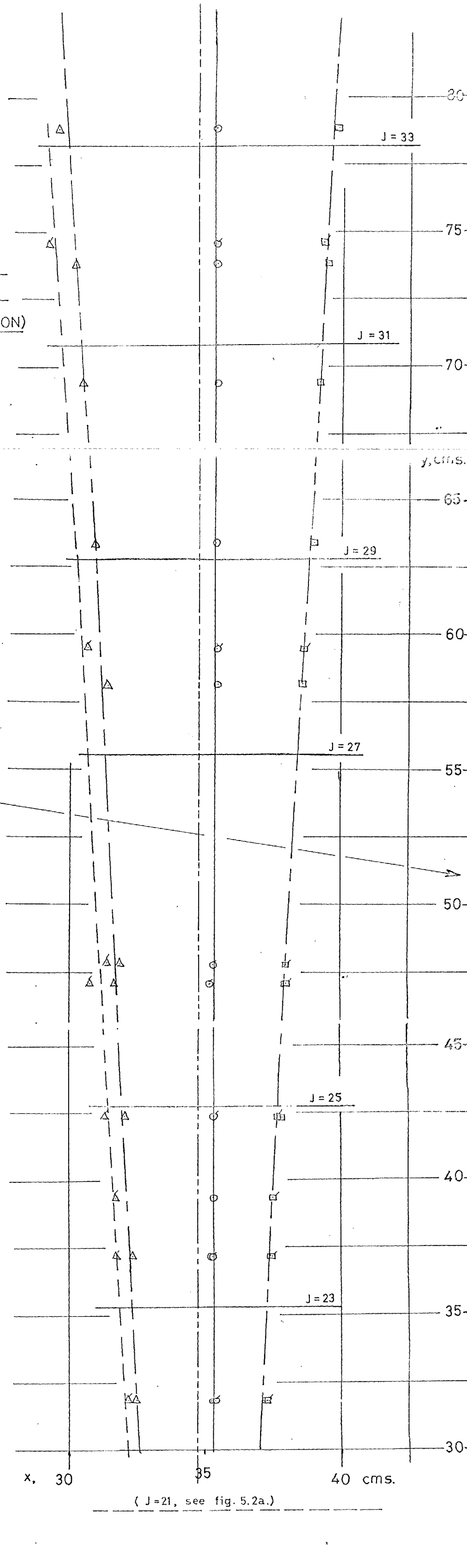
FIG 5.1 Sketch of possible traverse movements.

FIG. 5.2a THE CURVED MIXING LAYER.



J	S, cms.
1	12.6
3	16.8
5	21.1
7	25.5
9	29.9
11	34.4
13	38.8
15	43.1
17	47.2
19	51.2
21	53.6

FIG. 5.2b THE CURVED MIXING LAYER (VERTICAL PORTION)



Symbol notation as in fig. 5.2a.

Backplate position is x = 44.7

J	S, cms.
21	53.6
23	61.1
25	68.6
27	81.5
29	88.7
31	96.7
33	104.1

(J = 21, see fig. 5.2a.)

FIG. 5.3 Wake excess temperature.

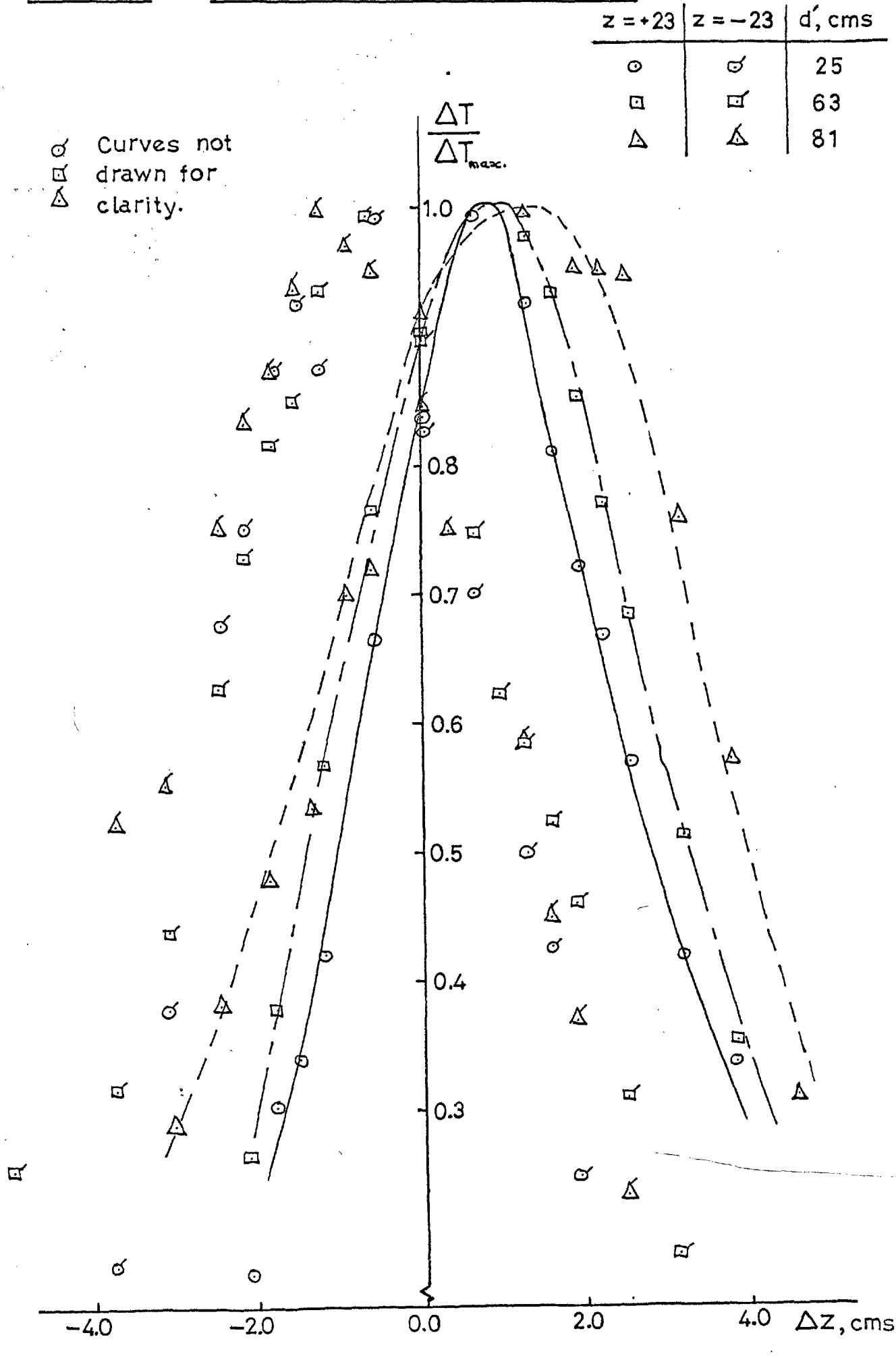


FIG. 5.4 Flow divergence.

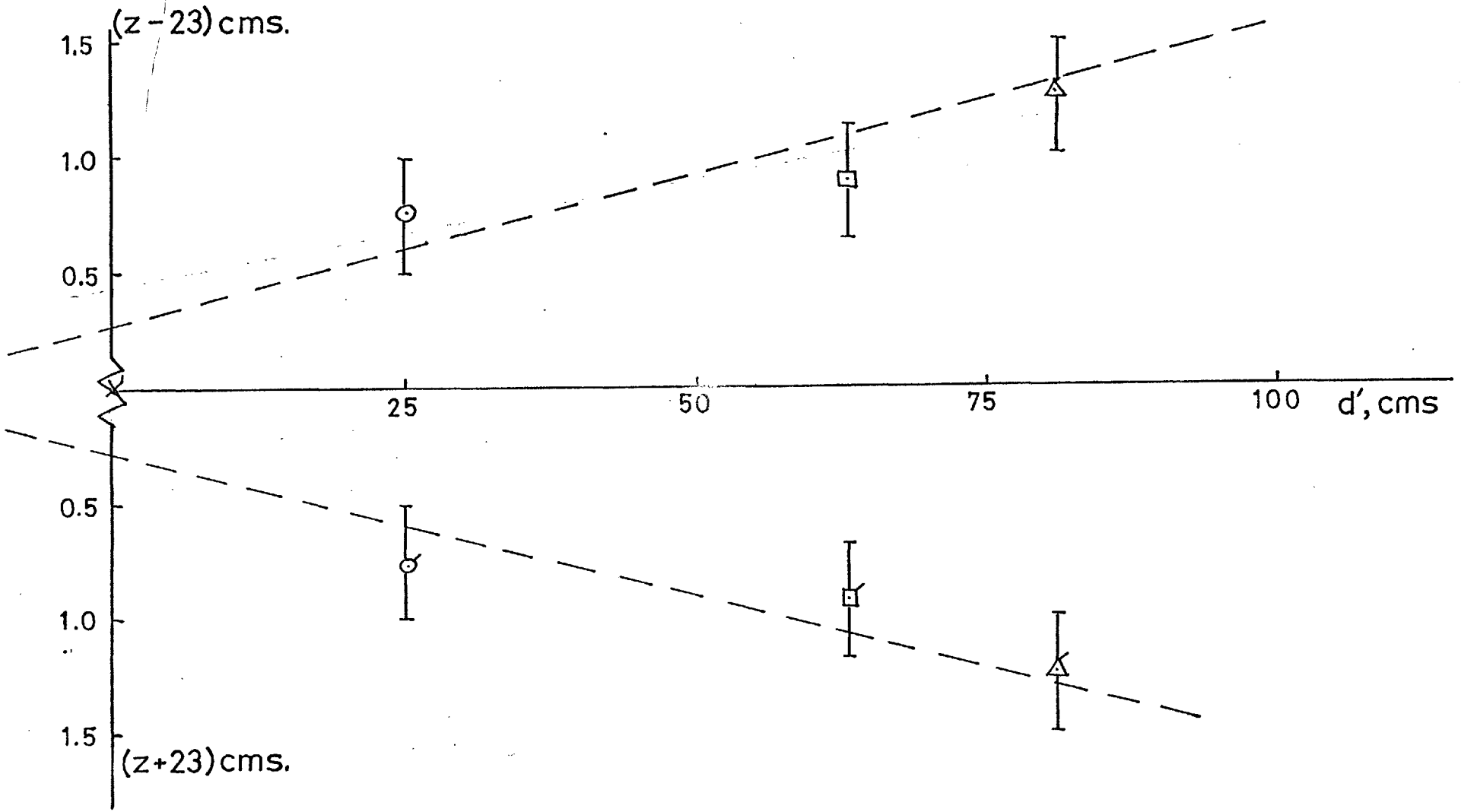
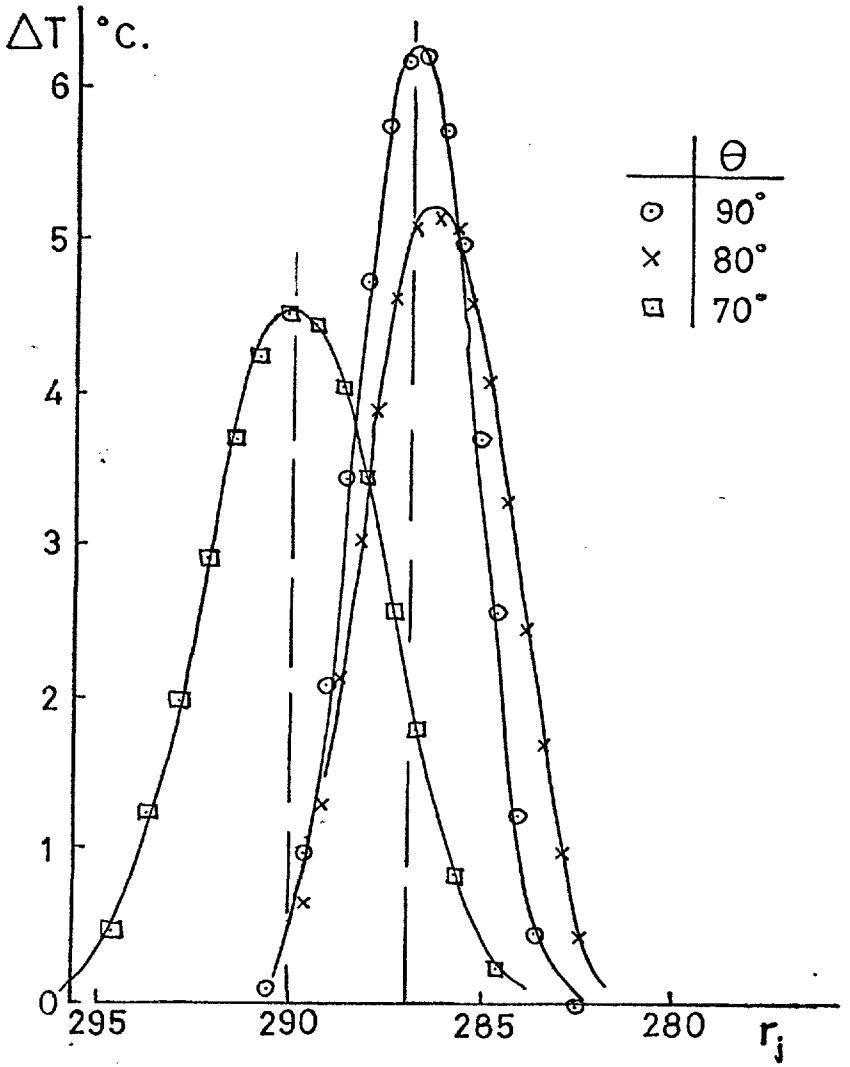


FIG. 5.5a Temperature profiles in wake of heated source.



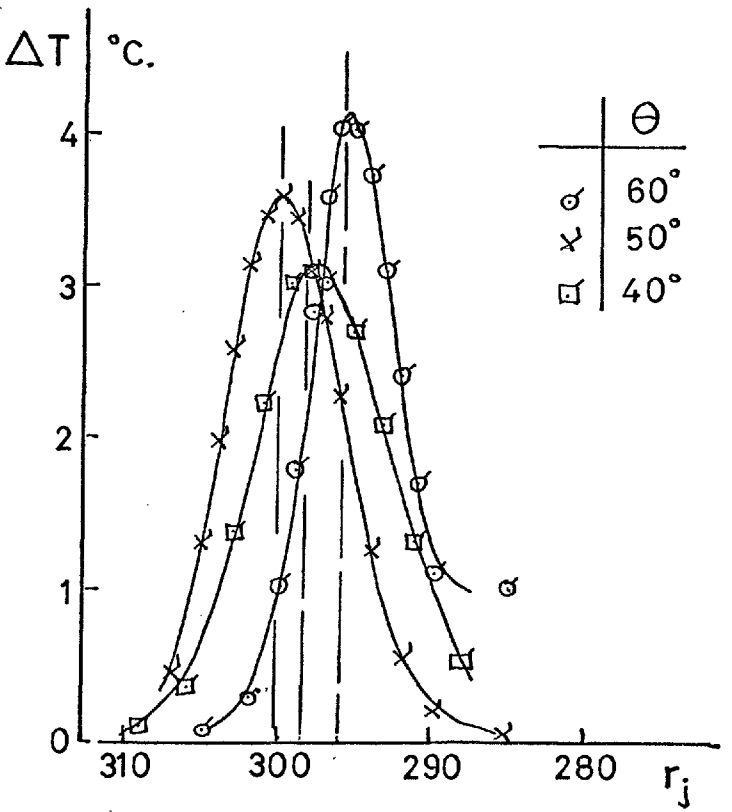


FIG. 5.5b Temperature profiles.

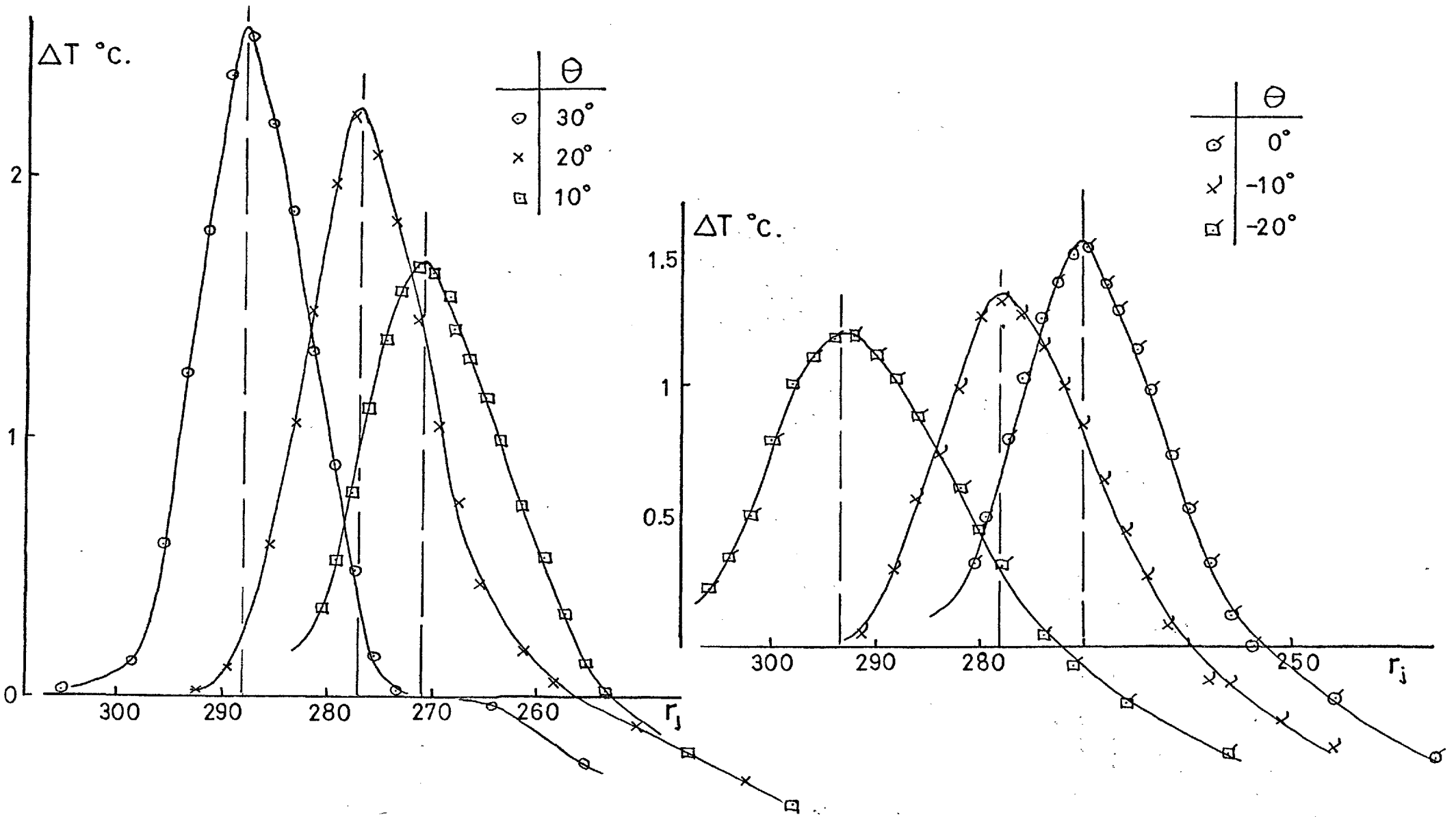


FIG. 5.6 Temperature along bounding streamline.

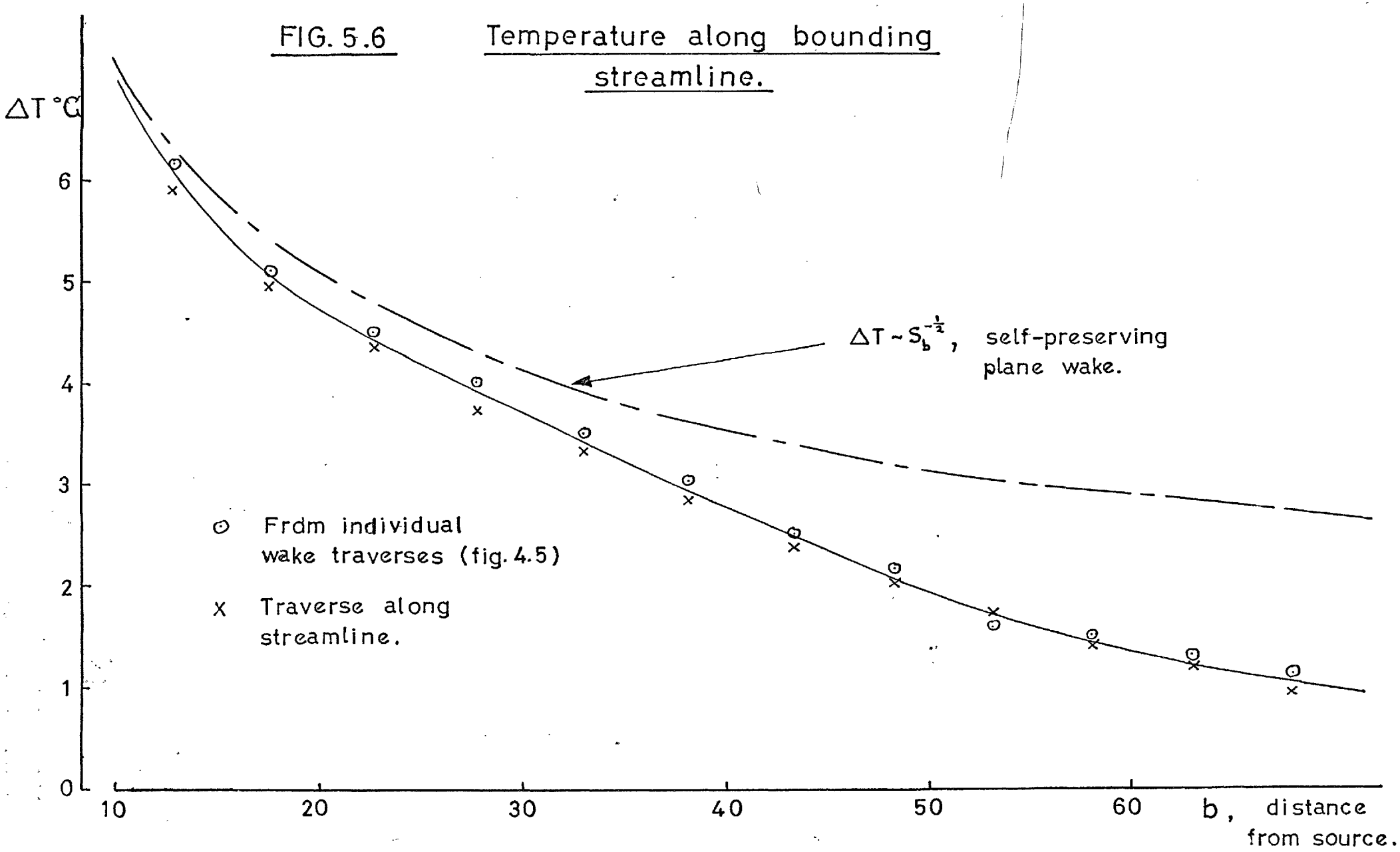


FIG. 5.7 Mean velocity along bounding streamline.

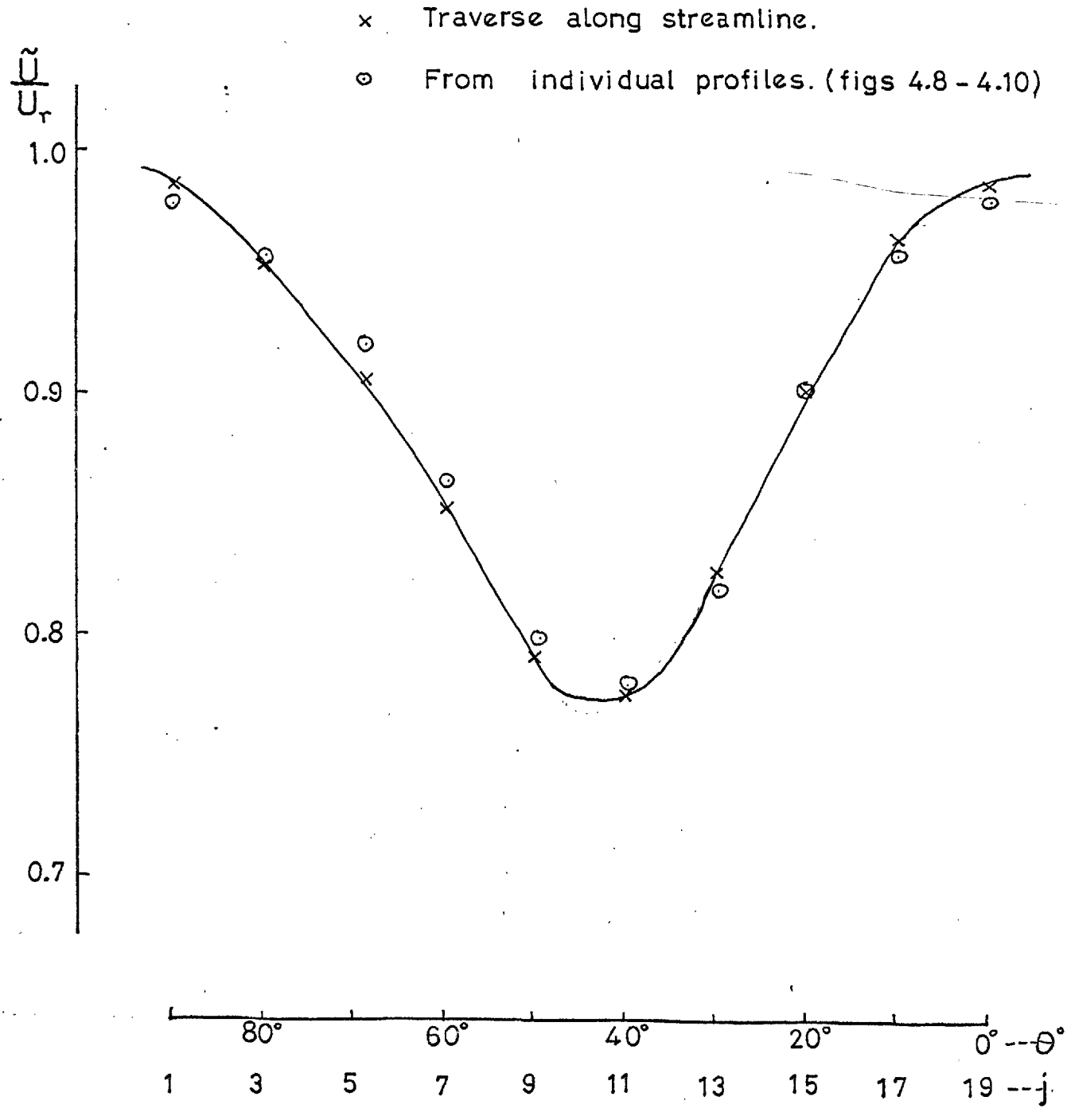


FIG. 5.8 Mean velocity profiles. (curved portion)

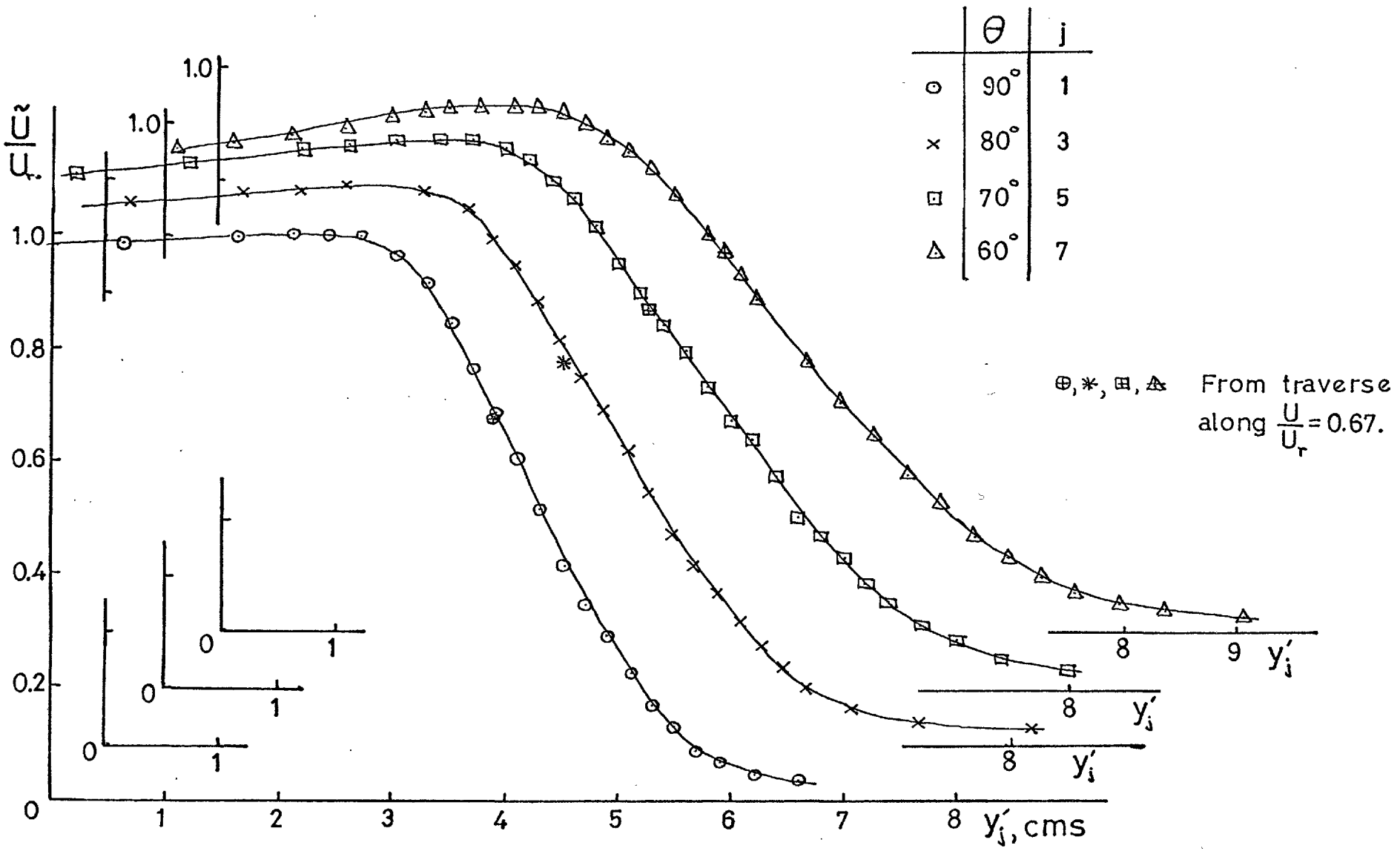


FIG. 5.9 Mean velocity profiles. (curved portion)

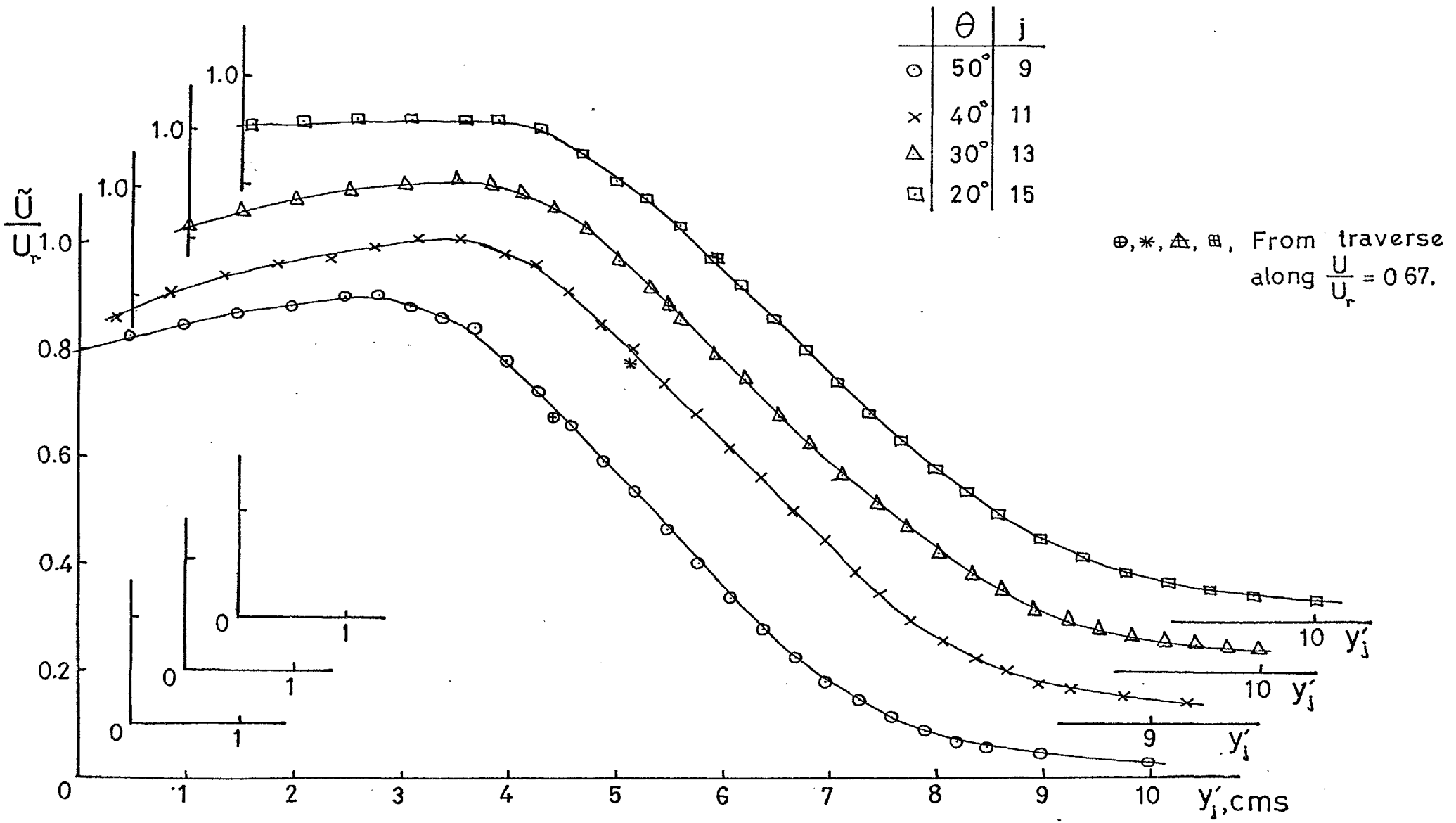


FIG. 5.10 Mean velocity profiles. (curved portion)

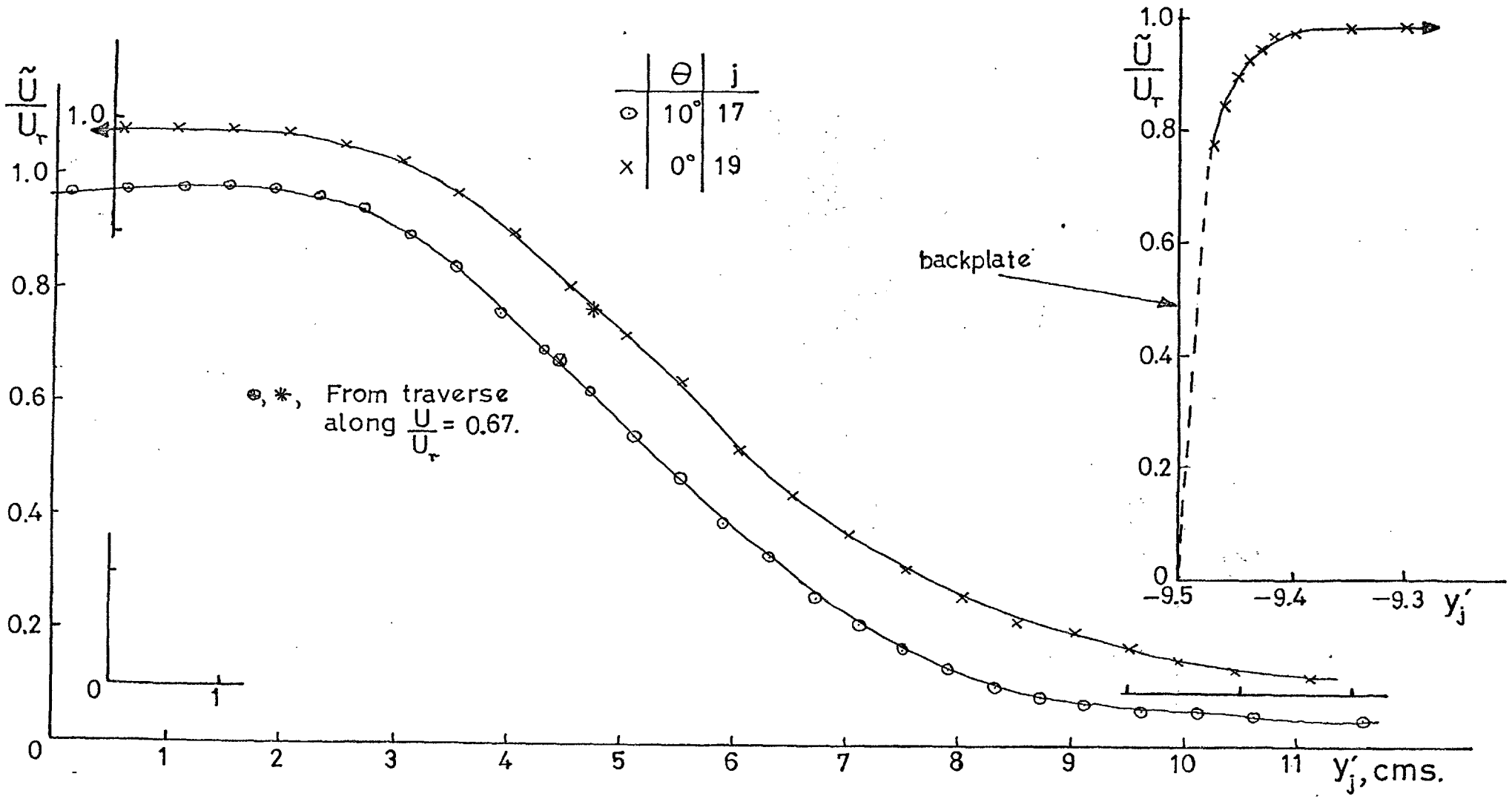


FIG 5.11 Mean velocity profiles (vertical portion)

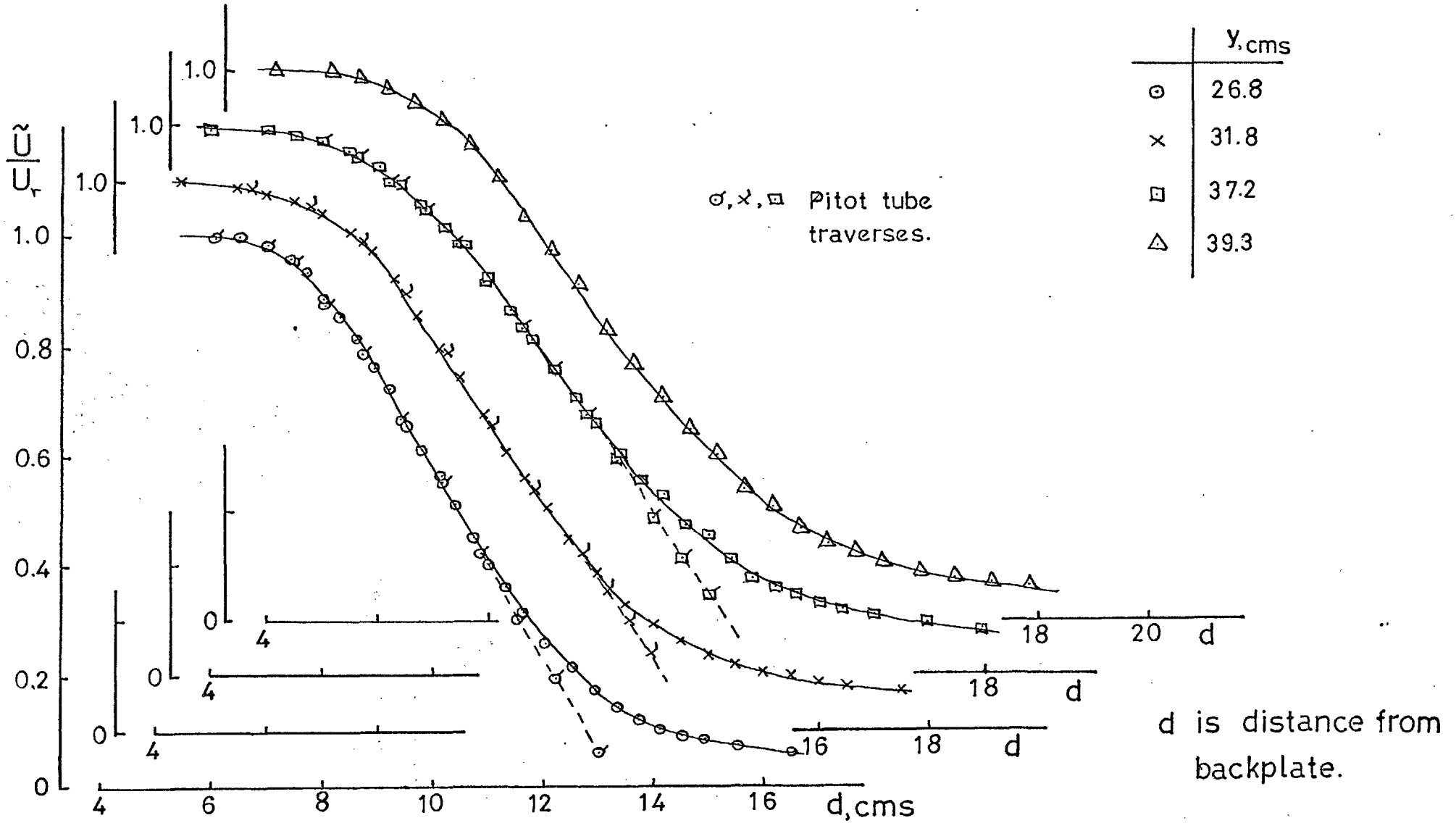


FIG. 5.12 Mean velocity profiles (vertical portion)

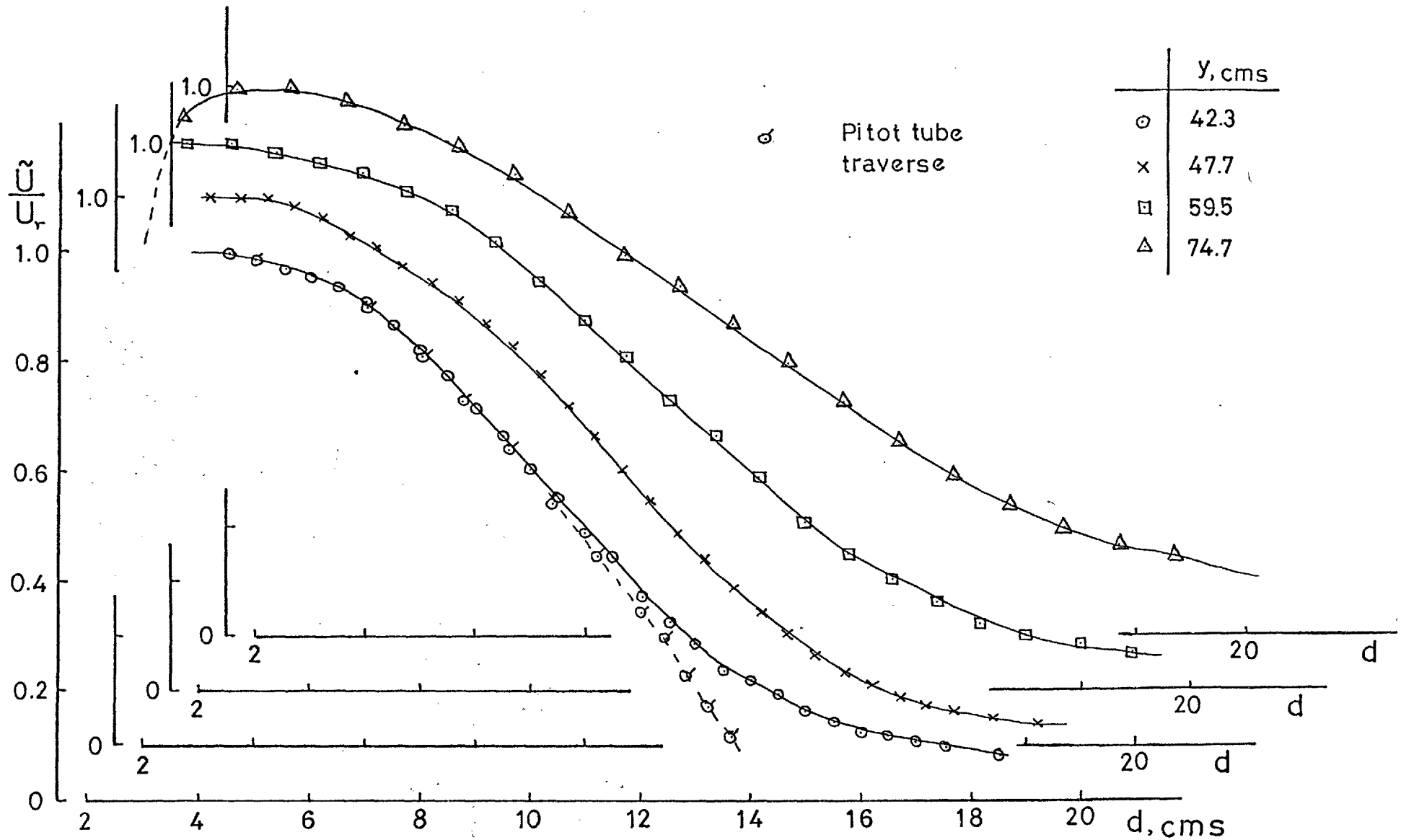
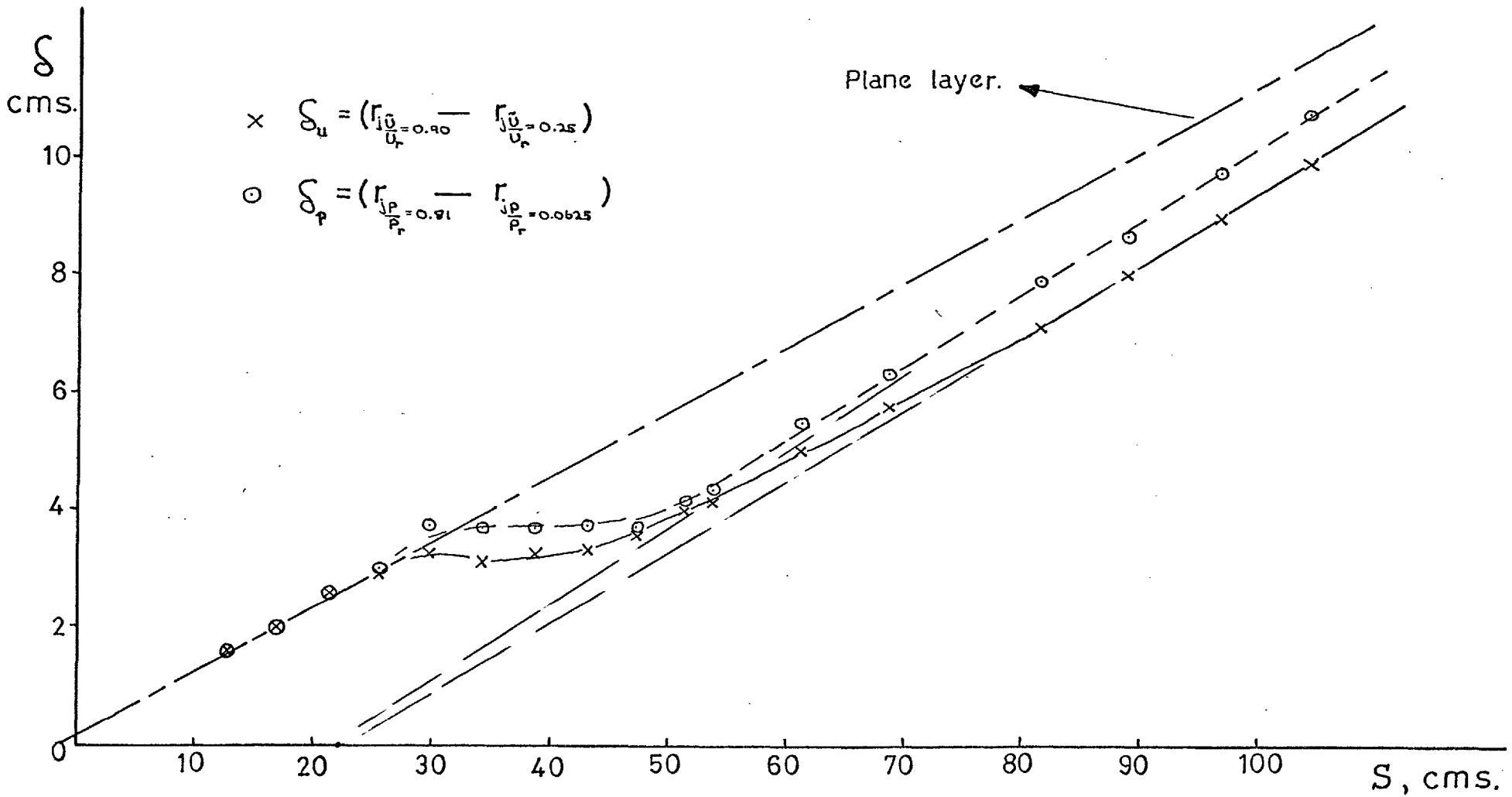


FIG. 5.13 Mixing layer growth rate.



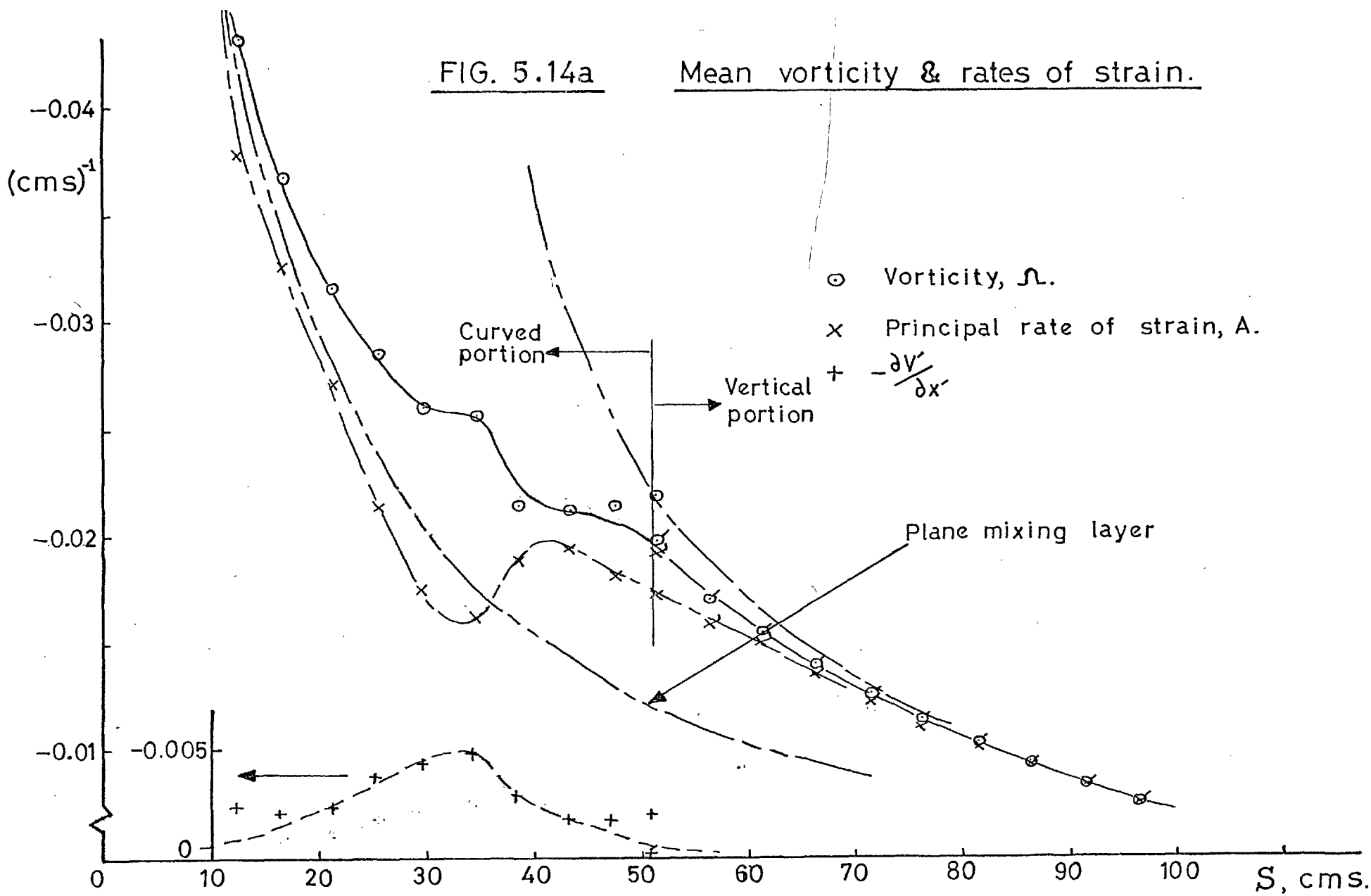

FIG. 5.14a Mean vorticity & rates of strain.
−0.04
(cms)⁻¹
−0.03
−0.02
−0.01
−0.005
0
Curved portion
Vertical portion
Plane mixing layer
⊙ Vorticity, Ω.
× Principal rate of strain, A.
+ −∂V′/∂x′
0
10
20
30
40
50
60
70
80
90
100
S, cms.

FIG. 5.14b Mean vorticity & Principal rate of strain.

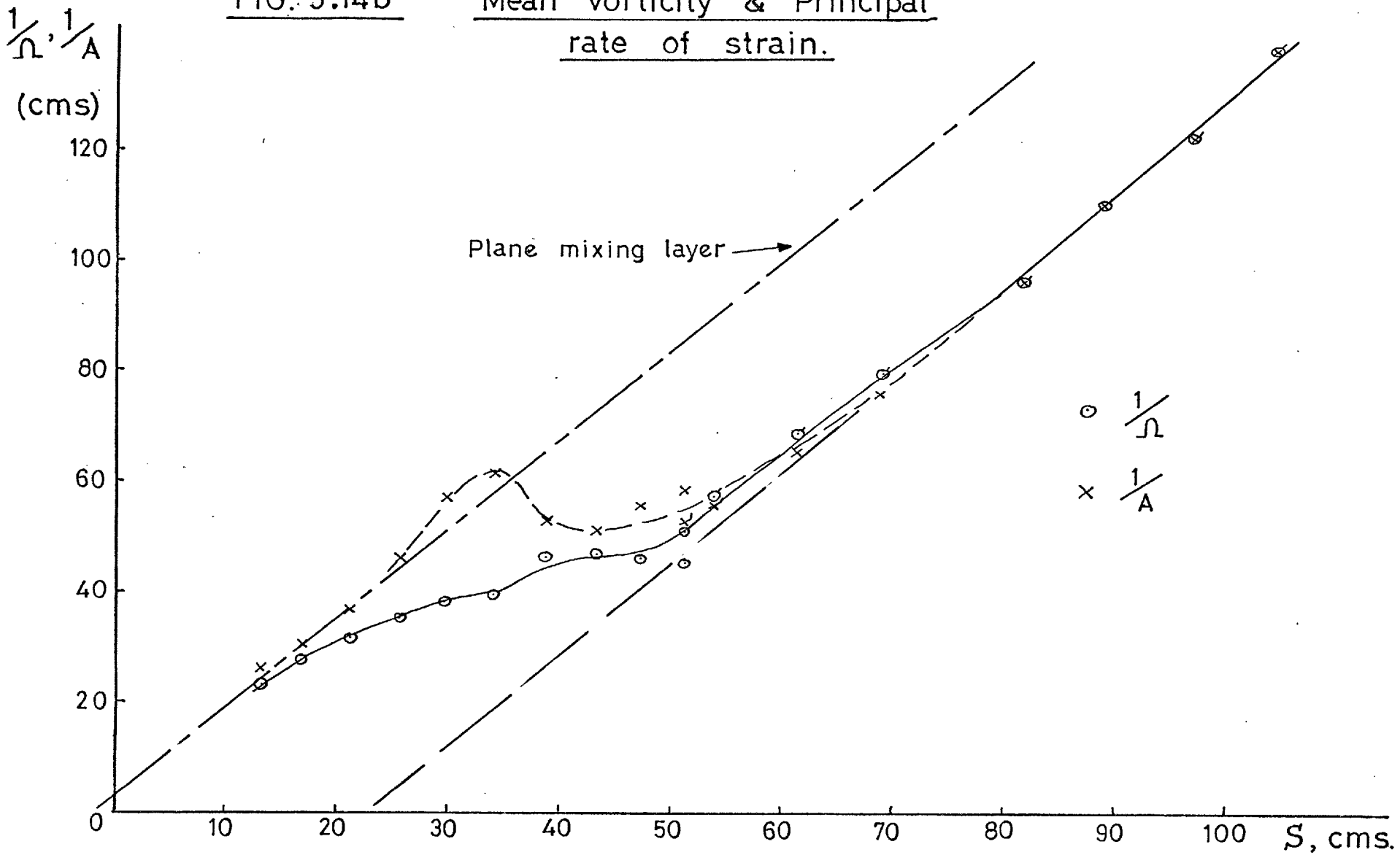


FIG. 5.15 Streamline direction.

J = 13, S = 38.8

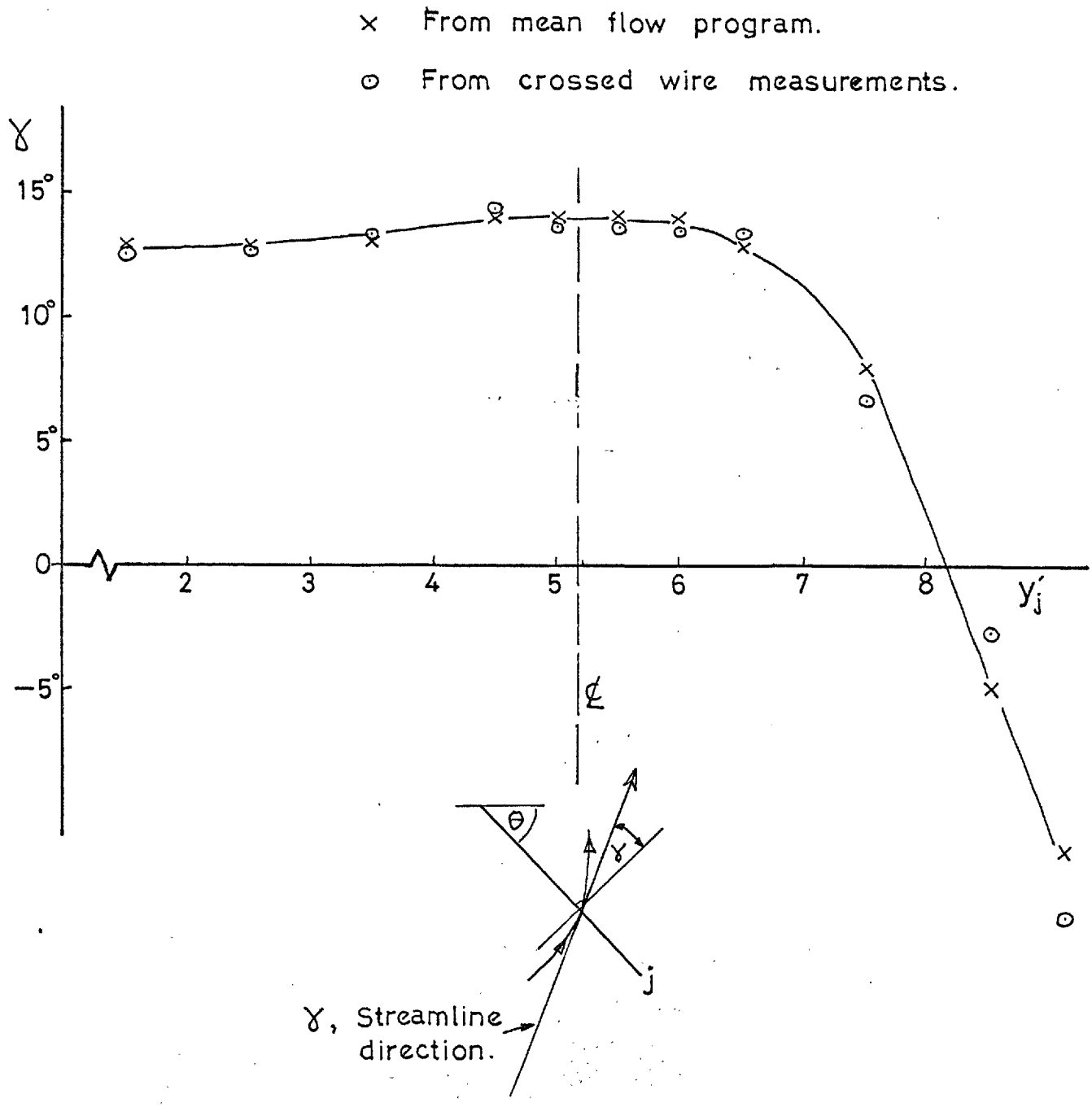


FIG. 5.16a. Turbulent energy & shear stress.

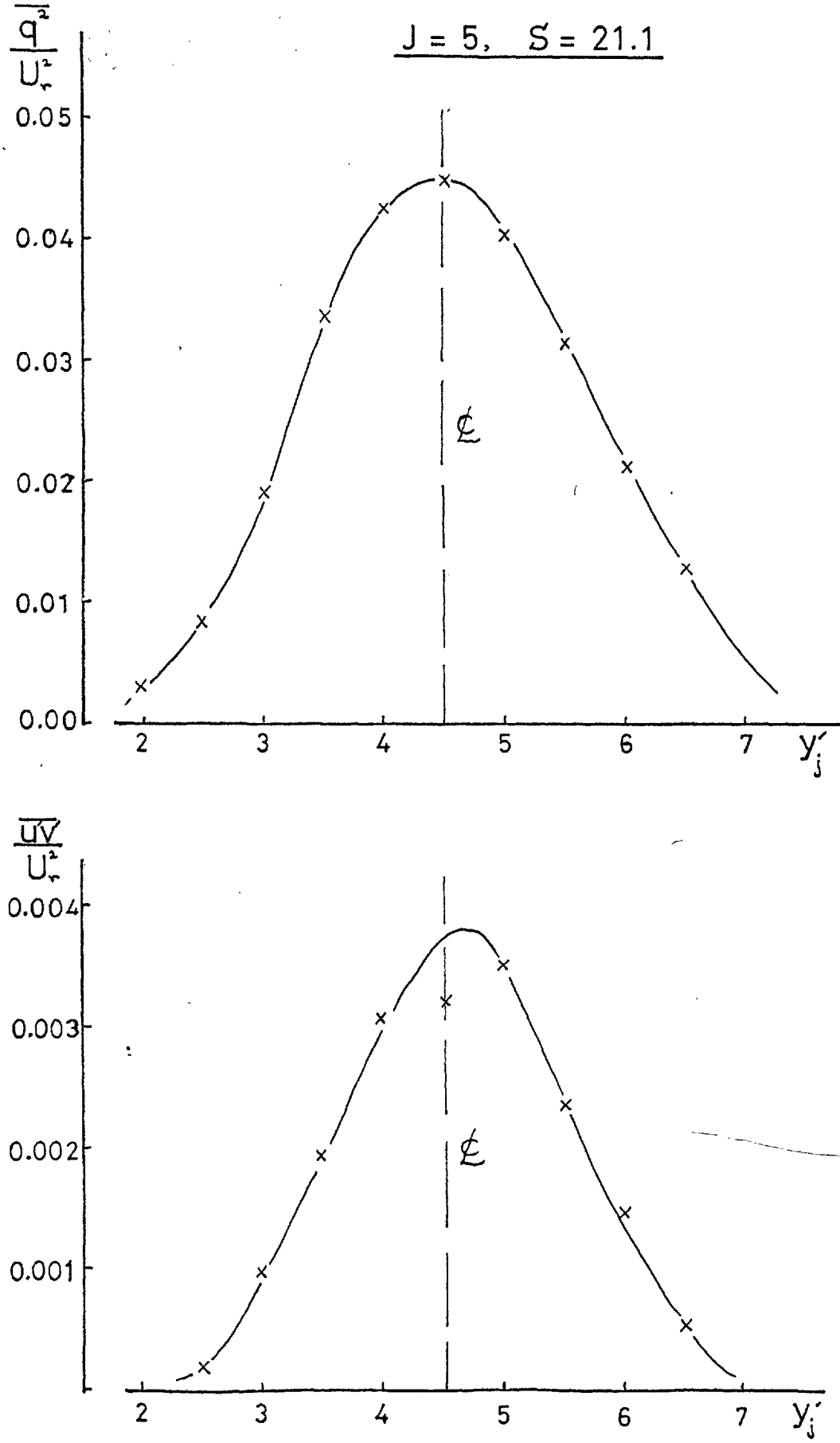


FIG. 5.16b. Turbulent energy & shear stress.

J = 9, S = 29.9

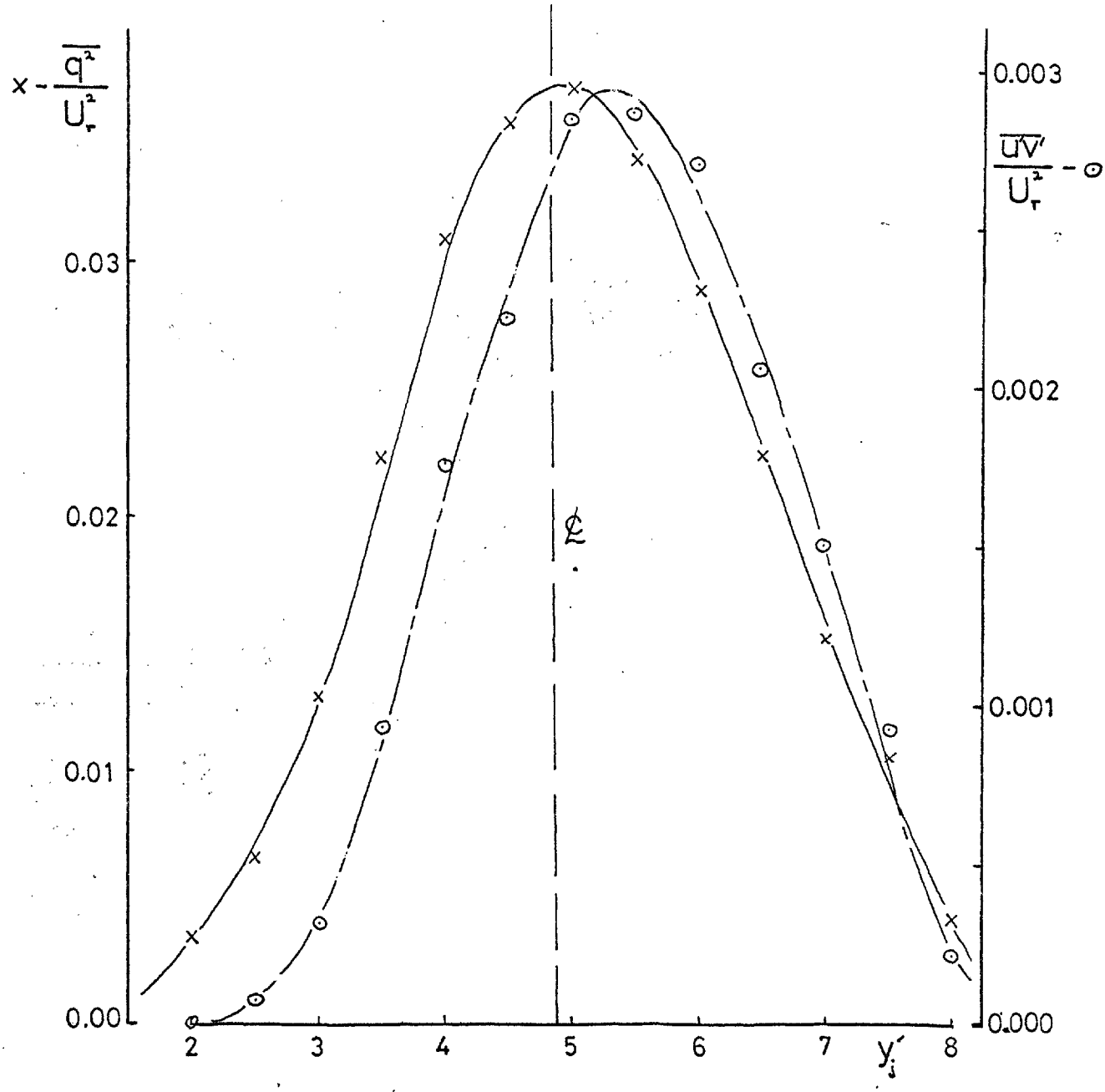


FIG. 5.16c. Turbulent energy & shear stress.

J = 11, S = 34.4

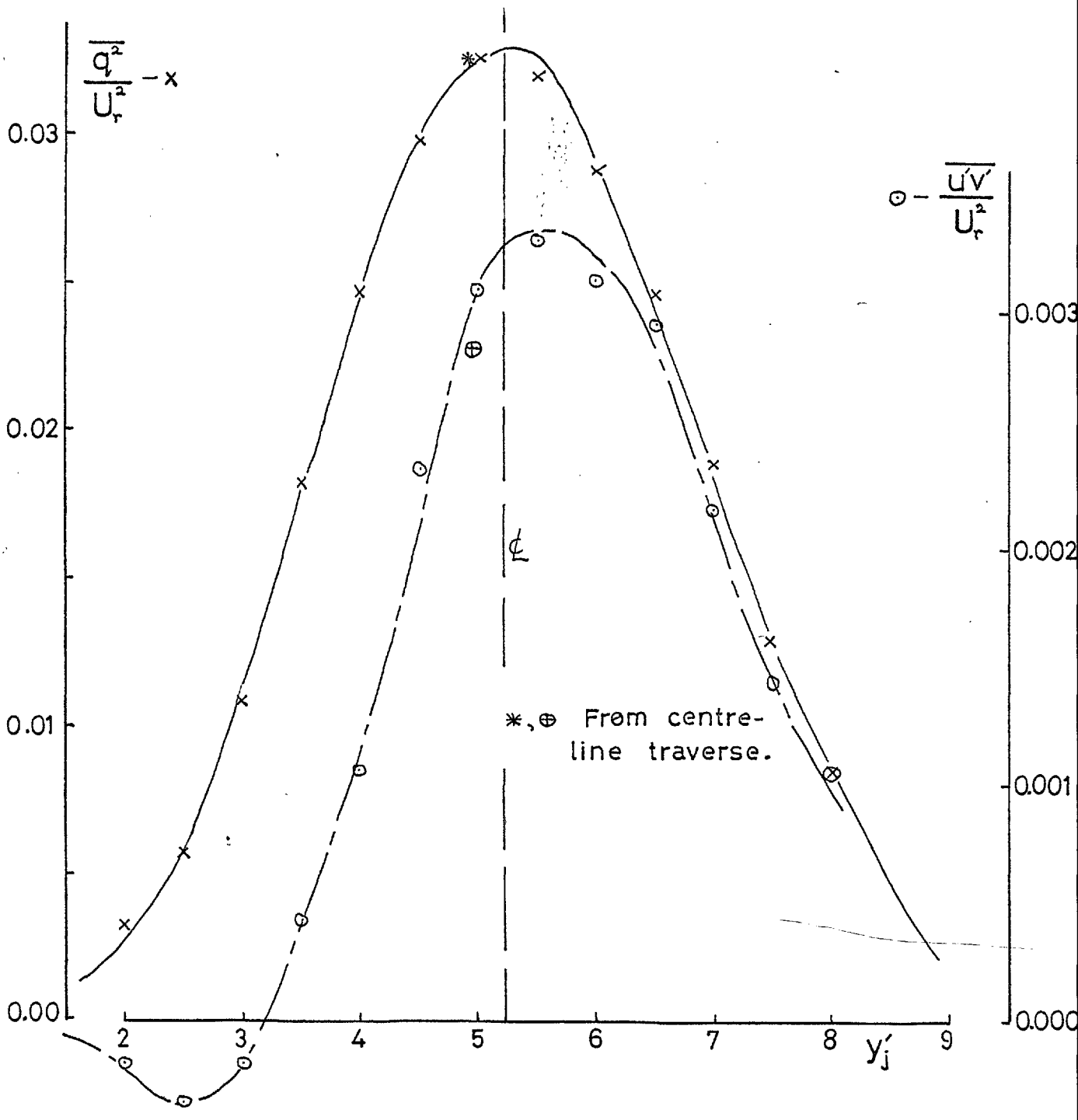


FIG. 5.16d. Turbulent energy & shear stress.

J = 13, S = 38.8

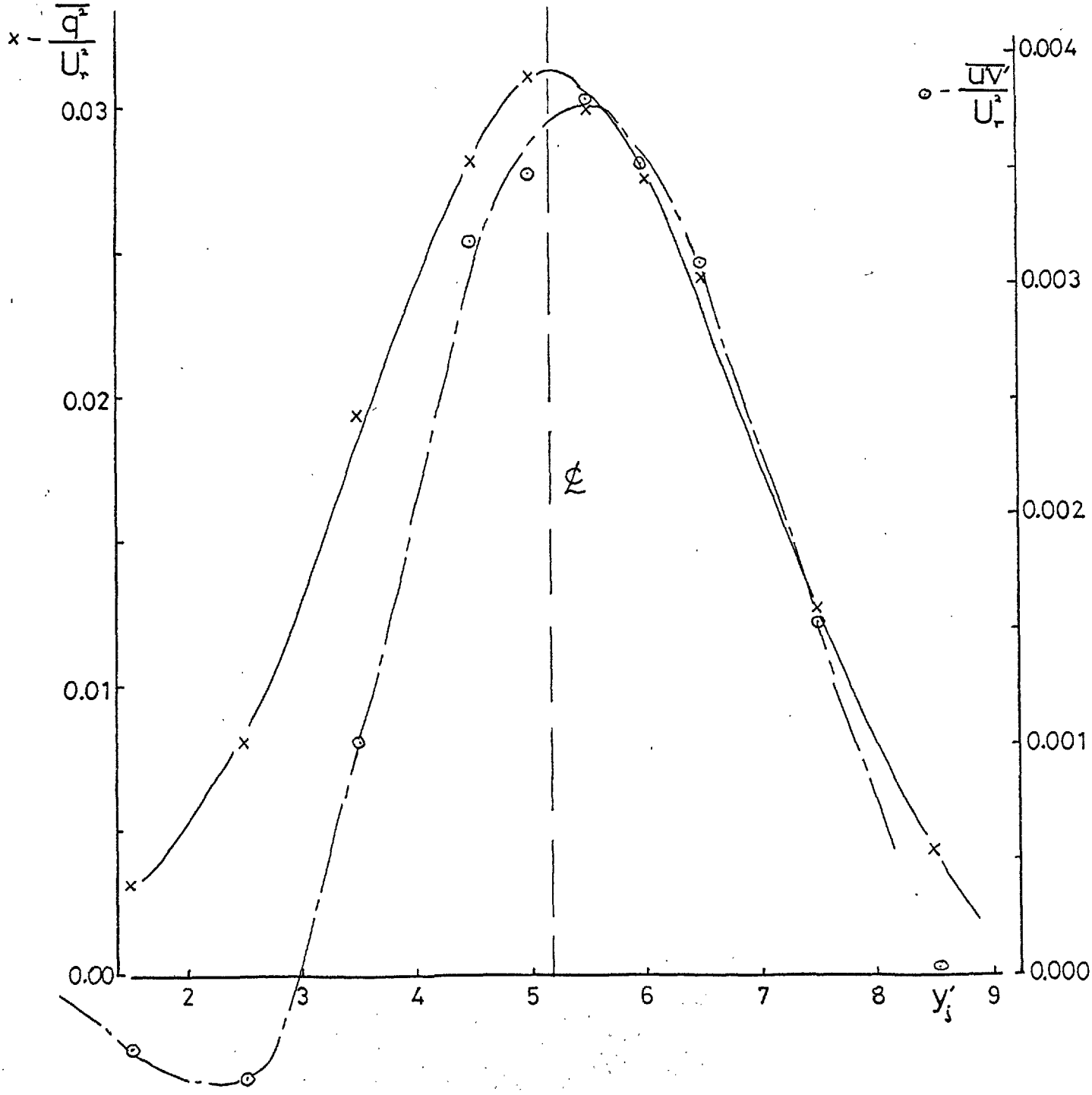


FIG. 5.16e. Turbulent energy & shear stress.

J = 23, S = 61.1

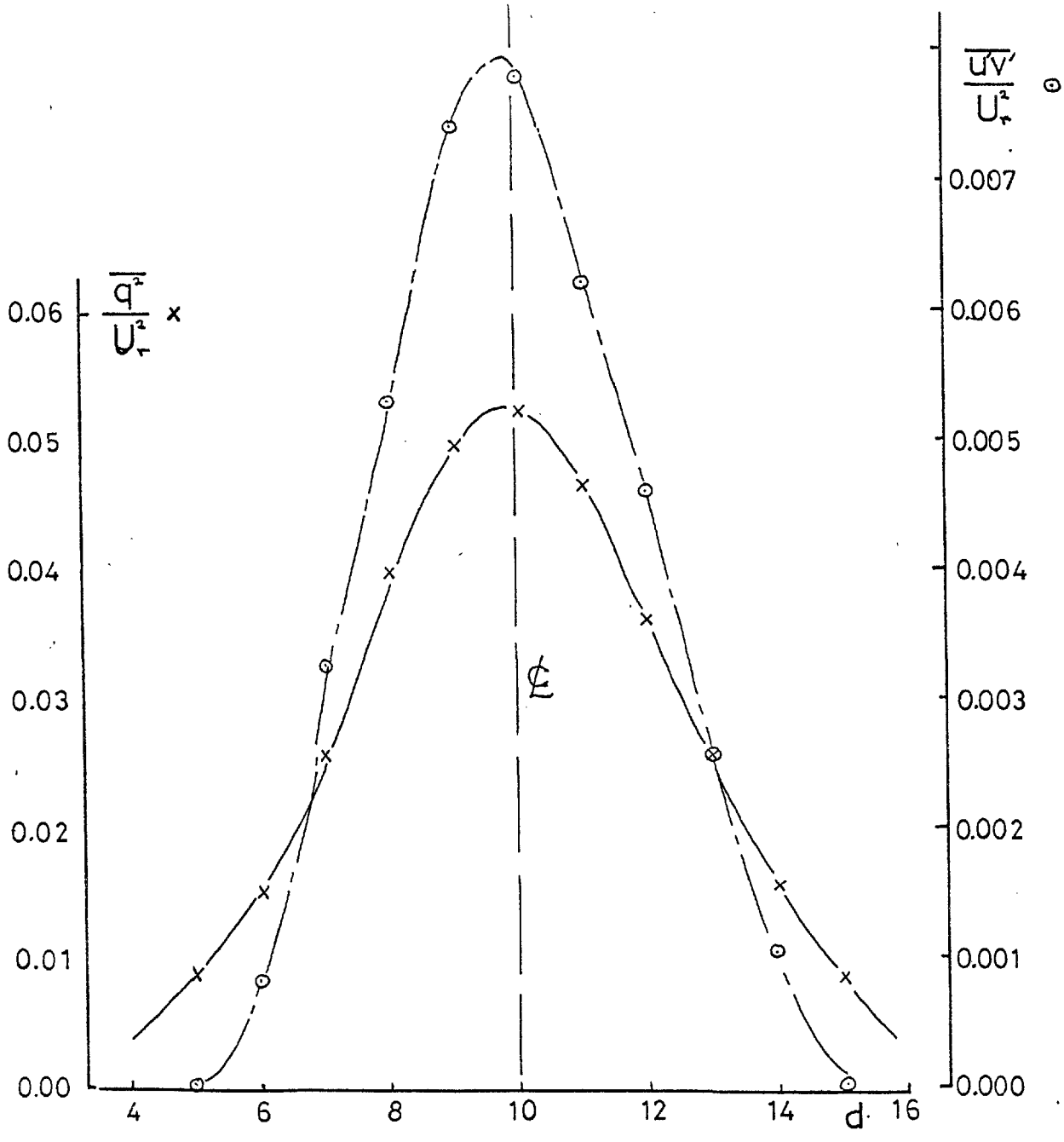


FIG. 5.16f. Turbulent energy & shear stress.

J = 27, S = 81.5

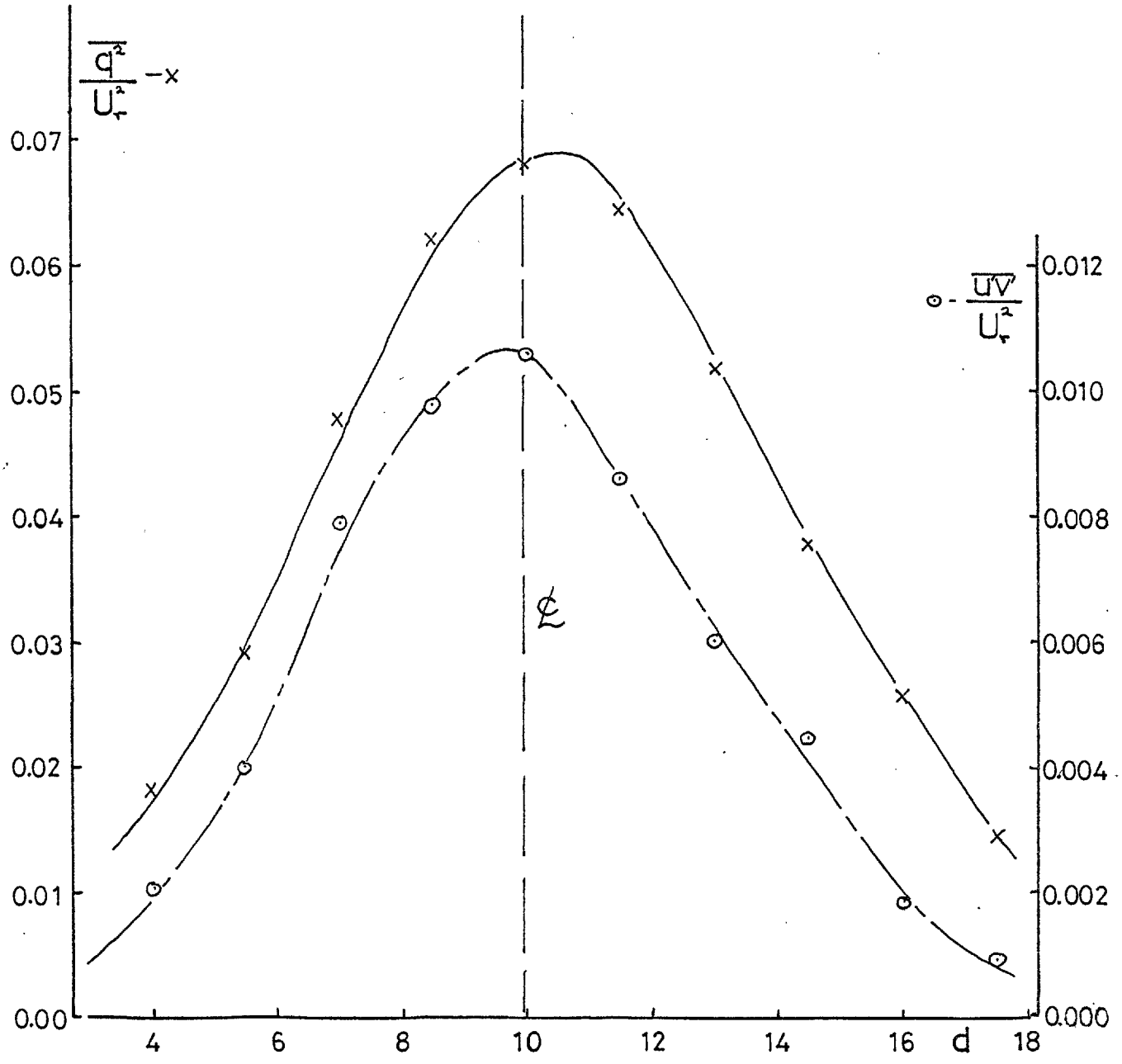


FIG. 5.17 Triple products.

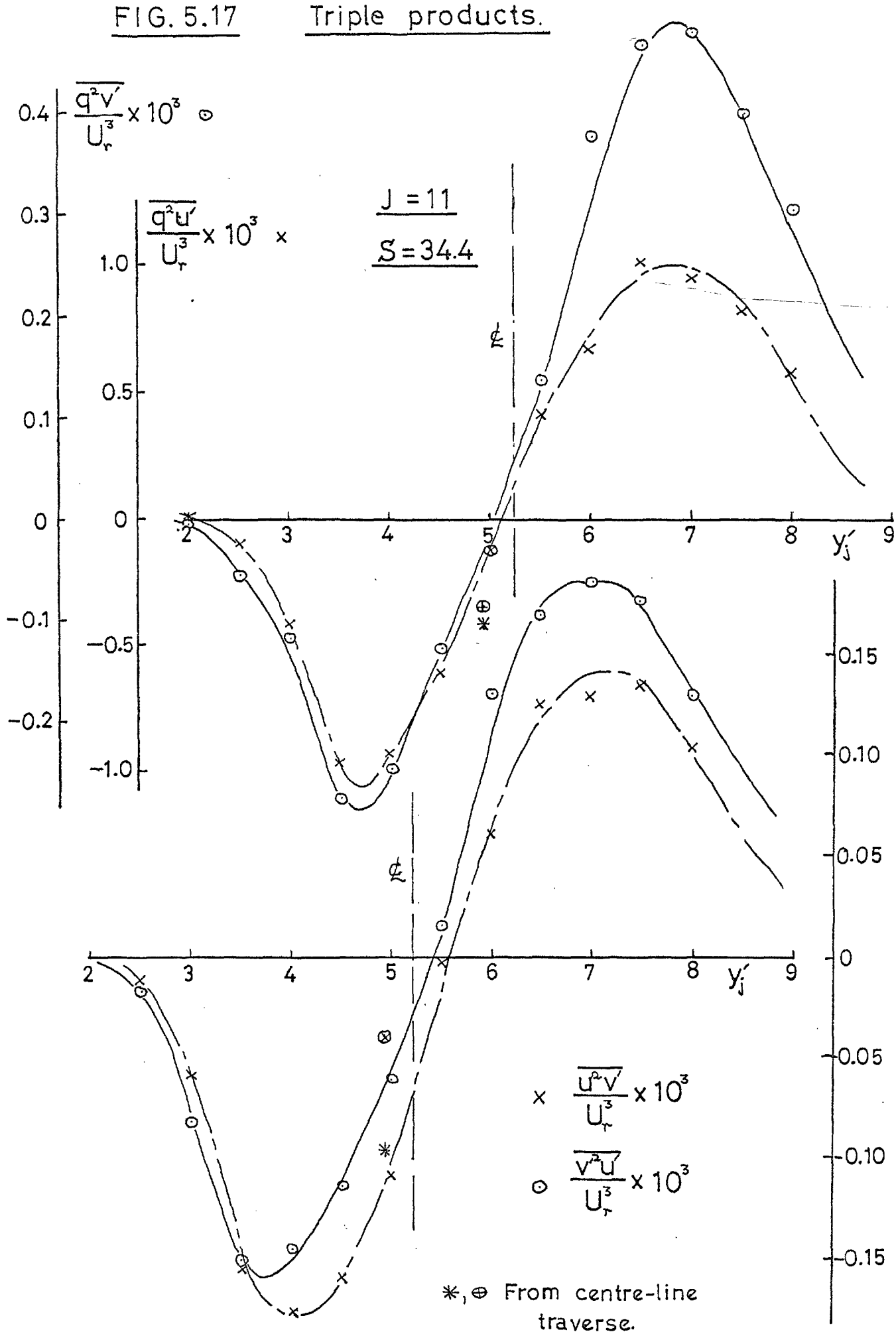


FIG. 5.18 u-component spectra along the centre-line.

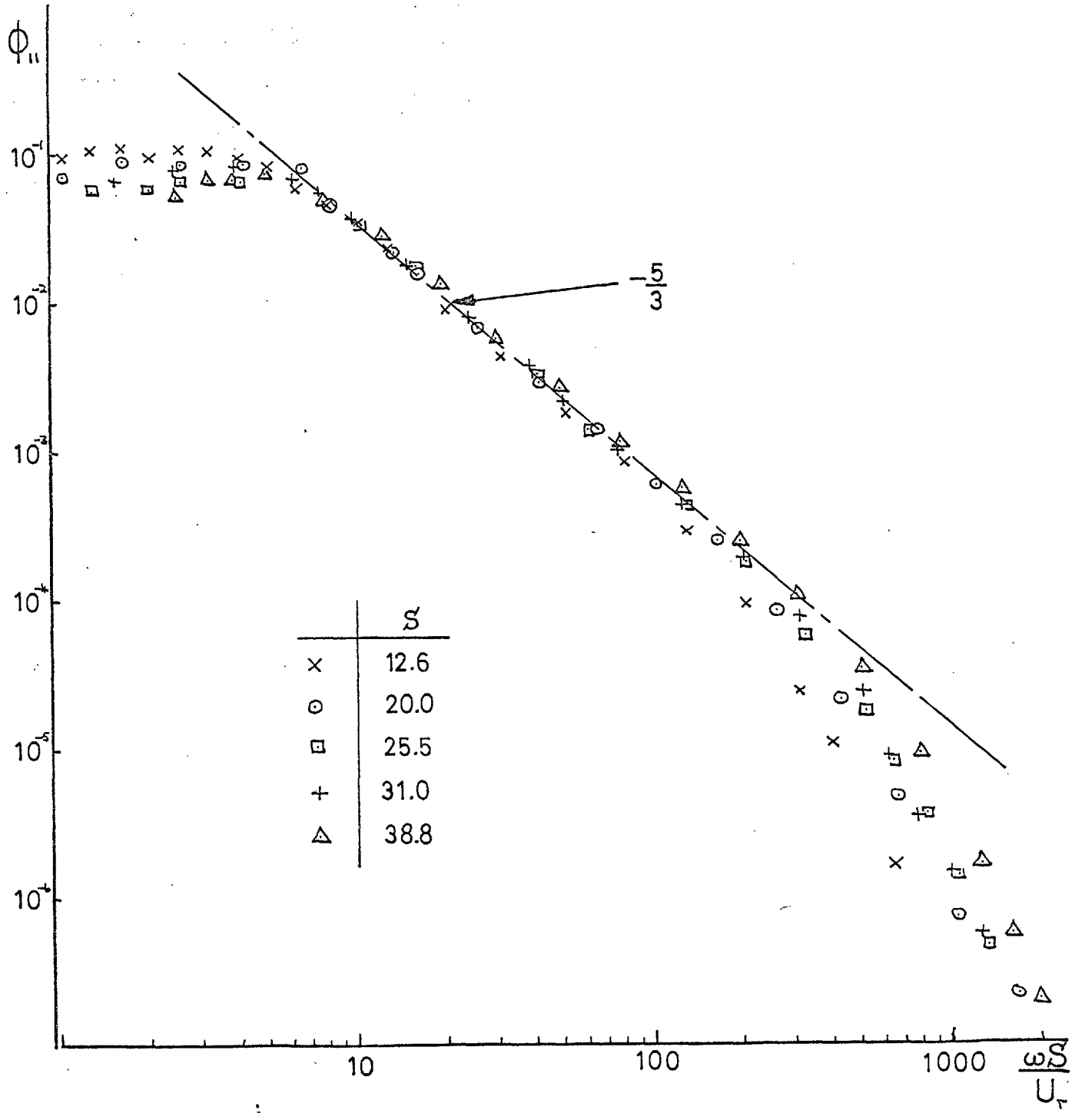


FIG. 5.19 u-component spectra along the centre-line.

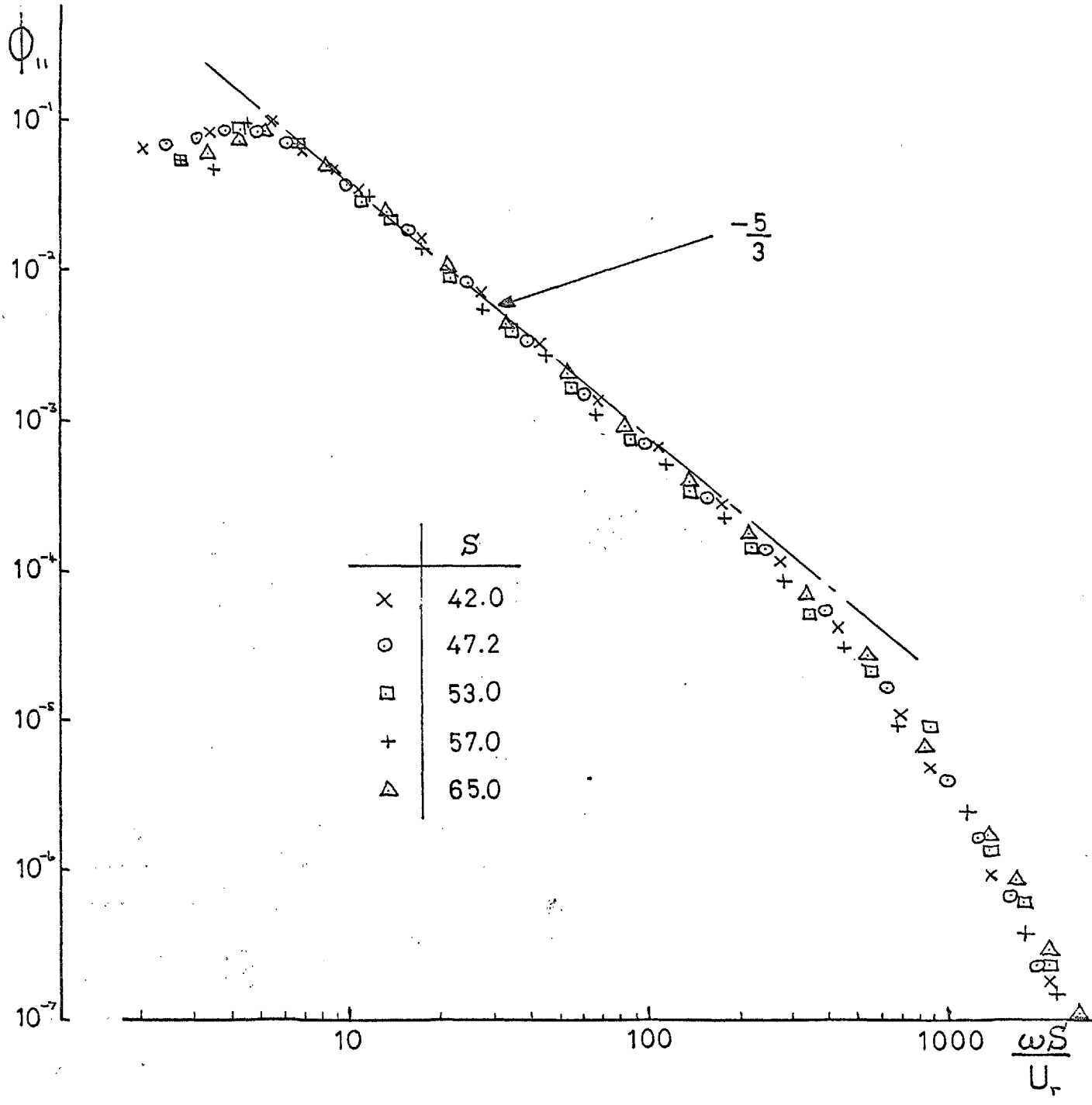


FIG. 5.20 u-component spectra along the centre-line.

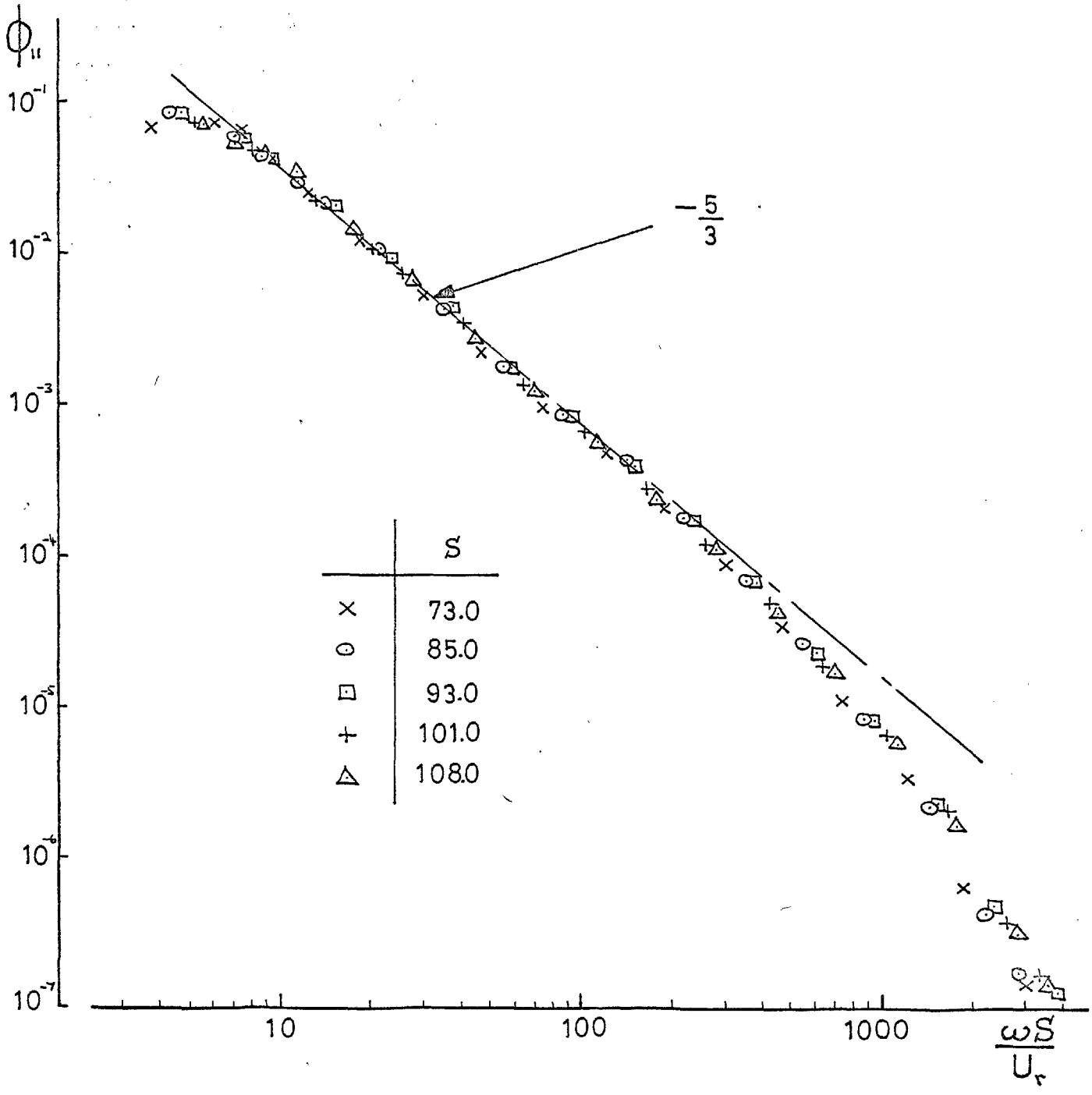


FIG. 5.21 u-component spectra.

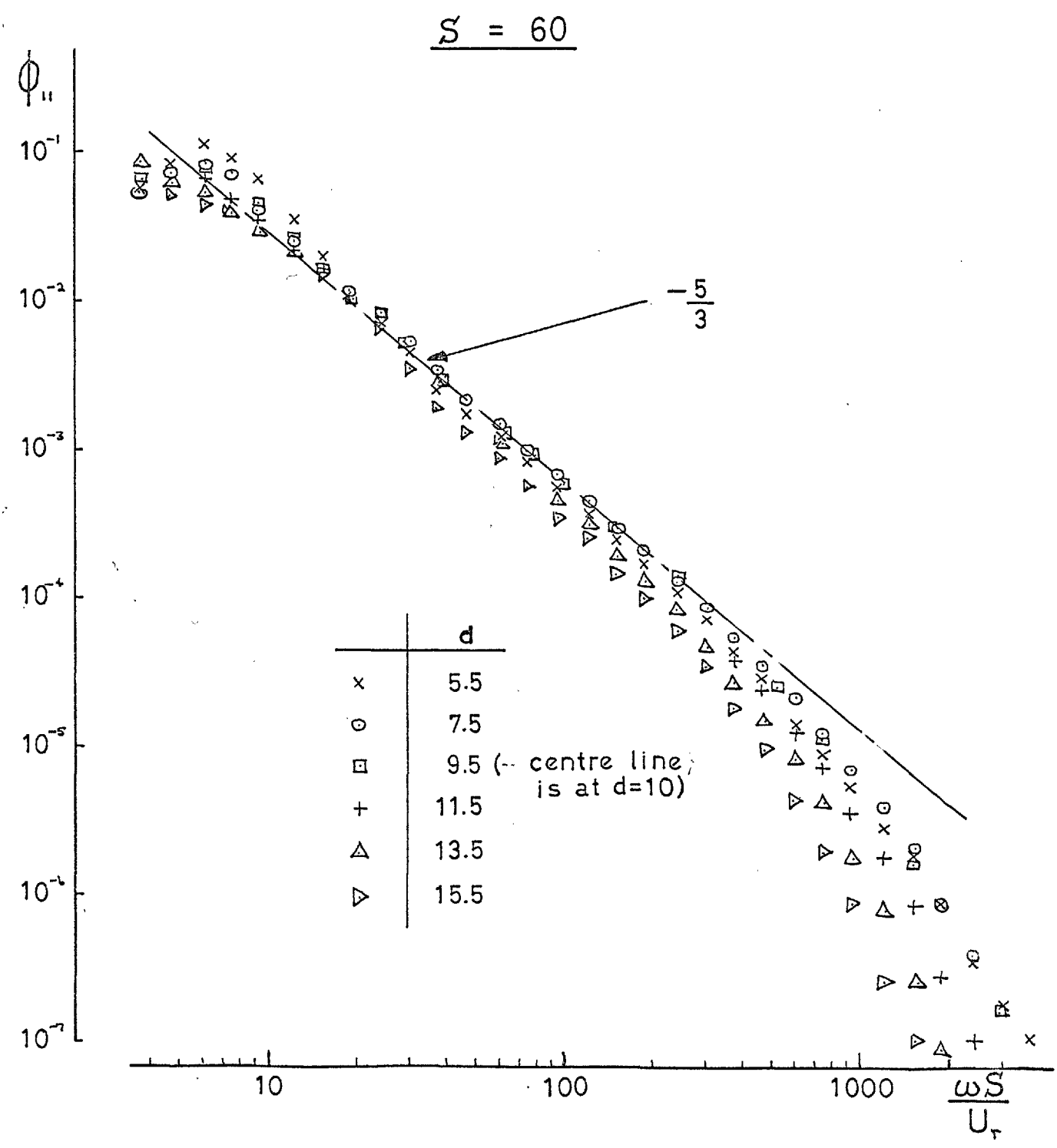
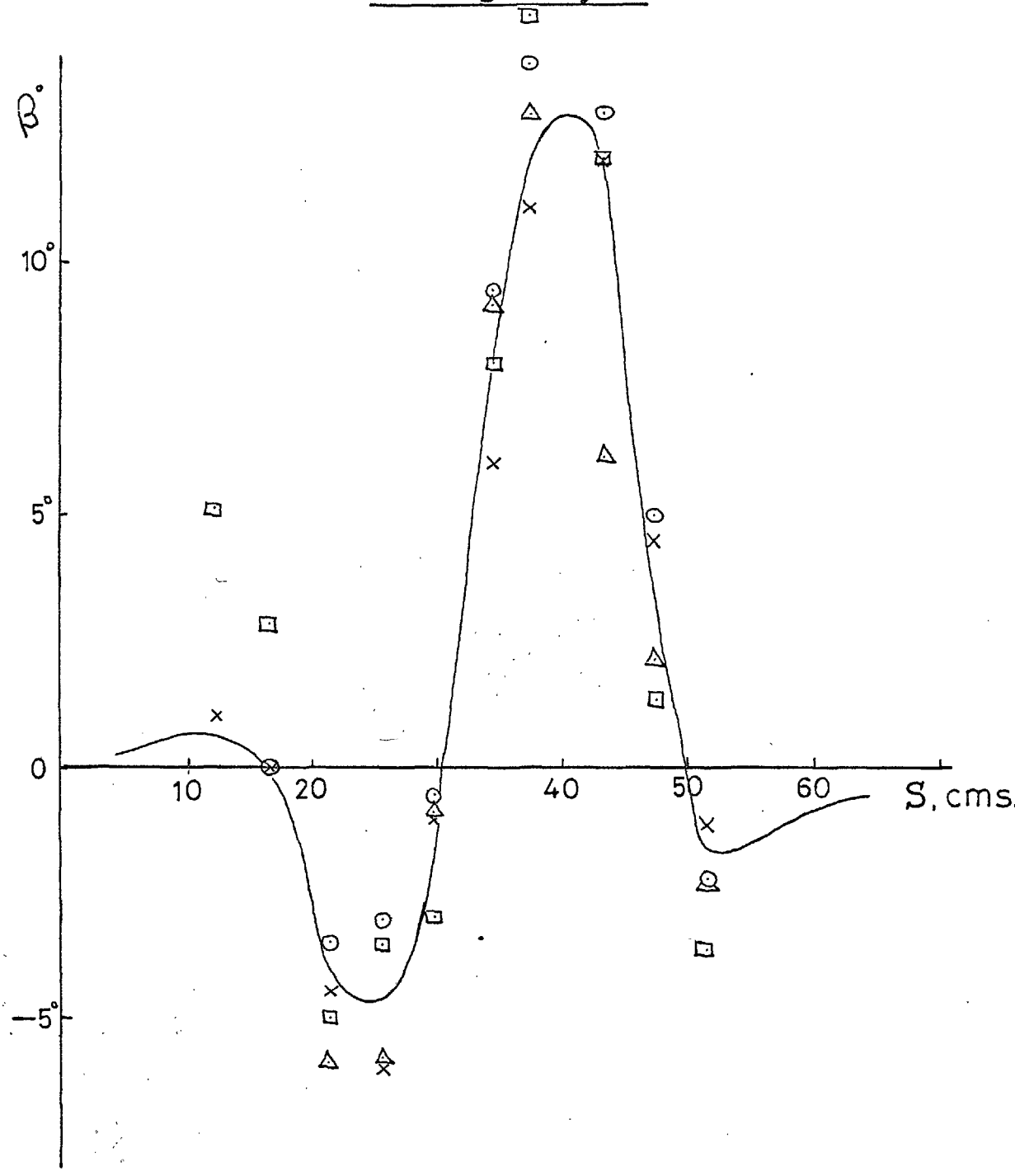


FIG. 5.22 Direction of curved mixing layer.



× β_1
○ β_2
△ β_3
□ β_4

For definitions see § 5.2.3

FIG. 5.23 Maximum turbulent energy & shear stress.

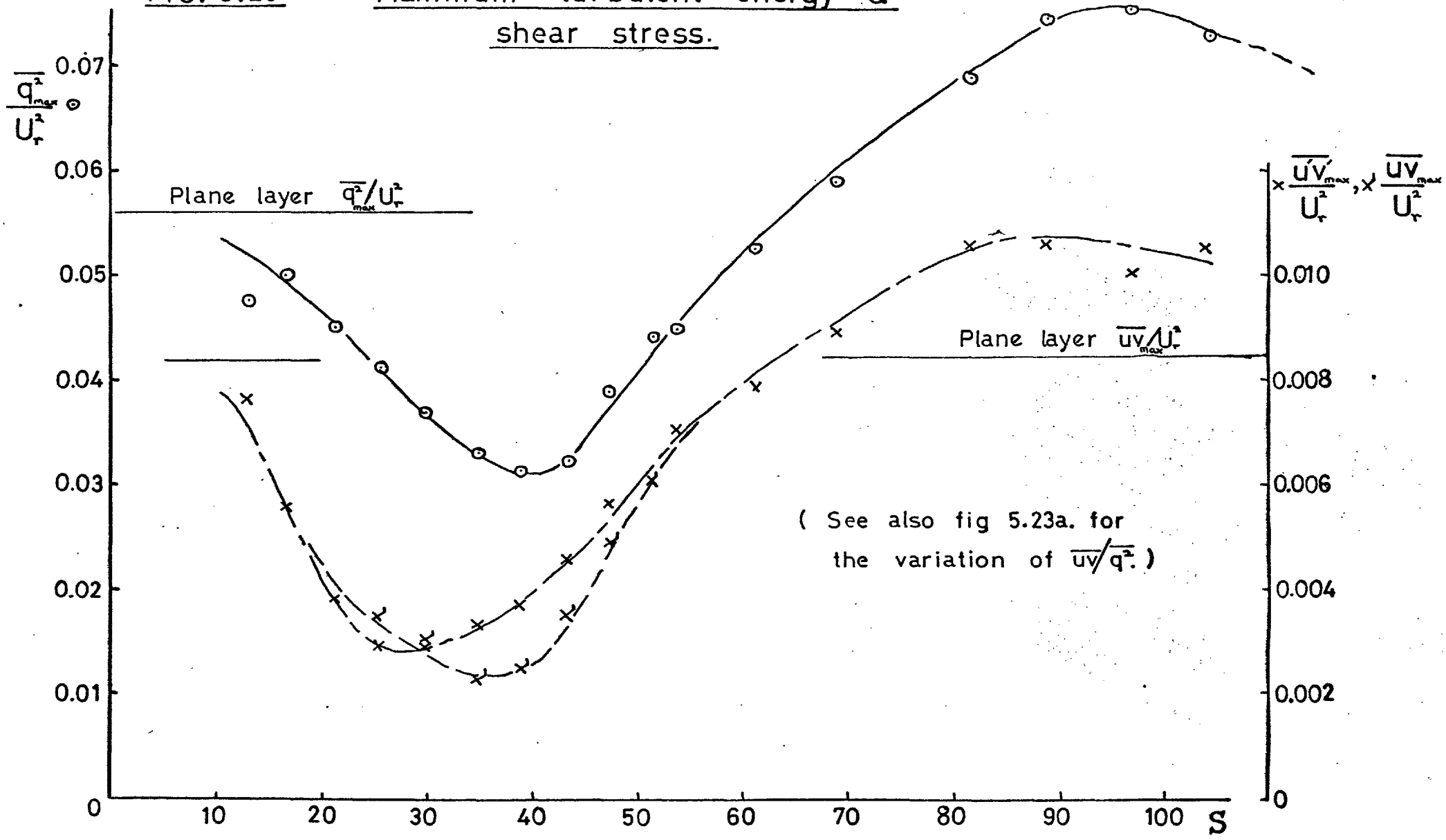


FIG. 5.23a. Variation of the 'structure' parameter, $\frac{\overline{uv}_{max}}{\overline{q^2}_{max}}$

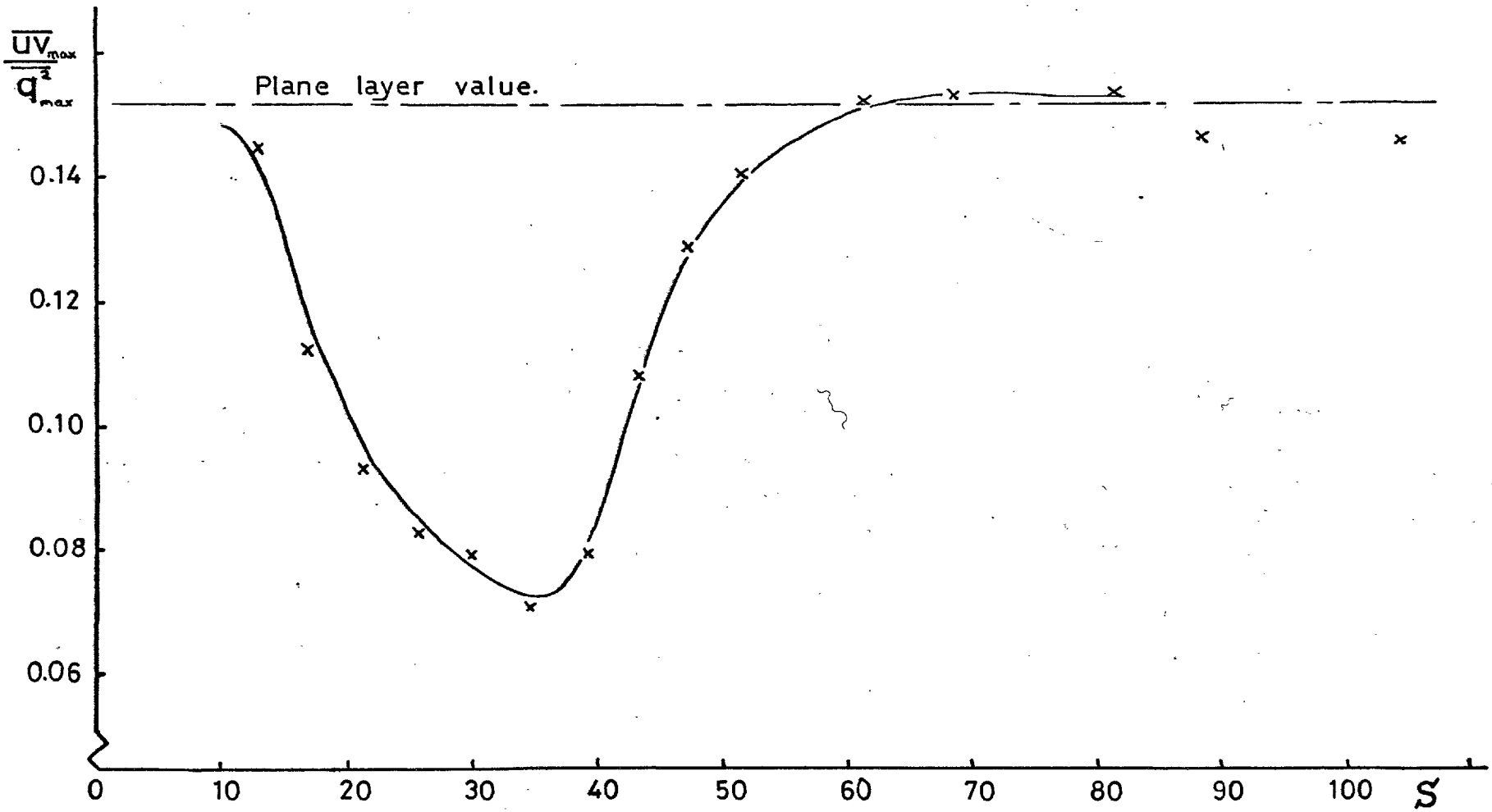
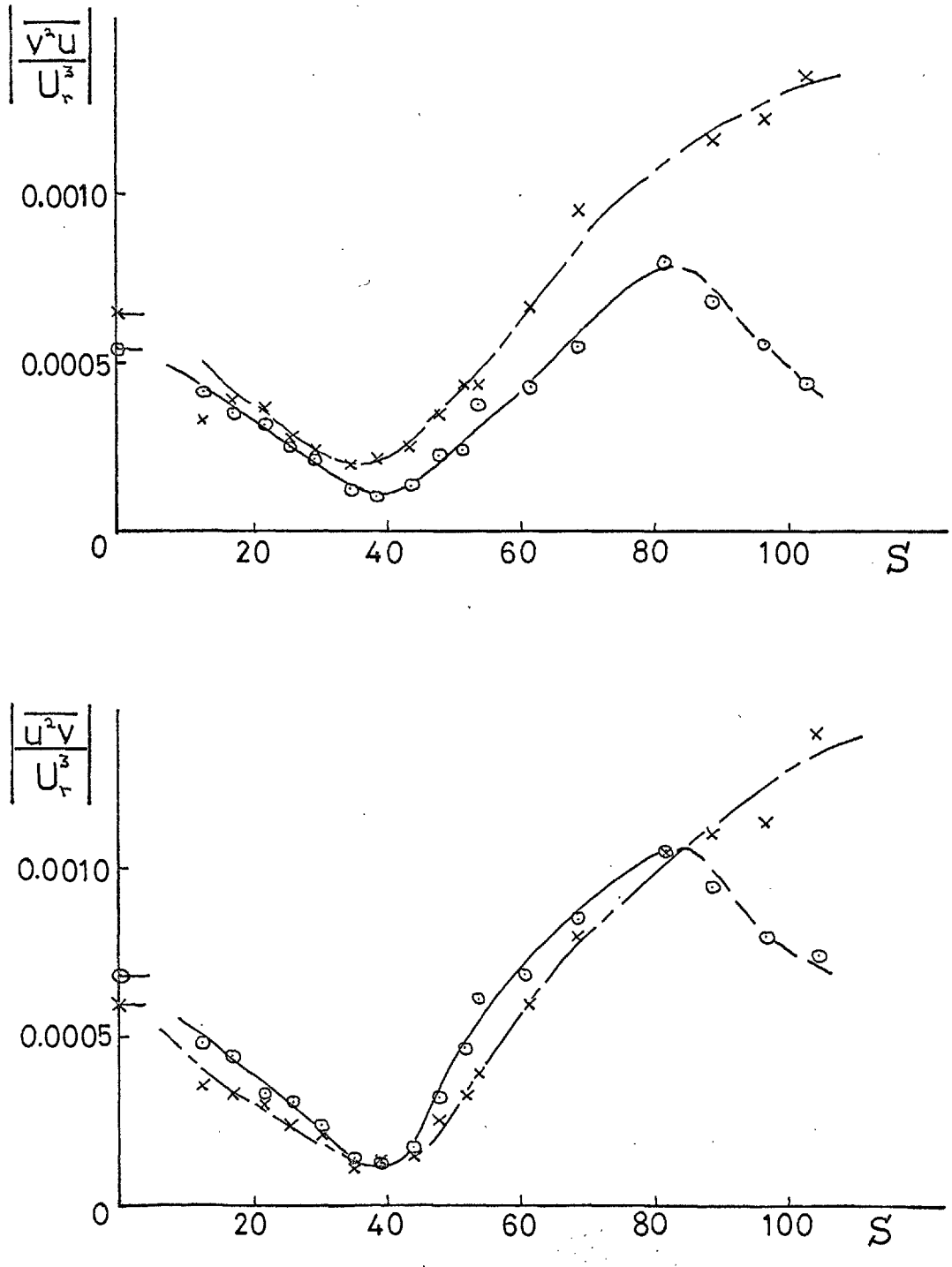
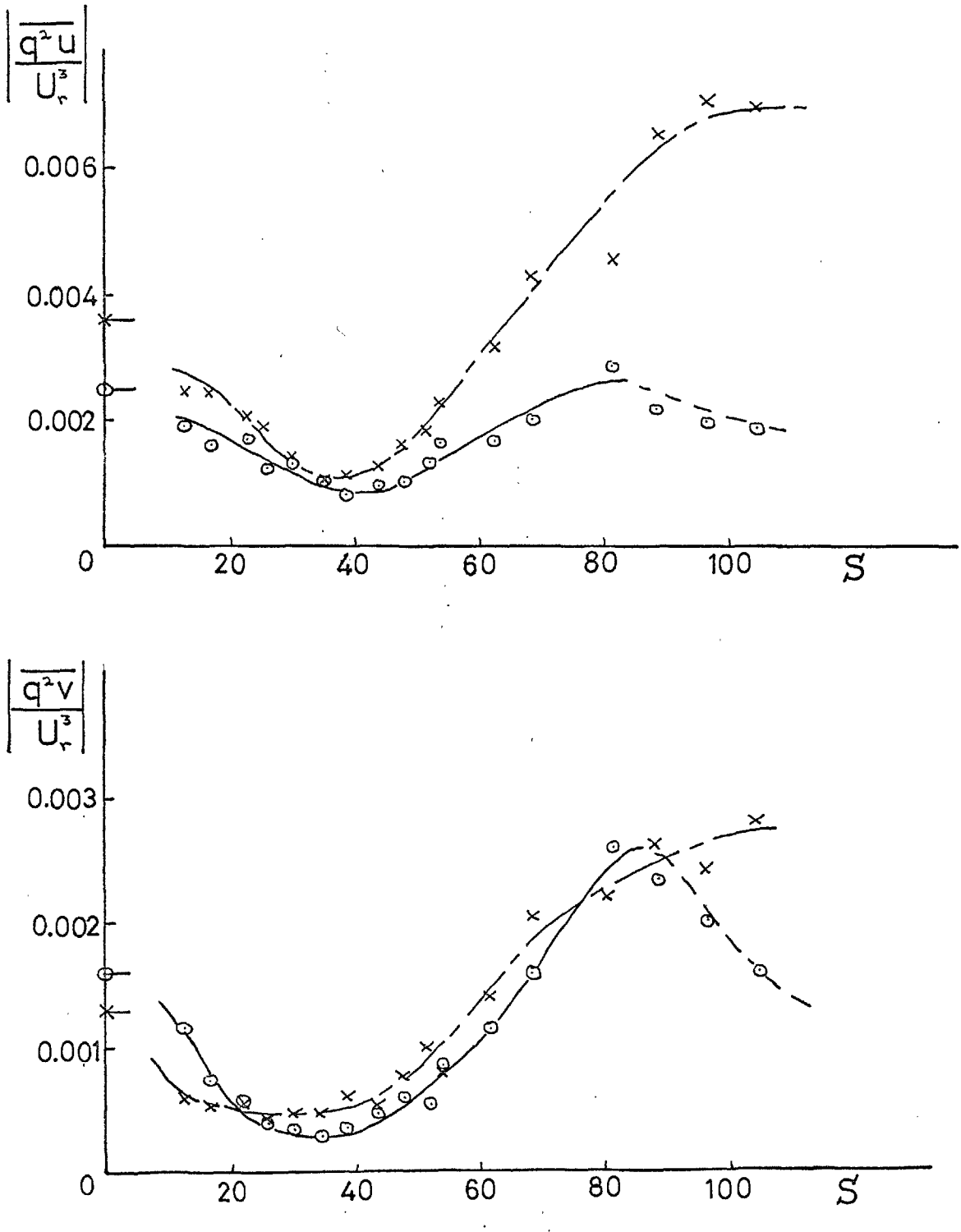


FIG. 5.24a. Maximum triple products



× ⊙ See fig. 5.24b.

FIG. 5.24b Maximum triple products.



× Maximum (+ve) value — low velocity side

⊙ Maximum (-ve) value — high velocity side

FIG. 5.25 Principal turbulent stress and mean rate of strain.

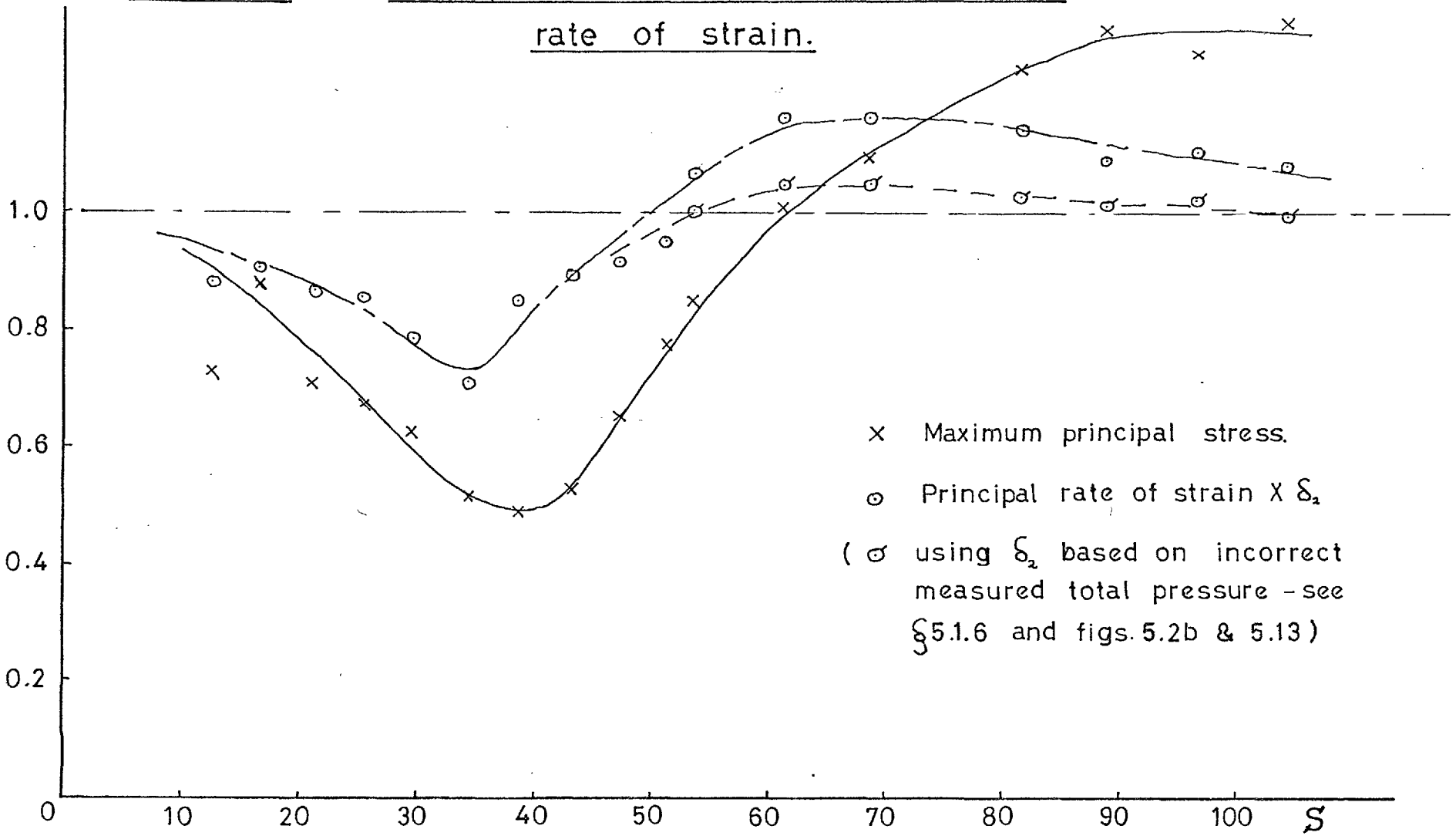


FIG. 5.26 Direction of principal stress and strain.

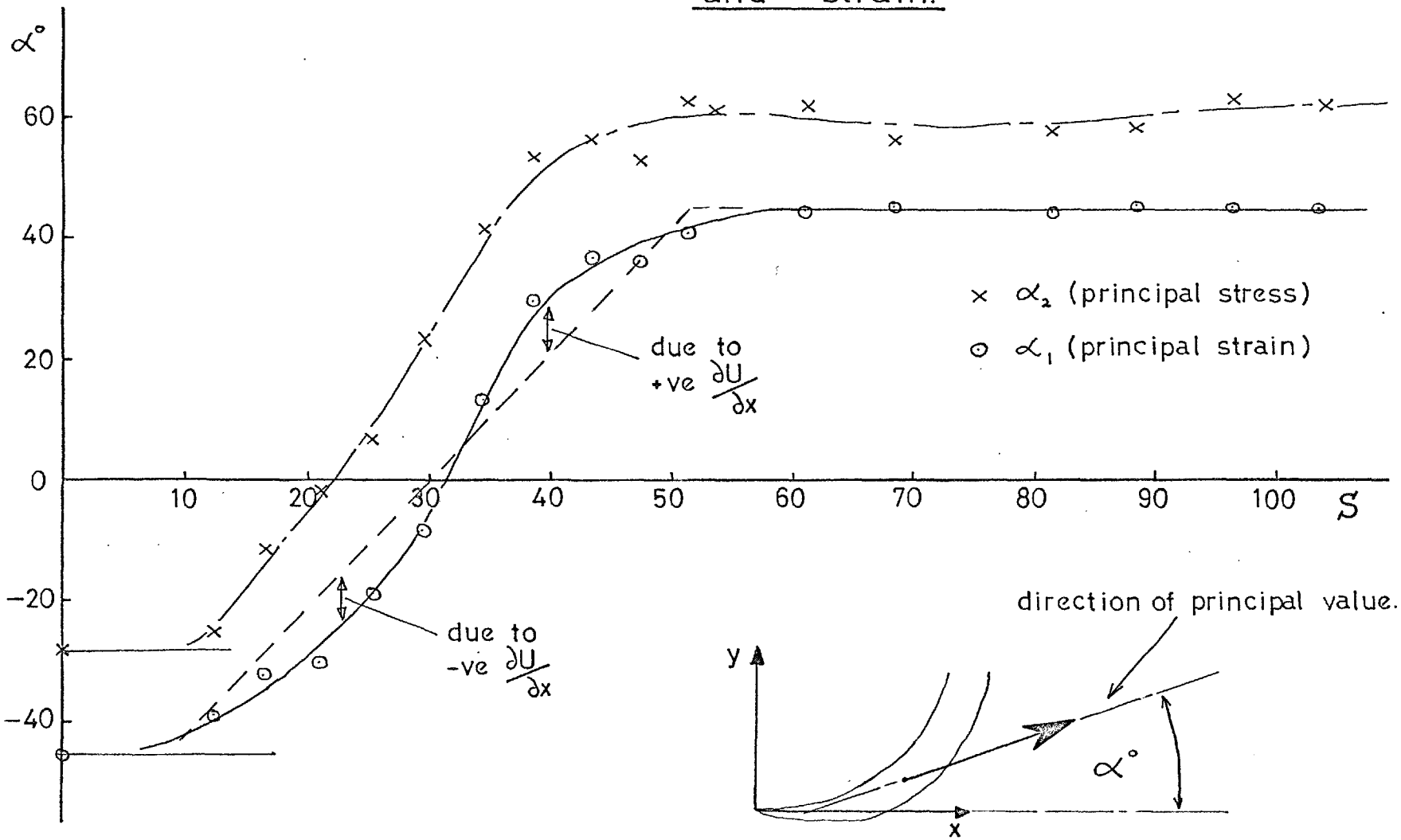


FIG. 5.27 Energy balance round the centre-line.

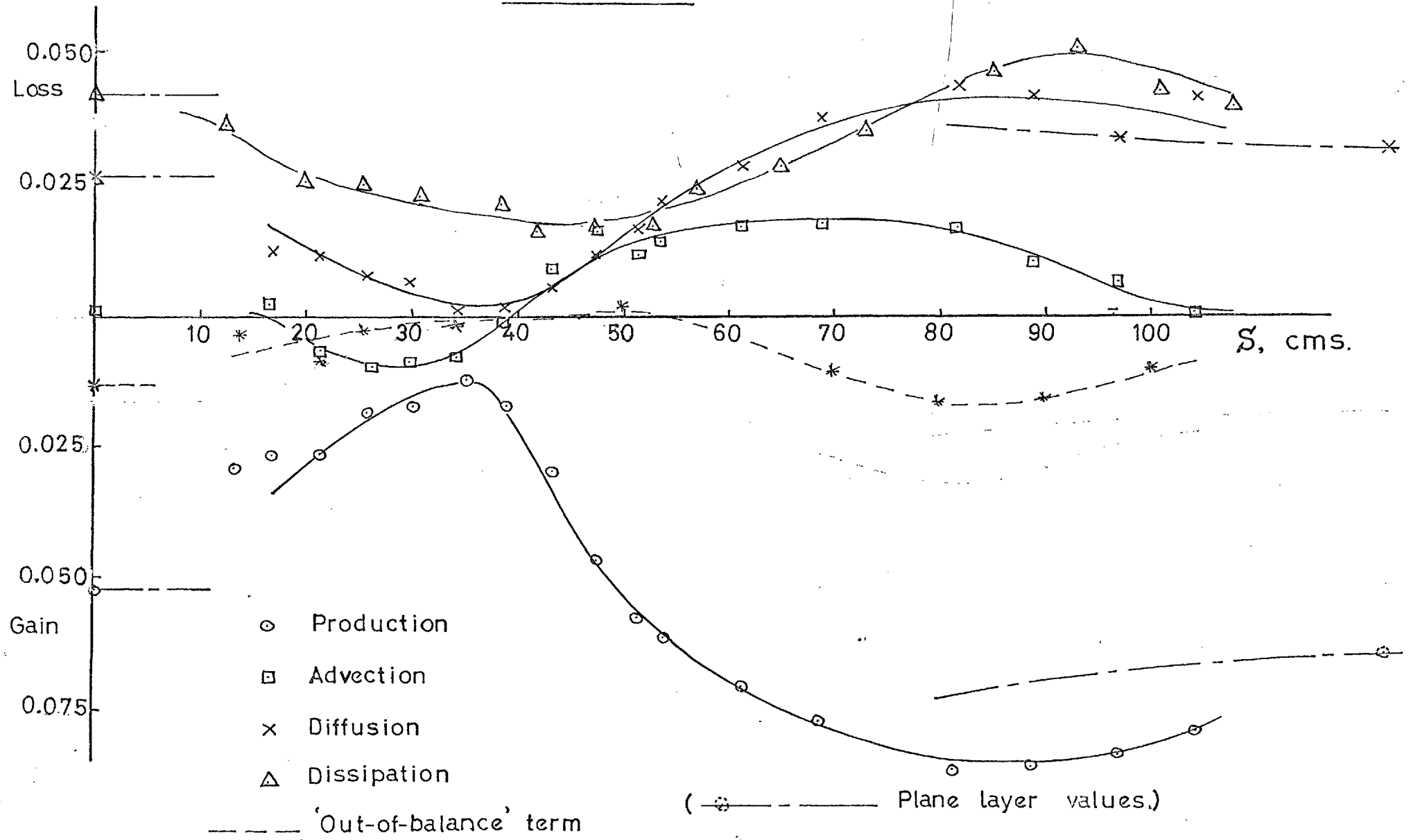
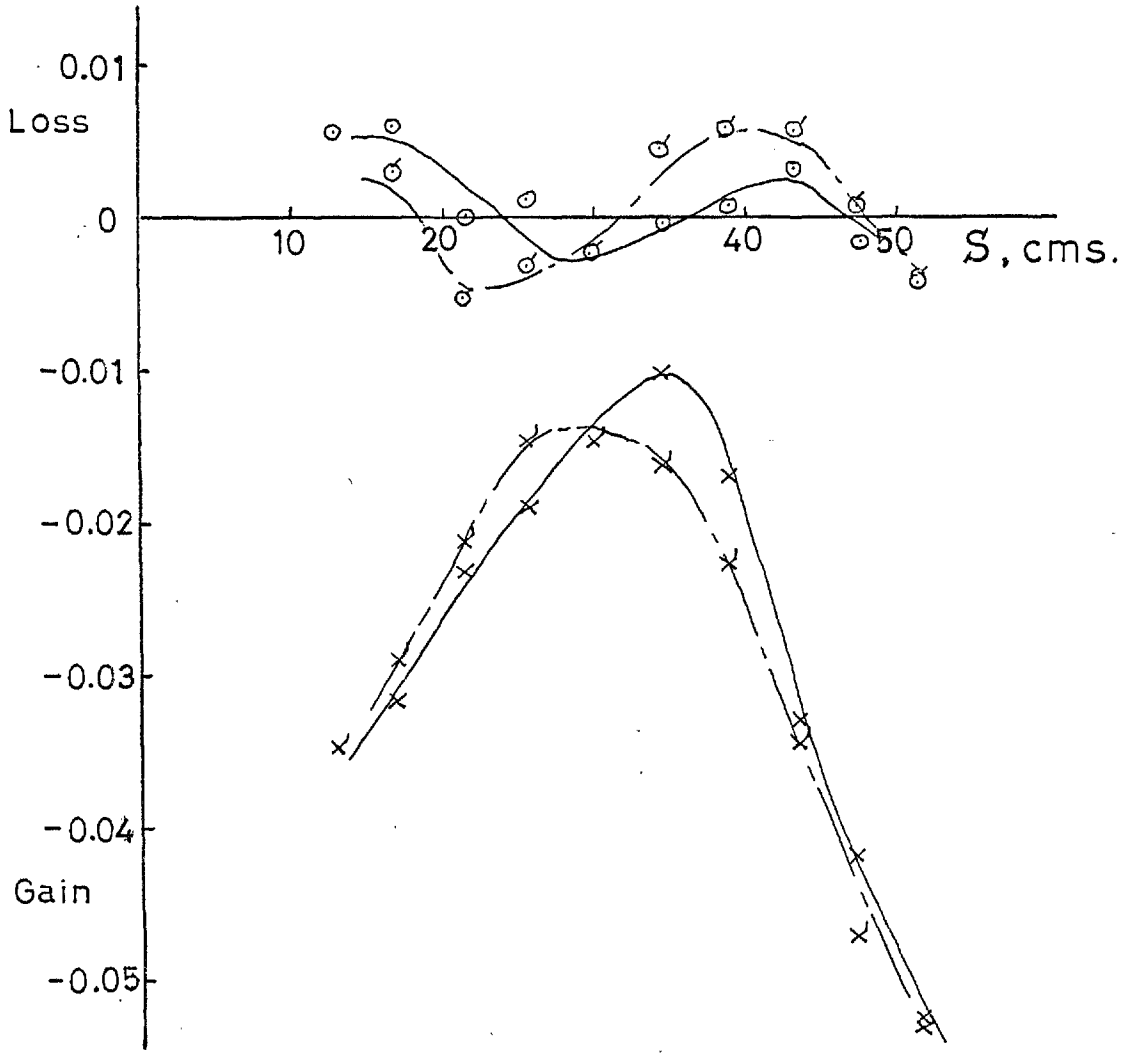


FIG. 5.28 The energy production terms (round the centre-line)



× Local streamwise axis (x', y') } Shear production.

× j-line axis (x_j', y_j') }

⊙ As above. } Normal stress production.

ơ }

FIG. 5.29 Accuracy checks (streamwise energy gradient)

(round the centre-line)

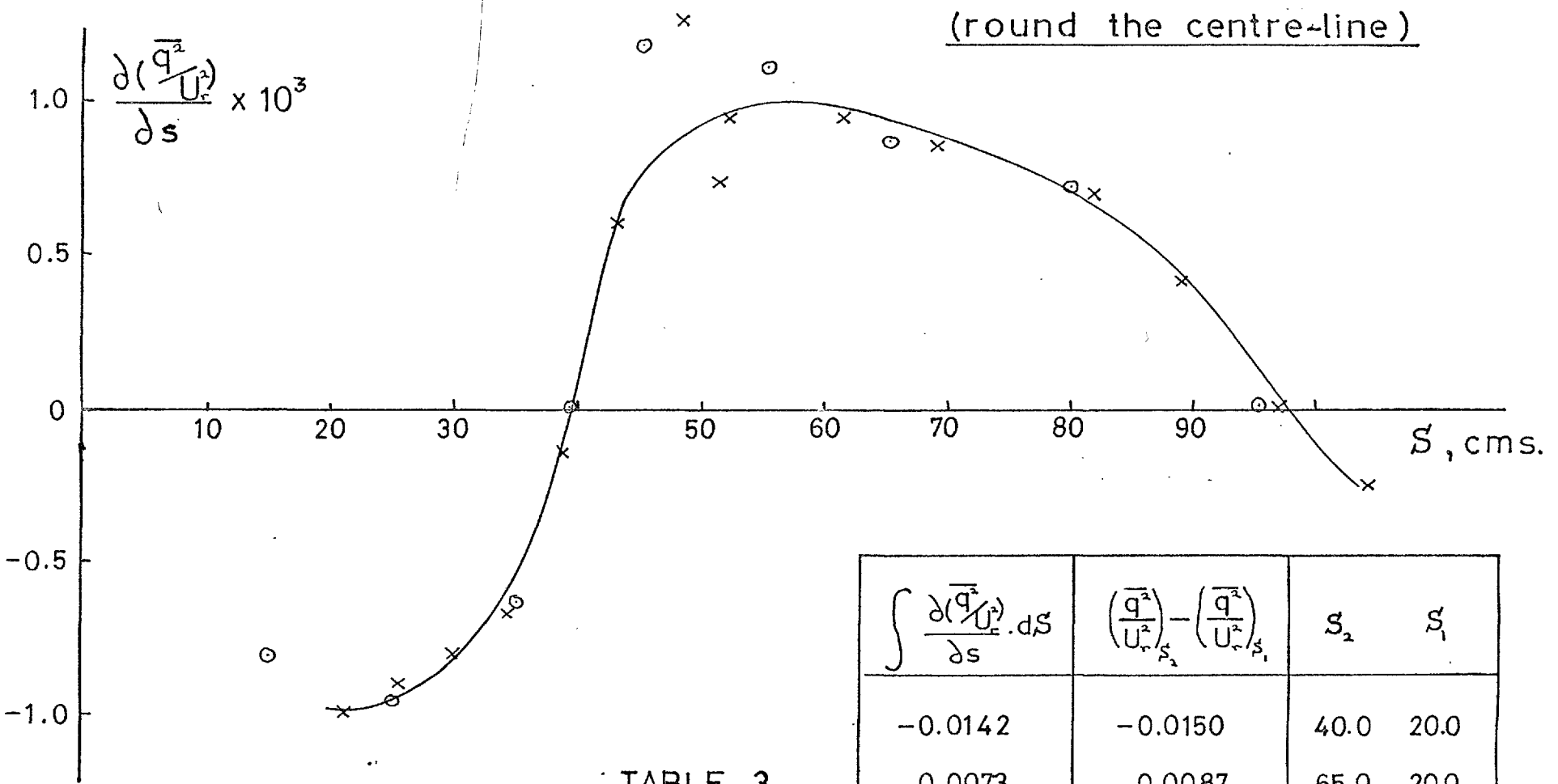
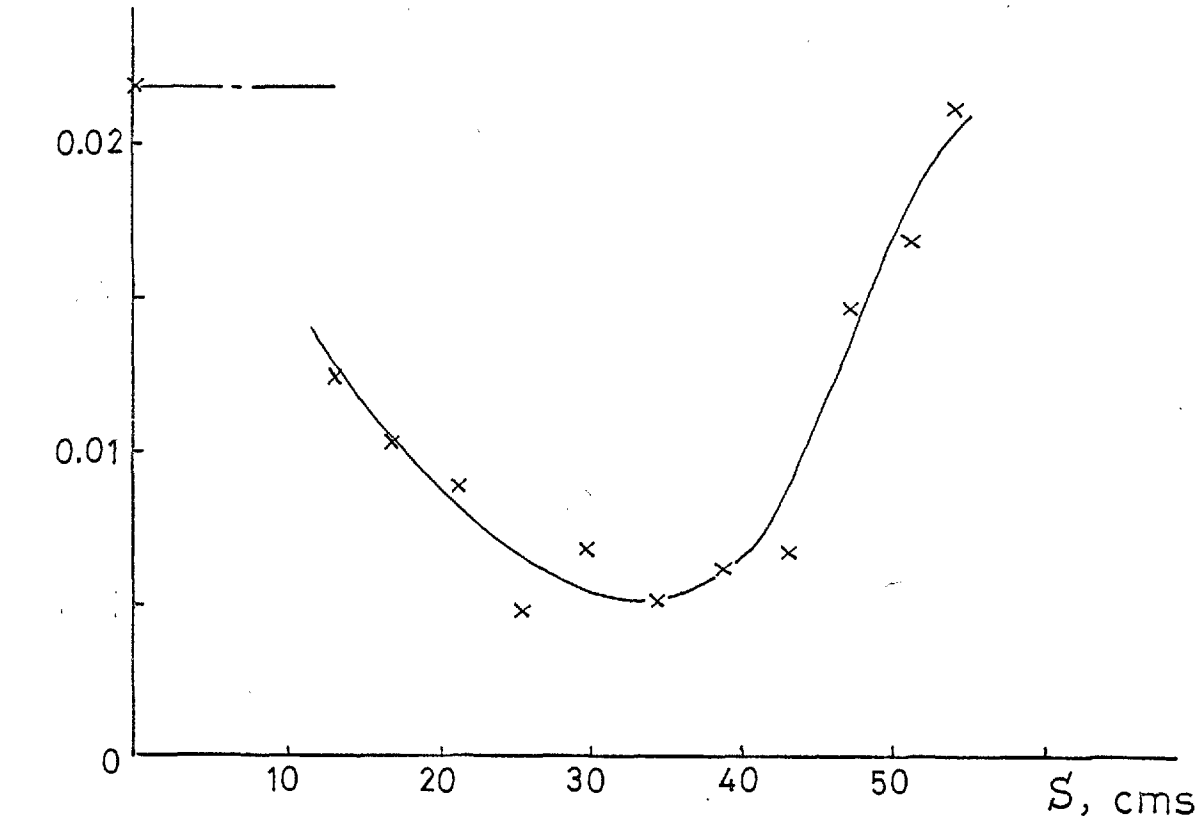
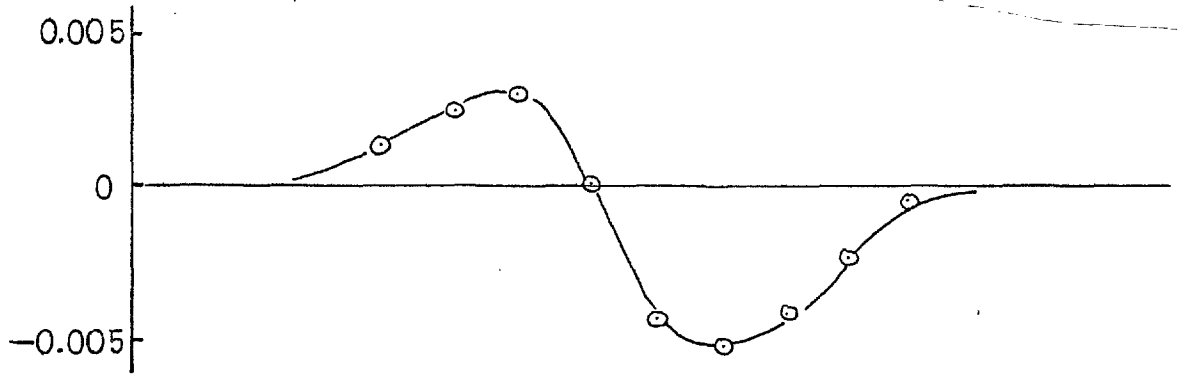


TABLE 3

$\int \frac{\partial(\overline{q^2}/U_r^2)}{\partial s} . dS$	$\left(\frac{\overline{q^2}}{U_r^2}\right)_{S_2} - \left(\frac{\overline{q^2}}{U_r^2}\right)_{S_1}$	S_2	S_1
-0.0142	-0.0150	40.0	20.0
0.0073	0.0087	65.0	20.0
0.0268	0.0285	97.5	20.0

FIG. 5.30 Triple velocity diffusion round the centre-line.





$\times$ $\dfrac{\partial(\overline{q^2 v'}/U_c^3)}{\partial y'_j} \times S$

$\odot$ $\dfrac{\partial(\overline{q^2 u'}/U_c^3)}{\partial x'_j} \times S$

FIG. 5.31 Typical $\overline{q^2u'}$ vs. x'_j for estimation of longitudinal gradients.

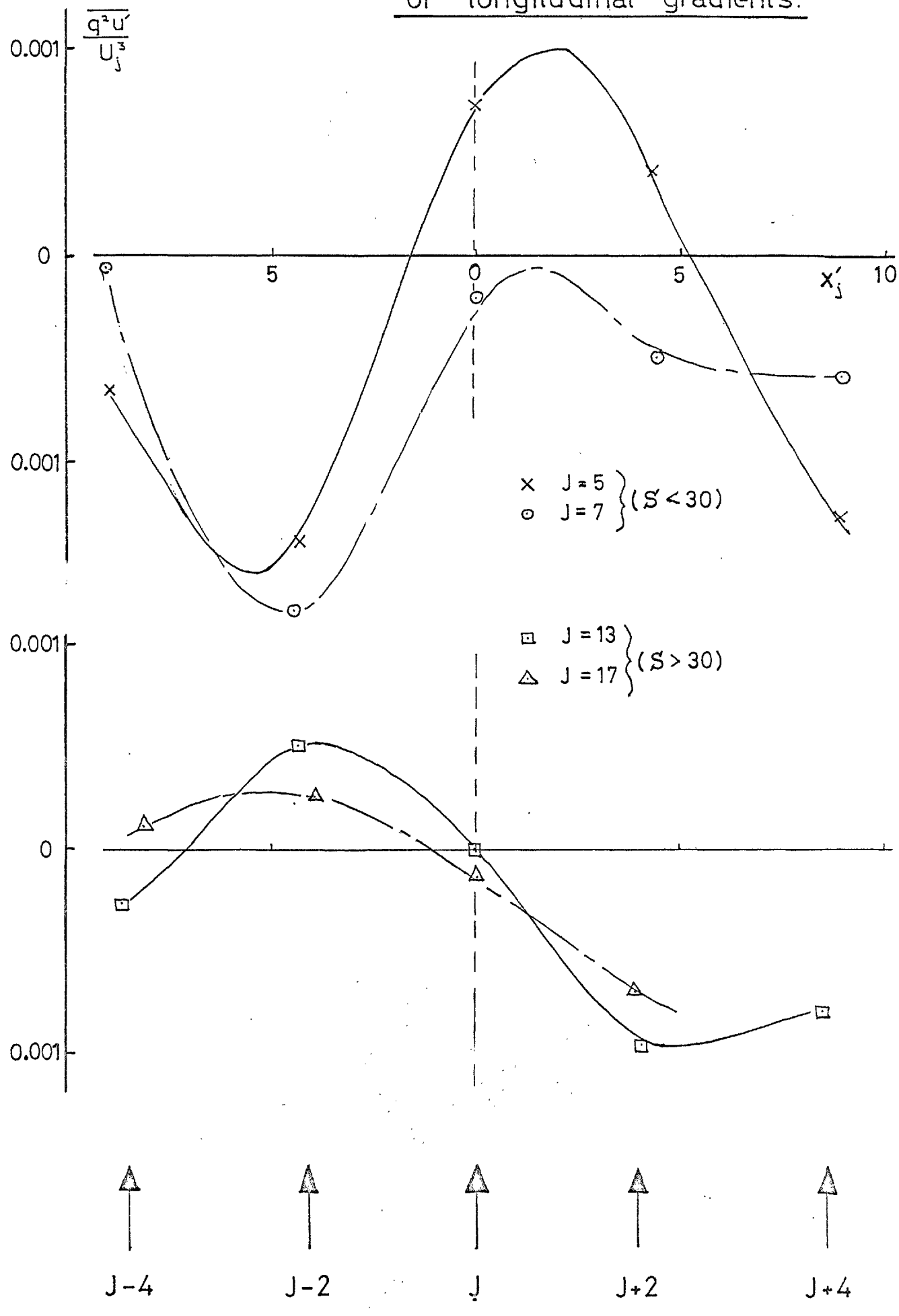


FIG. 5.32 Energy balance

$S = 34.4, J = 11$

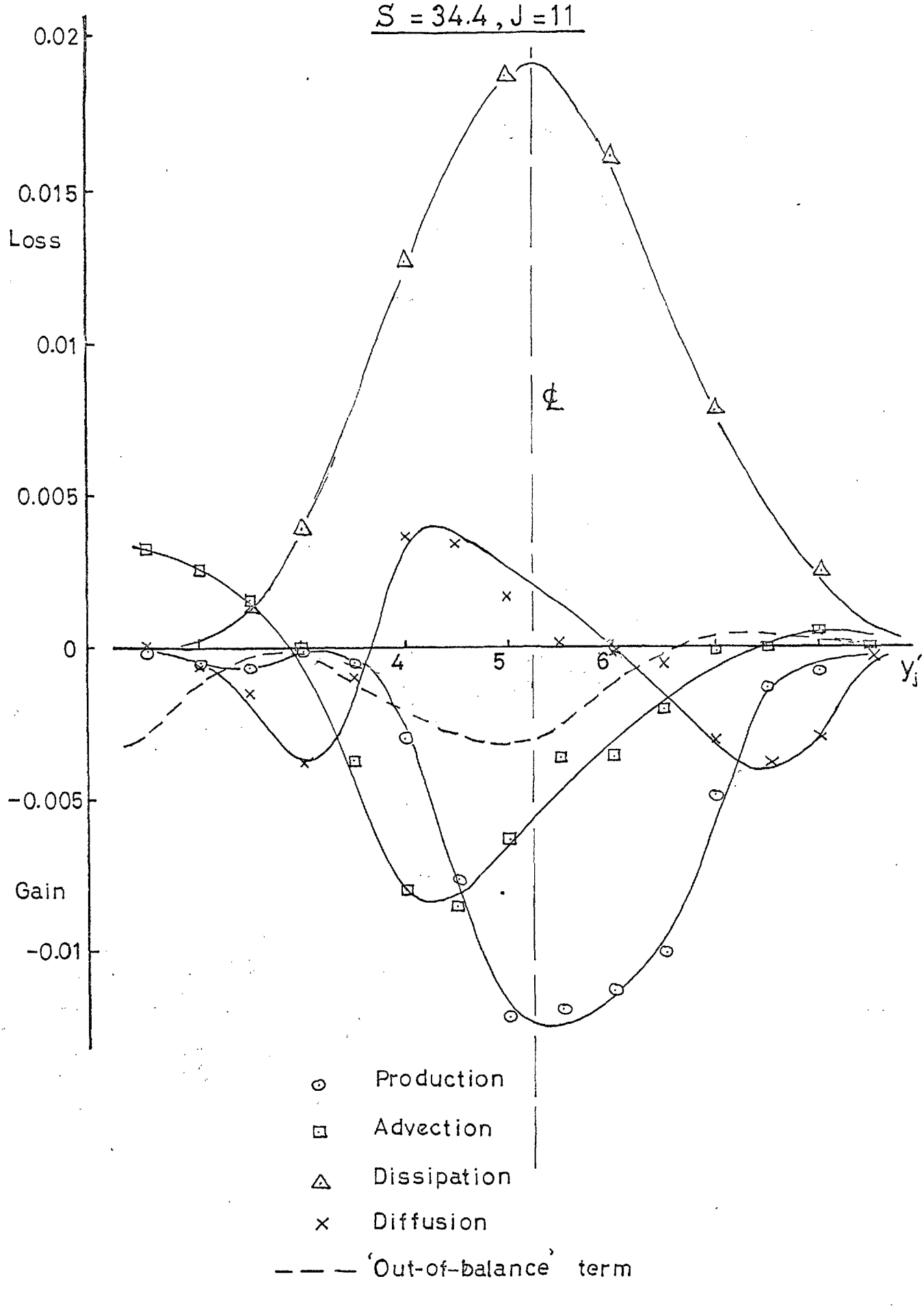
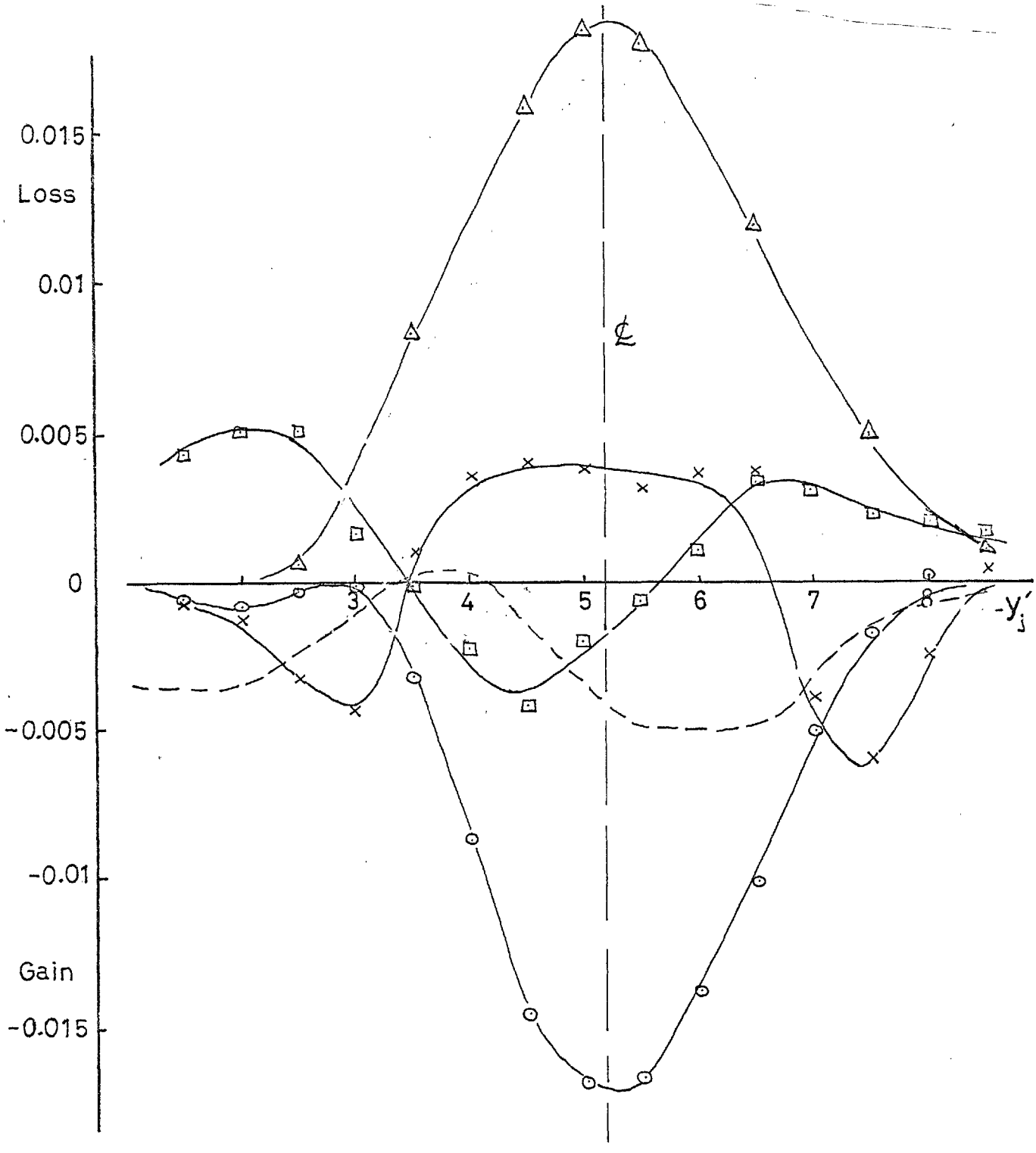


FIG. 5.33 Energy balance

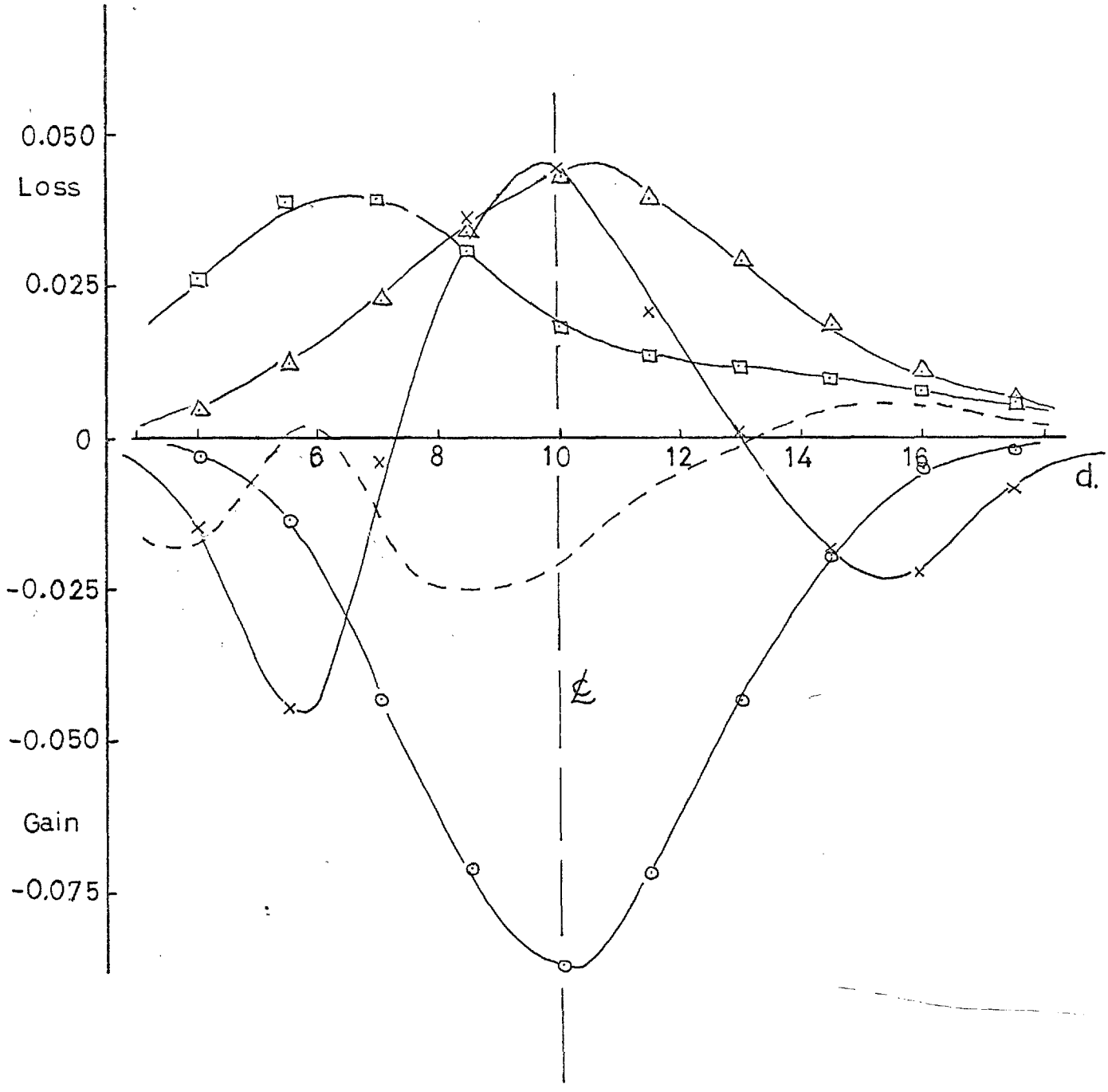
$S = 38.8, J = 13$



Symbols as in fig. 5.32

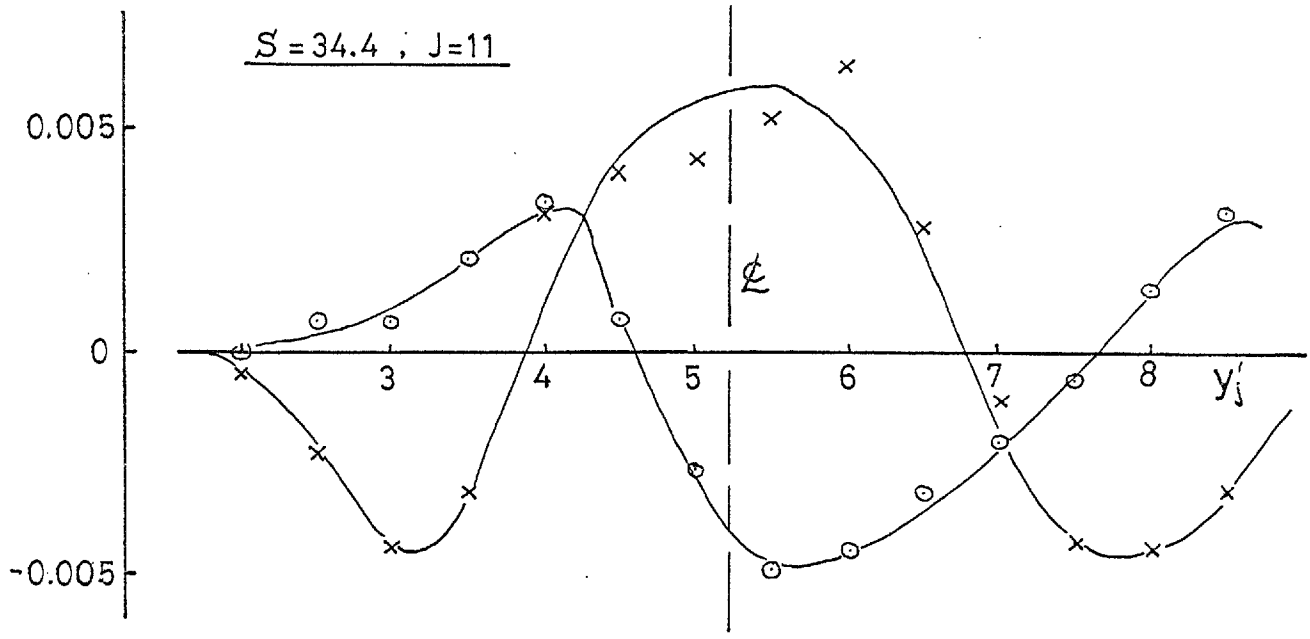
FIG. 5.34 Energy balance

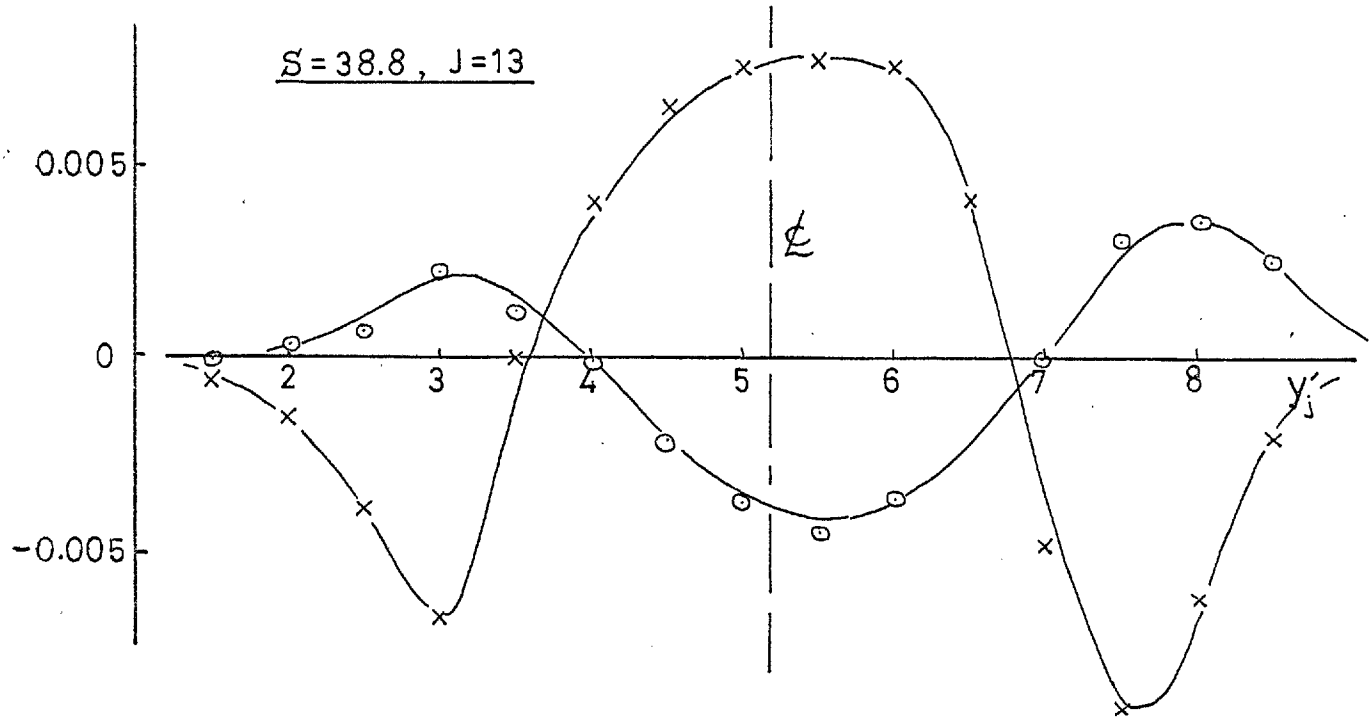
$S = 81.5$, $J = 27$



Symbols as in fig. 5.32

FIG. 5.35 Triple velocity diffusion.

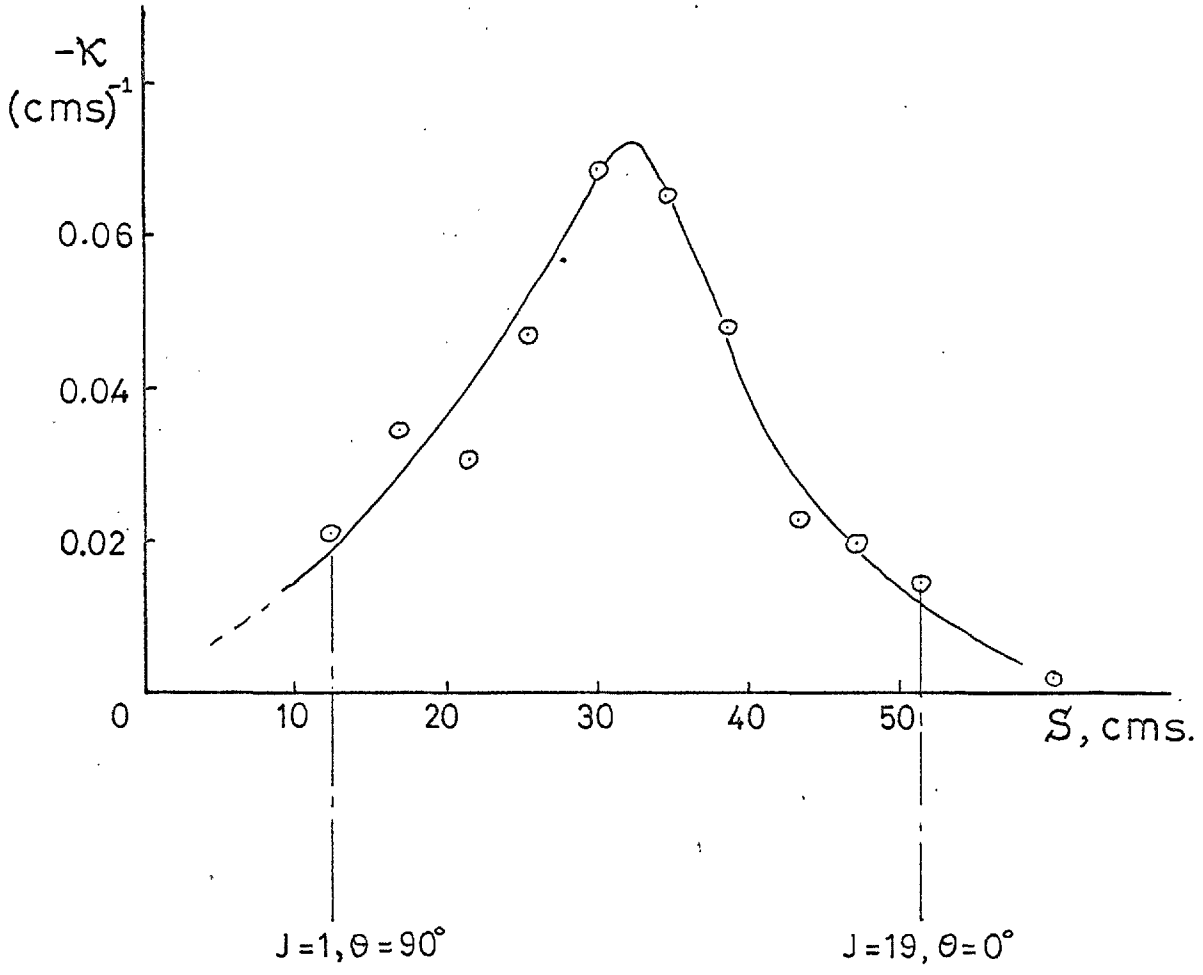




$$\frac{\partial\left(\overline{q^2 v'}/U_c^3\right)}{\partial y_j'} \times S$$

$$\frac{\partial\left(\overline{q^2 u'}/U_c^3\right)}{\partial x_j'} \times S$$

FIG. 5.36 Mixing layer curvature.



$$-\int_{j=1}^{j=19} \kappa . dS = 1.56$$

$$\theta_{j=19} - \theta_{j=1} \equiv \pi/2 = 1.571$$

FIG. 5.37 Shear stress balance round the centre line.

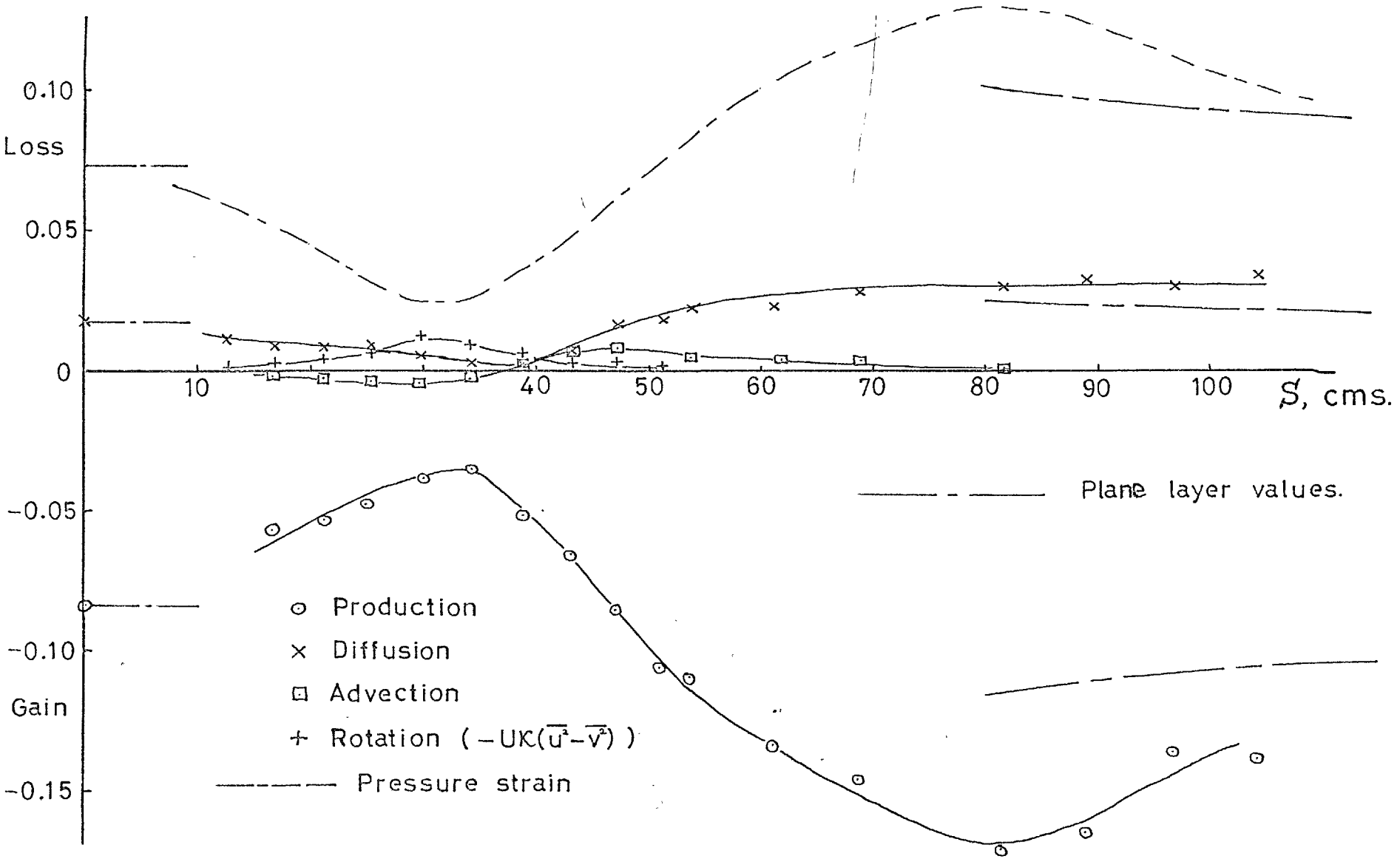
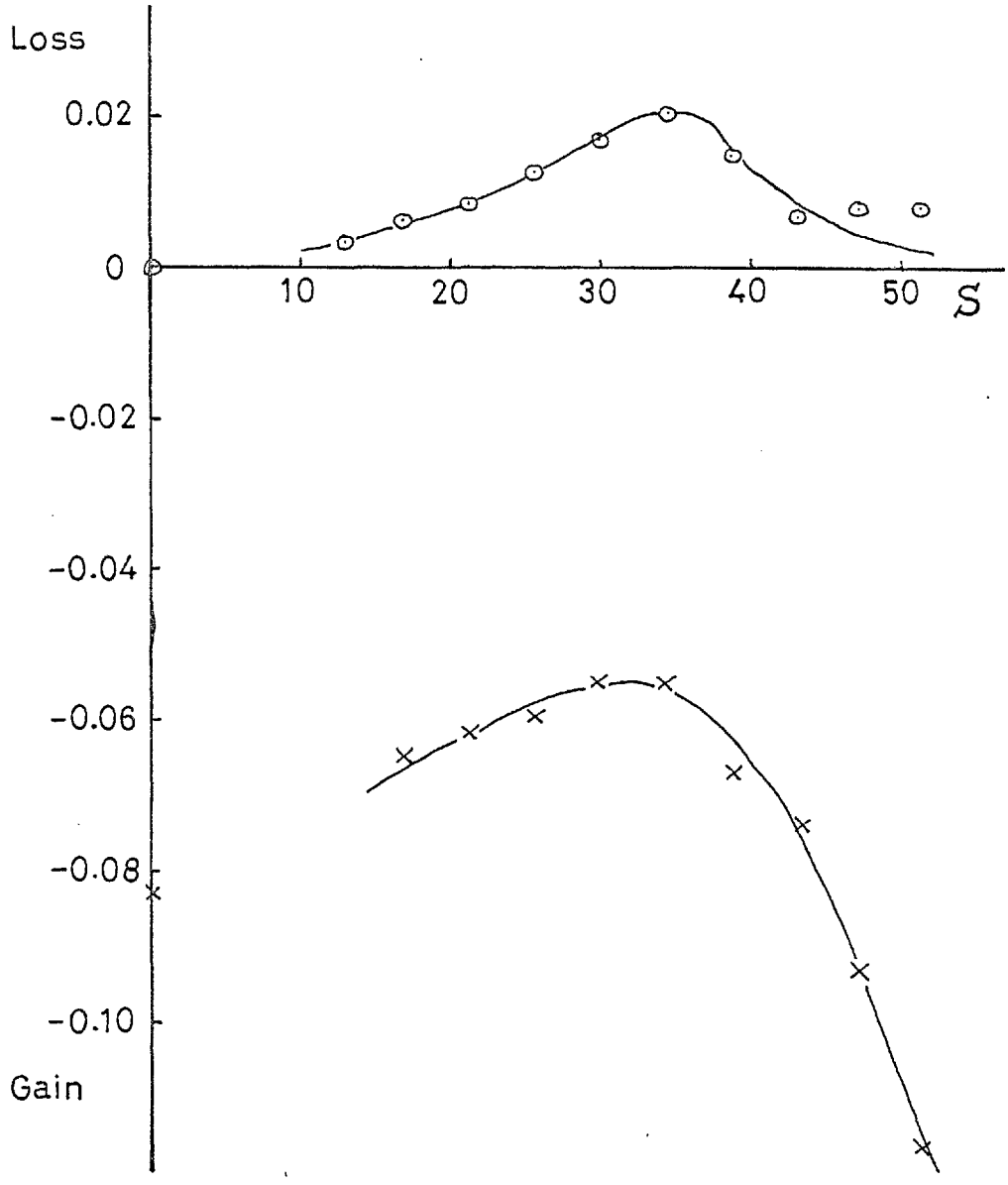


FIG. 5.38 The shear stress production terms around the centre line.



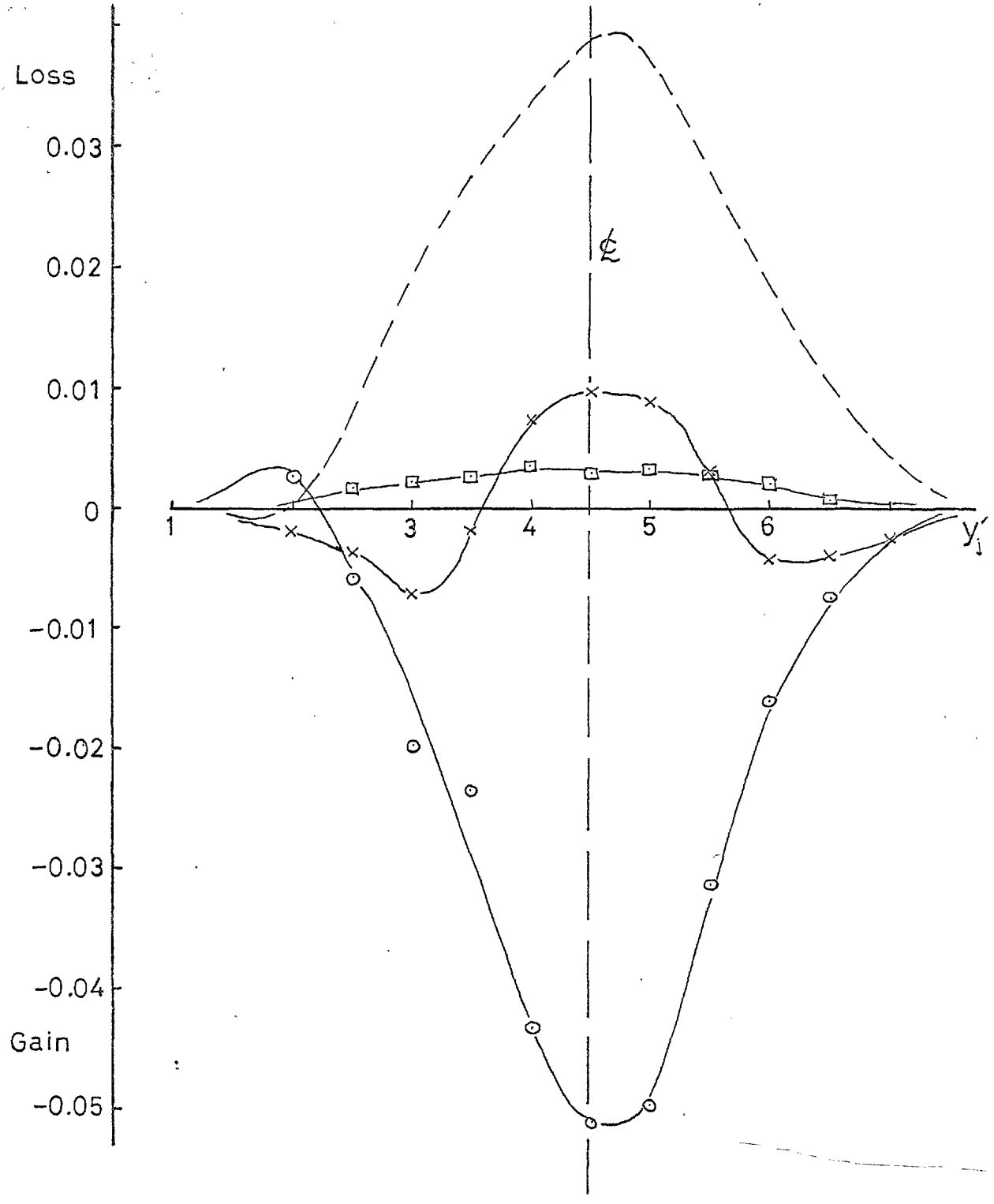
× $\overline{v^2}\frac{\partial U}{\partial n}$

⊙ $-\overline{u^2}UK$

$\left(\overline{u^2}\frac{\partial V}{\partial s} \sim 0\right)$

FIG. 5.39 Shear stress balance.

J = 5 , S = 21.1

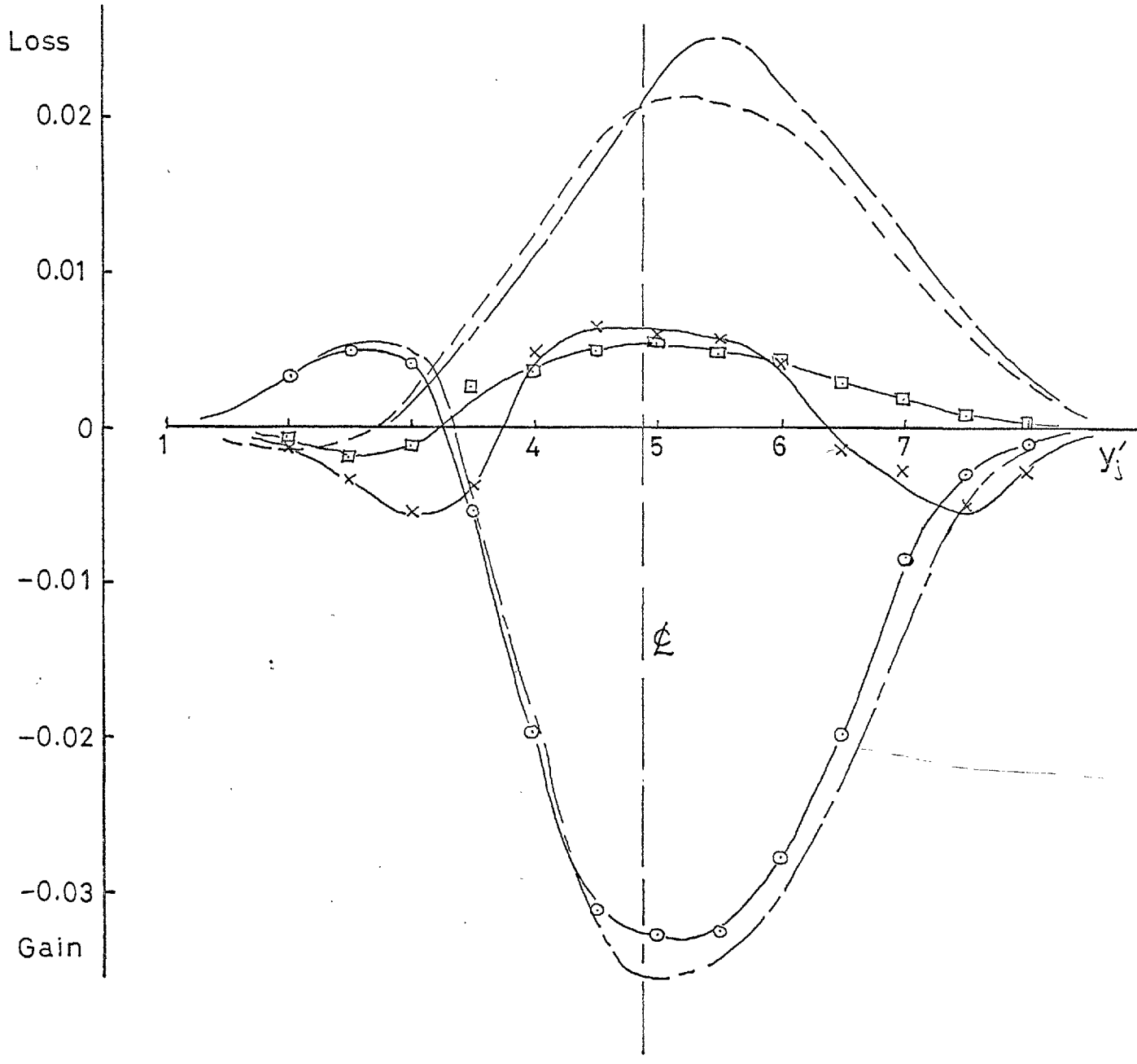


Symbol as in fig. 5.37

(x', y' axes used)

FIG. 5.40 Shear stress balance

J = 9 , S = 29.9

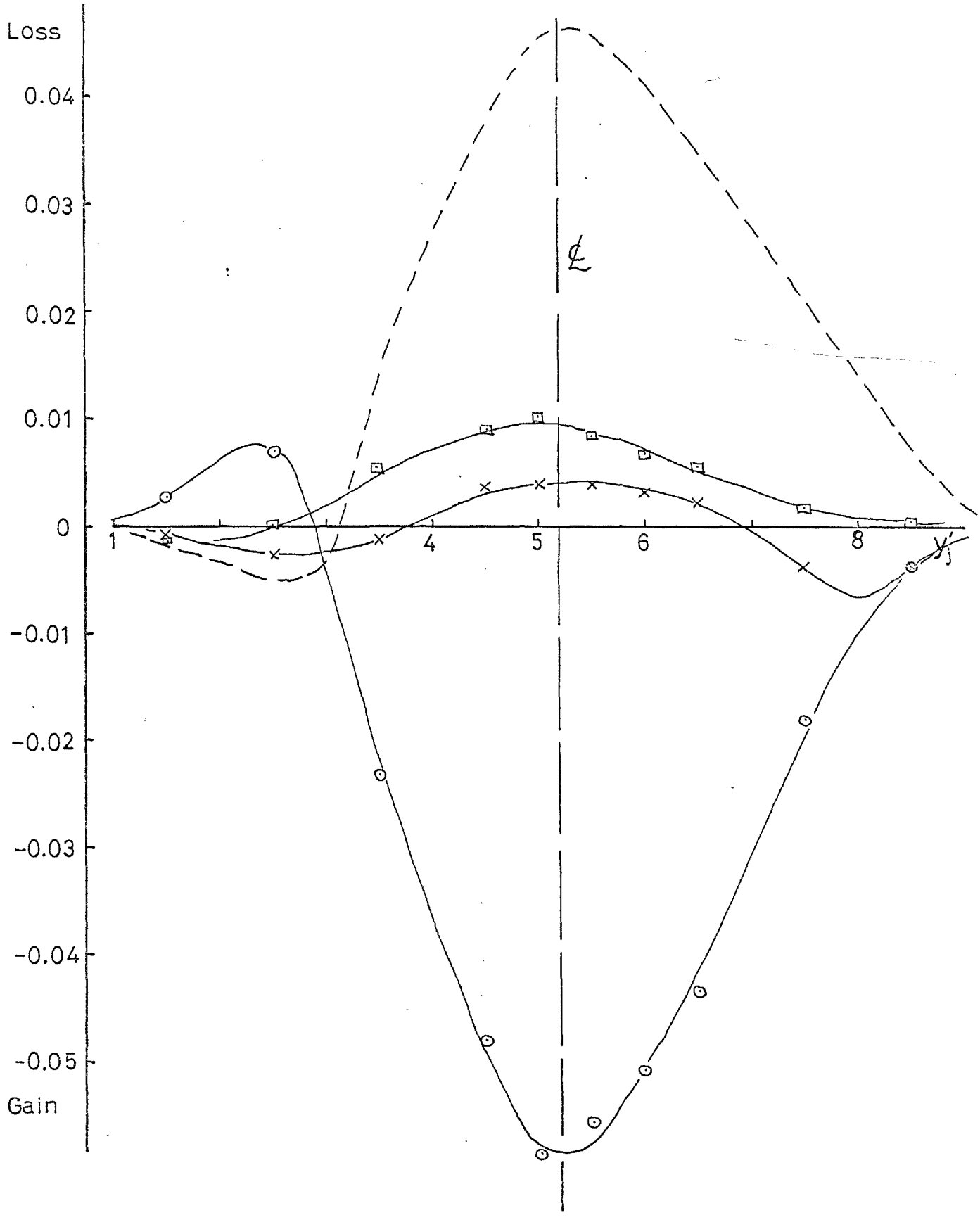


Symbols as in fig. 5.37

———- ——— Using streamline (s,n) co-ordinates, (rotation, advection & diffusion terms are not plotted.)

FIG. 5.41 Shear stress balance

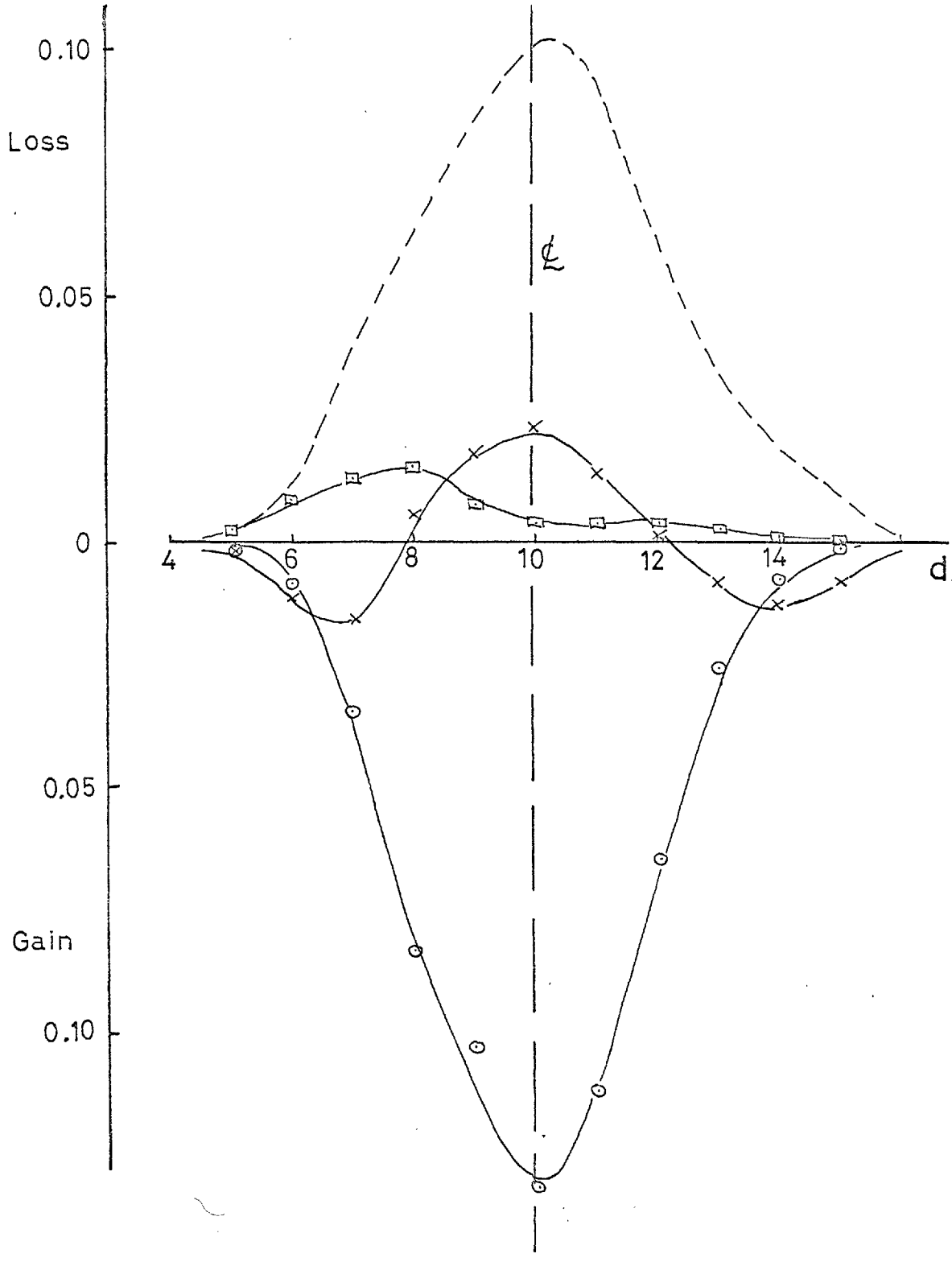
J = 13 , S = 38.8



Symbols as in fig. 5.37

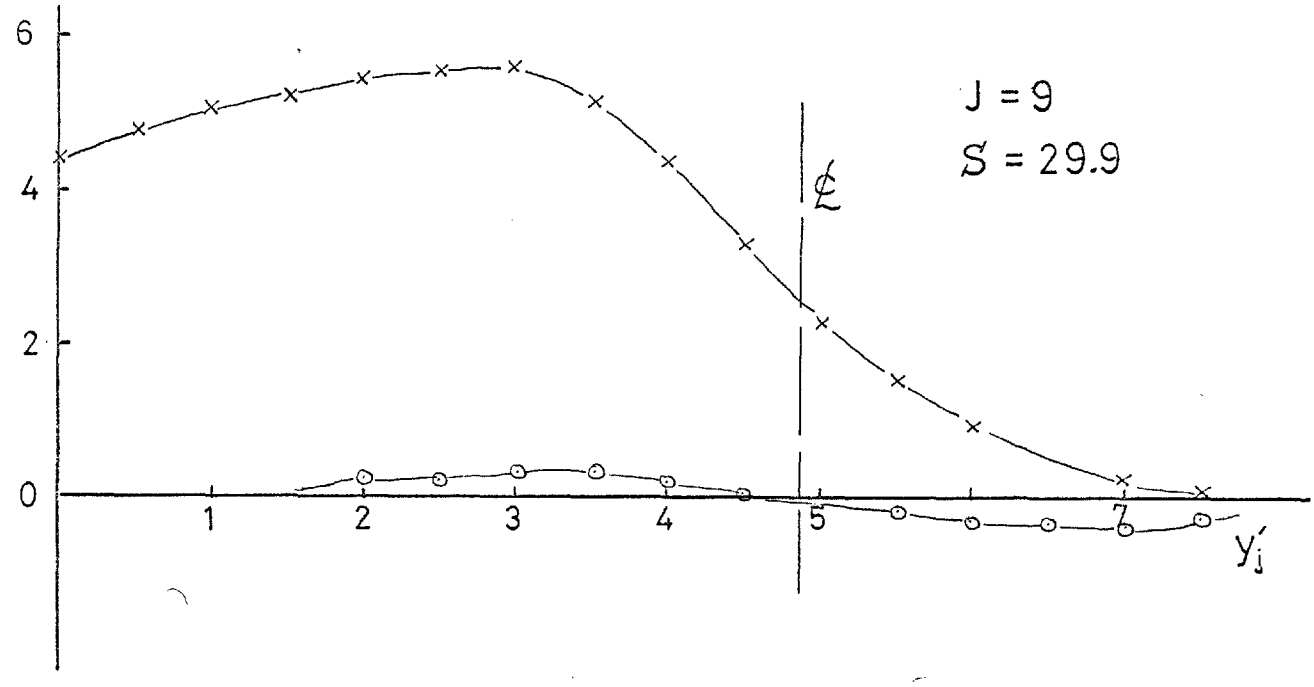
FIG. 5.42 Shear stress balance

J = 23 , S = 61.1



Symbols as in fig. 5.37

FIG. 5.43 Terms in the normal momentum equation.



× $-\kappa U^2/U_\tau^2 \times 10^2$

○ $h\,\partial\left(\overline{v^2}/U_\tau^2\right)/\partial n \times 10^2$

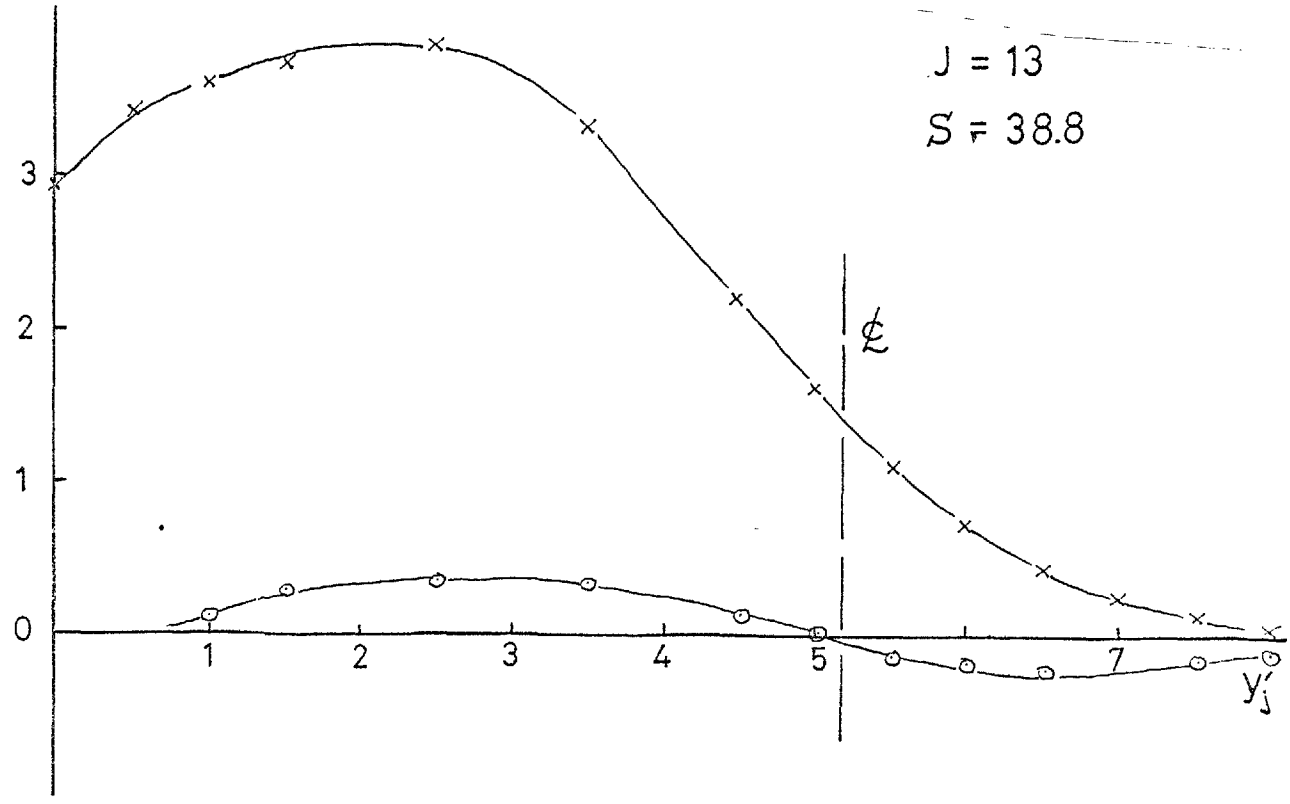
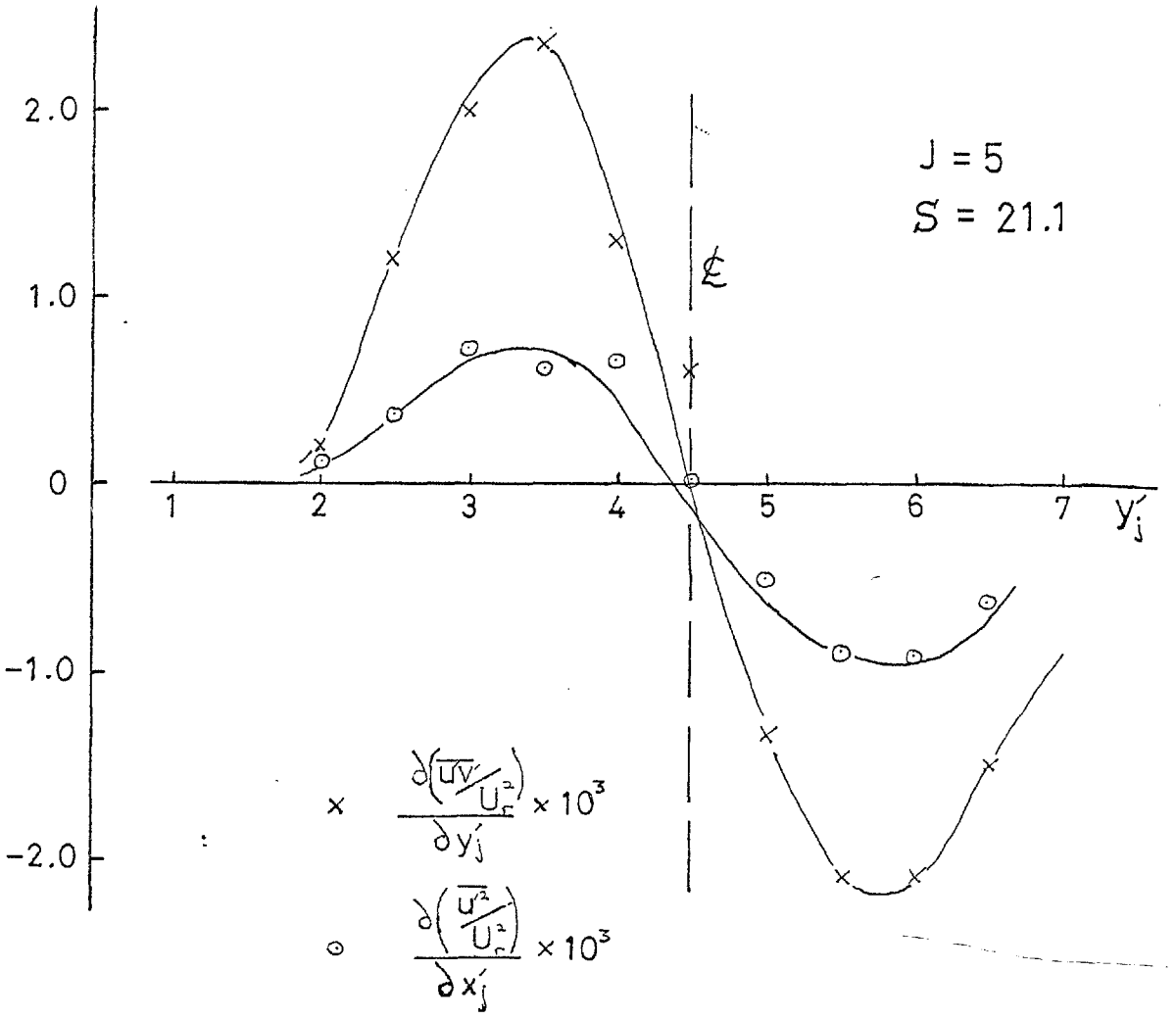


FIG.5.44 Turbulent terms in the streamwise momentum equation.



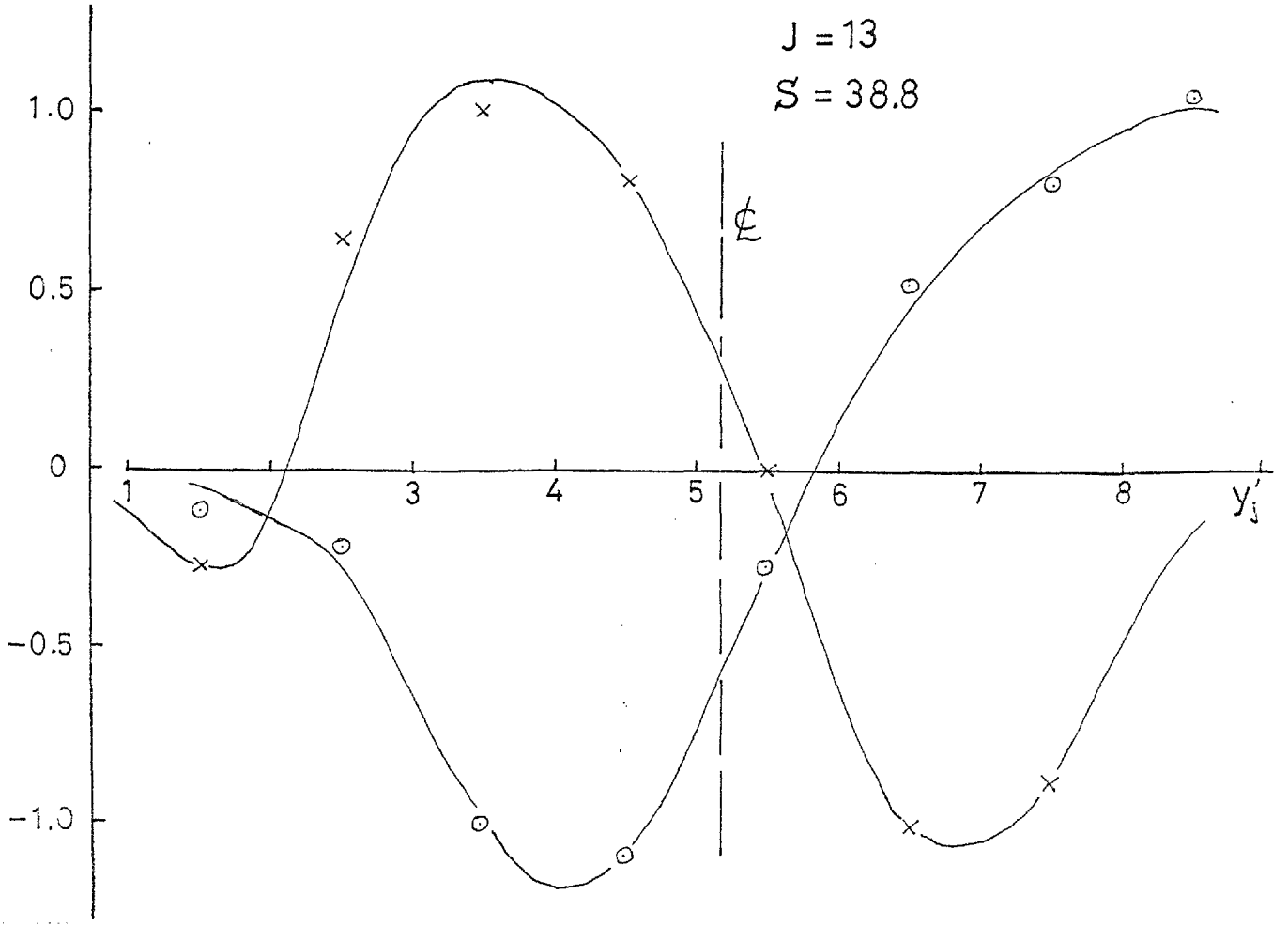
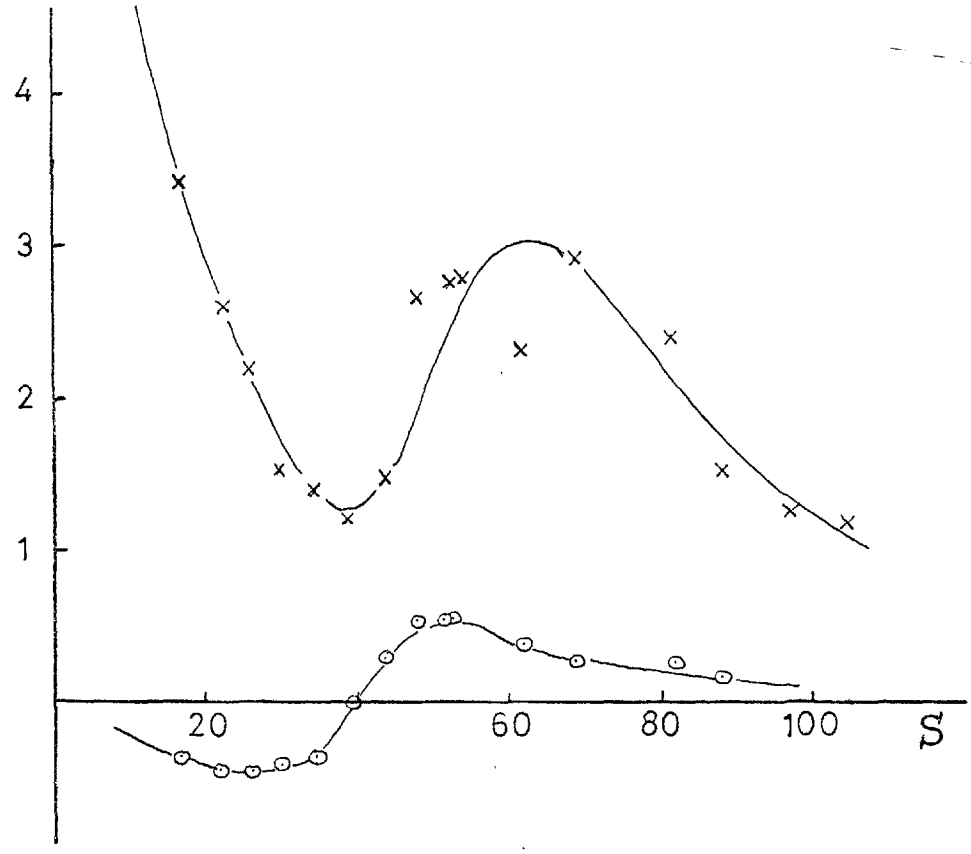


FIG. 5.45 Turbulence terms in the streamwise momentum equation.



× $\frac{\partial\left(\overline{uv}/U_r^2\right)}{\partial n} \times 10^3$ — Maximum value

⊙ $\frac{\partial\left(\overline{u^2}/U_r^2\right)}{\partial s} \times 10^3$ — Round the centre line

} see § 5.2.7

6. FURTHER RESULTS AND DISCUSSION

It was stated in Chapter 1 that the aim of the present experimental program was to gain more understanding of the effects of large curvature on turbulent shear flows, with a view to assisting in the evolution of viable calculation procedures. The preceding chapters have shown that there are certainly some interesting, and unexpected, phenomena and some of these are discussed in the first part of this Chapter.

The second section points out the ways in which the more common calculation methods would fail when applied to the present flow and indicates the probable direction in which the 'calculators' must move before being able to cope with such highly curved flows.

6.1 THE PHENOMENA

6.1.1 The Stabilising Nature of the Curvature ($S \lesssim 35$)

Since the radial gradient of the angular momentum, UR, is positive in this flow we would expect the curvature to have a stabilising effect (Section 1.2): the data amply demonstrate this. Following the initial reduction in the principal mean rate of strain, caused largely by an increase in the rotation term $\frac{\partial V'}{\partial x'}$, the principal turbulent stress decreases quite dramatically (Figure 5.25) and there is a corresponding decrease in the triple velocity products (Figure 5.24). It is interesting that the shear stress is reduced relatively more than the turbulent energy (Figure 5.23); in fact $\overline{uv}$ drops by a factor of 7 and $\overline{q^2}$ by a factor of less than 2. This implies that the large eddies have become less efficient as a means of shear stress production and indicates immediately that the turbulent structure itself is affected by the curvature - hardly a surprising result.

Similarly the data show that the shear stress, $\overline{uv}$, also drops relatively more than $(\overline{u^2} - \overline{v^2})$ and this is particularly evident on the high velocity side of the flow. One result of this behaviour is that the direction of the principal turbulent stress, given by

$$\alpha_2 = \tfrac{1}{2} \tan^{-1} \left(\frac{2\overline{uv}}{\overline{u^2} - \overline{v^2}}\right)$$

moves closer to the local mixing layer direction (Section 5.2.3). Figure 6.1 demonstrates this variation of α_2 along the line $\frac{P}{P_r} = 0.64$, and Figure 6.2 shows that the effect is greater on the high velocity side of the mixing layer. In contrast the direction of the principal rate of strain differs from the plane layer value of about 45^o by less than 5^o over most of the layer at J = 9.

The production, diffusion, dissipation (in the energy equation) and pressure-strain (in the shear stress equation) terms in the transport equations show corresponding decreases (Figures 5.27 and 5.37). However, there is a significant variation in the amount by which each term drops and, to illustrate this, Figure 6.3 shows the relative reduction of each term in the energy equation, deduced from the centre-line balance. The triple-velocity diffusion of turbulent energy is clearly reduced considerably more than either the production or the dissipation and in fact at S ~ 40 (where the advection is very small) the diffusion is extremely small so that the energy dissipation rate is quite close to the rate of production.

Figure 5.30 shows that although the lateral energy diffusion term has dropped to about 0.3 of its plane layer value by S = 40, the very small total diffusion is caused by a large negative increase in the longitudinal diffusion. This may not however be very significant since cartesian x_j', y_j' axes were used so that the individual terms may not be meaningful. In fact the 'longitudinal +

rotation' diffusion term in the shear stress balance is always at least an order of magnitude smaller than the lateral term (at least round the centre-line). In this case the lateral diffusion behaves similarly to the total energy diffusion, but since it is anyway quite small, the pressure-strain term virtually follows the shear stress production.

Such a reduction of the diffusion terms lends further weight to the assertion made above, that the curvature considerably weakens the large eddies. It is these eddies which are mainly responsible for the diffusion away from the centre of the plane mixing layer, so it seems that they become very inefficient in this energy transport process. Further evidence for this is presented below.

6.1.2 The 'Overshoot' on Removal of the Curvature ($S \leq 35$)

The stabilising effect of the curvature was an anticipated result and it was expected that, on removal of the curvature, there would be a slow monotonic return of, say, the turbulent energy to the plane mixing layer value. Figure 5.23 (and many others) demonstrates how wrong this expectation was and the steep rise, and overshoot, of the turbulent energy, shear stress, triple products, and associated transport equation terms appears to be a phenomenon not previously observed in turbulent flow.

There is nothing in the mean flow data that would explain such behaviour and we must look to the changes in turbulence structure for explanations of the phenomenon. Since the large eddy structure plays such an important part in the plane mixing layer it is natural to look at the effects of the curvature on the large eddies. It has already been stated in the previous section that the curvature appears to weaken these eddies substantially. They seem to become much less

efficient both as a means of shear stress production and of turbulent transport. A more direct evidence of the weakening of the large eddies is shown in Figure 6.4, where the 'relative large eddy strength', defined as

$$\{|\mathrm{Max}(\overline{q^2 v})| + |\mathrm{Min}(\overline{q^2 v})|\}/(\overline{q^2}_{max})^{3/2}$$

is plotted against S and is seen to drop by a factor of two.

Figure 6.5 shows the variation of the dissipation length scale, L_ε, and the microscale, λ, (defined in Section 4.4.1) around the centre-line of the curved mixing layer, and it is clear that the curvature affects L_ε far more than λ which, within the experimental accuracy, varies very little from the plane layer value, although there is a hint of a rise around S ~ 50. The dissipation length scale is reduced dramatically and in fact in the region of maximum curvature it is of the same order as the microscale. This is a reflection of the relatively large suppression of shear stress (since $L_\varepsilon = (\overline{uv})^{3/2}/\varepsilon$) and is further evidence of the weakening of the large eddies so that they are less able to transfer vorticity to the smaller scales. Beyond S = 40 there is a sharp rise (and overshoot) in L_ε. It is interesting that this rise, in common with that of the energy (and shear stress) diffusion term, Figure 6.3, does not occur until around S = 40, by which time the curvature has reduced to half its maximum value (Figure 5.36). On the other hand the rise in energy production starts somewhat earlier, as soon as the curvature starts to drop. This 'lag' of the diffusion term is about 12 cms, measured around the centre line, which corresponds to about $2.5/\frac{\partial U}{\partial y}$, or 3.5 δ_p, which is a typical large eddy lifetime. Further discussion of the lag effect is deferred to Section 6.2.2.

All the evidence suggests that the curvature suppresses the

large eddies, so there is very little turbulent diffusion away from the centre of the mixing layer. This results in a comparatively large surplus of energy production which rises sharply and subsequently 'rejuvenates' the larger scales causing a similar sharp rise in the diffusion.

6.1.3 Deductions from the Cross-Layer Balances

Comparisons of the energy and shear stress balances in the curved region (Figures 5.32 - 5.34 and Figures 5.39 - 5.42 respectively) with the corresponding plane layer balances (Figures 4.14 and 4.16) are interesting in a number of ways. Firstly it is clear that although the diffusion terms are considerably reduced, the reduction is somewhat less on the low velocity side than on the high velocity side of the flow. In fact in Figures 5.33 and 5.41 (J = 13) the positive loop in the diffusion at the low velocity edge is actually higher than that on the other side - the reverse of the plane mixing layer case. This implies that turbulent energy is transferred to the low velocity edge at a faster rate than to the high velocity edge.

The large eddies are mainly responsible for the entrainment of free stream fluid and it is interesting to note the effect of the distortion on either side of the mixing layer. It has been shown that the energy diffusion is reduced relatively more on the high velocity edge, so that the entrainment is presumably reduced relatively more on the high than on the low velocity edge of the flow. In contrast to the plane layer case, where the 'thicker' side of the flow (based on the lines $\frac{U}{U_r} = 0.67$ and $\frac{U}{U_r} = 0.90$) corresponds to an entrainment rate which is relatively less than that on the 'thinner' side, we would therefore expect, in the curved flow, the 'thickness' of the high velocity side to be reduced relatively less than that on the low

velocity side: this is precisely the effect noted - see Section 5.1.6.

Secondly, since $\frac{\partial U}{\partial y}$ and $\overline{uv}$ both change sign at the high velocity edge in the region of large curvature (Figures 5.9 and 5.16) there are corresponding 'loops' in the energy and shear stress production terms (e.g. Figures 5.32 and 5.41). This is a major cause of the low levels of production over the rest of the layer.

The other main feature is that the 'out-of-balance' term in the energy balances in the region of high curvature is quite high at the high velocity edge of the mixing layer. It is most unlikely that this is caused by errors in, say, the advection term and the only possible conclusion is that the pressure diffusion is relatively large in this region. Similarly, in the shear stress balances the pressure-strain term changes sign in this region but this could be in error since the pressure diffusion may be significant. It is difficult to say whether, in the energy balance, $\frac{\partial}{\partial s}(\overline{pu})$ or $\frac{\partial}{\partial n}(\overline{pv})$ (or both) is the cause of the increased pressure diffusion and, correspondingly, which term in the shear stress balance might be responsible for the 'apparent' positive pressure strain. Clearly more detailed investigations in this region could be worthwhile.

6.1.4 The Intermittency

In an attempt to learn more about the large scale structure the intermittency, γ, was measured in exactly the same way as described in Section 4.6.2. It was anticipated that the same criteria would work and no attempt was made to vary the threshold levels (k_1 and k_2 defined in Figure 4.17).

A selection of the results, plotted as the variation of γ at particular values of $\frac{P}{P_r}$ across the mixing layer, are compared with the plane layer results in Figure 6.6. It appears that the intermittency profiles get successively broader as the curvature

increases, due to large rises in γ at the high velocity edge. Various reasons for this behaviour were concocted ('centrifugal' arguments for example) before it was realised that the results did not correlate with the flatness factor results. The intermittency estimated from the u-component flatness factor (as described in Section 4.6.2) is shown, for J = 13, in Figure 6.6. Inspection of a few computer plots of the intermittency function showed that the fluctuations of uv (and u and v) in the irrotational regions at the high velocity edge (in the region of large curvature) were far greater than in the corresponding regions of the plane mixing layer. This resulted in apparent bursts of turbulence in the irrotational regions since the threshold levels were set too low, so that the measured intermittency was too high. In the vertical portion of the curved layer these large irrotational fluctuations were not evident, so that the criteria worked quite well. The resulting profiles are similar to the plane layer results, except that γ seems a little low at the low velocity edge: the intermittency estimated from the flatness factors is shown, for J = 27, in Figure 6.6 and is clearly closer to the plane layer profile.

Time did not permit further work on the digital program but undoubtedly other criteria could be devised to cope with this problem of relatively large irrotational fluctuations. Instead, some chart recordings of the crossed-wire anemometer outputs were made direct from the analogue tape recordings and the intermittency was estimated from these in the usual way (Section 4.6.2). The resulting intermittency values were considerably lower at the high velocity edge of the mixing layer. Typical examples, which agree with γ estimated from the flatness factor, are included, for J = 13, in Figure 6.6. Although the accuracy is not expected to be very high

as the sample length was so short (less than ½ second) the results still indicate a slight rise in intermittency at the high velocity edge of the layer. At the low velocity side, where the irrotational regions did not look very different from those in the plane layer, the results are close to those obtained from the digital technique.

Perhaps the most interesting result of the intermittency work is the conclusion that there are large fluctuations in the irrotational regions at the high velocity edge in the region of high curvature. The only obvious explanation for this behaviour, which may correlate with the apparently quite large pressure diffusion in the same region of the flow (see Section 6.1.3) is the presence of internal waves. In atmospheric flows it has been suggested that in very stable conditions, corresponding to large Richardson numbers, the turbulence changes character and is gradually replaced by gravity waves (see for example Lumley & Panofsky[42]). At the high velocity edge of the curved mixing layer typical Richardson numbers are certainly considerably higher than at the centre of the flow, so it is possible that an analogous phenomenon is occurring. Clearly this aspect of the work could usefully be examined in more detail.

6.2 'TOWARDS A CALCULATION METHOD'

6.2.1 The Equivalent Shear Layer Assumption

There are two general features of the results obtained in the curved mixing layer that may be particularly helpful in the formulation of calculation methods for such complex flows. In Section 5.2.3 it was shown that the various possible definitions of shear layer direction all coincide, so that it is not necessary to think in terms of principal stresses and rates of strain. This is a significant

simplification since transport equations for principal stresses would be particularly cumbersome.

It was anticipated that even if the use of principal stresses were necessary, transport equations for the normal stresses, in addition to the Reynolds shear stress, would be required. However, Figure 5.28 shows that the normal stress production term of the energy equation, which is usually neglected in the thin-shear-layer approximation, is quite small, at least along the centre line and particularly when referred to axes aligned with the shear layer direction. Figure 6.7 shows how this term and the term $\overline{u^2}\,\frac{\partial V}{\partial x}$ (again negligible in thin shear layers) compare with the usually dominant production terms in the energy and shear stress equations <u>across</u> the layer at J = 13. Clearly even in this flow, which has comparatively large extra strain rates, these terms are quite small except at the outer (low velocity) edge: this is of course precisely where they become noticeable in the plane mixing layer. Similarly the normal stress gradients in the mean momentum equations are not unduly large - Section 5.27 and Figures 5.43 - 5.45.

These two features might be expected to be evident in other highly curved flows and encourage one to believe first that in calculating flow fields including deflected shear layers the thin-shear layer approximation for the streamwise flow can be used (but retaining longitudinal diffusion terms) provided that co-ordinates aligned with the shear layer direction are used. Secondly, it might only be necessary to use a transport equation for the Reynolds shear stress, although it has been shown that $\frac{\overline{uv}}{q^2}$ changes by a factor of at least three round the centre-line (Section 6.1.1) and $\frac{\overline{v^2}}{u^2}$ is similarly far from constant so that to model the obvious structural changes in the turbulence may, after all, require some normal stress transport

equations, perhaps firmly pruned; the energy equation may suffice. The obvious necessity for a length scale equation (since L/δ_p varies, Figure 6.5b) is discussed in Section 6.2.2.

6.2.2 Probable Requirements of a Calculation Procedure

It was obvious from the start of the present work that most of the present-day calculation methods would be unable to cope with such a distorted shear layer; indeed, as stated in Chapter 1, this constituted a reason for performing the experiment. Any turbulent model which effects closure by use of the effective turbulent viscosity ν_T ($\nu_T = (\overline{q^2})^{\frac{1}{2}} l$ where l is a length scale proportional to that of the energy-containing motions) even if two transport equations are provided - one from which the length scale may be determined in addition to, say, the energy equation - cannot be expected to work where there are appreciable transport effects on the Reynolds stresses. Closures of the exact Reynolds-stress transport equations reduce to formulae of eddy-viscosity type if the transport terms are negligible (as in local-equilibrium flow) or if their ratio to the generation or destruction terms is a function of $\frac{y}{\delta}$ only (as in self-preserving flow), so that where the behaviour of the transport terms is more complicated eddy-viscosity formulae are probably no better than first approximations.

Figure 6.8 shows the variation of mixing length, defined in the usual way as

$$l = (\overline{uv})^{\frac{1}{2}} / \frac{\partial U}{\partial y}$$

around the curved layer centre-line. l drops by more than a factor of two and the eddy-viscosity is reduced by an even greater amount so that clearly no calculation method based on eddy-viscosity concepts could hope to succeed. Bradshaw[18], by drawing an analogy

between curvature and buoyancy effects, was able to include a simple curvature correction in his calculation method, as described in Section 1.2. Curvature effects on the turbulent structure were ignored since only the dissipation length parameter, L , used in the calculation method of Bradshaw et al.[19] was adjusted.

Bradshaw defines a 'flux Richardson number' R_f as the ratio of (minus) the v-component 'curvature production' to the u-component shear production. In our co-ordinates R_f is given by

$$R_f = 2\overline{uv}U\kappa/\overline{uv}\kappa \frac{\partial}{\partial n}\left(\frac{U}{\kappa}\right) = \frac{2S_c}{1 + S_c}$$

where $S_c = U\kappa/\frac{\partial U}{\partial n}$. This is identically equal to $(1 - \frac{A}{\Omega})$ (where A is the rate of strain and Ω the vorticity) which can be thought of as a 'non-thinness' parameter. The variation of R_f and S_c around the centre-line is shown in Figure 6.9a and Figure 6.9b shows R_f plotted against $(1 - L/L_o)$ where L_o is the dissipation length parameter in the plane layer. Following Bradshaw[18] and others we might expect R_f to be linearly related to L/L_o for small curvature,

$$\frac{L}{L_o} = 1 - \beta R_f \quad ,$$

where β is a constant which seems to be about 7 for positive R_f and L is used rather than the mixing length, l, since this is a non-equilibrium flow. The initial trend of Figure 6.9b suggests a β of about $4\frac{1}{2}$ but clearly any linear region which might exist is not very extensive. The two main features of the plot are the 'lag' effect, evidenced by the upward sweep of the curve at high values of R_f, and the 'overshoot' effect: L finally relaxes back to L_o from a <u>higher</u> value, and at <u>zero</u> R_f.

It may be possible to account for some of the lag by an equation for the 'effective' curvature, κ_e, of the form

$$T \frac{\partial \kappa_e}{\partial s} = \kappa_t - \kappa_e$$

where κ_t is the true (local) curvature, so that κ_e approaches κ_t with a 'time constant' T. Exploratory attempts to do this, taking T to be a typical large eddy lifetime, say 3.5 δ_p as in Section 6.1.2, have not been particularly successful. However, it is evident that further efforts in this direction would be useful although it is probable that a somewhat more sophisticated model of the effects of curvature on the large eddy structure would be required.

Probably the only sensible technique to adopt for calculation of complex flows is to use only equations derived from the Navier Stokes equations. Hanjalic & Launder[27] have recently devised a model which, in its general form, provides transport equations for all the Reynolds stresses and also the energy-dissipation rate (which provides an appropriate turbulent length scale), the exact equations being approximated term by term. For the present flow a length scale equation would almost certainly be needed and it may not even be sufficient to use only the length scale $((q^2)^{3/2}/\varepsilon)$ implicit in the dissipation transport equation.

Furthermore, since use of a single Reynolds stress transport equation, usually that for $\overline{uv}$, implies that the shear stress profile sufficiently defines the turbulent field, it may be necessary in the present case to use at least one further Reynolds stress equation - perhaps the energy equation - as indicated in Section 6.2.1.

There are two general points which arise from term-by-term approximation of the exact transport equations. Firstly, most recent workers represent the turbulent energy diffusion by a gradient - diffusion hypothesis. Figure 6.10 shows the variation of eddy diffusivity, defined by

$$\varepsilon_{ed} = \overline{vq^2} / \frac{\partial}{\partial y} (\overline{q^2}) \quad ,$$

and the equivalently defined coefficient, ε_{sd}, for the shear stress diffusion, across the layer at J = 11. Although there is some scatter, particularly for ε_{sd}, it is clear that there is a large difference between the maximum values on the two sides of the mixing layer; in the plane layer the difference (for the energy diffusion case) is only about 20%. (There is always a discontinuity at the centre since $\frac{\partial}{\partial y} (\overline{q^2})$ passes through zero). Simple gradient diffusion hypotheses may not therefore be sufficient in flows affected by large curvature, especially where the turbulent transpott processes are altered as radically as in the present case.

The second point concerns the representation of the pressure-strain term in the shear stress transport equation, $\overline{p(\frac{\partial u}{\partial y} + \frac{\partial v}{\partial x})}$. It can be shown (e.g. Hanjalic & Launder[27]) that this correlation originates from two types of physical process: a mutual interaction between the turbulent components and an interaction between the mean rate of strain and the turbulence. If the mean rates of strain are small only the first part of the pressure-strain term is significant and Rotta[44] suggested that in such a case the pressure strain was directly proportional to the anisotropy, so that

$$\overline{p(\frac{\partial u}{\partial y} + \frac{\partial v}{\partial x})} \; \alpha (\overline{uv} - \frac{1}{3} \overline{q^2}) \quad .$$

In the present flow, this assumption is inadequate, as we would expect, since the mean rates of strain are not small, and the approximated pressure-strain term must include mean velocity gradients. Hanjalic and Launder succeeded in reducing the second part of the term to a second order combination of Reynolds stresses, assuming that any inhomogeneities in the flow do not make a significant contribution;

their procedure might well be adequate for the present case.

Before summarising the basic results of the present work, mention should be made of the work of Wyngaard et al.[43] which, as far as the author is aware, is the only study of a curved mixing layer in the literature. Their mixing layer was generated and developed in a curved duct so that direct comparisons with the present work are difficult. However they have published what they term a 'representative' energy balance (the accuracy is not thought to be particularly good) across the mixing layer and it is clear that the general effects of the flow curvature, which was constant in their case, are similar to those found in the present study.

6.3 CONCLUSIONS AND SUGGESTIONS FOR FURTHER WORK

The most important phenomena which the experimental programme has highlighted can be summarised as follows.

1. Because of the stabilising nature of the curvature, the turbulent energy within the mixing layer is initially considerably reduced (by a factor of about three) as was anticipated.
2. The various terms in the energy and shear stress transport equations do not, however, decrease by similar amounts. In fact the diffusion terms are reduced by an order of magnitude whereas the production only drops by a factor of three, so that the turbulence structure within the mixing layer is radically altered. The basic change seems to be that the large eddies, responsible for most of the diffusive processes, are considerably weakened relative to the smaller-scale structure.

3. As a result of this change in structure there is a surplus of energy production in the region of maximum curvature, so that on removal of the curvature the turbulent energy recovers rapidly, overshooting its original plane layer value. Contrary to our expectations, the curved mixing layer therefore asymptotes to the ordinary plane mixing layer from a state of higher turbulent energy.

Inevitably in a work of this nature, there are many questions still to be answered. Perhaps one of the more interesting lines of investigation, as far as the actual physical phenomena are concerned, would be to examine the large eddy structure more closely. This could involve further work on the intermittency and perhaps correlation measurements. However, the basic aim of the original work (to gain understanding of basic phenomena in order to provide useful data for calculation methods) should be borne in mind. There is probably sufficient data and understanding to enable a wary calculator to attempt to construct a calculation procedure and, from his point of view, only when further data or physical insight are required should further experiments (in this flow) be undertaken. Summarising the more important points discussed in Section 6.2, he should note the following.

1. It will almost certainly be necessary to use only equations derived directly from the Navier-Stokes equations, but provided that the correct co-ordinates are used some of the approximations used for thin-shear-layer calculations may be adequate. The use of principal stresses should not be necessary.
2. Since the turbulence structure is grossly altered, the shear

stress equation alone would probably not be sufficient. At least one length scale equation would be needed in addition.

3. Care would need to be exercised in the representation of the turbulent diffusion terms, since it is these processes which are altered most by the curvature, and of the pressure-strain term, since the mean rates of strain are not small.

Initial efforts could include relatively simple attempts to account for the 'lag' effect described in the previous sections, and a suitable approximation of Hanjalic & Launder's[27] dissipation transport equation to see whether their general method could simulate the behaviour of, say, the dissipation length scale. Undoubtedly the rationale behind their general technique is the only one produced so far that could hope to succeed in such highly curved flows.

Whilst it is beyond the scope of this Thesis to attempt to formulate any calculation method, it is hoped that the data that have been accumulated and the corresponding phenomena investigated and discussed have at least provided a little more of the vital 'groundwork' that is required before any such method, suitable for complex flows, can be evolved.

FIG. 6.1 Direction of principal stress variation with distance along the line $\frac{P}{P_r} = 0.64$ (not the centre-line).

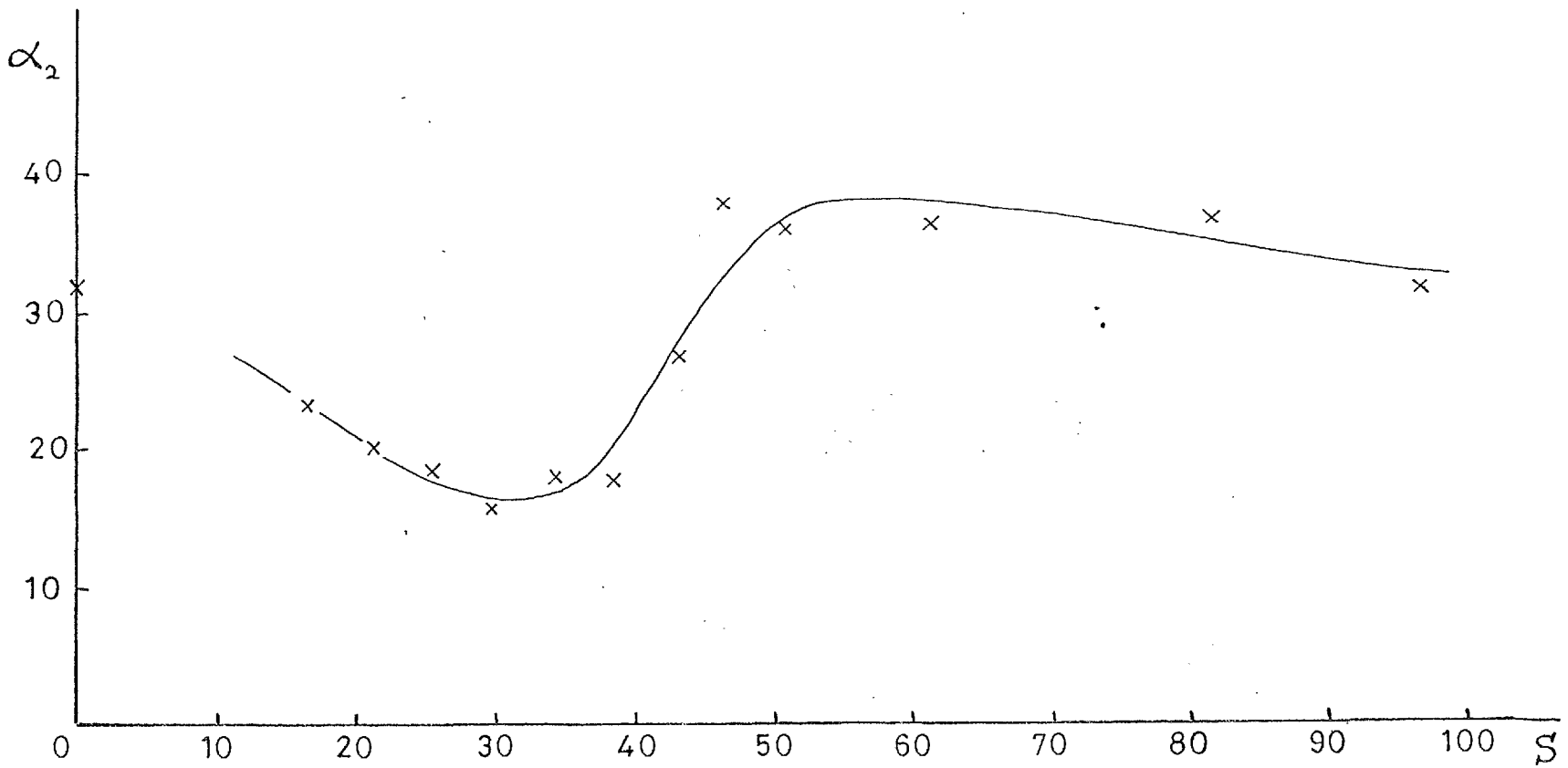


FIG. 6.2 Direction of principal stress along J = 9.

S = 29.9.

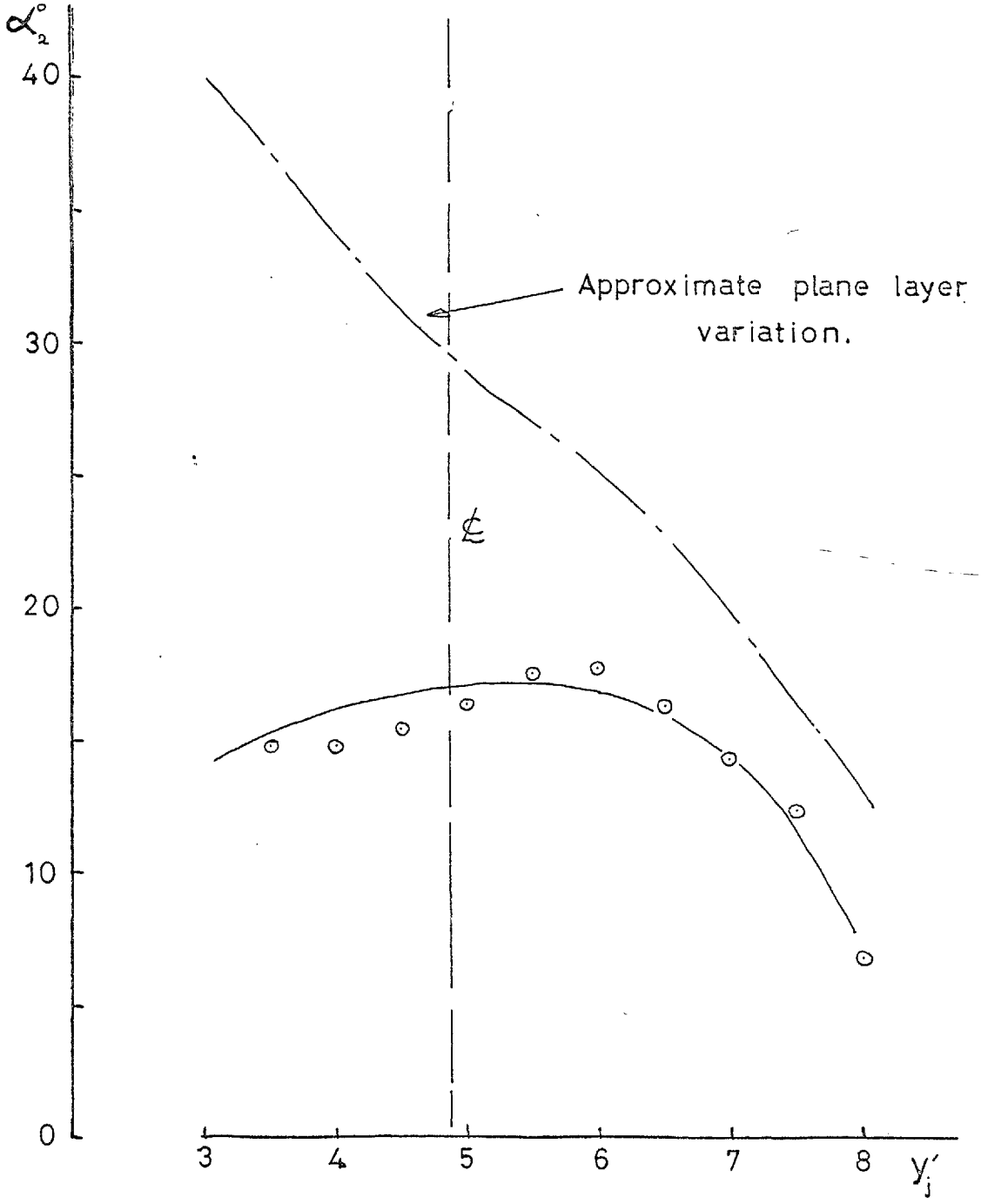


FIG. 6.3 Relative reduction in terms in energy transport equation round the centre-line.

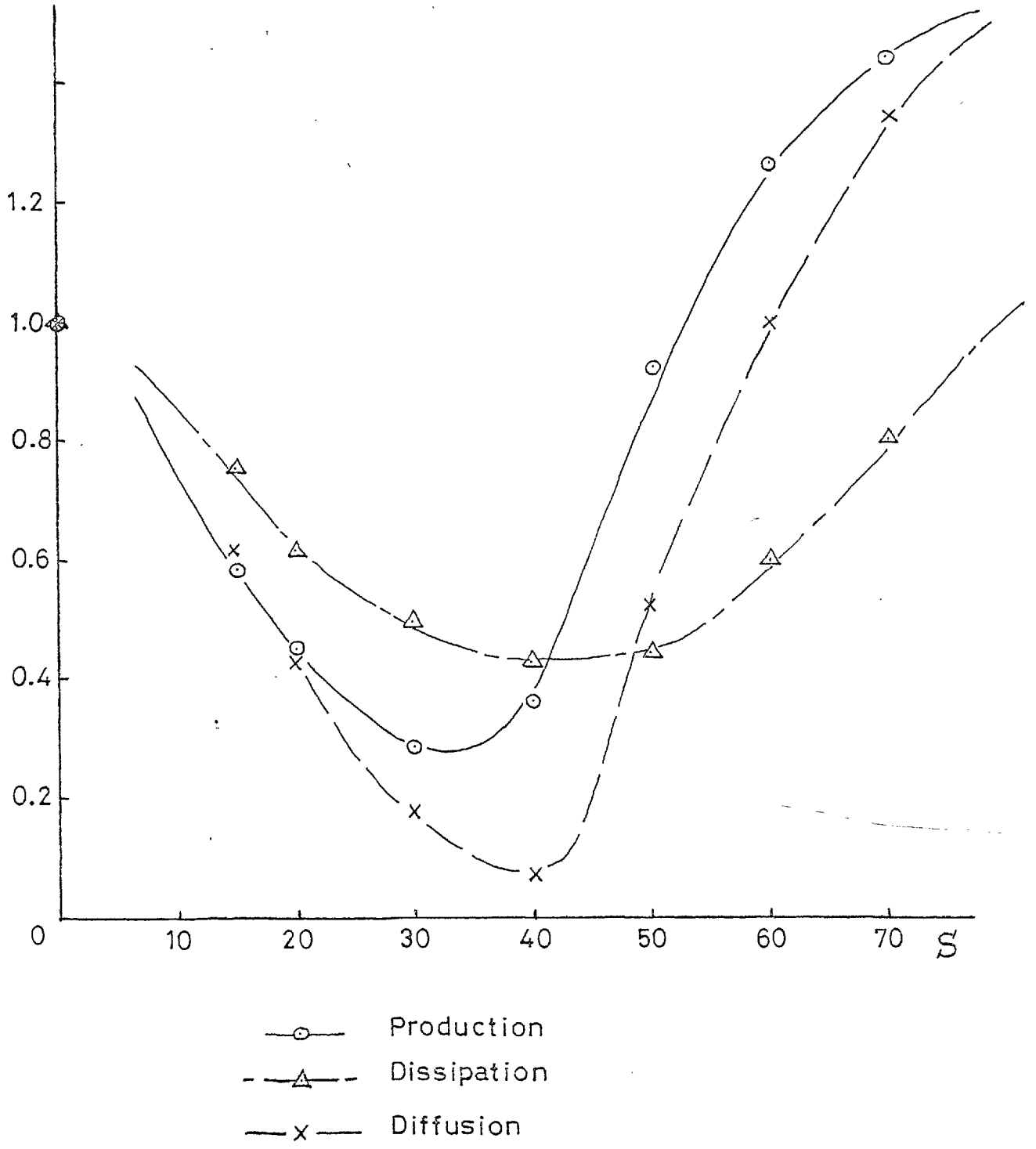


FIG. 6.4 Relative large-eddy strength.

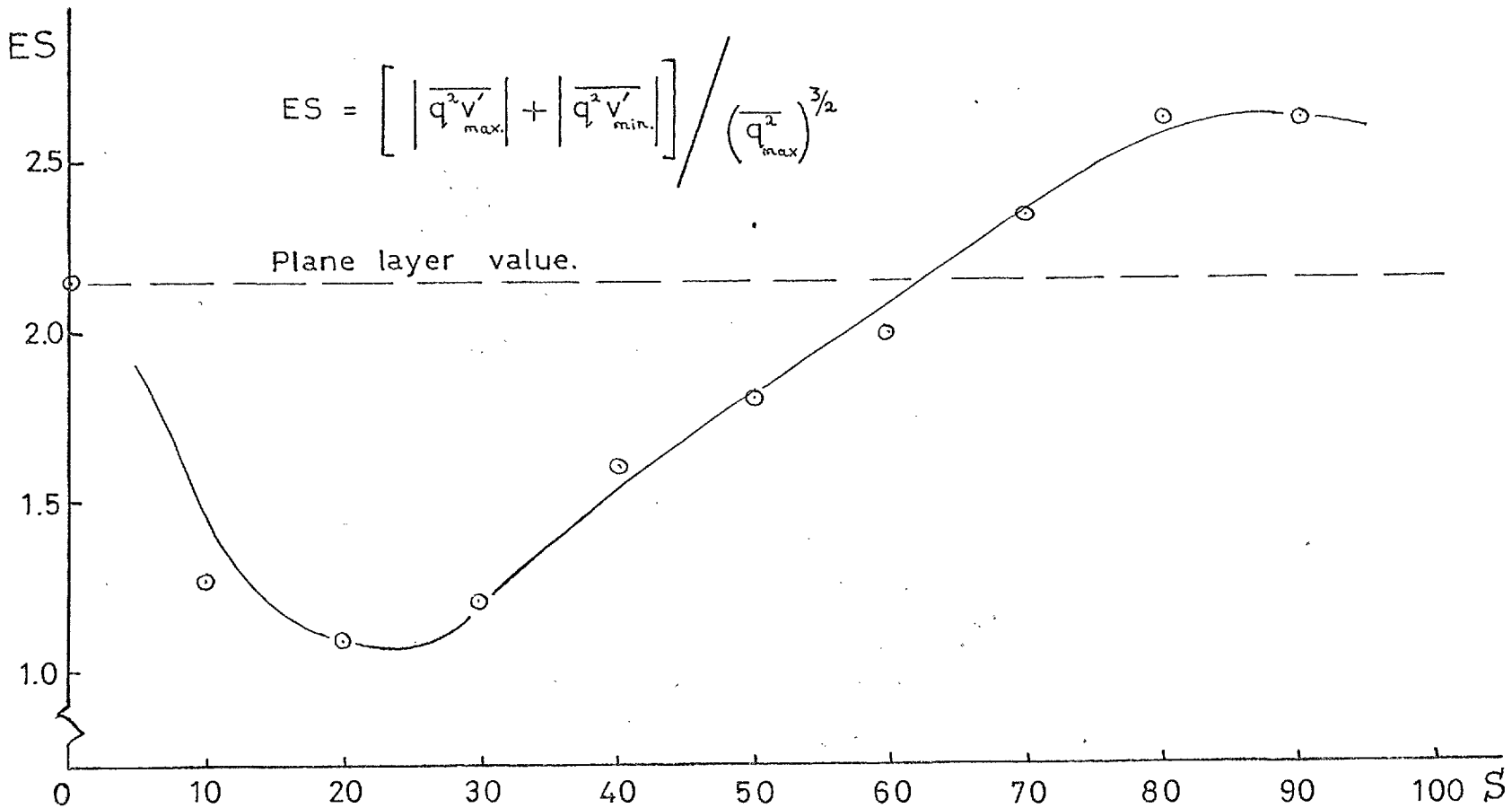


FIG. 6.5a Dissipation length scale & microscale

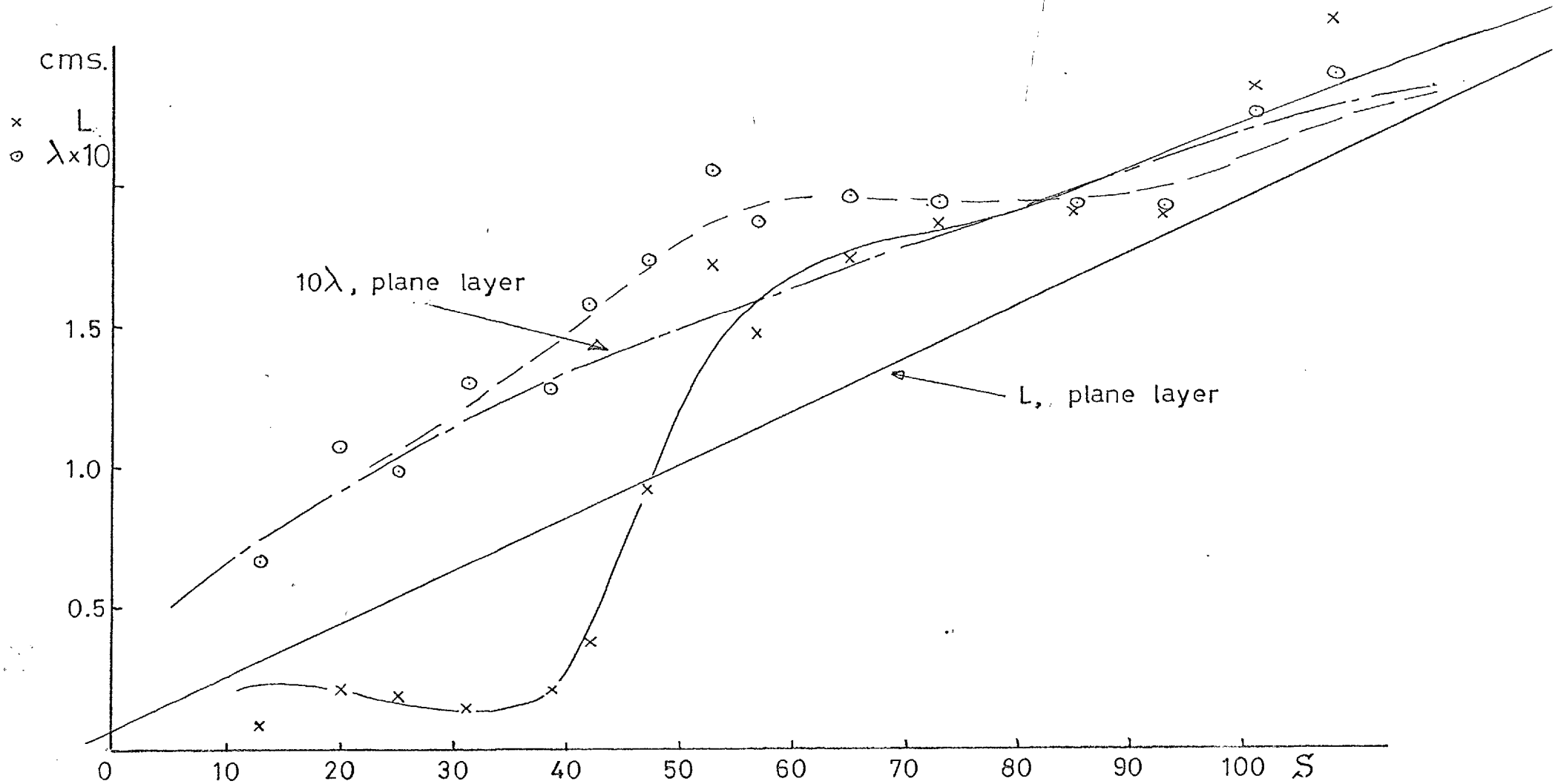


FIG. 6.5b Dissipation length scale & microscale.

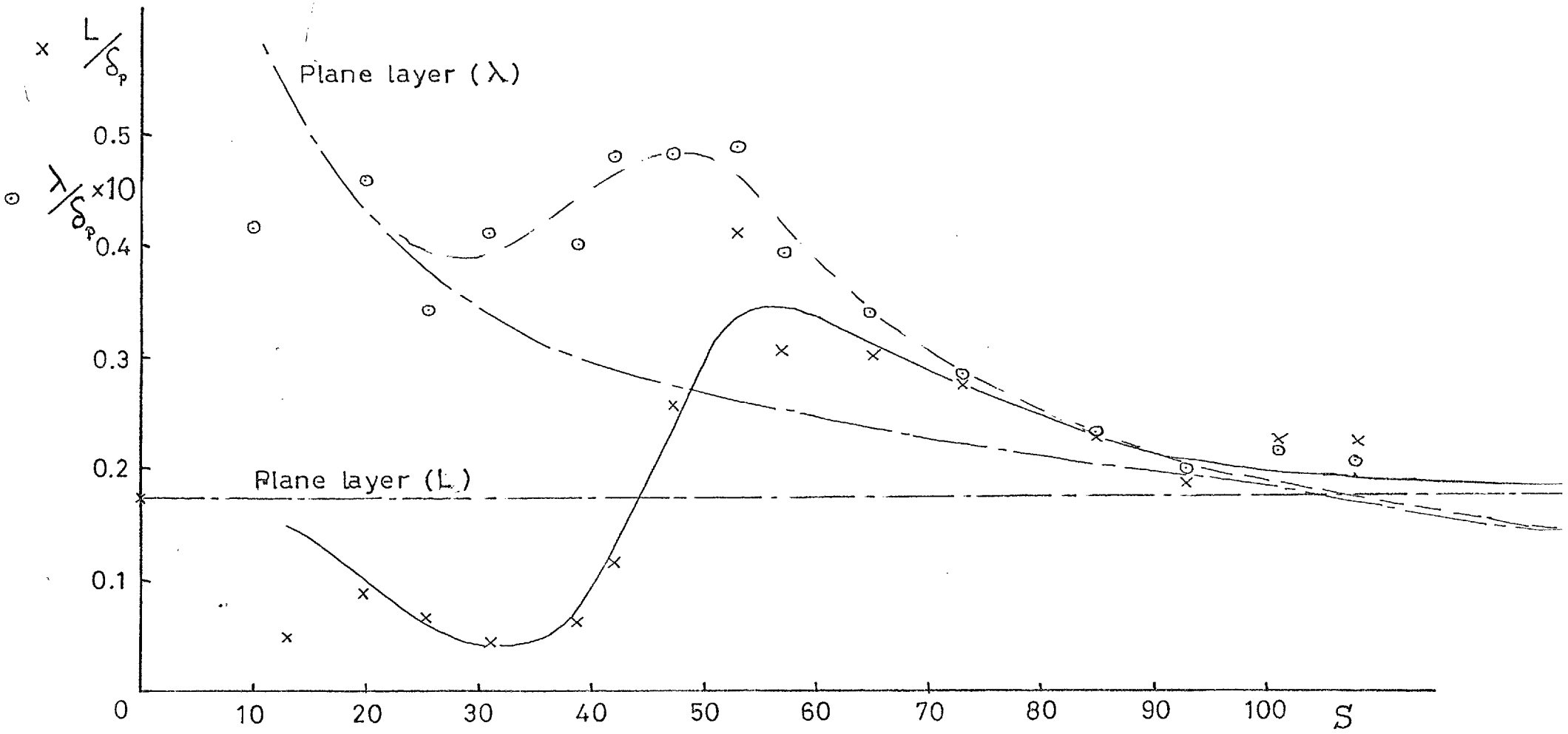
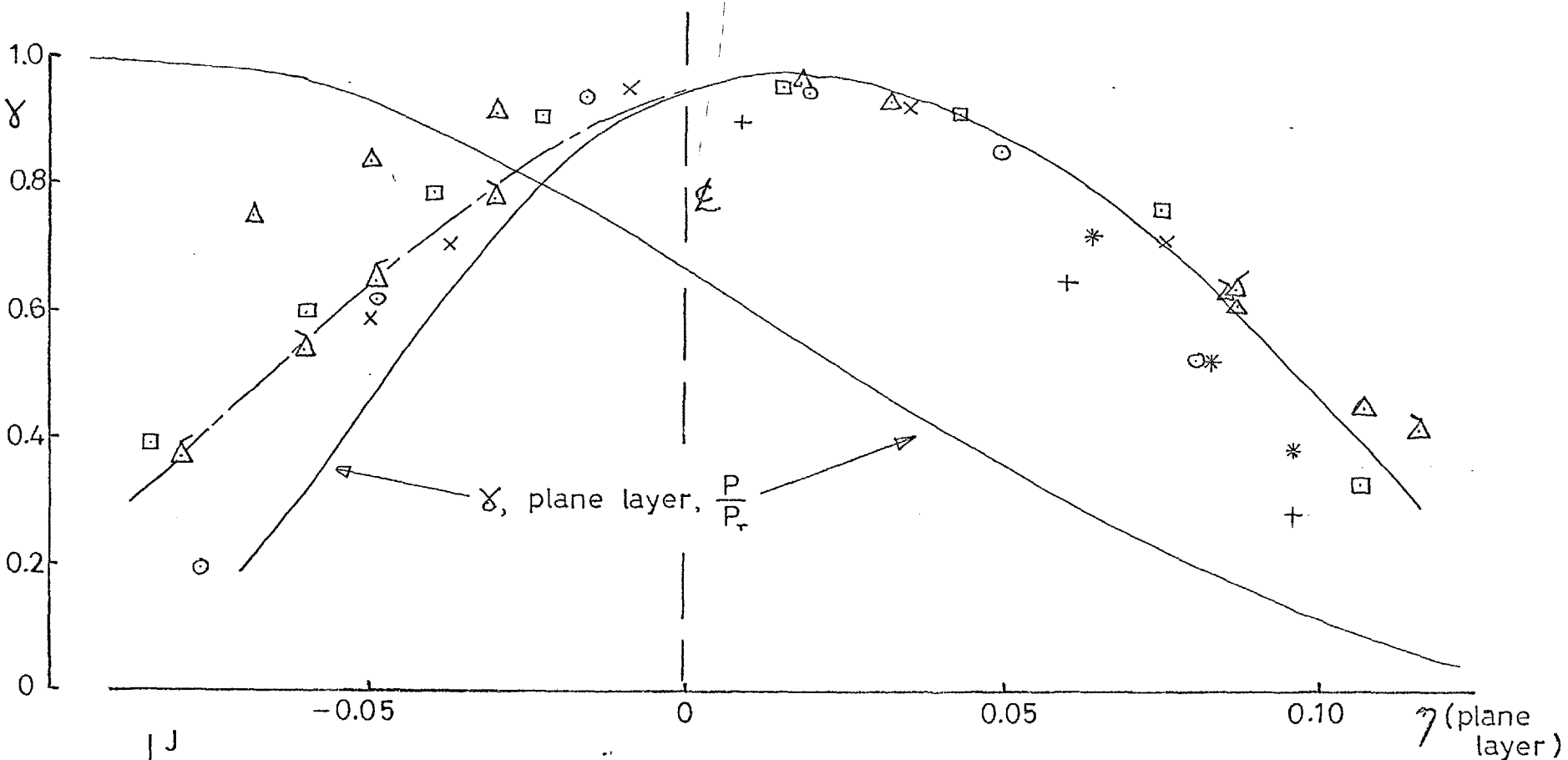


FIG. 6.6 The intermittency



J	
×	5
⊙	9
⊡	11
△	13
+	27

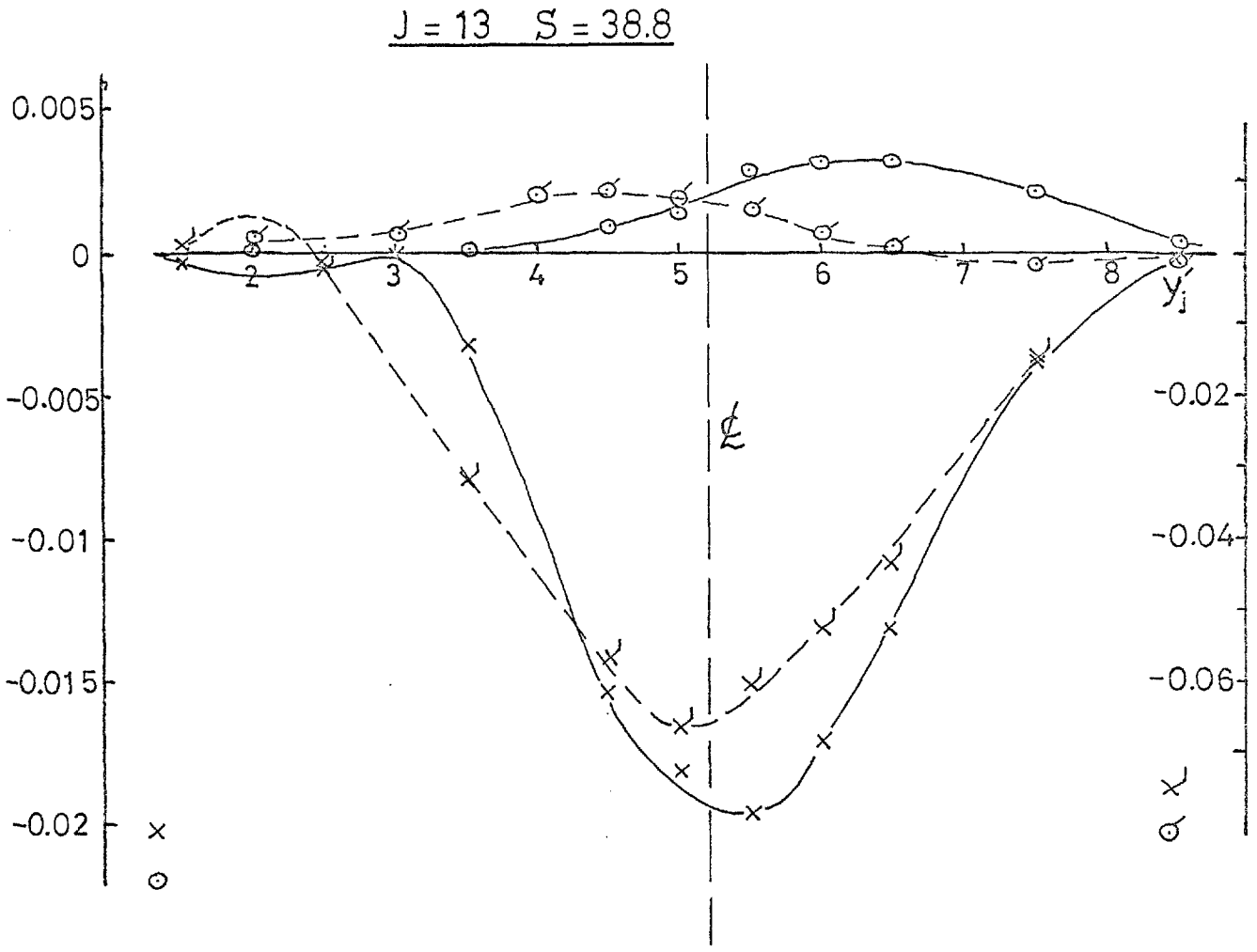
From digital program.

△ } J = 13 From chart recordings.
△ } From flatness factor.

* J = 27 " " " .

Other results omitted for clarity.

FIG. 6.7. Contributions to total production of energy & shear stress.



× $\overline{uv}\left(\frac{\partial U}{\partial y}+\frac{\partial V}{\partial x}\right).S$

⊙ $\left(\overline{u^2}-\overline{v^2}\right)\frac{\partial U}{\partial x}.S$

Energy Production.

× $\overline{v^2}\frac{\partial U}{\partial y}.S$

σ $\overline{u^2}\frac{\partial V}{\partial x}.S$

Shear stress Production.

FIG. 6.8 Variation of mixing length around centre-line.

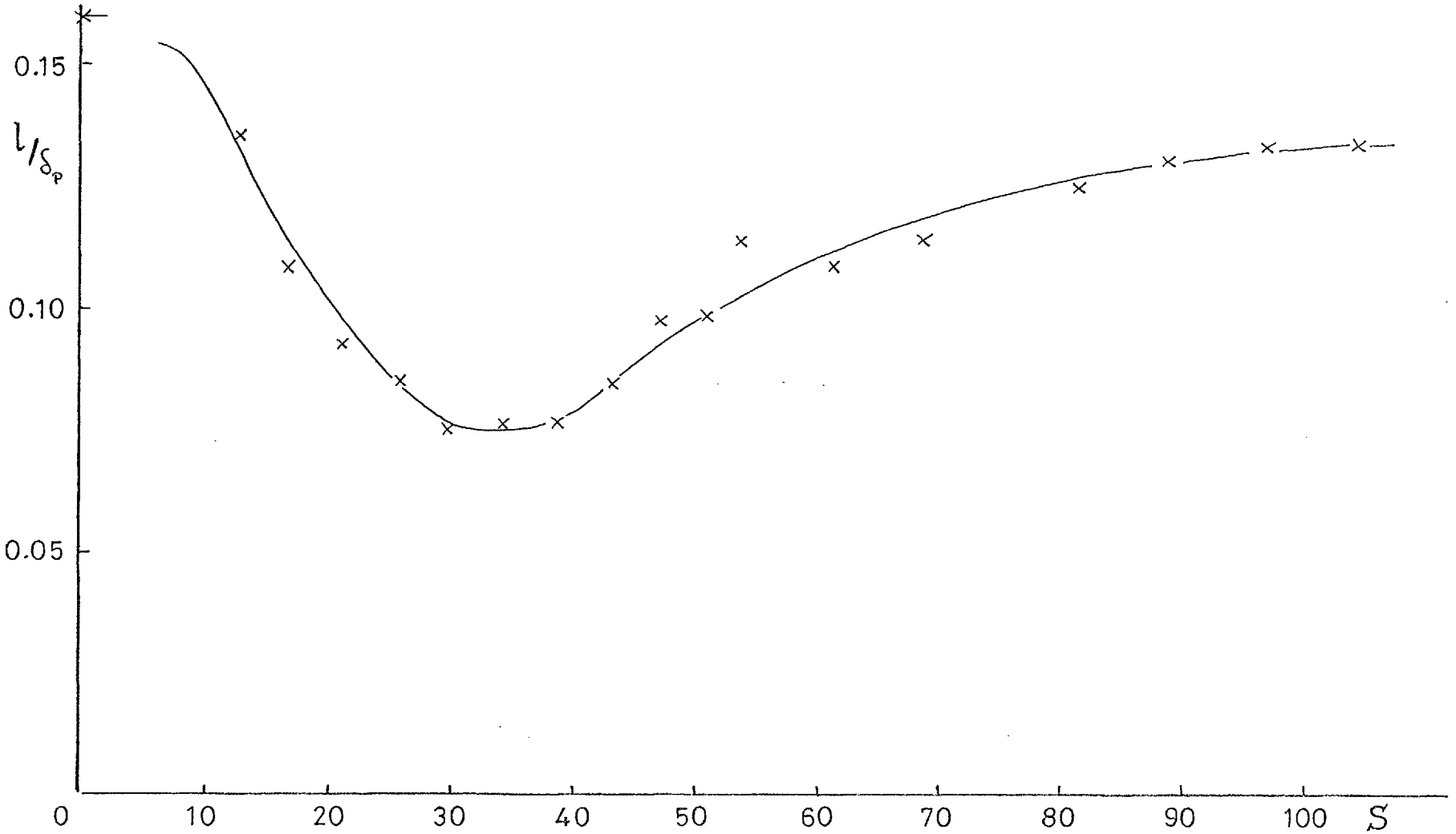
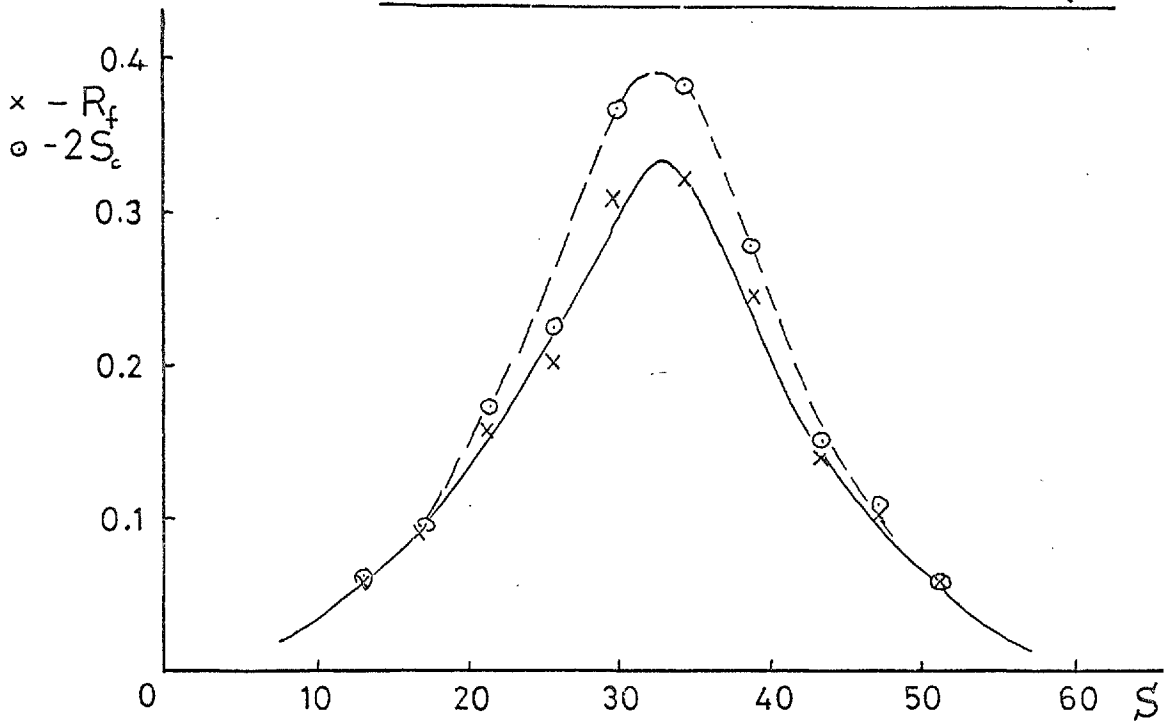


FIG. 6.9. Richardson number and its relation to the dissipation length scale — round the centre-line.



$$R_f = 2S_c/(1+S_c) \equiv 1 - A/\Omega$$

$$2S_c = 2U\kappa \frac{\partial U}{\partial y'}$$

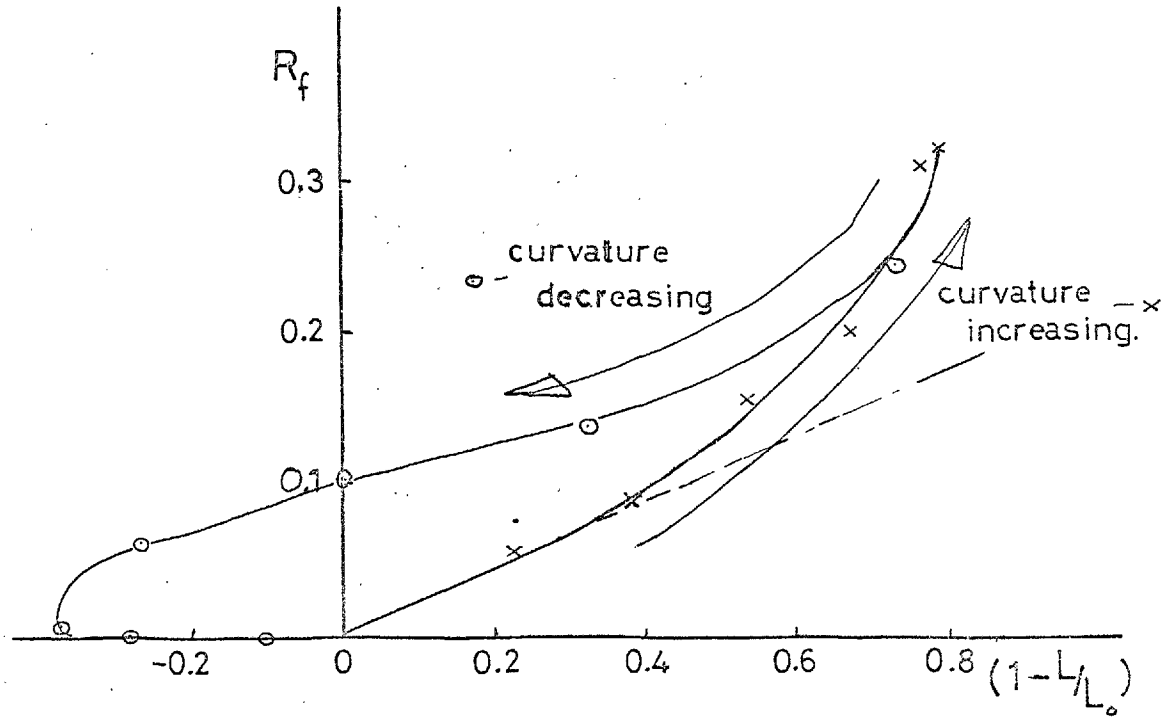
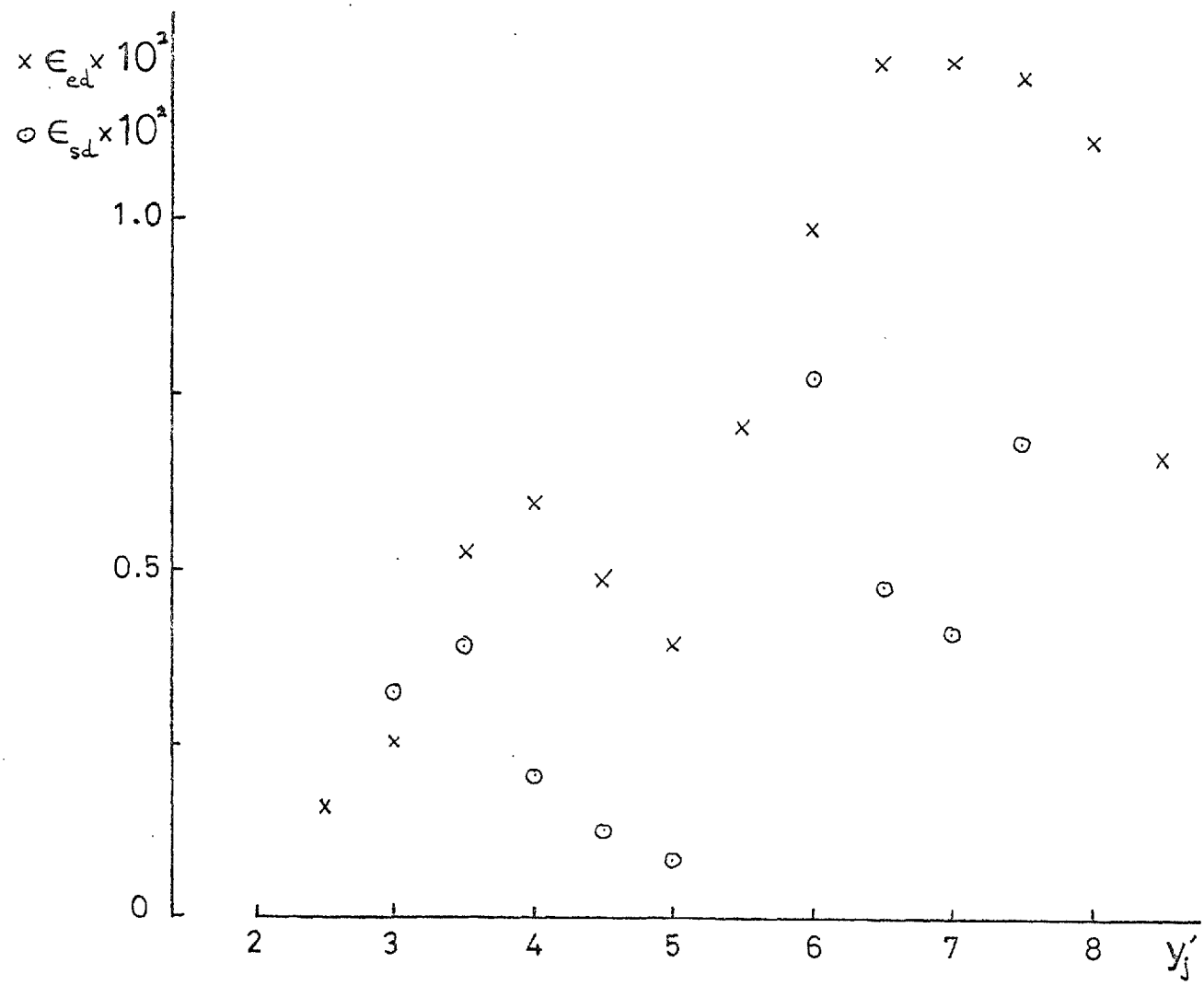


FIG. 6.10 Eddy diffusivity

J = 11

S = 34.3



$$\epsilon_{ed} = \frac{\overline{vq^2}}{\delta_u \cdot \frac{\partial \overline{q^2}}{\partial y'}}$$

$$\epsilon_{sd} = \frac{\overline{uv^2}}{\delta_u \cdot \frac{\partial \overline{uv}}{\partial y'}}$$

REFERENCES

1. LAMB, H. (1932). 'Hydrodynamics', 6th ed. Cambridge University Press, New York.

2. PRANDTL, L. (1961). 'Gesammelte Abhandbungen zur angewandten Mechanik,' Hydro-und Aerodynamik, 2, 570. Springer, Berlin.

3. RAYLEIGH, J.W.S. (1916). 'Dynamics of Revolving Fluids', Proc. Roy Soc. 6A, 148.

4. WATTENDORF, F.L. (1935). 'A Study of the Effect of Curvature on Fully Developed Turbulent Flow', Proc. Roy. Soc. 148A, 565.

5. ESKINAZI, S. & YEH, H. (1956). 'An Investigation of Fully Developed Turbulent Flow in a Curved Channel', J. Aero. Sci. 23,

6. STRATFORD, B.S., JAWOR, Z.M. & GOLESWORTHY, G.I. (1962). 'The Mixing with Ambient Air of a Cold Airstream in a Centrifugal Field', ARC CP.687.

7. SAWYER, R.A. (1963). 'Two-Dimensional Reattaching Jet Flows Including the Effect of Curvature on Entrainment', J. Fluid Mech. 17, 481.

8. GUITTON, D.E. (1964). 'Two-Dimensional Turbulent Wall Jets Over Curved Surfaces', McGill University Report 64-7.

9. PATEL, V.C. (1969). 'The Effects of Curvature on the Turbulent Boundary Layer', ARC R&M No. 3599.

10. SCHMIDBAUER, H. (1966). 'Turbulent Friction Layers Along Convex Surfaces', NACA TM791 (Trans. of Luftfahrtforschung 13, 160).

11. SCHUBAUER, G.B. & KLEBANOFF, P.S. (1951). 'Investigation of Separation of the Turbulent Boundary Layer', NACA Rep. No. 1030.

12. SO, R.M. & MELLOR, G.L. (1972). 'An Experimental Investigation of Turbulent Boundary Layers Along Curved Surfaces', NASA CR-1940.

13. PATEL, V.C. (1968). 'Measurement of Secondary Flow in Boundary Layers of a 180° Channel', ARC CP 1043.

14. JOHNSTON, J.P. (1970). 'The Effects of Rotation on Boundary Layers in Turbomachine Rotors', Dept. of Mech. Eng. Stanford Univ. Report MD-24.

15. HALLEEN, R.M. & JOHNSTON, J.P. (1967). 'The Influence of Rotation on Flow in a Long Rectangular Channel - An Experimental Study', Dept. of Mech. Eng. Stanford Univ. Report MD-18.

16. HUGHES, D.W. (1972). 'Swirling Flow in an Annular Diffuser with a Rotating Centre Body', Ph.D. Thesis, Cambridge Univ.

17. THOMPSON, B.G.J. (1965). 'The Calculation of Shape Factor Development in Compressible Turbulent Boundary Layers with and without Transpiration', Agardograph 97, 159.

18. BRADSHAW, P. (1969). 'The Analogy Between Streamline Curvature and Buoyancy in Turbulent Shear Flow', J. Fluid Mech. 36, 171.

19. BRADSHAW, P., FERRISS, D.H. & ATWELL, N.P. (1967). 'Calculation of Boundary-Layer Development Using the Turbulent Energy Equation', J. Fluid Mech. 28, 593.

20. WONG, F.W.F. (1970). M.Sc. Thesis, Department of Aeronautics, Imperial College.

21. BRADBURY, L.J.S. & CASTRO, I.P. (1972). 'Some Comments on Heat Transfer Laws for Fine Wires', J. Fluid Mech. 51, 487.

22. COLLIS, D.C. & WILLIAMS, M.J. (1959). 'Two-Dimensional Convection from Heated Wires at Low Reynolds Numbers', J. Fluid Mech. 6, 357.

23. RODI, W. (1972). 'A New Method of Analysing Hot-Wire Signals in Highly Turbulent Flow and its Evaluation in a Round Jet', Imperial College Mech. Eng. Report ET/EN/B/10.

24. CHAMPAGNE, F.H., SLEICHER, C.A. & WEHRMANN, O.H. (1967). 'Turbulence

Measurements with Inclined Hot Wires', J. Fluid Mech. 28, 153.

25. BRADSHAW, P. (1972). The Imperial College Aero. Dept. Digital Magtape Data Logging System, Aero Dept. TN-72-101.

26. BRANDT, A. & BRADSHAW, P. (1972). 'Apparatus and Programs for Digital Analysis of Fluctuating Quantities in Turbulent Flow', Imperial College Aero. Dept. Report 72-11.

27. HANJALIC, K. & LAUNDER, B.E. (1972). 'A Reynolds Stress Model of Turbulence and its Application to Thin Shear Flows', J. Fluid Mech. 52, 609.

28. VAN DYKE, M. (1964). 'Perturbation Methods in Fluid Mechanics', Academic Press.

29. TOWNSEND, A.A. (1956). 'The Structure of Turbulent Shear Flow', Cambridge Univ. Press.

30. WYGNANSKI, I. & FIEDLER, H.E. (1970). 'The Two-Dimensional Mixing Region', J. Fluid Mech. 41, 327.

31. BRADSHAW, P. & FERRISS, D.H. (1965). 'The Spectral Energy Balance in a Turbulent Mixing Layer', ARC CP 950.

32. BRADSHAW, P., FERRISS, D.H. & JOHNSON, R.F. (1964). 'Turbulence in the Noise-Producing Region of a Circular Jet', J. Fluid Mech. 19, 591.

33. RODI, W. (1972). Private Communication.

34. BRADSHAW, P. (1967). 'The Effect of Initial Conditions on the Development of a Free Shear Layer', J. Fluid Mech. 26, 225.

35. BATCHELOR, G.K. (1956). 'The Theory of Homogeneous Turbulence', Cambridge Univ. Press.

36. GRANT, H.L., STEWART, R.W. & MOILLIET, A. (1962). 'Turbulence Spectra from a Tidal Channel', J. Fluid Mech. 12, 241.

37. WYNGAARD, J.C. (1968). 'Measurement of Small-Scale Turbulence Structure with Hot Wires', J. Sci. Inst. 1, 1105.

38. WYGNANSKI, I. & FIEDLER, H.E. (1969). 'Some Measurements in the Self-Preserving Jet', J. Fluid Mech. 38, 577.

39. KOVASZNAY, L.G.S., KIBENS, V. & BLACKWELDER, R.F. (1970). 'Large Scale Motion in the Intermittent Region of a Turbulent Boundary Layer', J. Fluid Mech. 41, 283.

40. THOMAS, R. (1973). 'Conditional Sampling and Other Measurements in a Plane Turbulent Wake', J. Fluid Mech. 57, 549.

41. STEWART, R.W. (1956). 'Irrotational Motion Associated with Free Turbulent Flows', J. Fluid Mech. 1, 593.

42. LUMLEY, J.L. & PANOFSKY, H.A. (1964). 'The Structure of Atmospheric Turbulence', Monographs and Texts in Phys. and Astronomy XII, Wiley, New York.

43. WYNGAARD, J.C., TENNEKES, H., LUMLEY, J.L. & MARGOLIS, D.P. (1968). 'Structure of Turbulence in a Curved Mixing Layer', Phys. Fluids 11, 1251.

44. ROTTA, J. (1962). 'Turbulent Boundary Layers in Incompressible Flow'. In Progress in Aeronautical Sciences, 2, 1-121, Pergamon, Oxford.

45. CASTRO, I.P. (1970). 'The Pulsed Wire Anemometer - An Analysis to Determine the Errors Caused by the Probe Finite Yaw Response', Imperial College Aero. Report No. 70-07

46. FRENKIEL, F.N. (1967). 'Higher Order Correlations in a Turbulent Fluid', Phys. Fluids 10, 507.

47. BRADBURY, L.J.S. (1969). 'A Pulsed-Wire Technique for Velocity Measurements in Highly Turbulent Flows', NPL Aero. Report 1284.

48. MANDEL, J. (1964). 'The Statistical Analysis of Experimental Data', Wiley, New York.

49. BRADSHAW, P. (1967). 'The Turbulent Structure of Equilibrium Boundary Layers', J. Fluid Mech. 29, 625.

APPENDIX I

This Appendix is a copy of a paper published in Journal of Fluid Mechanics (1971), 49, Pt. 4, 657.

The work falls into two distinct sections: a theoretical treatment of the behaviour of the pulsed-wire probe and a description of a range of calibration experiments. The theoretical analysis was undertaken wholly by the first author, all the experimental work was done jointly, and the theoretical treatment of the possible sources of error in turbulent flow measurements, described in Chapter 5, and the Appendix of the paper, was the work of the second (present) author. This latter work is based on that described in Appendix IV of the present Thesis.

APPENDIX I

A pulsed-wire technique for velocity measurements in highly turbulent flows

By L. J. S. BRADBURY† AND I. P. CASTRO

Aeronautics Department, Imperial College

(Received 8 January 1969 and in revised form 24 September 1970)

The velocity measuring technique described in this paper consists of measuring the time of flight of a tracer of heated air from an electrically pulsed wire to one of two sensor wires which are operated as resistance thermometers. These sensor wires are at right angles to the pulsed wire and are placed one on either side of the pulsed wire. The instrument may be used in highly turbulent flows including regions in which flow reversals occur. The paper discusses the theoretical behaviour of the probe and the results of some calibration experiments.

1. Introduction

In a highly turbulent flow, instruments such as hot-wire anemometers and pitot-static tubes used for velocity measurements are subject to serious errors. This is due not only to the non-linear response of these instruments to fluctuations in the magnitude of the velocity vector, but also to their ambiguous response to variations in the flow direction. This paper describes a measuring technique which largely avoids these difficulties, and which can be used in highly turbulent flows including flow regions in which reversals of the flow direction occur. The technique is similar to that described by Bauer (1965) in which two fine platinum wires of 2·5 μ diameter mounted on hot-wire probes were used. These were placed parallel to one another with one wire downstream of the other. A tracer of heated air was introduced into the flow by pulsing the upstream wire with a voltage pulse of a few microseconds duration and the time taken for this tracer to reach the downstream wire was measured using the downstream wire as a simple resistance thermometer. This parallel-wire arrangement is very sensitive to flow direction and, in a turbulent flow, many of the heat pulses would miss the resistance wire altogether. However, by the simple expedient of placing the sensor wire at right angles to the pulsed wire, it is possible to produce an instrument with a wide yaw response which can be used in a highly turbulent flow. The aim of the present paper is to discuss the behaviour of such an instrument, and to draw more attention to the technique, which seems to have considerable potential for making measurements in highly turbulent flows under precisely the conditions where the hot-wire anemometer even in its linearized form is suffering seriously from errors due to its ambiguous yaw response.

Early work on this technique has already been discussed by Bradbury (1969)

† Present address: Mechanical Engineering Department, University of Surrey.

and some similar work has also been carried out by Tombach (1969). However, there are some important differences between Tombach's work and the present investigations, which greatly influence the usefulness of the technique. These differences will be discussed in § 5 after the details of the present work have been described.

2. Theoretical considerations

2.1. *The ideal response of a crossed-wire probe*

The probe under consideration consists of three wires (figure 1). The central wire is the pulsed wire and on either side of this are the sensor wires with their axes perpendicular to the pulsed-wire axis. Before considering the real behaviour of

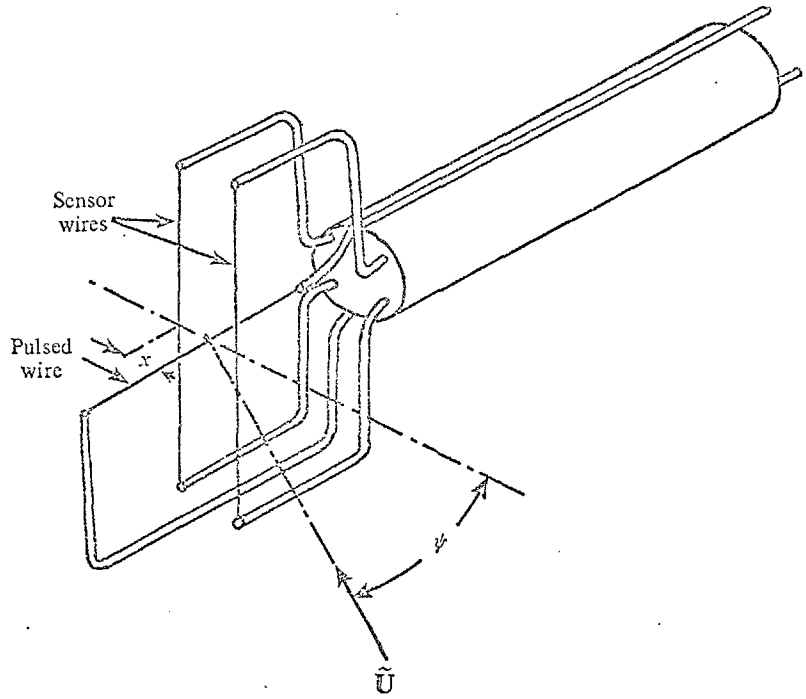


FIGURE 1. Sketch of a pulsed-wire probe.

such a probe, it is useful to describe the ideal response that would give unambiguous measurements of velocity. In an ideal probe, the pulsed-wire temperature would jump instantaneously from ambient temperature to some much higher temperature and be held there while the resultant tracer of heated air was convected away with the instantaneous velocity of the stream passing the probe. If both thermal and viscous diffusion effects were small, the time taken for the front of the tracer to reach a sensor wire would be $t = x/(|\mathbf{U}| \cos \psi)$ where x is the distance between the pulsed and sensor wires and ψ is the angle between the direction normal to the plane of the probe and the instantaneous velocity vector $\tilde{\mathbf{U}}$ (see figure 1). The plane of the probe is defined here as the plane parallel to all three wires in the probe. Thus, from the time of flight, the magnitude of the

velocity vector resolved at right angles to the plane of the probe could be obtained. The use of two sensor wires, one on either side of the pulsed wire, would ensure that the direction of the flow at that instant could be unambiguously determined; the only restriction would be in the length l of the wires since $\tan^{-1}(l/2x)$ gives the largest angular deviation of the flow direction that could be sensed by the probe. In the probes to be described later on, l/x was about 5 giving a maximum flow deflexion angle of about 70°. If a sufficient number of these time of flight measurements were made at a particular station then the technique would give both the mean and fluctuating components of velocity in the direction at right angles to the plane of the probe, and velocities in any direction could be studied simply by aligning the probe in that direction. The only other restriction on the probe would be that it would not properly respond to turbulent fluctuations which had a length scale appreciably less than the probe dimensions.

With this brief description of an ideal probe response, we can now look at the real response in some detail. Bauer has considered some aspects of the behaviour of the pulsed-wire technique but some further elaboration is needed because the behaviour of the crossed-wire probe is different from the parallel-wire probe in a number of important ways. The analysis is restricted to a flow which is steady during the time of flight of the heat tracer, and the object of the analysis is to highlight the influence of the various parameters that arise in the problem. It is worth pointing out that the results of the analysis are not necessary for the practical application of the technique in much the same way as detailed knowledge of the heat-transfer laws for fine wires is not necessary in the more usual application of constant-temperature hot-wire anemometers. However, in order to exploit fully measurement techniques of this sort, it is clearly important to study the influence of the various parameters involved.

In § 2.2 the temperature variation with time of the pulsed wire is considered. Then, in § 2.3 the temperature field produced downstream of the pulsed wire and the response of the sensor wire to it are considered for the case in which thermal diffusion is neglected. The important modification to these results from thermal diffusion is then examined in § 2.4. Attention is then given in § 3 to the practical problems of applying the technique and results of calibration experiments are discussed in § 4. Finally, in §§ 5 and 6, the results of measurements in highly turbulent flows are described.

2.2. *The temperature variation of the pulsed wire*

The suffix notation used in the following discussion is as follows. The suffices f and w refer to properties of the flow and wire respectively. However, in the case of the wires, if the properties refer specifically to either the pulsed or sensor wire, the suffix w will be replaced by either p or s as the case may be.

The temperature variation of both the pulsed wire and sensor wires can be studied from the equation

$$\underbrace{\frac{V^2}{r}}_{\text{Electrical heating}} = \underbrace{\rho_w c_w \frac{\pi d^2 l}{4}\frac{d\theta_w}{dt}}_{\text{Heat stored in wire}} + \underbrace{\pi k_f l N_w(\theta_w - \theta_f)}_{\text{Heat convection by stream}}, \qquad (1)$$

where θ_w, θ_f are the wire and flow temperatures respectively; d is the wire diameter and l its length, ρ_w and c_w are the density and specific heat of the wire material; r is the wire resistance, V the voltage across the wire, N_w the Nusselt number and k_f the thermal conductivity of the gas flowing past the wire. The appropriate temperature at which this thermal conductivity is evaluated depends on the particular heat-transfer law that is chosen. Because of the variety of such laws that are available, some experimental investigations into heat-transfer laws were carried out. These are reported in a separate paper (Bradbury & Castro 1971), but the conclusion arising from this work is that it is sufficient for the calculation of convective time constants – which is, in fact, the only use made of the law in the present paper – to use a simple law in which fluid properties are evaluated at ambient temperature. The actual form of law used is the expression proposed by Collis & Williams (1959) without any wire temperature loading term included. Under these circumstances and at the Reynolds numbers encountered in the present experiments, their relationship is

$$N_w = 0{\cdot}24 + 0{\cdot}56R^{0{\cdot}45}, \tag{2}$$

where $R = Ud/\nu$ is the wire Reynolds number. All experimental heat-transfer laws are derived from steady-state heat-transfer measurements, but it is usually assumed that they will apply to unsteady flows provided $\tau U/d \gg 1$ where τ is the characteristic time for the unsteady flow. This condition is always fulfilled in the present experiments.

In the experiments to be described later, the pulsed wire was subjected to an essentially constant voltage pulse with a duration of only several microseconds which is much less than the time constant for appreciable convection

$$T_p = \rho_p c_p d^2/(4k_f N_p).$$

Under these circumstances, heat convection can be ignored and the temperature rise of the wire from equation (1) is given by

$$(V/l)^2 \hat{t} = \rho_p c_p \sigma_p \theta_p (1 + \tfrac{1}{2}\alpha\theta_p + \tfrac{1}{3}\beta\theta_p^2), \tag{3}$$

where α and β are the first and second temperature coefficients of resistance respectively which it is necessary to include because of the very high temperatures reached. σ_p is the wire resistivity at some reference temperature which, for convenience, we may take as ambient temperature rather than 0 °C. All other temperatures and properties are also measured relative to ambient temperature. $\hat{t}$ is the duration of the voltage pulse.

After the almost impulsive rise of temperature, the pulsed-wire temperature decays exponentially due to heat convection.

$$\theta_p/\theta_{p_i} = \exp(-t/T_p), \tag{4}$$

where θ_{p_i} is the wire temperature at the end of the voltage pulse and T_p is the pulsed-wire convection time constant.

2.3. *The temperature downstream of the pulsed wire and the sensor wire response neglecting the influence of thermal diffusion*

From the point of view of the temperature distribution produced by the pulsed wire, we can regard the pulsed-wire temperature variation as consisting of an instantaneous increase of temperature to the value given by equation (1) followed by the exponential decay with the convective time constant of the wire T_p. If we neglect for the moment the influence of thermal diffusion in smearing out the sharp front of the heat tracer, we have that the heat being convected away by the stream at a distance x from the pulsed wire is equal to the heat flow released from the pulsed wire at an interval of time equal to x/U earlier and it is given by

$$Q = N_p k_f \pi \theta_p = \rho_f c_f U \int_{-\infty}^{\infty} \theta_f dy, \tag{5}$$

where θ_f is the fluid temperature downstream of the pulsed wire, and where it is assumed that the velocity is everywhere equal to the free-stream velocity U. This neglect of the viscous wake will be discussed later with the experimental results. From (4) and (5), the integrated temperature distribution downstream of the pulsed wire in a convenient non-dimensional form is given by

$$\frac{\int_{-\infty}^{\infty} \theta_f dy}{\theta_p x} = \frac{\pi N_p}{P} \exp\left(-\frac{t - x/U}{T_p}\right) H\left(\frac{x}{U}\right), \tag{6}$$

where P is the Péelet number, Ux/κ, and $H(x/U)$ is a Heaviside step function. We can now consider the sensor-wire response to this temperature field.

The sensor wire is operated as a simple resistance thermometer and the constant current passing through it is sufficiently small to enable the electrical heating term in equation (1) to be neglected. When the tracer of heated air arrives, there will be an output voltage from the sensor wire given by

$$\frac{i\alpha r}{l} \int_{-l/2}^{+l/2} \theta_s(y)\, dy, \tag{7}$$

where i is the constant current, r and l are the wire resistance and length respectively and $\theta_s(y)$ is the variation of sensor wire temperature over its length. If the sensor wire is much longer than the width of the heat tracer, we have from equation (1), for the relation between the flow and sensor-wire temperature

$$\int_{-l/2}^{+l/2} \theta_s dy \approx \int_{-\infty}^{\infty} \theta_s dy = \frac{e^{-t/T_s}}{T_s} \int_0^t e^{t/T_s} \left[\int_{-\infty}^{\infty} \theta_f dy\right] dt, \tag{8}$$

where T_s is the sensor-wire time constant. It has been assumed so far that conduction along the length of the wires is not important. As will be discussed later on, the half width of the thermal wake is $\delta = O(2(\kappa_f x/U))^{\frac{1}{2}}$. The time for appreciable conduction is therefore $O(\delta^2/4\kappa_w)$ and, if conduction is to be neglected, this time must be much longer than the sensor-wire time constant, T_s. This reduces to the condition that $(P/16N_s)\,(k_w/k_f)\,(d_s/x)^2$ must be much less than unity.

But, in practice, this quantity has values between about 0·1 and 0·7 so that the influence of conduction along the wires may not necessarily be negligible. However, although the temperature distribution may be affected by conduction, it is easy to show that the integral of the temperature over the length of the wire is not affected so that (8) is not in error due to conduction effects.

Using (6) in (8) we obtain

$$\frac{\int_{-\infty}^{\infty}\theta_s dy}{\theta_{p_i}x}=\frac{\pi N_p}{P}\frac{T_p}{T_p-T_s}\left[\exp\left(-\frac{t-x/U}{T_p}\right)-\exp\left(-\frac{t-x/U}{T_s}\right)\right]H\left(\frac{x}{U}\right), \qquad (9)$$

when $T_p \neq T_s$.† This equation gives the response of a sensor wire to a sharp-fronted pulse which subsequently decays in an exponential manner. A rather obvious point is that it shows that the sensor-wire signal does not depend on the distance x between the pulsed wire and the sensor wire except in so far as the time of flight is affected. This is simply a consequence of the conservation of heat, i.e. for a uniform flow velocity, $\int_{-\infty}^{\infty}\theta_f dy$ does not depend on the wire spacing.

The response of the sensor wire shows a discontinuity in slope at time $t = x/U$ with an initial value in non-dimensional terms given by

$$\frac{x^2}{\kappa}\frac{d}{dt}\left[\frac{\int_{-\infty}^{\infty}\theta_s dy}{\theta_{p_i}x}\right]=\pi N_p\frac{x}{UT_s}. \qquad (10)$$

The signal also has a maximum value given by

$$\left[\frac{\int_{-\infty}^{\infty}\theta_s dy}{\theta_{p_i}x}\right]_{\max}=\frac{\pi N_p}{P}\left(\frac{T_p}{T_s}\right)^{-T_s/(T_p-T_s)} \qquad (11)$$

which occurs at time

$$\frac{t}{T_s}=\frac{T_p}{T_p-T_s}\log\frac{T_p}{T_s}+\frac{x}{UT_s}. \qquad (12)$$

Thus, in the absence of diffusion, there would be no difficulty in determining the time of flight because of the discontinuity in slope at $t = x/U$, and, in particular, if the signal were differentiated, this would exhibit a step rise at $t = x/U$ which could be used to trigger an electronic comparator to obtain the time of flight. Before considering the vital question of how diffusion alters these results, one further point should be noted. If we assume roughly that the wire Nusselt number $N \sim P^{0.45}$, the amplitude of the sensor-wire signal shows a variation with free-stream velocity that is like $U^{-0.55}$, so that over, say, a 20 : 1 speed range, there is a variation in signal level of about 5·2 : 1. By contrast, the initial slope of the sensor-wire signal varies more slowly, like $U^{-0.1}$, so that if differentiated signals were used, the amplitude variation would be much less than that of the original signals, and this has an important bearing on possible ways of recording the time of flight, as will be discussed later.

† If $T_p = T_s$, a somewhat different expression is obtained.

2.4. *The influence of thermal diffusion on the sensor-wire signals*

The influence of thermal diffusion can be studied by using solutions of the equation for the convection and diffusion of heat in a stream, namely

$$\frac{\partial \theta_f}{\partial t} + U\frac{\partial \theta_f}{\partial x} = \kappa\left(\frac{\partial^2 \theta_f}{\partial x^2} + \frac{\partial^2 \theta_f}{\partial y^2}\right). \tag{13}$$

It is again assumed that the velocity is everywhere equal to the free-stream velocity. By introducing the variable $X = x - Ut$ in place of x, the ordinary heat-conduction equation is recovered whose solution can be compounded of simple point heat sources. Thus, the solution of (13) for the thermal wake produced by a pulsed wire with an exponentially decaying temperature is given by

$$\frac{\theta_f(x,y,t)}{\theta_{p_i}} = \frac{N_p}{4}\int_0^{Ut} \frac{\exp\left(-\dfrac{t-x'/U}{T_p}\right)\exp\left(-\dfrac{U}{4\kappa x'}y^2\right)\exp\left(-\dfrac{U(x-x')^2}{4\kappa x'}\right)}{x'}\,dx'. \tag{14}$$

This integral has a convenient asymptotic behaviour given by

$$\frac{\theta_f(x,y,t)}{\theta_{p_i}} \sim \frac{N_p}{2}\left(\frac{\pi}{P}\right)^{\frac{1}{2}}\exp\left(-\frac{t-x/U}{T_p}\right)\exp\left(-\tfrac{1}{4}P\left(\frac{y}{x}\right)^2\right) \times\left[\frac{\operatorname{erf}(\frac{1}{4}P)^{\frac{1}{2}} - \operatorname{erf}[(\frac{1}{4}P)^{\frac{1}{2}}(1-tU/x)]}{1+\operatorname{erf}(\frac{1}{4}P)^{\frac{1}{2}}}\right], \tag{15}$$

which requires that the Péclet number

$$P = Ux/\kappa \gg 1, \quad (y/x)^2 \ll \tfrac{1}{4}P \quad \text{and} \quad T_p \gg 2x/(UP^{\frac{1}{2}}).$$

The physical interpretation of this solution is that when $P \gg 1$, longitudinal diffusion is significant only near the front of the pulse and it is this term in (13) which gives rise to the functions containing erfs in (15). As discussed by Bauer (1965), this function is like a step function with a rise time of $4x/(UP^{\frac{1}{2}})$. In this time, the rise is about 90 % complete. Away from the front of the pulse, lateral diffusion dominates, and the solution in this region tends to

$$\frac{\theta_f(x,y,t)}{\theta_{p_i}} \sim \frac{N_p}{2}\left(\frac{\pi}{P}\right)^{\frac{1}{2}}\exp\left(-\frac{t-x/U}{T_p}\right)\exp\left(-\tfrac{1}{4}P\left(\frac{y}{x}\right)^2\right), \tag{16}$$

which is the 'quasi-steady' boundary-layer solution of (13) without the longitudinal diffusion term. The solution is quasi-steady because the pulsed-wire temperature is decaying exponentially, and for this solution to be valid, it is necessary that the pulsed-wire time constant should be much longer than the time for appreciable diffusion, i.e. $T_p \gg 2x/(UP^{\frac{1}{2}})$.

In the case of an unyawed probe, the integral of the flow temperature may be obtained from (15) to give

$$\frac{\int_{-\infty}^{\infty}\theta_f\,dy}{\theta_{p_i}x} = \frac{\pi N_p}{P}\exp\left(-\frac{t-x/U}{T_p}\right)\left[\frac{\operatorname{erf}(\frac{1}{4}P)^{\frac{1}{2}} - \operatorname{erf}[(\frac{1}{4}P)^{\frac{1}{2}}(1-tU/x)]}{1+\operatorname{erf}(\frac{1}{4}P)^{\frac{1}{2}}}\right]. \tag{17}$$

This result differs from the earlier expression without longitudinal diffusion (equation (6)) only by the step-like erf function and it is a result that one might well have written down intuitively without the necessity of the foregoing analysis.

Substituting in (8) for the sensor-wire response, we now obtain the following expression for $T_p \neq T_s$:

$$\frac{\int_{-\infty}^{\infty}\theta_s dy}{\theta_{p_i}x} = \frac{\pi N_p}{P(1+\operatorname{erf}\chi)}\frac{T_p}{T_p-T_s}\left\{\exp\left(-\frac{t-x/U}{T_p}\right)\left[\operatorname{erf}\chi-\operatorname{erf}\chi\left(1-\frac{tU}{x}\right)\right]\right.$$
$$\left.-\exp\left(-\frac{t-x/U}{T_s}\right)\exp\left[\left(\frac{\lambda x}{2\chi U}\right)^2\right]\left[\operatorname{erf}\left(\chi+\frac{\lambda x}{2\chi U}\right)-\operatorname{erf}\left(\chi\left(1-\frac{tU}{x}\right)+\frac{\lambda x}{2\chi U}\right)\right]\right\}, \tag{18}$$

where $\chi = (\frac{1}{4}P)^{\frac{1}{2}}$, $\lambda = (1/T_s)-(1/T_p)$. This expression is useful because it enables the sensor-wire response to be studied with all the main physical parameters included with the exception of the influence of the pulsed-wire viscous wake.

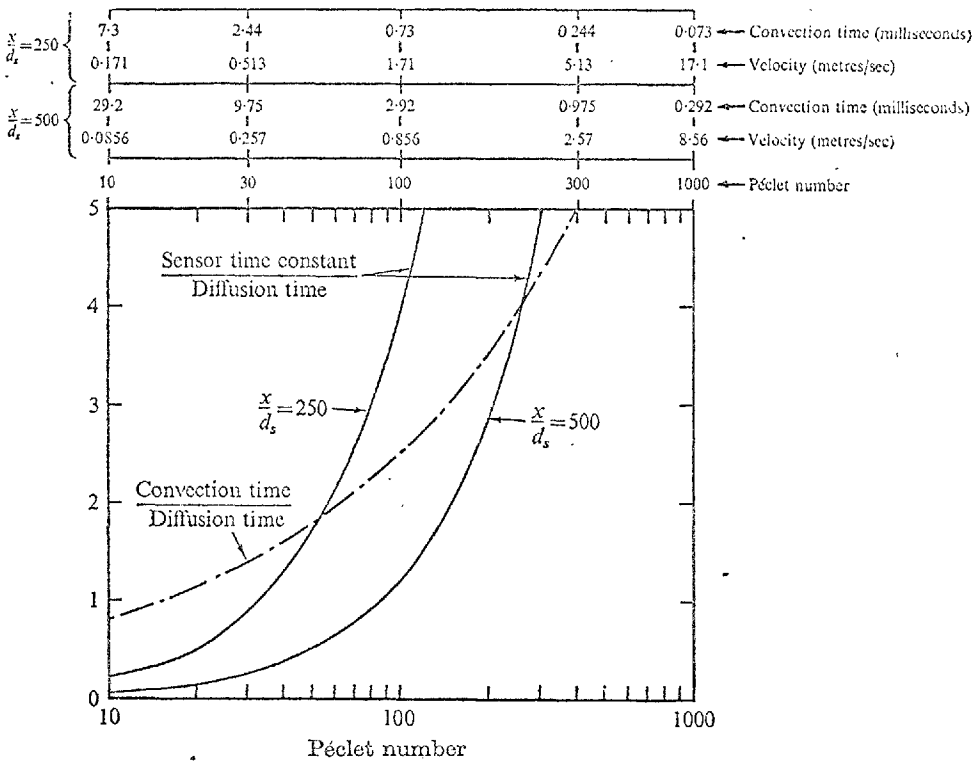


FIGURE 2. Characteristic times of pulsed-wire probes.

However, the interpretation which is put upon the expression depends on the relative magnitudes of the various characteristic times. These characteristic times are (i) the convection time, $T_c = x/U$, (ii) the time taken for the diffusive front to pass, $T_d = 4x/(UP^{\frac{1}{2}})$, (iii) the sensor-wire time constant, $T_s = (\rho_s c_s d^2)/(4k_f N_s)$, (iv) the pulsed-wire time constant, T_p. At this stage, it is pertinent to consider examples of typical probes in order to establish practical values of these characteristic times. The probes used in the majority of the experiments consisted of a pulsed wire of 10μ diameter and a sensor wire of 5μ diameter. The spacing between them varied typically from 1·25 mm to 2·5 mm and figure 2 shows the

ratios of these time constants to one another for these two spacings which are equal to values of x/d_s of 250 and 500 respectively. The results are given as a function of Péclet number, but, in order to give some idea of the real times involved, two additional abscissa scales are shown in which the velocity and convection times for the two typical probes are given. At the lower velocities (which in practical terms are less than, say, 2 m/sec), the diffusion time is

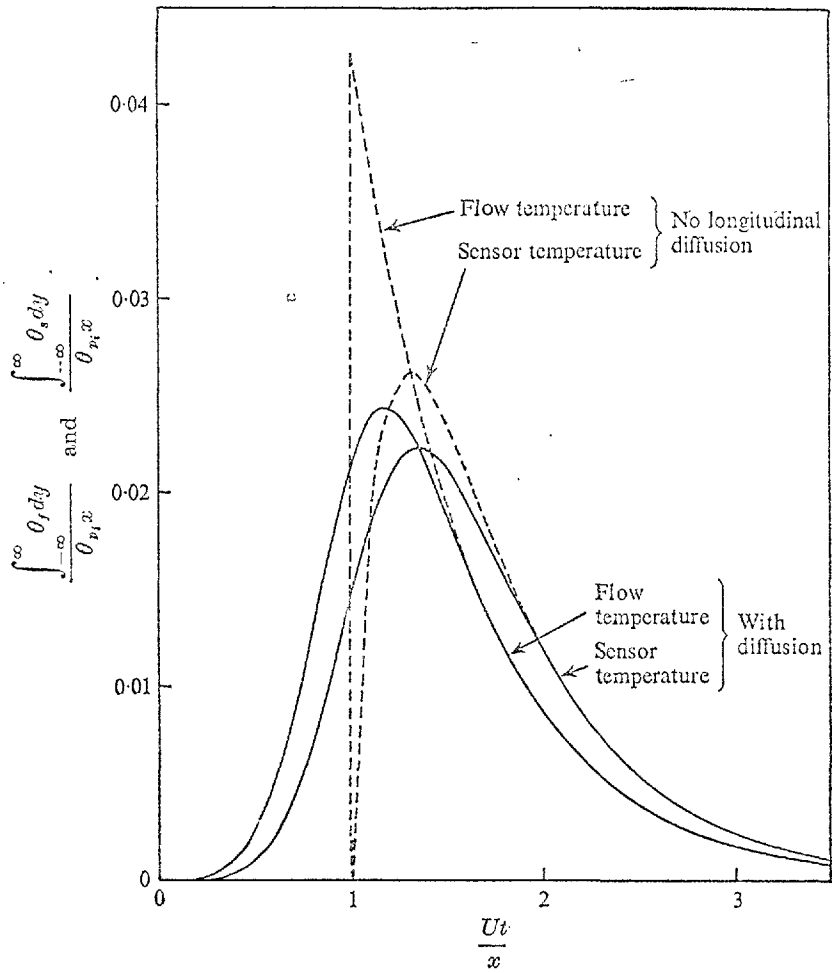


FIGURE 3. The flow and sensor-wire temperature variation, Péclet number = 30.

$$\frac{d_p}{d_s} = 2; \quad \frac{x}{d_s} = 500; \quad \frac{UT_d}{x} = 0{\cdot}730; \quad \frac{UT_s}{x} = 0{\cdot}177; \quad \frac{UT_p}{x} = 0{\cdot}600.$$

comparable to and eventually more than both the convection time and sensor-wire time constants. However, as the velocity is increased, this situation is inverted and the diffusion time rapidly becomes very short compared with the convection time and the sensor-wire time constant.

In order to typify the type of sensor-wire signals that are obtained at the two extremes of Péclet number discussed above, equations (17) and (18) have been

used to calculate both the flow temperature and sensor-wire temperature variations at two Péclet numbers of 30 and 300 for a spacing ratio, x/d_s, of 500 and a pulsed-wire to sensor-wire diameter ratio, d_p/d_s, of 2. The results, which are shown in figures 3 and 4, have a comparatively simple physical interpretation. When the diffusive front has passed (i.e. $tU/x > 1+2/P^{\frac{1}{2}}$), both the flow temperature and sensor-wire temperature approach the results obtained in which diffusion is

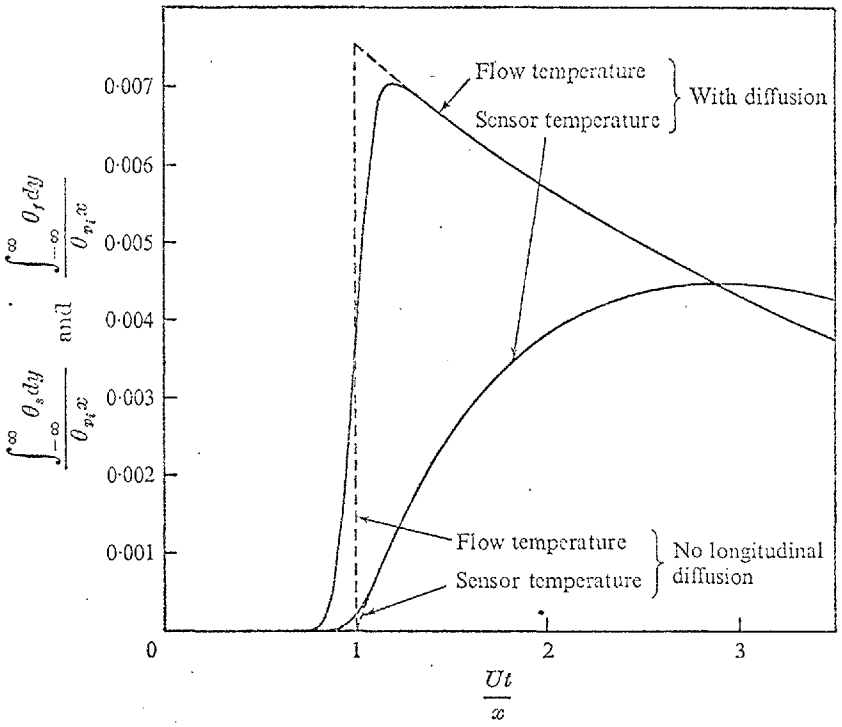


FIGURE 4. The flow and sensor-wire temperature variation, Péclet number = 300.

$$\frac{d_p}{d_s}=2;\quad \frac{x}{d_s}=500;\quad \frac{UT_d}{x}=0{\cdot}231;\quad \frac{UT_s}{x}=1{\cdot}094;\quad \frac{UT_p}{x}=3{\cdot}595.$$

neglected, namely, equations (6) and (9). In the neighbourhood of the pulse front, the influence of longitudinal diffusion is to replace the discontinuity in slope that occurred without longitudinal diffusion by a transition region. In particular, if the sensor-wire time constant is much less than the diffusion time, the sensor-wire signal tends to follow the flow temperature variation (see figure 3). At the other extreme, when the sensor-wire time constant is much longer than the diffusion time, the relationship between the sensor-wire signal and the flow temperature given by equation (8) reduces in the neighbourhood of the diffusive front to the simple form

$$\int_{-\infty}^{\infty}\theta_s dy=\frac{1}{T_s}\int_0^t\left(\int_{-\infty}^{\infty}\theta_f dy\right)dt.$$

In other words, the sensor wire behaves initially as a simple integrator of the free-stream temperature. Under these circumstances, the transition region extends only for the duration of the diffusion time, and thereafter the signal

rapidly approaches the form given by (9) in which diffusion is neglected. It is perhaps easier to visualize these results if it is remembered that the relationship between the flow temperature and sensor-wire temperature is exactly analogous to the relationship between the input voltage applied across a resistor and a capacitor in series and the output voltage taken across the capacitor. The RC time is equivalent to the sensor-wire time constant and the results for low and high Péclet number correspond to a low and high frequency signal respectively.

The influence of diffusion is therefore to introduce some uncertainty as to precisely when the sensor-wire signal corresponds to the time of flight. A number of possibilities exist for overcoming this uncertainty but the simplest technique is that suggested by Bauer in his original paper. This involves observing the

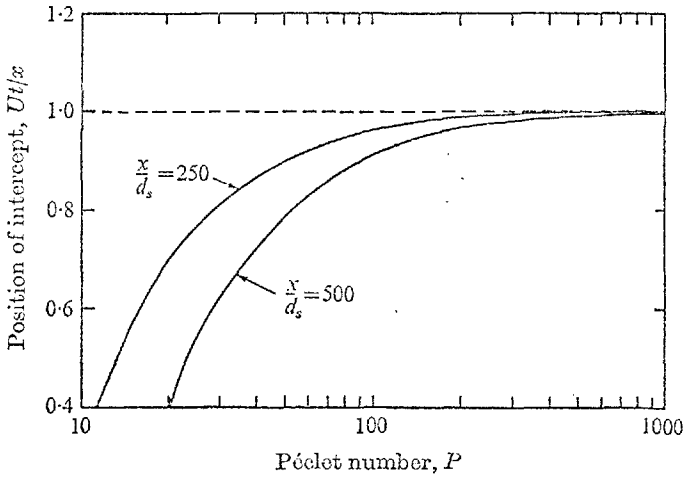


FIGURE 5. The influence of Péclet number on the intercept times. $d_p/d_s = 2$.

sensor-wire signals on an oscilloscope, and effectively extrapolating back onto the zero signal axis from the position of the maximum slope. For this to be accurate, it is necessary for the diffusion time to be small compared with the sensor-wire time constant so that the rise of the sensor-wire signal after the diffusive front has passed is still nearly linear. Figure 4 typifies such a situation. However, as the results in figures 2 and 3 show, there is always a lower bound to this technique because the diffusion time increases more rapidly than the sensor-wire time constant as the Péclet number is reduced. In order to give some idea of the errors that might be expected from this technique at the lower Péclet numbers, the position of the intercept from the maximum slope position has been calculated from equation (18) for our two typical probes. These results (figure 5) show that the intercept technique can be used down to Péclet numbers in the region of 100 without the errors being too significant. In practical terms, this corresponds to velocities of about 1 m/sec. Moreover, the experimental results discussed in § 4.2 show that the effect of the pulsed-wire viscous wake, which has so far been neglected, is to extend still further the lower bound below that suggested by these theoretical results.

Although the intercept technique has been used fairly extensively in measurements so far carried out, it is laborious in a highly turbulent flow to record a sufficient number of oscilloscope traces to determine both the mean and turbulent velocities. One alternative to the use of an oscilloscope is to digitize the signals and analyse them on a computer. This is the technique used by Tombach (1969), but it requires comprehensive facilities which were not available in the present experiments. Another possibility is to use the intercept technique with a digital counter. The counter could be set to run when the pulse is fired, and its output gated when the sensor-wire signal reached a number of predetermined trigger levels. If these trigger levels were on the near linear rise of the sensor-wire signal, the position of the intercept could be obtained from the counter readings. However, as discussed earlier, there is a strong variation in the amplitude of the sensor-wire signals with velocity so that it would be necessary to make use of a substantial number of trigger levels in order to ensure that accurate intercept positions could be obtained over a wide speed range. This technique therefore also requires sophisticated instrumentation since it is effectively equivalent to digitizing the signal except that instead of digitizing voltages at set intervals of time, one would be recording times at set intervals of voltage. In this particular problem, this is a much more efficient approach to digitization, and although a computer would still be required to analyse the signals, it is possible to envisage on-line use of the instrument using this approach whereas this is almost certainly not possible if the signal is digitized in the more usual manner.

Neither of the above techniques is very simple and a more direct approach which has been explored in the present investigations is to make use of the differentiated sensor-wire signals. In the absence of diffusion these differentiated signals would exhibit a sharp step at $tU/x = 1$, and a counter could be triggered at any level below the step amplitude to obtain the time of flight. The variation in the step amplitude in the absence of diffusion is given by (10), and, as has already been discussed, this exhibits a much slower variation with free-stream velocity than the amplitude of the undifferentiated signal. The effect of diffusion is again to smooth out the step discontinuity, and figure 6 shows typical results obtained by differentiating (18) and calculating the output signals for a probe with $x/d_s = 500$ and $d_p/d_s = 2$. For a trigger level fixed at a signal level corresponding to

$$(x^2/\kappa)\, d\left[\int_{-\infty}^{\infty} \theta_s dy \Big/ (\theta_{p_i} x)\right] \Big/ dt = 1,$$

the time of flight obtained in this way is shown in figure 7 as curve 1. These results show that if a departure from linearity of, say, 5 % on velocity is regarded as acceptable then this technique could be used down to Péclet numbers in the region of 100 again. The advantage of this technique is that it is not too sensitive to the trigger level setting. For example, if the trigger level were set at a signal level corresponding to

$$(x^2/\kappa)\, d\left[\int_{-\infty}^{\infty} \theta_s dy \Big/ (\theta_{p_i} x)\right] \Big/ dt = \frac{1}{2},$$

the time of flights results would now be as shown in curve 2 in figure 7. Although these latter flight times are below the true flight times, the calibration would still

be reasonably linear over a Péclet number range from 150 to 1000, and in any case, the influence of the slight non-linearity in the calibrations could be removed in the subsequent computation of the results.

With this description of the sensor-wire signals in steady flow, the experimental problems of using a pulsed-wire probe can now be discussed.

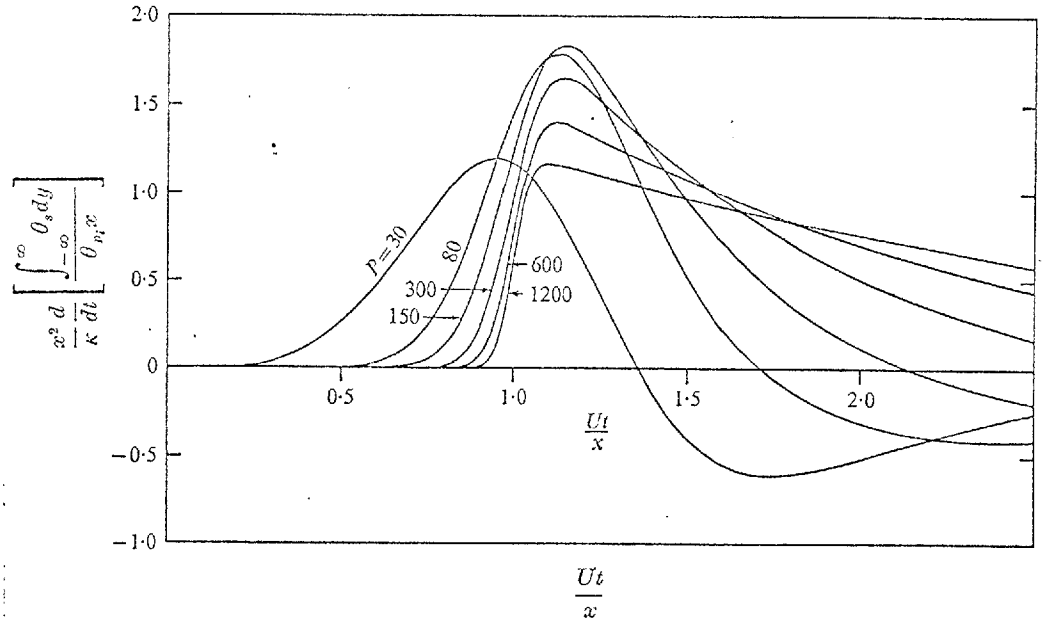


FIGURE 6. Examples of differentiated sensor-wire signals at different Péclet numbers. $x/d_s = 500$; $d_p/d_s = 2$.

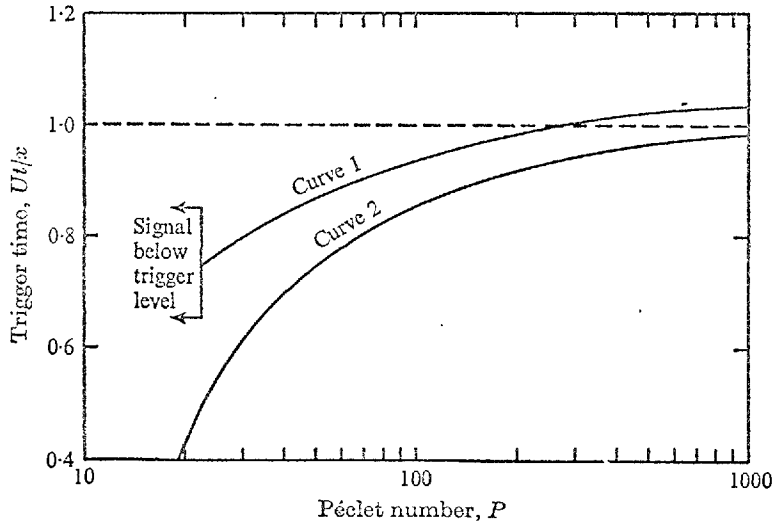


FIGURE 7. The influence of Péclet number and trigger level on the differentiated signal trigger times. $d_p/d_s = 2$.

3. Details of the experiments

The design of pulsed-wire probes and the way in which they are operated depends not only on the dynamics of the convection and diffusion of the heat pulse but also on some of the practical electronic and mechanical constraints that arise. These include problems of signal-to-noise ratio and the influence of electrical coupling between the pulsed-wire and sensor-wire circuits. As these factors are of central importance to the successful development of the technique, they will be discussed in some detail.

3.1. *The probe design and its electrical circuitry*

All the probes used have been broadly similar to the one sketched in figure 1. Most of the experiments have been carried out with sensor wires of 5 μ diameter platinum and with pulsed wires of either 10 μ diameter platinum or 10 μ diameter nickel wire. Both platinum and nickel are suitable materials for pulsed wires

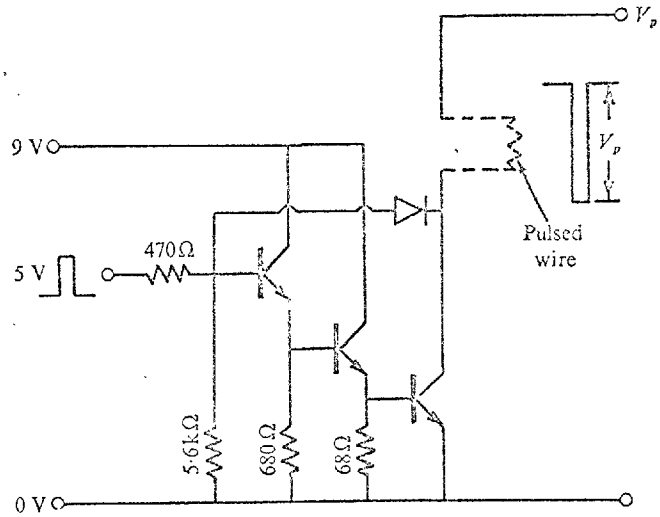


FIGURE 8. The transistor switch (Texas 2M2243 transistors).

because they are capable of operating at high temperatures (i.e. in excess of 600 °C) without oxidizing. On the other hand, tungsten wire, which is admirably suited for use as the sensor wires, is not suitable for pulsed wires because it oxidizes at the comparatively low temperature of about 300 °C.

The duration of the pulses used to produce the tracer of heated air ranges from a few microseconds up to about 30 μsec with peak currents as high as 8 amps although a more typical figure is 4 amps. Although there is nothing intrinsically difficult about making a circuit to produce such pulses, figure 8 shows the circuit for the transistor switch used in the present experiments. A number of types of transistor were tried, but those shown are particularly satisfactory in giving pulses with a rise and fall time of better than 0·5 μsec. The circuit can switch a current of about 4 amps through any resistance with a limitation on the transistor of a maximum collector voltage V_p of about 80 volts. For higher currents, two of

the switches can be operated in parallel. The switches give pulses of almost constant voltage and they can be driven from an ordinary low power pulse generator.

The sensor-wire circuit that is of interest for the moment is only the simple bridge and low-noise amplifier part of the circuit shown in figure 9. The rest of the circuit relates to the automatic aquisition of the times of flight and will be discussed later in § 6. The two sensor wires are operated as arms in a simple bridge with the current supplied by an ordinary 1·5 volt dry cell battery. The output is taken across the bridge centre points so that the polarity of the signal depends on which sensor wire picks up the heat pulse; the signal polarity therefore gives the flow direction. The only major problem with the sensor-wire circuit arises from the electrical coupling between the pulsed-wire circuit and sensor-wire circuit. Although these two circuits are not connected by any 'real' wires, there is in reality both capacitative and inductive coupling between the two circuits, especially at the probe head where the wires and their supports form parallel loops admirably designed to maximize mutual inductance! In principle, operating the wires in the arms of a bridge should cancel out any common-mode interference signal but, for a variety of reasons, this does not occur and, every time a pulse is fired, there is a pick-up signal on the sensor-wire circuit of a few millivolts – this is many times larger than the sensor-wire signal from the heat tracer which is typically about 100 μV. This pick-up signal is of a short duration and, in itself, is not important. But, if any low-pass filtering is used to improve the signal-to-noise ratio, the interference signal acquires a decay time which is of the order of the reciprocal of the cut-off frequency. This causes difficulties at higher speeds as will be discussed later.

We turn now to the design of the probe itself and the influence of signal-to-noise ratio considerations both on the geometry of the probe and the operating current through the sensor wires. If an extensive yaw response of, say, $\pm 70°$ is required, it is necessary that all the probe wires should be about five times longer than the spacing between the pulsed wire and the adjacent sensor wires. As far as the influence of signal-to-noise ratio is concerned, two factors should be noted. First, provided the sensor wire is long enough to intercept the entire heat pulse, the sensor-wire signal is independent of the wire length. Second, as discussed in § 2.3, we would expect from heat conservation arguments that the amplitude is not dependent on the spacing between the pulsed wire and sensor wires apart from the usually weak influence of longitudinal diffusion and possibly also the effect of the pulsed-wire viscous wake. We have therefore the somewhat surprising situation that neither the spacing nor the wire length have a very strong influence on the signal amplitude. On the other hand, noise will be directly proportional to the wire length; this includes both electronic noise from the amplifier and also any response that the sensor wire has directly to the airstream flowing past it either to temperature fluctuations as a resistance thermometer or to velocity fluctuations as a hot-wire anemometer; these sources of noise will be discussed shortly. It would appear therefore that there is a strong motive to reduce the spacing between the wires as much as possible, and this would also be helpful in reducing the size of the probe relative to the length scales of the

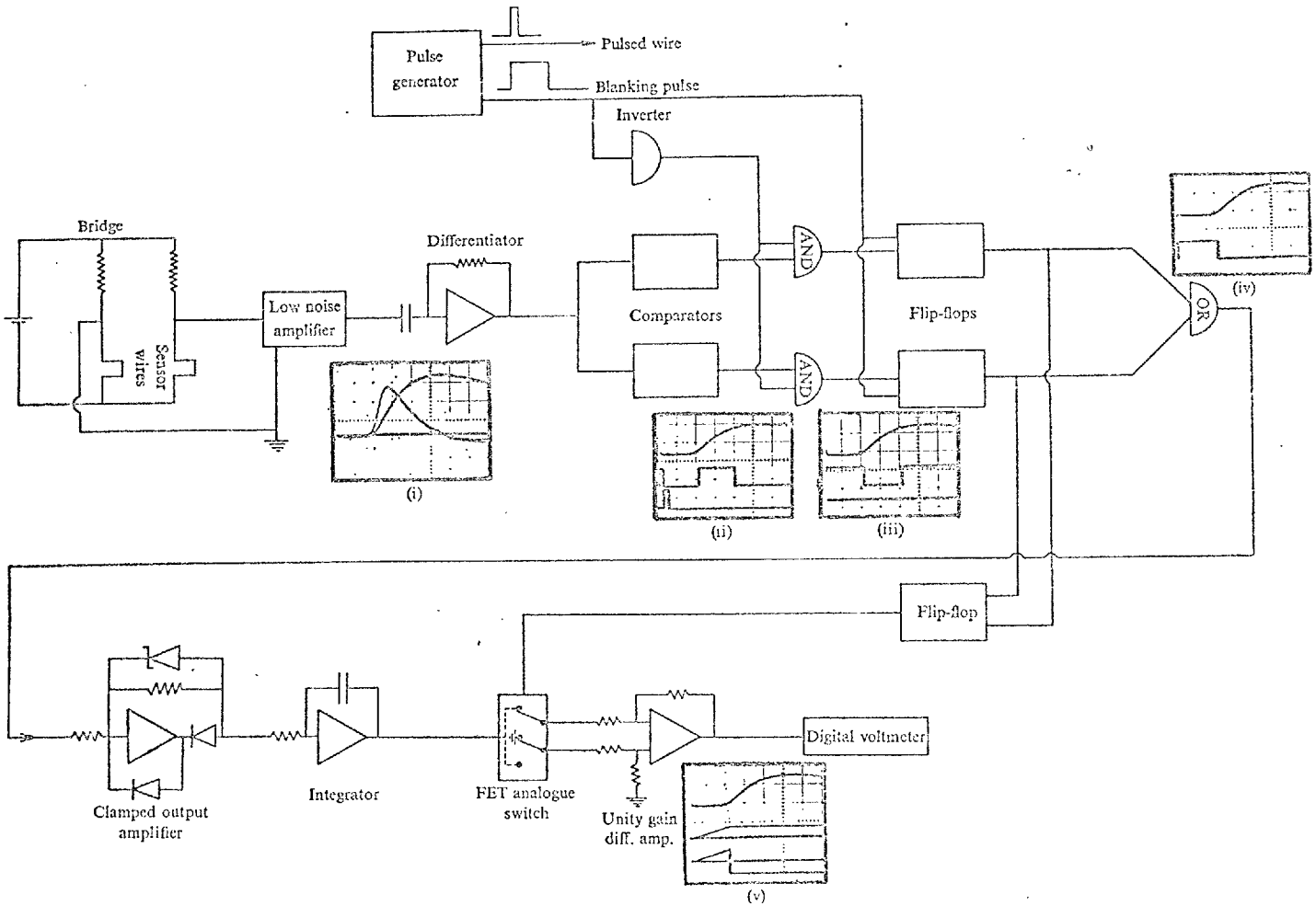


FIGURE 9. Circuit for the automatic measurement of flight times.

turbulence. However, there are two factors which set a broad limit to the permissible reduction of this spacing. The first is that it does not seem advisable to reduce the Péclet number below, say, 50 even though the experimental results discussed later in § 5 show that the influence of longitudinal diffusion on the apparent time of flight is much less than might be expected from the theoretical arguments in § 2.4. If we set 1 m/sec as a typical lower bound on velocities of interest, this gives a spacing of about 1·25 mm for a Péclet number of 50. On the other hand, at the higher velocities, the time of flight eventually becomes comparable to the decay time of the pick-up signal discussed earlier, and the signal from the heat pulse merges into the decaying 'tail' of the interference signal. This decay time is typically 100 μsec which therefore limits the maximum speed for a 1·25 mm spacing to about 14 m/sec. Thus, from a consideration of these various factors, it would seem that, with the present experimental arrangements, it is expedient for the spacing between the pulsed wire and sensor wires to be not less than about 1·25 mm. In order to obtain an adequate yaw response, this requires that the wire lengths should not be less than about 6·25 mm say. This is a much larger probe than the average hot-wire anemometer, and it might seem that errors due to the probe size might be more significant than in the case of a hot-wire anemometer. However, as will be discussed later in § 5, experiments so far carried out do not show any strong effects under normal conditions, and it is certainly possible to carry out investigations in the normal wind-tunnel environment although the larger scale of flow encountered, say, in meteorology and in heating and ventilating problems would provide an admirable area in which to apply the technique.

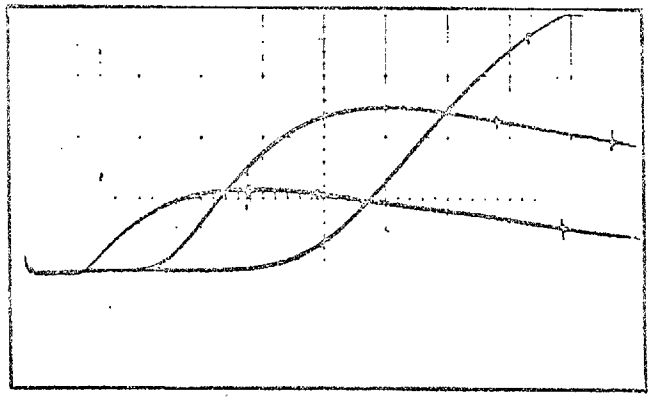
We also have to consider the problem of choosing the sensor-wire current for the optimum signal-to-noise ratio. In addition to the electronic noise from the amplifier, the wire appears to retain some sensitivity to the airstream flowing past it. At very low currents (say, below 1 milliamp for a wire of 5 μ diameter), this is probably due to small temperature fluctuations that occur in the stream but, as the current is increased (say, above 5 milliamps), the wire begins to respond like an ordinary hot-wire anemometer to fluctuations in the velocity. No attempt to examine this problem quantitatively has yet been made but it seems likely that the 'noise' output will be of the form

$$\underset{\substack{\text{Electronic noise}\\ \text{from amplifier}}}{e} + \underset{\substack{\text{Response to temperature}\\ \text{fluctuations in the stream}}}{a_1 i} + \underset{\substack{\text{Response to velocity}\\ \text{fluctuations in the stream}}}{a_2 i^2}$$

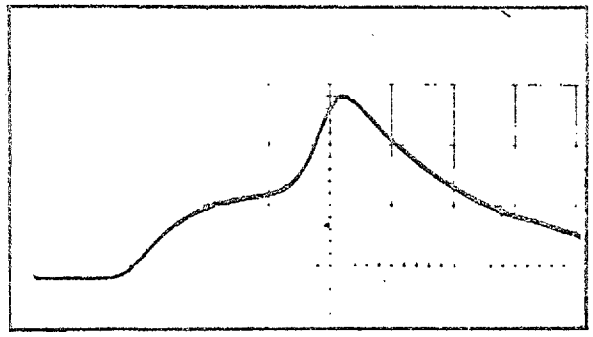
where a_1 and a_2 depend not only on properties of the wire, but also on the magnitude of the velocity and temperature fluctuations that occur in the stream. The signal level will tend to vary directly with the current so that the signal-to-noise ratio behaves like $i/(e + a_1 i + a_2 i^2)$. Initially, this ratio increases with current; it then reaches a maximum and, finally, when the wire begins to behave substantially like a hot-wire anemometer, the signal-to-noise ratio will fall away like $1/i$. This seems to accord with one's impressions when carrying out experiments, and it is a fairly simple matter to adjust the current to obtain a reasonable signal-to-noise ratio. For 5 μ diameter platinum sensor wires, this current invariably lies in the region of between 0·5 and 3 milliamps. Below 0·5 milliamps, the

influence of electronic noise begins to be significant whereas if the current exceeds 5 milliamps, say, the wire clearly begins to respond directly to velocity fluctuations.

One final point about the probe design should be made. The thermal stresses set up when the pulsed wire is heated can cause it to mechanically vibrate the rest of the probe. The resulting strain gauging of the sensor wires gives a spurious signal which partially obscures the convected heat pulse signal. This problem can be overcome by ensuring that the pulsed wire is not taut across the probe supports. In cases where mechanical 'ringing' occurs, it is invariably sufficient to kink the pulsed wire carefully to eliminate the problem.



(*a*)



(*b*)

FIGURE 10. Examples of sensor-wire signals. (*a*) At different flow velocities, sweep speed 0·5 msec/cm. (*b*) In turbulent flow.

4. Results of calibration experiments

Some typical signals for a crossed-wire probe in steady flow are shown in figure 10(*a*). They exhibit all the features discussed earlier and a number of careful calibrations have been carried out to compare with the theoretical results. The aim of this work was to try to highlight any problem areas in obtaining a proper understanding of the pulsed-wire probe behaviour. It is worth pointing out at the outset that it is not easy to make these comparisons with any accuracy because, in addition to the basic observations of the sensor-wire signals, it is

necessary to know a good deal about the experimental environment. For example, it is necessary to know the lengths and diameters of both the pulsed and sensor wires, the correct heat-transfer relationship from the wires to the airstream, the pulsed-wire temperature, the temperature coefficient of the wire material and the resistance per unit length of the sensor wires and current passing through them. Some of these quantities are easy to obtain and others are not so easy, but the combination of them all and the need during the calibration experiment itself to avoid breaking any of the wires, all result in an experiment which is difficult to keep under proper control.

4.1. *The pulsed-wire temperature*

In order to make comparisons with the theoretical results, it is necessary for the pulsed-wire temperature at the end of the pulse, θ_{pi}, to be known. Equation (3) gives this in terms of the voltage per unit length and duration of the pulse. It should be noted that the wire diameter does not enter into the relationship in this form. Before carrying out the calibration experiments, it seemed a prudent exercise to check whether the temperatures given by this expression were achieved in practice. A number of different diameter wires were used with pulse lengths ranging from 5 μsec to 35 μsec. The voltage and current applied to the wire were obtained from oscilloscope traces similar to the one shown as an inset in figure 11. The current trace was obtained using a Tetronix current probe. The temperature rise at the end of the pulse was obtained from the observed resistance change. The experimental values obtained in this way are compared with the equation (3) in figure 11, and the agreement is reasonably satisfactory. The values of the first temperature coefficient of resistance, α, and the resistivity, σ, used in evaluating the results are 0·0035/°C and 11·2 ohm cm both based on 0 °C. These differ slightly from the values for pure platinum and they were obtained from the experiments of the present authors on the heat-transfer laws for fine wires. In the absence of any better guide, the other properties of the wire material were assumed to be the same as for pure platinum. Although no great claim is made for the accuracy of the experiments, the experimental results do lie consistently below the values obtained from equation (3). This discrepancy is not greatly affected by the values of the material properties used, and it would appear to be a genuine discrepancy. It cannot, however, be attributed to heat conduction, convection, or radiation losses, because these would have shown up as a variation in the experimental results for different duration pulses. No satisfactory explanation can be offered for the discrepancy at the moment, but, since some electrical 'ringing' was apparent in the voltage pulse, it may be simply due to the capacitance or inductance of the pulsed-wire probe and the leads to it.

It is also worth pointing out that the lifetime of a pulsed wire is strongly dependent on the temperature to which it is pulsed. For platinum, it would appear that, provided this temperature does not exceed about 500 °C or 600 °C, the lifetime of the wire is virtually indefinite. However, once the temperature is taken above this point, the lifetime becomes extremely uncertain. In some cases, a wire can be operated for long periods at pulsed temperatures in the region of 1000 °C, but, on other occasions, the wire will break after one or two pulses. Since

it is an advantage from the point of view of a good signal-to-noise ratio to always operate the pulsed wire at as high a temperature as possible, there is a continual temptation to operate at the very elevated temperatures with the result that one becomes very adept at replacing wires. In the calibration experiments, the wires were deliberately operated at a very conservative temperature in order to minimize the possibility of breaking the pulsed wire before the experiments were completed. It is also worth noting that every time a wire is pulsed, it produces an audible 'click', and this provides a quick check on whether or not the pulsed wire and its associated circuitry is operating correctly.

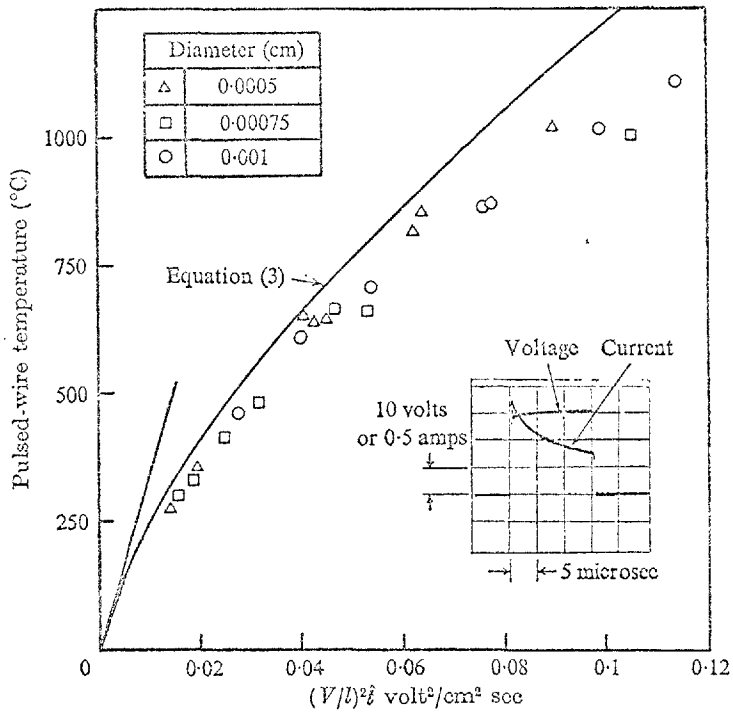


FIGURE 11. Pulsed-wire temperature. Insert is a typical voltage and current pulse.

For the purpose of comparison with the theoretical results of sensor-wire signals, the pulsed-wire temperatures have been taken as the mean of the experimental values and the values obtained from equation (3). In this way, the pulsed-wire temperatures should not be in error by more than about 10 %.

4.2. *Steady velocity calibrations*

From oscilloscope traces of the sort shown in figure 10(*a*), comparisons with the theoretical results obtained earlier are possible. To simplify the comparisons, only measurements of the intercept time, the maximum amplitude and the time to the maximum amplitude have been obtained from the trace photographs. These quantities can conveniently be used to give an indication of the agreement between the theoretical and experimental results. In addition, a calibration was carried out at very low velocities (down to 0·3 m/sec), and these traces were digitized on a Northern Instruments Memory Oscilloscope.

The mean-flow calibrations obtained from the position of the intercepts are shown in figure 12 for two probes, and they are typical of the many calibrations that have been obtained. In both cases, it was difficult to obtain accurate time-of-flight measurements at the highest velocities shown because of the electrical pick-up signal. The calibration shown for probe A was particularly carefully carried out, and included the digitized results at very low velocities. The apparent spacing between the pulsed and sensor wires obtained from the calibration was 1·68 mm for probe A and 2·92 mm for probe B. These appear to be about 10 % greater than the measured spacings which is presumably some measure of the general influence of the pulsed-wire viscous wake.

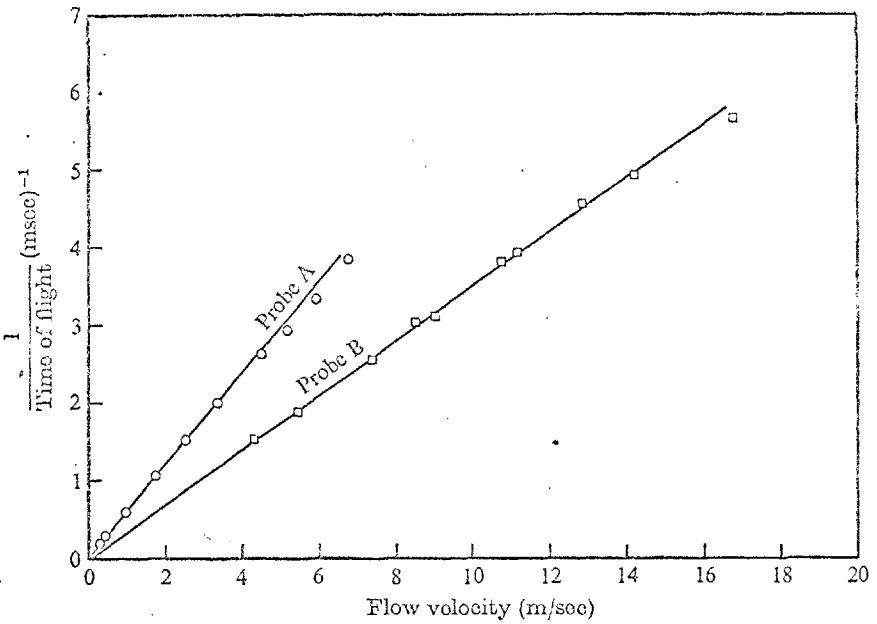


FIGURE 12. Crossed-wire probe calibrations from intercept times.

The theoretical variation of the maximum signal and the time to this maximum signal are shown in figures 13 and 14 respectively where they compared with the experimental results. The agreement is quite satisfactory in showing the general trends although, as has already been explained, very precise agreement cannot perhaps be expected. The influence of longitudinal diffusion on these results is very small, and the results differ significantly from the simple expressions given as equations (11) and (12) only for Péclet numbers below about 40.

Finally, figure 15 compares the complete digitized signals obtained at low velocities with the theoretical distributions. These comparisons are very interesting because they seem to show a clear influence of the pulsed-wire viscous wake on the time of flight. At the highest velocity shown (1·73 m/sec and a Péclet number of 140), the agreement between the theoretical and experimental signal is very good, and the signal is typical of those in which the effects of thermal diffusion are small (cf. figure 4). However, the theoretical distributions at the two lower velocities (0·98 m/sec and 0·28 m/sec, corresponding to Péclet numbers of

80 and 23 respectively) show that thermal diffusion has moved the intercept positions well forward of the convective time of flight $tU/x = 1$ as has already been illustrated in figure 5. But, the experimental results do not exhibit this same

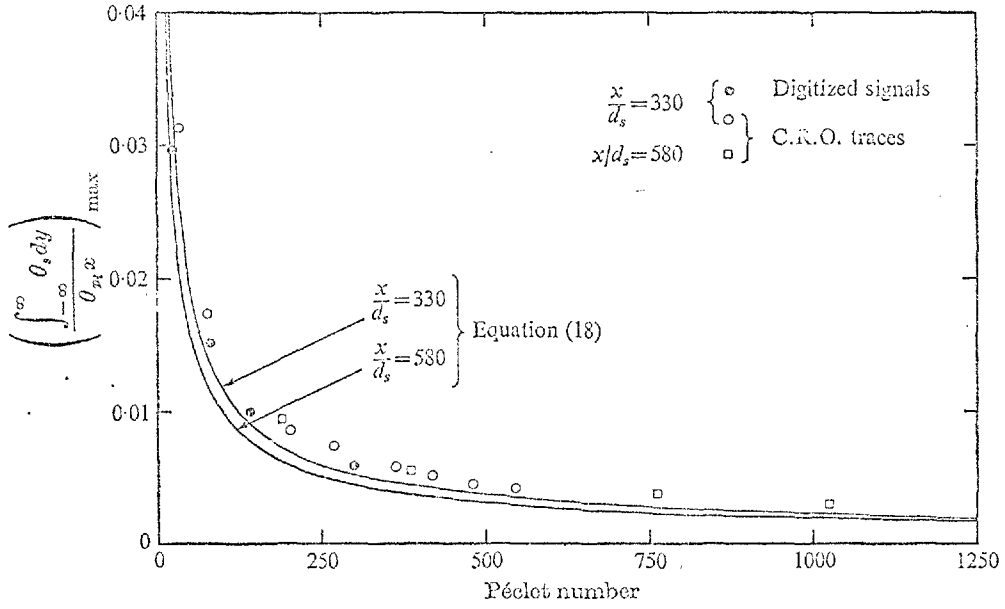


FIGURE 13. Amplitude of sensor-wire signals.

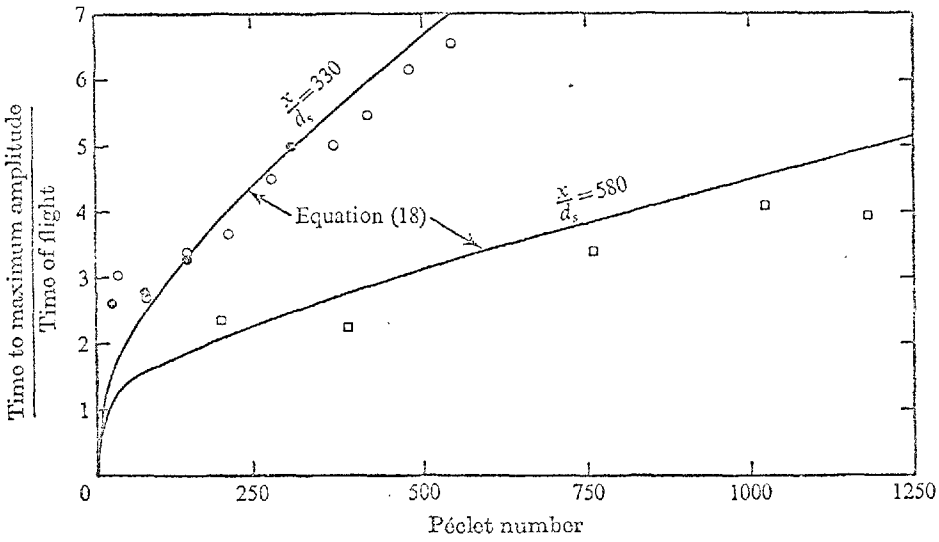


FIGURE 14. Time of maximum amplitude of sensor-wire signals.
See figure 13 for symbols.

forward movement of the intercept position, although the shapes of the signals are very similar to the theoretical distributions. This is probably due to the increasing influence of the viscous wake at low Reynolds numbers, and it would appear fortuitous that probe calibrations remain linear at Péclet numbers well

below those at which thermal diffusions effects might have been expected to have a strong influence on the apparent time of flight. Although this appears to be generally true, it is obviously an area where more work is required.

4.3. *Yaw response*

Although it would be possible to calculate a theoretical yaw response from the work in § 2.4, it is sufficient for present purposes to discuss the response in more general terms.

The yaw response of a pulsed-wire probe has to be considered in two planes at right angles to one another. Consider first the situation in which the direction of

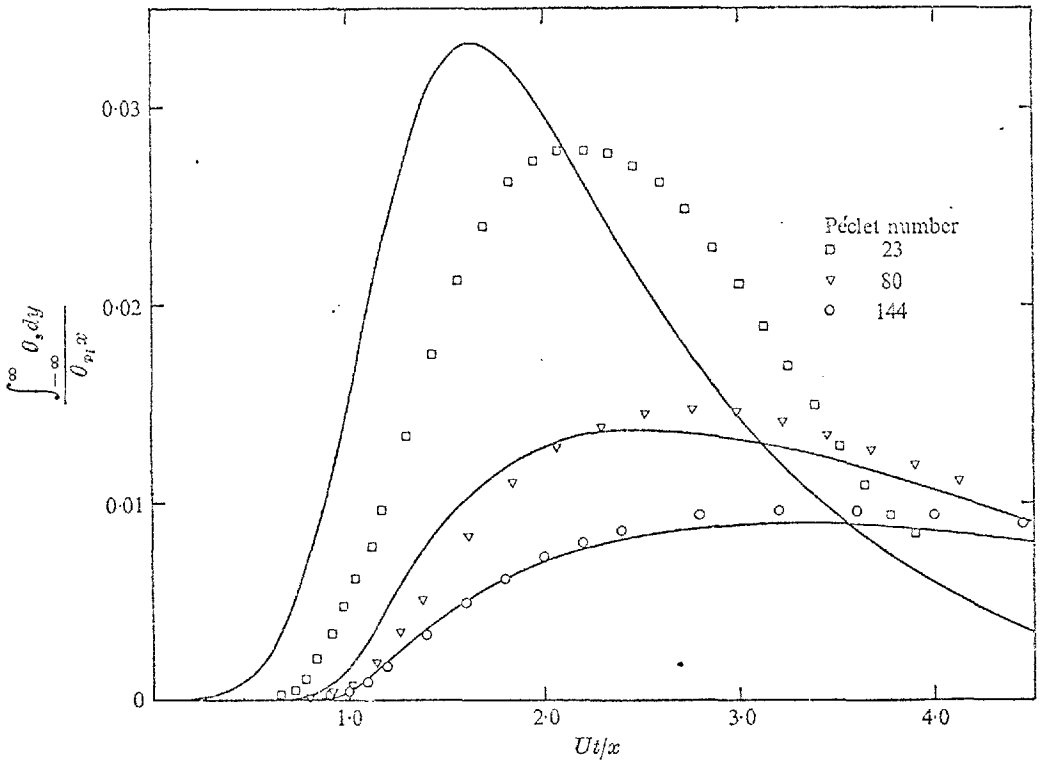


FIGURE 15. Comparison between theoretical and experimental sensor-wire signals. $d_p/d_s = 2{\cdot}1$; $x/ds = 330$. ——, equation (18).

lateral diffusion is along the axes of the sensor wires. If we assume that only the normal component of velocity is effective in the heat transfer to and from wires, the only influence of the yaw is to decrease the effective Péclet number by a factor $(\cos\theta)$ compared to the unyawed case. Consequently, the yaw response should be close to the ideal cosine response for the higher Péclet numbers, and the results shown in figure 16 would seem to confirm that this is the case. As far as the signal amplitudes are concerned, these will increase with yaw because of the reduction in the effective Péclet number (see equation (11)) and the variation will lie between $1/\cos\theta$ and $1/(\cos\theta)^{0{\cdot}55}$ depending on the pulsed-wire Reynolds number.

The results in figure 16 are not inconsistent with this argument. At the very large yaw angles, the influence of the wire supports begins to manifest itself, and the signal amplitudes decrease. Also there is some variation in the time of flight due to the wake from the probe supports, but a useful response is nevertheless maintained up to angles in the region of 80°.

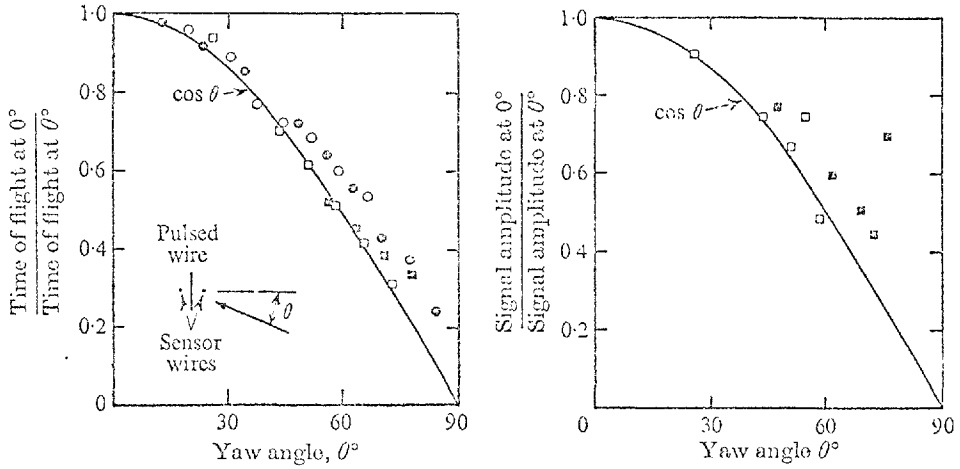


FIGURE 16. Yaw response of crossed-wire probe. Closed and open symbols refer to opposite sides of the axis of symmetry. ○, ○, 1·7 m/sec; □, □, 7·4 m/sec.

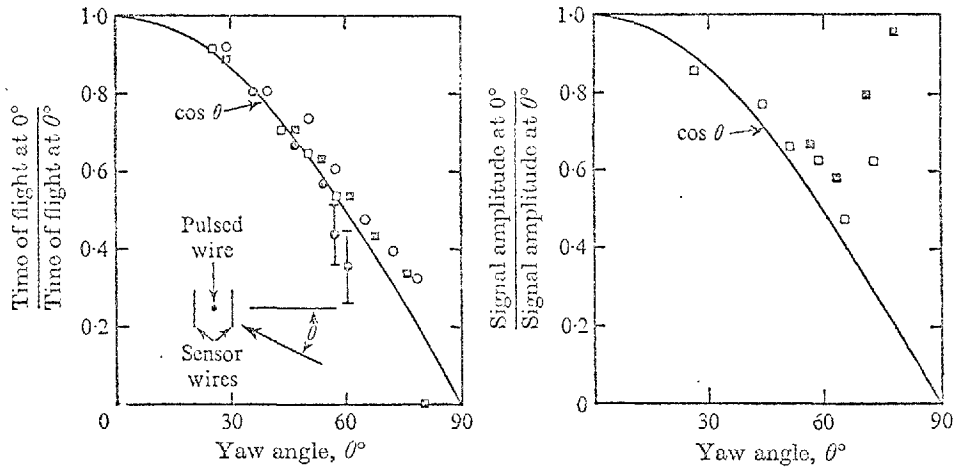


FIGURE 17. Yaw response of crossed-wire probe. See figure 16 for symbols.

When the probe is yawed in the other plane, lateral diffusion spreads the pulse in the plane at right angles to the sensor-wire axes, and it has the effect of increasing the duration of the diffusive front of the pulse by a factor $1/(\cos\theta)$ for small angles of yaw. However, for the higher Péclet numbers, the position of the intercept should not be significantly affected by the yaw, and the results in figure 17 again show this to be so. Because the sensor wires are now cutting across the width of the pulse, one would expect the signal amplitudes to increase with yaw angle initially like $1/(\cos\theta)$ although there will also be a weak influence from variations in the sensor-wire time constant due to the yaw. The results in figure 17

show that the amplitudes do increase in roughly this way although, at very large yaw angles, the amplitudes again diminish due to probe interference.

5. Measurements in a turbulent flow

Having established the general behaviour of the probe, its application to turbulent flow measurements can now be considered. There are two techniques for turbulent flow measurements which have so far been used. The first and simplest is to display the sensor-wire signals on a storage oscilloscope and estimate the intercept positions from these traces. Although this is laborious, it is quite feasible to make measurements in this way provided that not too many measurements need to be made. The measurements behind bluff bodies of Bradbury (1969) and Castro (1971) were made in this way. However, if extensive measurements are to be made, an automatic means of recording the flight times is needed and a system is described in § 6 which has now been used in a variety of highly turbulent flows. However, whatever system of recording flight times is used, it is necessary to consider the influence of the turbulence on the probe response.

The first point is to have some guide as to the number of flight times that it is necessary to record in order to achieve a prescribed accuracy. For normally distributed velocity fluctuations, the appropriate approximate expressions for the estimation of sample size in the determination of the mean velocity and intensity are (Mandel 1964)

$$n = \frac{t^2\overline{u^2}}{(\Delta U)^2}; \quad n = \frac{t^2\overline{u^2}}{2(\Delta(\overline{u^2})^{\frac{1}{2}})^2}, \tag{19}$$

where n is the number of samples taken in order to ensure that estimates of the mean velocity and turbulent intensity are within $\pm\Delta U$ and $\pm(\Delta(\overline{u^2})^{\frac{1}{2}})$ respectively of the true values. t is a parameter called the Student's t-distribution function which has values of 1·96 for a 95 % probability of being within the interval and 1·645 for a 90 % probability. These are approximate expressions and they assume that the number of samples taken is large which, in this case, means greater than, say 50. As an example, if the turbulent intensity relative to some reference velocity was 50 %, then, in order to determine the mean velocity to within ± 5 % of the reference velocity with 95 % probability, it would be necessary to record 385 flight times. Under these circumstances, the intensity would be within 6·9 % of the true intensity with 95 % probability. These estimates do not, of course, include the effects of experimental errors.

We turn now to a discussion of the reduction of the time-of-flight measurements. The most satisfactory way of reducing the data is to plot the integrated velocity probability distribution. This involves simply plotting the number of signals n that are present in the velocity range from $-\infty$ to u_n, say. Figure 18 shows such a distribution obtained in a reverse flow region using intercept measurements from a storage oscilloscope. The mean velocity U is given by

$$U = (1/N)\int_0^N u_n\,dn,$$

where N is the total numbers of sample taken. It is worth mentioning that, when an oscilloscope is used, there is inevitably a velocity range in these distributions centred about the zero velocity point for which tracer signals will not appear on the oscilloscope screen at all; this band is shown in figure 18 for the particular sweep speed used. As a consequence, the shape of the probability distribution in this range cannot be determined. However, provided these 'no signal' traces are counted in the results, the probability distributions should still be correct outside this region and a smooth curve can usually be drawn through the experimental points. In fact, the act of drawing a 'smooth' curve through a limited

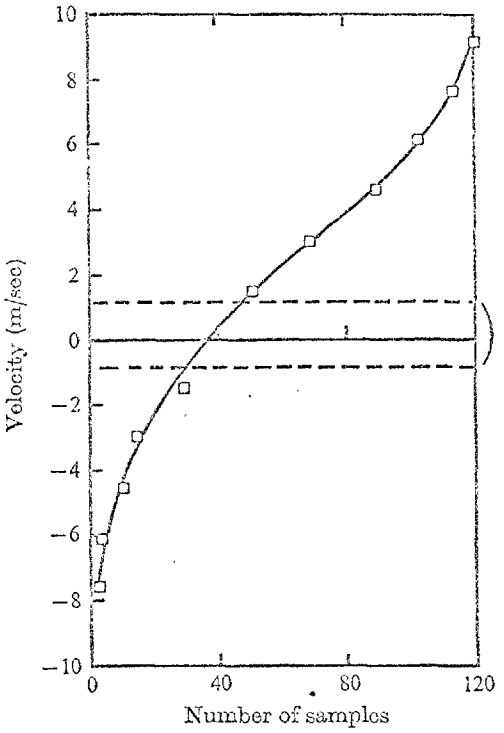


FIGURE 18. Integrated probability distribution in the region one diameter downstream from a circular cylinder. Region in between dotted lines is velocity band not observable on the oscilloscope.

number of experimental points on the probability curve almost certainly gives a higher accuracy for the estimation of the mean velocity and intensity than would be expected from the straightforward statistical expressions given earlier (equations (19)). Another source of error is that, even with an automatic means of recording flight times, some heat tracers will miss the sensor wires in a highly turbulent flow because of the finite yaw response of the pulsed-wire probe. The errors arising from these missed tracers will be considered in a moment, but it is again important from accuracy considerations to include these as zero-velocity results as should the occasional ambiguous signals which occur. These latter signals result presumably from heat pulses arriving at the limit of the probe yaw response.

Having obtained the mean velocity, the probability distribution can also be used to determine the turbulent intensity since

$$\overline{u^2} = (1/N)\int_0^N (u_n - U)^2\, dn.$$

Intensity estimates from storage oscilloscope measurements are certainly less accurate than the mean velocity results because large deviations from the mean velocity contribute strongly to the intensity level, and these are precisely the readings which are difficult to obtain accurately on an oscilloscope. The very high velocities require the measurement of a small distance on an oscilloscope and the very low velocity signals may not appear on the screen at all! Automatic methods of recording flight times, however, considerably reduce experimental errors of this sort.

We consider now errors arising from the tracers which the sensor wires do not pick up because of the finite yaw response of the pulsed-wire probe. In order to give some idea of the errors, the case of a normally distributed isotropic turbulent flow has been considered for which it is possible to obtain some surprisingly simple expressions (see appendix). If the probe is capable of picking up heat-tracer signals within two cones of half angle ϕ, one on either side of the pulsed wire, then the probability of missing a heat tracer is

$$p = \cos\phi \exp\left[\frac{-\sin^2\phi}{2(\overline{u^2}/U^2)}\right]. \tag{20}$$

It should be noted that as $\overline{u^2}/U^2 \to \infty$, then $p \to \cos\phi$ which, as one would expect, is simply the ratio of the area of the sphere subtended externally to the two cones to the total area of the sphere. The error arising from the missed 'tracers' in the case of the mean velocity is

$$\frac{E(U)}{U} = \frac{U_m - U}{U} = -p\cos^2\phi, \tag{21}$$

where U_m is the estimated mean velocity and U is the true mean velocity. In the case of the intensity, the error is

$$\frac{E((\overline{u^2})^{\frac{1}{2}})}{(\overline{u^2})^{\frac{1}{2}}} = \frac{((\overline{u^2})^{\frac{1}{2}})_m - (\overline{u^2})^{\frac{1}{2}}}{(\overline{u^2})^{\frac{1}{2}}} = \left[(1 - p\cos^2\phi) + \frac{p\cos^2\phi}{\overline{u^2}/U^2}[2 - \cos^2\phi(1+P)]\right]^{\frac{1}{2}} - 1. \tag{22}$$

In both cases, the 'missed' tracers are included in the estimates as zero-velocity results. For the sake of brevity, it is perhaps appropriate not to devote too much time to an analysis of these results since this can be left to the interested reader. However, as an example, figures 20 and 21 show the relative errors in mean velocity and intensity as a function of the turbulent intensity for probes with yaw limits of 50°, 60° and 70°. As far as mean velocity is concerned, the significance of these results needs to be considered fairly carefully in order to avoid obtaining an incorrect impression of the errors. For example, as the intensity tends to infinity, the relative error in mean velocity tends to $(-\cos^3\phi)$. However, the limit of infinite intensity corresponds in practice only to a turbulent free

stagnation point so that a finite relative error in the measurement of a zero mean velocity may not be too important! In many cases, it is more appropriate to relate the errors to some fixed reference velocity such as the free-stream velocity and, for the majority of experiments, even the 50° probe would give acceptable

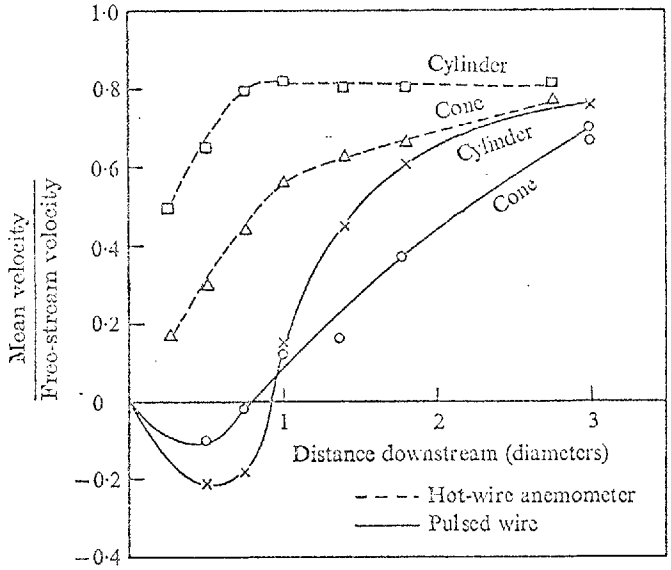


FIGURE 19. Pulsed-wire and hot-wire anemometer measurements of mean velocity behind a cylinder and a cone.

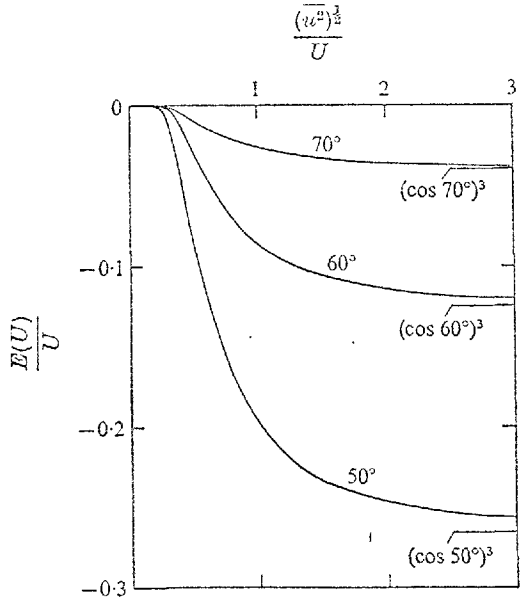


FIGURE 20. The error in the measurement of mean velocity due to the probe finite yaw response.

results for the measurement of mean velocity. The results for intensity are more intriguing. As the intensity tends to infinity, the relative error in the intensity tends to $-([1-\cos^3\phi]^{\frac{1}{3}}-1)$. Again, a probe with a yaw limit of 50° would be

acceptable for many experiments at these high turbulence levels. But, the intensity error also exhibits a maximum at a much lower intensity. This arises from the $(p\cos^2\phi)/(\overline{u^2}/U^2)$ term in equation (22) which has a maximum when $(\overline{u^2})^{\frac{1}{2}}/U = \sin\phi/2^{\frac{1}{2}}$ and, in fact, the maximum intensity error occurs very close to this intensity. The reason for this error must be that when the root-mean-square angle of the fluctuations is close to the yaw limit of the probe, the 'missed' tracers make a strong and erroneous contribution to the intensity measurement whereas, at the higher intensities, the probability of genuine zero-velocity signals occurring

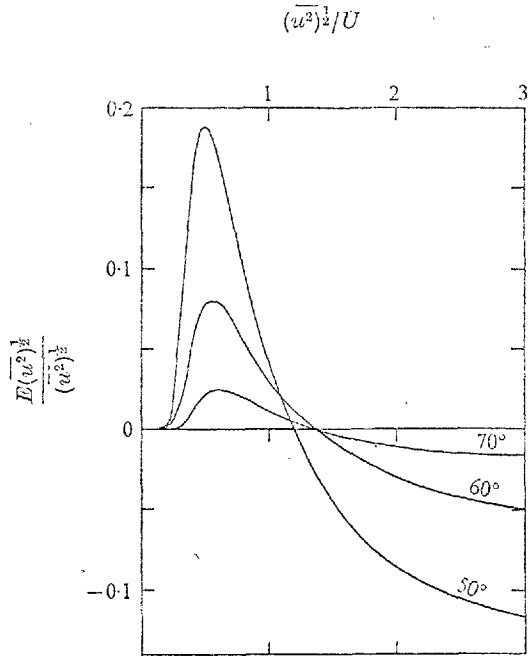


FIGURE 21. The error in the measurement of turbulent intensity due to the finite yaw response of the probe.

is higher, and the influence of the missed tracers is not then so significant. It would appear that if measurements over an extensive range of intensities are to be made, it is necessary to have a yaw limit of not less than, say, 60° if errors of 10 % or more are to be avoided.

In the discussion so far, the effect of the probe size relative to the length scales of the turbulence has been neglected. It has proved extremely difficult to make any analytic estimates of the effects of finite probe size but the following general comments may be of interest. There seem to be two main effects. The first concerns the effect of the probe size on the accuracy of the measurements. If we neglect for the moment the influence of longitudinal diffusion, the sensor wire of a large probe in turbulence would still exhibit a discontinuity of slope when the pulse front arrived. However, this time of flight would correspond to the most rapidly arriving part of the pulse front and it is not difficult to see that this would give rise to values of the mean velocity that were too large and values of intensity that were too small. The length of a sensor wire in a probe which intercepts signals

is of the order of $x((\overline{v^2})^{\frac{1}{2}}/U)$ where x is the spacing between the pulsed and sensor wires, and $((\overline{v^2})^{\frac{1}{2}}/U)$ is the ratio of the turbulent intensity along the wire axes to the local mean velocity normal to the probe. We might expect the error in the measurements to be a function of this length to some characteristic length scale of the energy bearing eddies, say, the integral scale, L_x. Attempts to estimate this error analytically have not yet proved successful, but a single experiment has been carried out in a turbulent stream with a turbulent intensity of about 45 %. In this experiment, measurements of both mean velocity and intensity were made with different spacings between the pulsed and sensor wires corresponding to a range from $0{\cdot}4L_x$ to $2{\cdot}0L_x$. No consistent variation in the mean velocity and intensity estimates with different spacings was found and, in fact, surprisingly good agreement with hot-wire anemometer measurements was obtained within the confidence limit of the sample size taken, in this case ± 4 % of the local mean velocity. It would appear therefore that probe size effects may be generally less significant than one might expect from a probe which has wire lengths typically two or three times those of an ordinary hot-wire anemometer probe. The other point to be considered on probe-size effects is the influence of the small-scale turbulence on the probe response. As a means of illustrating this problem it is useful to refer to figure 10(*b*) which shows a sensor-wire signal that is typical of those obtained in the present experiments in turbulent flows. There is little ambiguity about the arrival of the pulse front, but subsequently, the signal becomes irregular due to the presence of the turbulence. This irregularity is not important until it begins to obscure the arrival of the front. What seems to happen in practice is that if a probe is positioned in a particular flow, such as the reverse flow region behind a bluff body, and the mainstream speed is increased from zero, the sensor-wire signals begin by being very similar to those obtained in steady flow although the times of flight fluctuate considerably. As the Reynolds number is increased, the signal amplitudes diminish, as would be expected from the results of § 4.2, and, as the extent of the turbulence spectrum increases, the irregularity in the sensor-wire signals becomes more marked until a point is reached when the signals are so irregular that estimations of the times of flight are no longer possible. Numerous attempts have been made to estimate this effect theoretically assuming local isotropy of the small eddy structure. But, it has proved more difficult than one might expect to explain the observed behaviour of the probe, and, apart from the conclusion that it is best to have the largest scale of flow possible for a given Reynolds number, the results of the analysis have not been very useful. However, from a practical standpoint it seems possible with the normal scale of wind-tunnel experiments to obtain reasonable signals although it is clearly an advantage to have the scale of the experiments as large as the facilities will allow.

A number of examples of measurements with the pulsed hot-wire anemometer have now been published but, as a single example of the type of measurement that can now be made, figure 19 shows a comparison between pulsed-wire and linearized hot-wire measurements of mean velocity along the centre-line of the flow downstream of a circular cylinder and also an 18:1 tapered circular cylinder. These results were the first measurements made with the pulsed-wire probe

(Bradbury 1969) and, for a variety of reasons, they are perhaps the least satisfactory. However, they serve to illustrate the essential feasibility of the instrument for making measurements in flow regions where the hot-wire anemometer is subject to gross errors.

Tombach (1969) used the intercept technique for measurements with a cross-wire probe in a turbulent jet of foreign gas. There are a number of important differences between his work and the present investigations but the main one seems to be that the turbulence scale in his experiments was too small compared with the probe dimensions to give clear individual traces. As a consequence, the sensor-wire signals were digitized and an 'average' sensor-wire signal obtained on a computer. However, if this is done, the instrument immediately becomes highly non-linear and, in particular, estimates of the turbulent intensity become extremely difficult to make.

6. A system for the automatic measurement of the flight times

Measurements of the intercept positions from an oscilloscope are convenient only if there are a limited number of measurements to be made. An alternative scheme to speed up data aquisition has been studied using differentiated wire signals along the lines discussed in § 2.4. The complete circuitry of the system is shown in figure 9. Although this circuit may seem fairly formidable it took only a short while to develop using a modular instrumentation system developed by B. J. Belcher in the Aeronautics Department at Imperial College. This system used operational amplifiers and a variety of logic integrated circuits built into a range of modules with patch board front panels. These may be readily interconnected, and it is possible to build up fairly sophisticated systems without too much development work.

The basic sensor-wire signal is first amplified and differentiated, see the first inset diagram in figure 9. Because of the subsequent deterioration in signal-to-noise ratio, it is necessary to pass the resulting signal through a low pass filter set at about 10 kHz. As a result of both the differentiation and the filtering, the pick-up signal from the pulsed wire at the beginning of the sensor-wire trace is considerably longer than the original pulse, and it has a decay time constant typically of the order of 100 μsec. The differentiated signal is then fed to two comparators which are set to trigger at a voltage of about a half the maximum value of the differentiated signal. As discussed earlier, the setting of the comparator trigger level is not too critical. The comparators are set to trigger off signals of opposite polarity so that outputs are obtained irrespective of the flow direction. In addition to the signal from the heat pulse, the comparators are also triggered by the initial pick-up signal so that the signals from the comparators are similar to the two lower traces shown in the second inset diagram in figure 9. The comparator outputs arising from the electrical pick-up signal are eliminated by passing the comparator outputs through two AND gates which are initially blanked off by a pulse of about 100 μsec duration, and which is produced from the pulse generator at the same time as the heat-tracer pulse is fired. Signals similar to those shown in the third inset diagram in figure 9 are then obtained.

These two AND gate outputs are then fed into two RS Flip Flops which produce step-like signals with a duration equal in length to the time from the firing of the heat-tracer pulse to the arrival of a signal at the sensor wires sufficient to trigger the two comparators. Both comparators may be triggered by the heat-tracer signal from the one sensor wire because the differentiated sensor-wire signal swings both positively and negatively, but it is obviously the shorter of the two times which corresponds to the desired time of flight. The selection of the shorter time step is obtained by passing the flip-flop outputs through an OR gate (fourth

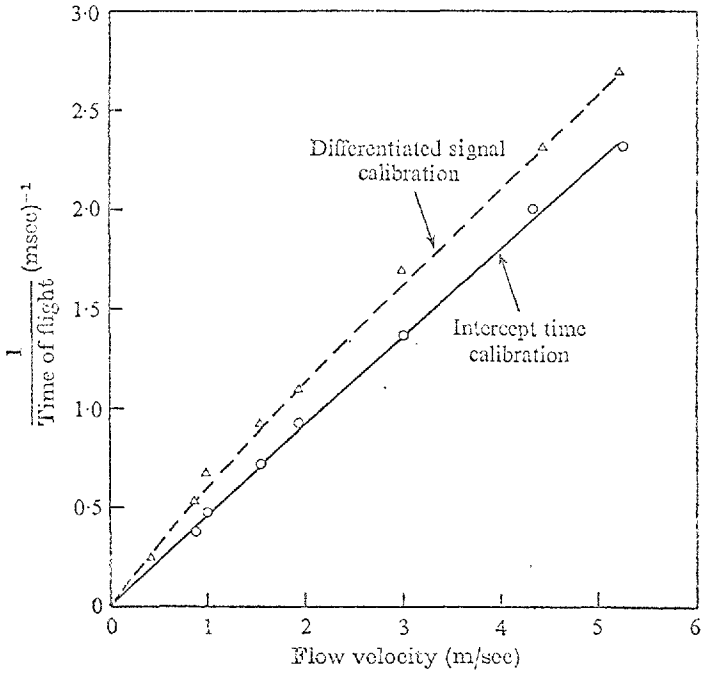


FIGURE 22. Comparison between a differentiated signal calibration and an intercept time calibration.

diagram in figure 9). The OR gate output is then fed through an operational amplifier with an accurately clamped maximum output voltage level so that it gives a pulse of fixed amplitude with a duration equal to the time of flight. This is fed to an integrator which produces a ramp whose final amplitude is proportional to the time of flight. This is then passed through a switched amplifier which produces a final output with a polarity dependent on which of the two comparators is triggered first. The fifth diagram in figure 9 shows the two types of switched amplifier output that can occur – one in which the integrator polarity is correct and the other where the polarity is switched on the arrival of the heat pulse. Therefore, the final output is a d.c. voltage whose amplitude is proportional to the time of flight and whose polarity gives the flow direction. In the present arrangement, this voltage is displayed on a digital voltmeter and the value punched out on paper tape.

Figure 22 shows a calibration from a differentiated sensor-wire signal compared

with the intercept time calibration. The calibration is now slightly curved as would be expected from the theoretical arguments in § 2.4. But, this slight non-linearity can be removed in the subsequent computation of the velocities.

Numerous measurements have now been made with this automatic system in a variety of flows and they confirm the usefulness of the technique in studying highly turbulent flows. It is, of course, possible to set up different circuitry to automatically measure the time of flight and the precise choice is probably best dictated by what type of instrumentation is available to the experimenter.

7. Concluding remarks

This paper has described the results of both theoretical and experimental investigations into a pulsed-wire probe using a time-of-flight technique for velocity measurements. The technique seems to have considerable potential for exploring highly turbulent flows which hitherto have not been amenable to proper experimental investigation. However, although the present work represents a start on the development of the technique, it is clear that there are many aspects of the probe behaviour that requires further investigation. These include the yaw response, the influence of the pulsed-wire wake and the general behaviour of the probe at very low Péclet numbers. Also, there is clearly a need for developing the technique in a form which makes it simpler to use. The particular system explored in the present work is clearly workable, but other techniques perhaps along the lines suggested in § 2.4 should also be investigated.

In addition to the applications described in this paper, the technique could also be used in gas mixtures and, in fact, Mequaid & Wright (1971) have already made an interesting application of the pulsed-wire probe to measurements in a low turbulence level flow of variable density. Another possible application is to use two probes for more elaborate spatial and temporal correlation measurements.

There are, of course, other techniques which are being developed for use in highly turbulent flows. Multiple hot-wire arrays could possibly be used although the 'untangling' of the results might require a prohibitive effort. Also, the accuracy of hot-wire anemometer measurements depends on a sensitive 'analog' calibration whereas the pulsed-wire calibration depends only on the probe geometry – it is very nearly a 'digital' instrument. In addition, the application of laser Doppler techniques for velocity measurement are currently being studied. But, although the potential of these techniques is considerable, they involve a high degree of sophistication in instrumentation and, for many applications, the use of a somewhat simpler technique such as the pulsed-wire probe may be more appropriate.

Appendix. Errors due to the finite yaw response of a pulsed-wire probe

For a normally distributed isotropic turbulence, the joint probability density function is

$$f(u,v,w) = \frac{1}{(2\pi\overline{u^2})^{\frac{3}{2}}} \exp\left[\frac{-(u-U)^2-v^2-w^2}{2\overline{u^2}}\right].$$

The probability of missing a tracer is

$$p = 1 - \iiint_{\text{cones}} f(u,v,w)\,du\,dv\,dw,$$

where the integration is restricted to the two cones on either side of the pulsed wire within which the sensor wires will pick up signals. If we introduce a radial velocity $v_r = (v^2+w^2)^{\frac{1}{2}}$ inclined at an angle ψ to the xy plane, we have

$$v = v_r \sin\psi, \quad w = v_r \cos\psi.$$

For the downstream cone with a half angle ϕ, this change of co-ordinates gives

$$I_d = \iiint_{\substack{\text{downstream}\\ \text{cone}}} f(u,v,w)\,du\,dv\,dw$$
$$= \frac{1}{(2\pi\overline{u^2})^{\frac{3}{2}}} \int_0^\infty \left[\int_0^{u\tan\phi} \int_0^{2\pi} v_r \exp\left[\frac{-(u-U)^2 - v_r^2}{2\overline{u^2}}\right] d\psi\, dv_r \right] du.$$

It should be noted that the upper limit on the integration with respect to v_r is $u\tan\phi$ which ensures that the integration is limited to the downstream cone. The evaluation of this integral is straightforward (see Castro 1970) and it gives

$$I_d = \frac{1}{2}\left(1 + \operatorname{erf}\frac{U}{(2\overline{u^2})^{\frac{1}{2}}}\right) - \tfrac{1}{2}\cos\phi \exp\left[-\frac{\sin^2\phi}{2(\overline{u^2}/U^2)}\right]\left(1 + \operatorname{erf}\frac{U\cos\phi}{(2\overline{u^2})^{\frac{1}{2}}}\right).$$

The integral for the upstream cone is obtained by writing $-U$ for U in this expression and the probability of missing a tracer then reduces to

$$p = \cos\phi \exp\left[\frac{-\sin^2\phi}{2(\overline{u^2}/U^2)}\right]$$

which is equation (20) in the main text.

The measured mean velocity including the missed tracers as zero velocity results is given by

$$U_m = \iiint_{\text{cones}} u f(u,v,w)\,du\,dv\,dw.$$

The measured intensity including the missed tracers is given by

$$\overline{u_m^2} = \iiint_{\text{cones}} (u-U_m)^2 f(u,v,w)\,du\,dv\,dw + pU_m^2$$
$$= \iiint_{\text{cones}} u^2 f(u,v,w)\,du\,dv\,dw - U_m^2,$$

where it should be noted that the intensity is evaluated relative to the estimated mean velocity and not to the true mean velocity. This seems a more consistent approach to adopt. The evaluation of these integrals is tedious but it results finally in the expressions given in the main text as equations (21) and (22).

REFERENCES

BAUER, A. B. 1965 Direct measurement of velocity by hot wire anemometry. *A.I.A.A. J.* 3, 1189.

BRADBURY, L. J. S. 1969 A pulsed-wire technique for velocity measurements in highly turbulent flows. *NPL Aero Report* 1284.

BRADBURY, L. J. S. & CASTRO, I. P. 1971 Some comments on heat transfer laws for fine wires. *J. Fluid Mech.* To be published.

CASTRO, I. P. 1970 The pulsed wire anemometer – an analysis to determine the errors caused by the probe finite yaw response. *Imperial College Aeronautics Dept. Report.*

CASTRO, I. P. 1971 Wake characteristics of two-dimensional perforated plates normal to an airstream. *J. Fluid Mech.* 46, 599.

COLLIS, D. C. & WILLIAMS, N. J. 1959 Two-dimensional convection from heated wires at low Reynolds numbers. *J. Fluid Mech.* 6, 357.

MANDEL, J. 1964 *The statistical analysis of experimental data.* New York: Interscience.

MCQUAID, J. & WRIGHT, W. 1971 The measurement of fluctuating velocities in flows of gas mixtures using a pulsed wire anemometer. To be published.

TOMBACH, I. H. 1969 Velocity measurements with a new probe in inhomogeneous turbulent jets. Ph.D. thesis, California Institute of Technology.

APPENDIX II

This Appendix is a copy of a paper published in Journal of Fluid Mechanics (1972), 51, Pt. 3, 487.

The authors were jointly responsible for all the work described in this paper.

APPENDIX II

Some comments on heat-transfer laws for fine wires

By L. J. S. BRADBURY† AND I. P. CASTRO

Aeronautics Department, Imperial College, London

(Received 24 September 1970 and in revised form 3 August 1971)

The semi-empirical heat-transfer laws of Collis & Williams (1959) and Davies & Fisher (1964) give values of the heat-transfer rates for the flow past fine wires which are generally very different from one another. This paper describes some measurements of heat-transfer and convective time constants which show that the relationship of Collis & Williams is the more representative expression.

1. Introduction

During an investigation into a pulsed-wire technique of velocity measurements (Bradbury & Castro 1971) it was necessary to make use of a heat-transfer law for the flow past heated fine wires of the sort used in hot-wire anemometry. Two apparently careful investigations of this heat-transfer law are those of Collis & Williams (1959) and Davies & Fisher (1964). The heat-transfer law proposed by Collis & Williams for the wire Reynolds number range $0{\cdot}02 < R < 44$ (R based on the diameter of the wire) is given by

$$N_m(\theta_m/\theta_a)^{-0{\cdot}17} = 0{\cdot}24 + 0{\cdot}56R_m^{0{\cdot}45}, \tag{1}$$

where θ_a is the ambient fluid temperature and θ_m is the mean of the fluid and wire temperatures. The fluid thermal conductivity and the kinematic viscosity appearing in the Nusselt number N_m and the Reynolds number R_m are evaluated at this mean temperature. In contrast to this expression, Davies & Fisher proposed the following relationship:

$$N_h = 0{\cdot}425R_a^{\frac{1}{2}}, \tag{2}$$

where the thermal conductivity appearing in the Nusselt number N_h is evaluated at the wire temperature and the kinematic viscosity appearing in the Reynolds number R_a is evaluated at the ambient fluid temperature. It will be noted that the suffices a, h and m are used to denote quantities evaluated at the ambient fluid temperature, the hot-wire temperature and the mean of the two respectively.

These two laws are generally very different from one another, and in order to illustrate this, figure 1 shows a comparison between the two laws for wires at essentially ambient temperature and at 600 °C. In order to make a direct comparison between the heat-transfer rates predicted by the two laws the Nusselt numbers have been calculated from (1) and (2) and then converted to a common form based on fluid properties evaluated at ambient temperature. A similar adjustment to the Reynolds numbers has also been made. At the lower temperature there is almost a two to one difference in the heat-transfer rates predicted by

† Present address: Mechanical Engineering Department, University of Surrey.

the two laws, but as the wire temperature is increased this difference decreases until the two laws are almost coincident at 600 °C.

Because of the common usage of constant-temperature hot-wire anemometers there is less interest in the precise form of fine wire heat-transfer laws than in the days when constant-current hot-wire anemometry predominated. Nevertheless,

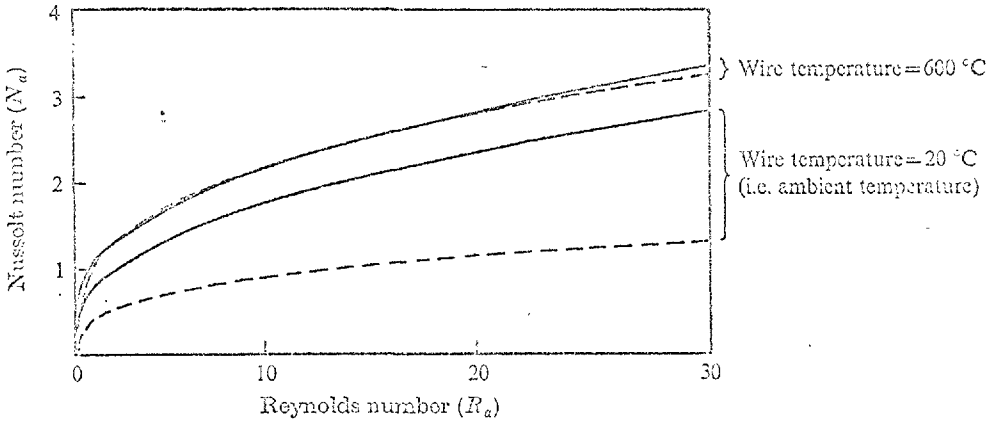


FIGURE 1. Comparison of heat-transfer laws for fine wires. ——, Collis & Williams; – – – –, Davies & Fisher.

it is obviously important to resolve discrepancies of the sort found between the relationships of Collis & Williams and Davies & Fisher. This was the aim of the experiments described in this paper. It should be made clear that these experiments were not intended as a definitive study of heat-transfer laws, but in view of the size of the discrepancy between equations (1) and (2) it seemed that a few reasonably careful measurements ought to be sufficient to show which of the two laws is the more representative for the heat transfer from fine wires.

The results of the present measurements strongly support relationships of the type suggested by Collis & Williams. The experiments consisted not only of heat-transfer measurements but they also included some direct measurements of wire convective time constants. These latter measurements give some particularly pertinent results for deciding between the relative validity of the two laws.

2. Heat-transfer measurements

The two quantities that have to be evaluated from the experimental results are the wire Reynolds number R and the Nusselt number N. In practical terms the Nusselt number can be written as

$$N = \frac{i^2 r_h}{\pi k_f l} \frac{\alpha r_0}{(r_h - r_a)},$$

where r_h and r_a are the wire resistances at the hot-wire temperature θ_h and the fluid ambient temperature θ_a respectively. α is the temperature coefficient of resistance, i is the current through the wire of length l and diameter d, k_f is the fluid thermal conductivity. There is no disagreement between Davies & Fisher and other experimenters over the ability to measure i, r_h and l accurately;

the nub of their criticism of previous work concerns the measurement of α and r_a. Their contention is that measurements of these quantities are carried out at very low current densities and are likely to be in error by as much as 20 % owing to the influence of thermo-electric effects present in the bridge network used for making the measurements. The effect of this error would be particularly significant at very low overheat ratios, and they claim that heat-transfer measurements at low wire temperatures must be regarded as unreliable. However, no evidence of Peltier effects of the type described in their experiments could be found in the present work.

Nominal diameter (in.)	Measured diameter (in.)	Resistance per centimeter at 20° C. (Sample lengths of about 0·5 cm)	Resistivity at 20 °C (ohm cm)
0·0002	$0{\cdot}000203 \pm 5 \times 10^{-6}$	51·9	10·6
0·0003	$0{\cdot}000315 \pm 10 \times 10^{-6}$	22·5	11·3
0·0004	$0{\cdot}000412 \pm 14 \times 10^{-6}$	13·4	11·5
		Average value	11.2

TABLE 1. Platinum wire

An ordinary Wheatstone bridge was used for the heat-transfer measurements. The variable arm consisted of a high-quality decade resistance box and the fixed arms used wire wound resistors of 0·01 % accuracy. The current through the wires was obtained by measuring the voltage drop across the fixed resistor in series with the hot wire. This voltage was measured on a four decade digital voltmeter with a least significant figure equivalent to 2·5 microvolts on its most accurate range. This voltmeter was also used to balance the bridge.

The wires used in the majority of the experiments were platinum Wollaston wires from Johnson, Matthey & Co. Ltd. The platinum used in Wollaston wire is not pure but apparently contains about 0·3% of iridium and rhodium. Samples of the wires after etching were examined under a scanning electron microscope and a typical example is shown in figure 2(*a*) (plate 1). An interesting feature of the platinum wires is the longitudinal striations on the surface. Presumably these arise from the drawing process used in their manufacture. Variations in diameter (or roundness) over the length of the samples examined were not very significant although, on the basis of resistance measurements, there were perhaps more consistent variations of about 5 % over longer lengths of the wire. A few measurements were also made with nickel wire† (nominal diameter of 0·0005 in.) and figure 2(*b*) (plate 1) shows a sample of this wire. This was a sample of wire from an old reel of nickel wire and some oxidation of the surface had clearly taken place.

The 'cold' resistances of the electron microscope samples were measured and table 1 summarizes the results for the platinum wires.

† The object of the nickel wire tests was to check that if the thermo-electric effects were arising from the wire junctions then tests with a different wire material might show some inconsistency.

The wires used in the heat-transfer measurements were mounted on a probe giving a wire length usually of about one centimetre so that aspect ratios ranged from about 1000 to 2000. A number of wires were used in the experiments and table 2 gives the 'cold' resistance per unit length of these wires. These values differ slightly from those from the electron microscope samples given in table 1. This is presumably because of small variations in the wire diameter.

Nominal diameter (in.)	Resistance per centimetre	Estimated mean diameter (in.)
0·0002	49·0	0·00021
0·0003	22·2	0·00032
0·0004	12·2	0·00043

TABLE 2

The temperature coefficient of resistance of the wires was measured by mounting the probes in a test tube immersed in a variable-temperature water bath. The temperature coefficient of resistance was found to be 0·0035 per °C for the platinum wire and 0·0059 per °C for the nickel wire.

A criticism by Davies & Fisher of previous work was that 'cold' resistance measurements were probably in error owing to stray thermo-electric voltages present in the bridge network; they cited an example in their own experiments of how this could give rise to errors, typically of 20 %, in the values of cold resistance measurement. However, in the present experiments measurements of 'cold' resistance levelled off as the current through the wires was reduced and the values did not increase again – as they did in the example quoted by Davis & Fisher – even though the current densities and dissipation levels were extended well below those reported by Davies & Fisher. They also attributed the apparent departure of the wire material properties from the International Standard values as being a result of these thermo-electric effects. However, the influence of iridium and rhodium impurities in platinum is to increase the resistivity and reduce the temperature coefficient. Results given by Darling (1961) and Rhys & Taimsalu (1969) show that the observed differences are of about the right order for an impurity level of 0·3 %. Since no significant thermo-electric effects could be found in the present experiments, it is concluded that the departures found both in the present experiments and those previously carried out by Collis & Williams and others would seem to be genuine, although the evidence is admittedly circumstantial.

The measurements of the Nusselt number were made in a low turbulence stream with wire temperatures ranging from between 20 °C and 600 °C above ambient temperature. Most of the tests were carried out with wires whose aspect ratios were in the range 1000 to 2000. However, two tests were also carried out with wires of lower aspect ratios of about 270 and 800. All the results were corrected for aspect ratio effects using the simple relationship

$$N_{\mathrm{u}}(\infty) = N(m)\left[1 - \frac{d}{l}\left(\frac{k_w}{k_f N(m)}\right)^{\frac{1}{2}}\right],$$

where $N(m)$ is the measured Nusselt number and $N(\infty)$ is the corrected Nusselt number for an infinite wire, k_w is the thermal conductivity of the wire material and k_f is the thermal conductivity of the fluid. This expression can be derived on the assumption that the aspect ratio is large and that the overheating ratio is small. Whilst these conditions were not strictly fulfilled in all the test cases, the object of the tests at the lower aspect ratios was to check the overall consistency of the experimental results.

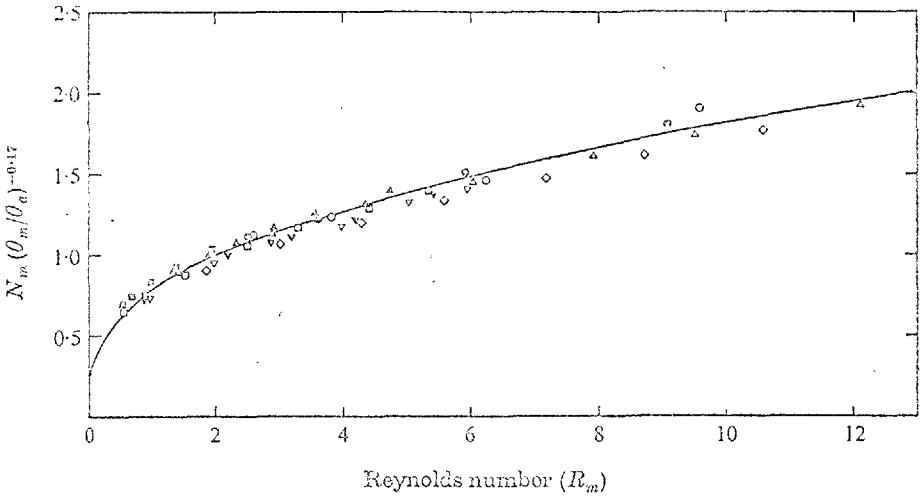


FIGURE 3. Heat-transfer results compared with the Collis & Williams law (solid line). □, ⊡, 0·0002 in. Pt wire, aspect ratio. 1760, wire temperature 125 °C, 507 °C above ambient respectively; ○, ⊙, 0·0003 in. Pt wire, aspect ratio 1850, wire temperature 20 °C, 40 °C above ambient respectively; ▽, 0·0003 in. Pt wire, aspect ratio 274, wire temperature 100 °C above ambient; ▽, 0·0004 in. Pt wire, aspect ratio 795, wire temperature 125 °C above ambient; △, ▲, 0·0004 in. Pt wire, aspect ratio 1350, wire temperature 145° C, 615 °C above ambient respectively; ◇, 0·0005 in. Ni wire, aspect ratio 1270, wire temperature 105 °C above ambient.

At the lowest aspect ratio tested, the correction amounted to about 15 % on the Nusselt number whereas the correction for the other results was only a few per cent. However, although the consistency of the final correlation was not greatly affected by the correction, it served to demonstrate that there is no unexpected influence of aspect ratio on the measurements. These few aspect ratio tests were undertaken as a precautionary measure because Davies & Fisher's measurements were all carried out at comparatively low aspect ratios and it seemed expedient to check the possibility of some untoward aspect ratio effect.

The experimental results are shown first in figure 3 plotted in terms of the fluid properties evaluated at the mean temperature. They show good agreement with Collis & Williams' relationship and there is no systematic difference between the high and low overheat ratio results. The nickel wire results are also reasonably consistent with the platinum wire results. In contrast to this, figure 4 shows some selected results at two extreme overheating ratios evaluated first on the mean temperature basis as in figure 3 (unblocked symbols) and then with the thermal

conductivity of air evaluated at the wire temperature and the kinematic viscosity evaluated at ambient temperature (blocked symbols). The effect of using the temperature loading suggested by Davies & Fisher is to spread out the experimental points and, as might be expected from figure 1, it is only at temperatures in the region of 600 °C that good agreement with their relationship is found. It seems almost inconceivable that errors due to Peltier effects should be the same in both the present experiments and the work of Collis & Williams, and the

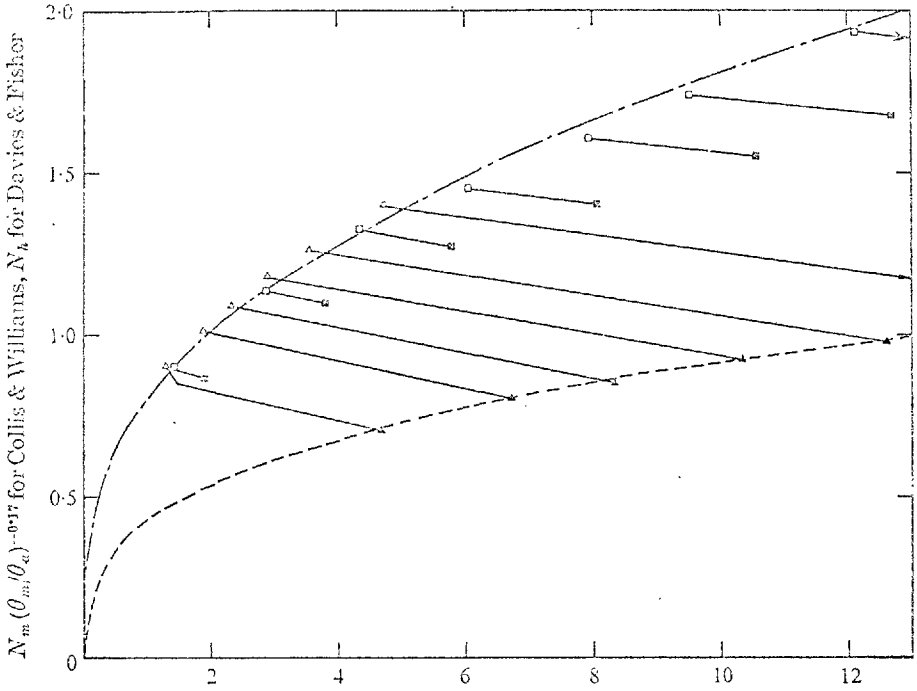


FIGURE 4. The influence of the reference temperature on the heat-transfer results. – – –, Davies & Fisher; ——, Collis & Williams. 0·0004 in. Pt wire, aspect ratio 1350; □, ■, 145 °C; △, ▲, 615 °C; unblocked symbols based on the mean temperature; blocked symbols based on the wire temperature for k and the ambient temperature for ν.

obvious conclusion is that Davies & Fisher's relationship is not satisfactory for a wide range of temperatures. However, it could be argued that we have only repeated the errors of earlier experiments and for this reason it is pertinent to include some direct measurements of wire convective time constants that have been made.

3. Measurements of the convective time constants

In the pulsed-wire experiments by the authors, the wires were subject to a very short duration voltage pulse and then permitted to cool by forced convection. By operating the wires with a small constant current passing through them it was possible to observe the decay of the wire temperature. If we neglect the possible

influence of variations of fluid properties during the decay, this decay should be exponential with a time constant given by $\rho_w c_w d^2/4k_f N$, where ρ_w and c_w are the density and specific heat of the wire material respectively, d is the wire diameter, k_f is the thermal conductivity of the fluid and N is the Nusselt number. In fact, the observed decays were indistinguishable from an exponential decay and a whole series of time constant measurements were made with different diameter wires at two values of the initial wire temperature of about 250 °C

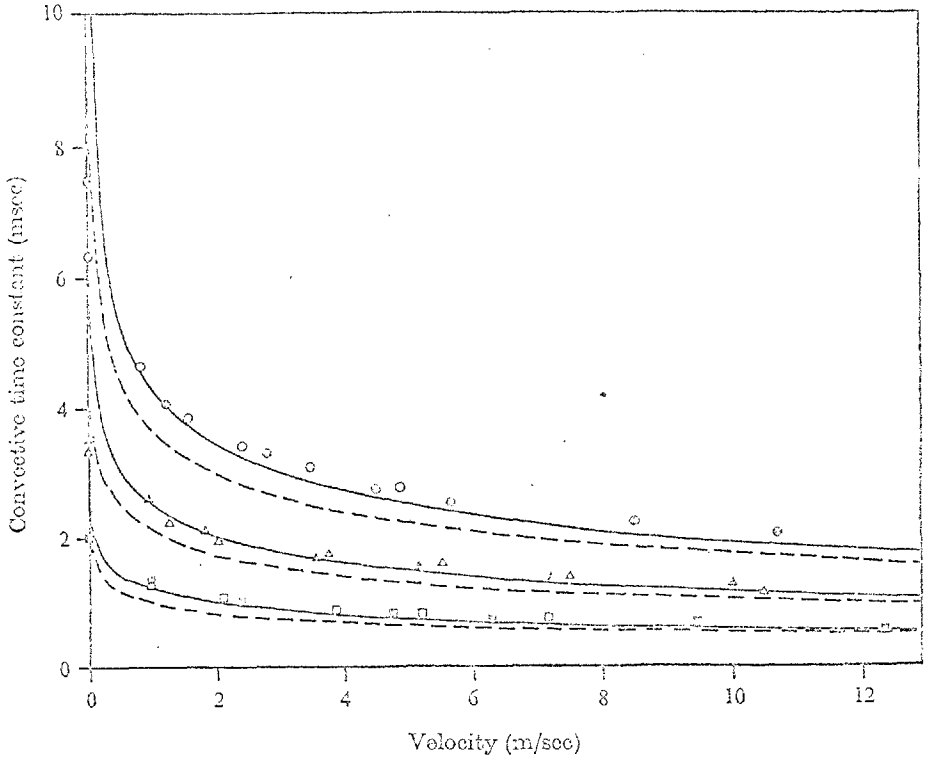


FIGURE 5. Convective time constants for platinum wires. Curves show Collis & Williams' law; ——, ambient mean temperature; – – –, 300 °C mean temperature; the upper, middle and lower pairs of curves refer to wires of diameters 0·00043 in., 0·00031 in. and 0·0021 in. respectively. ○, ●, 0·00043 in. diameter; △, ▲, 0·00031 in. diameter; □, ■, 0·00021 in. diameter; unblocked symbols refer to peak temperatures of 550 °C; blocked symbols are results for peak wire temperatures of 250 °C.

and 500 °C. The results of these measurements are shown in figure 5. The interesting feature of these results is that there does not seem to be any measurable influence of the initial temperature on the decay time. This suggests that the product $k_f N$ in the time constant denominator should not depend on temperature. Although neither the relationship of Collis & Williams nor that of Davies & Fisher is entirely consistent with this finding, the Collis & Williams relationship gives values of $k_f N$ which are far less sensitive to wire temperature than those obtained from Davies & Fisher's expression. To illustrate this figure 5 also shows the time constants calculated from Collis & Williams expression for mean wire

temperatures of 300 °C and ambient temperature. The ambient temperature results are close to the experimental values but the higher temperature calculations show some influence of temperature on the time constants which one might have expected to be observable in the experimental results. If, however, the time constants are calculated using Davies & Fisher's relationship, there is a much greater influence of the temperature used. To give one example figure 6 shows the measured time constants for the 0·0004 in. diameter wire compared with time constants obtained from Davies & Fisher's relationship for two hot-wire temperatures of 600 °C and essentially ambient temperature. The influence of temperature is far more significant and the decay times differ considerably from those observed. The point about these time constant measurements is that they are not dependent on measurements of cold resistance in the same way as the heat-transfer measurements and they therefore provide separate support for the greater validity of the Collis & Williams relationship. However, the apparent insensitivity of the decay times found in the experimental results suggests that even the Collis & Williams relationship may not necessarily represent the best compromise for an empirical heat-transfer law.

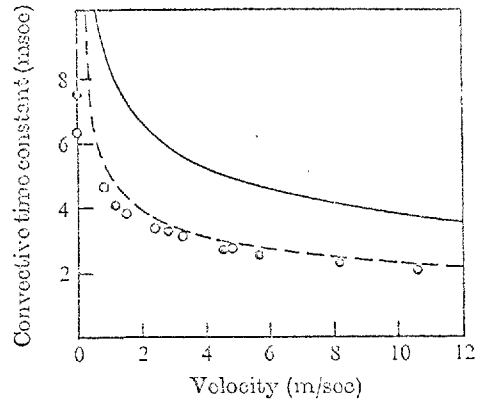
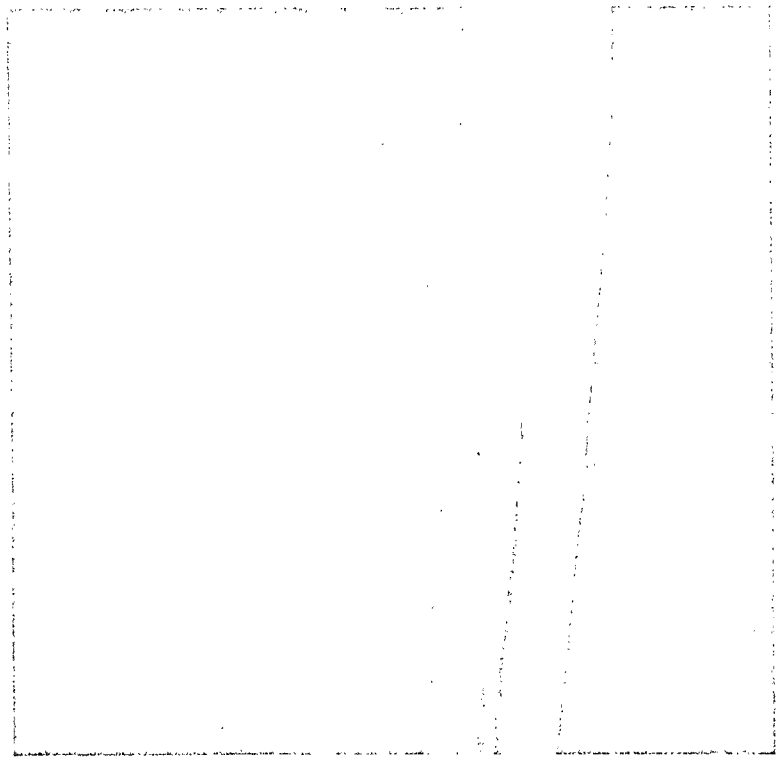


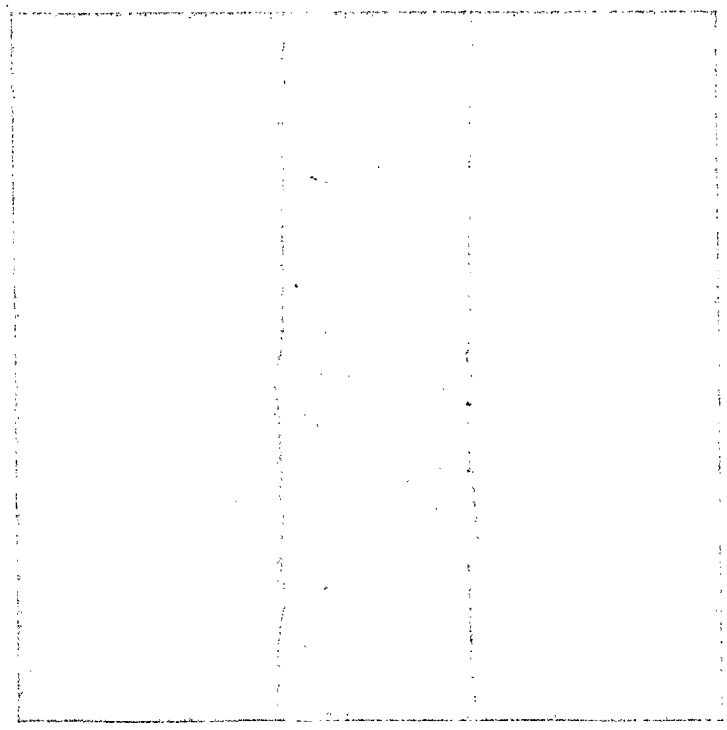
FIGURE 6. Convective time constants for 0·00043 in. diameter platinum wires. ——, Davies & Fisher, wire at ambient temperature; – – –, Davies & Fisher, wire at 600 °C. Unblocked symbols refer to peak temperatures of 550 °C, blocked symbols are results for peak temperatures of 250 °C.

4. Concluding remarks

There is a considerable discrepancy between the heat-transfer relationship proposed by Collis & Williams (1959) and Davies & Fisher (1964). On the basis of the present experiments it would appear that the Collis & Williams relationship is the more representative expression for a wide range of wire temperatures. However, the wire convective time constant measurements would appear to show that a reference temperature more heavily weighted towards ambient temperature would be more appropriate for collapsing heat-transfer results than the mean temperature.



(*a*)



(*b*)

FIGURE 2. Electron microscope photographs of the wires. (*a*) 0·0002 in. diameter platinum, (*b*) 0·0005 in. diameter nickel.

BRADBURY AND CASTRO

(*Facing p.* 493)

REFERENCES

BRADBURY, L. J. S. & CASTRO, I. P. 1971 A pulsed-wire technique for velocity measurements in highly turbulent flows. *J. Fluid Mech.* 49, 657–691.

COLLIS, D. C. & WILLIAMS, M. J. 1956 Two-dimensional convection from heated wires at low Reynolds numbers. *J. Fluid Mech.* 6, 357–389.

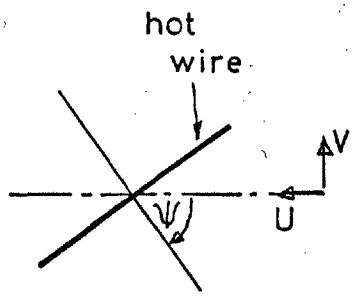
DARLING, A. S. 1961 Rhodium–platinum alloys. *Platinum Metals Rev.* no. 2.

DAVIES, P. O. A. L. & FISHER, M. J. 1964 Heat transfer from electrically heated cylinders. *Proc. Roy. Soc.* A 280, 486–527.

RHYS, D. W. & TAIMSALU, P. 1969 Effect of alloying additions on the thermo-electric properties of Platinum. *Englehard Tech. Bull.* 16, no. 2.

APPENDIX III

ANALYSIS OF CROSSED-HOT WIRE DATA



For a hot wire inclined at $(90 - \psi)^{o}$ to the x-direction (usually, but not always the direction of the mean flow) the basic response equation can be written, assuming a cosine-law response

$$E^2 = E_o^2 + B\,(U\cos\psi + V\sin\psi)^n \quad . \qquad \text{AIII.1}$$

where E, U and V are all instantaneous values. For the present work we have used an 'effective' cosine law response and measured the 'effective' angle, ψ_e, as described in Chapter 2. ψ_e is not exactly equal to the geometrical angle ψ. In this Appendix ψ is written for ψ_e. Equation AIII.1 neglects the presence of any W component of velocity (which of necessity is normal to the axis of the wire). However it can be shown that, if there is no mean W and if the w-fluctuations are small compared with the mean value of $(U\cos\psi + V\sin\psi)$, the errors are small.

The mean flow calibration was always performed in a non-turbulent free stream with V = 0, so that

$$E^2 = E_o^2 + B\cos^n\psi . U^n \quad . \qquad \text{AIII.2}$$

Throughout this work we have required turbulence quantities non-dimensionalised by the reference velocity, U_r, so that it is convenient to write

$$B\cos^n\psi = \frac{E_r^2 - E_o^2}{U_r^n} \quad .$$

Substituting in equation AIII.2 gives

$$\left(\frac{E^2 - E_o^2}{E_r^2 - E_o^2}\right) \cdot \cos^n\psi = \frac{U\cos\psi + V\sin\psi}{U_r} \quad . \qquad \text{AIII.3}$$

It is now not necessary to measure the slope of the calibration curve directly: a simple measurement of the reference velocity (i.e. dynamic pressure) enables $E_r^2 - E_o^2$ to be read off the calibration.

For a crossed wire probe with effective angles ψ_1 and $-\psi_2$ we have, from equation AIII.3

$$\left[\frac{E_1^2 - E_o^2}{E_{1_r}^2 - E_o^2}\right]^{1/n} \cos\psi_1 = \frac{U}{U_r}\cos\psi_1 + \frac{V}{U_r}\sin\psi_1$$

and

$$\left[\frac{E_2^2 - E_o^2}{E_{2_r}^2 - E_o^2}\right]^{1/n} \cos\psi_2 = \frac{U}{U_r}\cos\psi_2 - \frac{V}{U_r}\sin\psi_2 \quad . \qquad \text{AIII.4}$$

Solving equations AIII.4 for U and V gives

$$\frac{U}{U_r} = \frac{\left[\frac{E_1^2 - E_{o_1}^2}{E_{1_r}^2 - E_{o_1}^2}\right]^{1/n} \cdot \tan\psi_1 + \left[\frac{E_2^2 - E_{o_2}^2}{E_{2_r}^2 - E_{o_2}^2}\right]^{1/n} \tan\psi_2}{\tan\psi_1 + \tan\psi_2}$$

and

$$\frac{V}{U_r} = \frac{\left[\frac{E_1^2 - E_{o_1}^2}{E_{1_r}^2 - E_{o_1}^2}\right]^{1/n} + \left[\frac{E_2^2 - E_{o_2}^2}{E_{2_r}^2 - E_{o_2}^2}\right]^{1/n}}{\tan\psi_1 + \tan\psi_2} \qquad \text{AIII.5}$$

Programs DIGAN and CS4C compute $\frac{U}{U_r}$ and $\frac{V}{U_r}$ by adding the mean values of E_1 and E_2 (inputed on cards) to the fluctuating parts e_1 and e_2 (from the A/D conversion) and substituting in equation AIII.5. Program CS4C (used only to obtain the intermittency) forms the various powers and cross-products of U and V at this stage and then at the end of the program subtracts the necessary terms involving the mean values

(e.g. $\overline{uv} = \overline{UV} - \overline{U}.\overline{V}$). This has the disadvantage of magnifying the errors caused by the presence of any small spurious d.c. levels on the incoming e_1 and e_2 signals. Program DIGAN is therefore arranged to subtract the mean values of $\overline{U}$ and $\overline{V}$ from equation AIII.5 before forming the quantities of interest. The mean of the resulting signals ($\overline{u}$ and $\overline{v}$) should then be zero and any small deviations from zero are caused by

(i) small d.c. errors on the incoming signals.

(ii) Errors caused by using $\overline{U}$ and $\overline{V}$ calculated using equation AIII.5 and $\overline{E_1}$ and $\overline{E_2}$. These will only be noticeable at high turbulent intensities.

The final results are corrected by subtracting any small d.c. terms, as in CS4C but it can be shown that this procedure gives results less dependent on the spurious d.c. levels.

APPENDIX IV

STATISTICS OF THE INSTANTANEOUS VELOCITY VECTOR AND THE CONSEQUENT ERRORS IN HOT-WIRE MEASUREMENTS

IV.1 THE PROBLEM

In a turbulent flow the velocity vector not only varies in magnitude but also, because turbulence is by nature a three-dimensional phenomenon, varies in its orientation to some fixed axis system. All conventional measurement techniques therefore require a knowledge of the yaw (and pitch) response of the instrument. In many practical cases it is sufficient to assume that variations in the angle of the instantaneous velocity vector are small (usually because the turbulent intensity, measured with respect to the local mean velocity, is small) so that the instrument is only required to operate in a known fashion over a small range of flow yaw angle. Most round-nosed pitot tubes for instance, measure the total pressure accurately as long as the flow angle never exceeds 15 - 20° from the probe axis. Similarly, hot-wires can be assumed to obey the cosine law for flow angles greater than about 20° from the wire axis. In such cases it is of course usually unnecessary to have a detailed knowledge of the flow-angle probability function.

However, in flows having high turbulent intensities, the probability of instantaneous flow angles being greater than the limit of the instruments defined yaw response is not necessarily small, and in this case there may well be significant errors. Generally, a knowledge of the flow angle probability distribution would not in itself permit an accurate assessment of such errors (except in the case of the pulsed hot wire anemometer which is essentially a digital

instrument) but it would certainly be helpful to know when the errors are likely to be large. Put another way, the problem can be stated as 'how high must the turbulent intensity be before errors caused by the instrument's inadequate (or ill-defined) yaw response become significant?'

To answer this question it is clearly necessary to have some detailed information about the flow angle statistics and the first part of this Appendix presents some basic theory with that in mind. Secondly, of course, the answer will depend on the particular instrument used and, whilst this work was motivated by interest in the pulsed hot-wire anemometer, the second part of the Appendix is an attempt to apply the conclusions of the first part to the ordinary hot-wire anemometer and in particular, the crossed hot-wire.

There is no fundamental reason why the theoretical considerations should not be applied to any instrument and indeed Castro[45] has applied them to the case of the pulsed hot wire where in certain circumstances it is possible to derive analytical expressions for the actual errors caused by the probe's finite yaw-response.

IV.2 THE FLOW ANGLE PROBABILITY DISTRIBUTION

IV.2.1 Analytic Solutions

It is generally agreed that in most practical fully turbulent flows the velocity distributions are not very different from Gaussian distributions. Usually only when higher order correlations or velocity derivatives are considered does the turbulence exhibit significant non-Gaussianity (e.g. Frenkiel[46]). At the centre of the plane mixing layer for instance, where the turbulent intensity is quite high compared with many turbulent flows, the flatness factors of the three velocity components are all about 3 (Figure 4.10) so

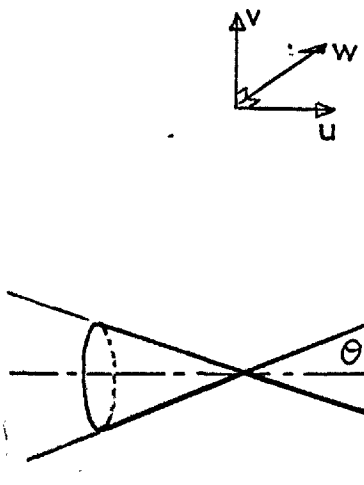
that whilst the flow is quite highly organised and is certainly not isotropic (except at the very high frequency end of the spectrum) it does seem that the actual velocity distributions are not far from Gaussian. There is evidence to suggest that the flatness factors only rise considerably above the Gaussian value when the flow is intermittent and in the turbulent regions themselves it remains at about 3 (see, for example, Wygnanski & Fiedler[30]). Even measurements in the very highly turbulent wake of a bluff body (using a pulse-wire anemometer) have shown the u-component to be nearly Gaussian (Bradbury[47]).

The exact form of the velocity probability distribution is not important for the present purpose, so that it is undoubtedly sufficient to assume normality of the three velocity distributions. This assumption immediately enables us to write down the joint probability function of the velocity vector, which, if we neglect any correlation between the u or v and the w components of velocity, and if we assume that the mean lateral component, W, is zero, becomes

$$F = 1/(\sqrt{2\pi})^3 \alpha_u \alpha_v \alpha_w \sqrt{1 - r^2} \cdot \exp\{\frac{-(u - U)^2}{2\alpha_u^2(1 - r^2)} - \frac{(v - V)^2}{2\alpha_v^2(1 - r^2)}$$

$$+ \frac{2r(u - U)(v - V)}{2\alpha_u\alpha_v(1 - r^2)} - \frac{w^2}{2\alpha_w^2(1 - r^2)}\}$$

where α is the turbulent intensity, and r_{12} is the correlation coefficient, $\frac{\overline{uv}}{\sqrt{\overline{u^2}}.\sqrt{\overline{v^2}}}$. The above assumptions merely restrict the analysis to the usual practical cases of two-dimensional mean flow, whilst procuring a massive simplification of the algebra and later numerical solutions. The basic problem is now to calculate the probability, P, that the instantaneous velocity vector lies within a semi-infinite cone of included angle 2θ, aligned with its axis in the u-direction. In general of course we may require P for a cone aligned in any direction. This is a much



more difficult problem and it is far easier to solve the former case and then, if we need the latter, apply a relatively simple transformation of axes.

The required probability is just the integral of the velocity distribution function over the three-dimensional region inside the semi-infinite cone, i.e.

$$P = 1/(\sqrt{2\pi})^3\, \alpha_u\alpha_v\alpha_w\sqrt{1 - r^2} \iiint_{\substack{\text{over}\\ \text{cone}}} \exp\{-\frac{(u-U)^2}{a_1^2} - \frac{(v-V)^2}{a_2^2} + \frac{2r(u-U)(v-V)}{a_{12}^2} - \frac{w^2}{a_3^2}\}dudvdw \qquad \text{AIV.2}$$

where $a_1^2 = 2\alpha_u^2(1 - r^2)$, etc. There is no analytic solution to this general problem and therefore a numerical technique has to be used. Before describing the general results, it is instructive to investigate a few limiting cases which can be attacked analytically. Not only does this give some useful physical insight, but it provides some 'test cases' to check the accuracy of the numerical program.

Case 1. Isotropic Turbulence

If we assume the turbulence to be isotropic we can write $r = 0$, $a_1^2 = a_2^2 = a_3^2 = a_{12}^2 = 2\alpha^2$. The probability then becomes

$$P = 1/(\alpha\sqrt{2\pi})^3 \iiint_{\substack{\text{over}\\ \text{cone}}} \exp\{\frac{-1}{2\alpha^2}(u-U)^2 + (v-V)^2 + w^2)\}dudvdw.$$

If we also assume that the instrument axis is facing the mean flow direction (which is usually the case) we can put $V = 0$ and the above

expression is then integrable. After a suitable transformation of axes and many pages of algebra it can be shown that

$$P = \tfrac{1}{2}\left[1 + \mathrm{erf}\left(\frac{U}{\alpha\sqrt{2}}\right)\right] - \tfrac{1}{2}\cos\Theta\, e^{\frac{-\sin^2\Theta.U^2}{2\alpha^2}}\left[1 + \mathrm{erf}\frac{U\cos\Theta}{\alpha\sqrt{2}}\right] \qquad \text{AIV.3}$$

This clearly has the correct behaviour in the limits: if $\Theta = 0^\circ$ P vanishes, and if $\Theta = 90^\circ$ $P = \frac{1}{2}(1 + \mathrm{erf}\frac{U}{\alpha\sqrt{2}})$, which is simply the probability that the instantaneous velocity vector is positive. If the local turbulent intensity $(\frac{\alpha}{U})$ is zero, P is unity for all Θ (laminar flow) and if $\frac{\alpha}{U}$ is infinite (i.e. at a stagnation point) $P = \frac{1}{2}(1 - \cos\Theta)$, which is simply the ratio of the surface area subtended on a sphere by the cone of semi-angle Θ to the total surface area $(4\pi r^2)$.

Figure AIV.1 shows how P varies with $\frac{\alpha}{U}$ and Θ. It is obvious that for moderate turbulent intensities there are unlikely to be very significant measurement errors unless the instrument's yaw-response is very restricted.

Case 2 The Effect of Non-Zero Correlation Coefficient

It is interesting to investigate the effect of a non-zero correlation coefficient on the above results and this is most easily done by including in P the probability of the velocity vector lying within the semi-infinite cone facing the -ve u-direction. This reduces the algebra somewhat since all the error function terms cancel out. Since some instruments (notably the laser anemometer and the pulsed wire anemometer) have the capability of distinguishing between +ve and -ve u-components this simplification is also justifiable on practical grounds. Assuming equal turbulent intensities and a zero mean V component as before, it can be shown that the total probability of the velocity vector lying within the infinite cone of semi-angle Θ is given by

$$P_T = 1 - \frac{1}{2\pi}\int_0^{2\pi} \frac{1 - r\sin\phi\tan\theta}{(1 + s^2\tan^2\theta - 2r\sin\phi\tan\theta)^{\frac{1}{2}}}$$

$$\exp\{\frac{-U^2}{a^2d^2}\tan^2\theta(1 - r^2)\}d\phi \qquad \text{AIV.4}$$

where $a^2 = 2\alpha^2(1 - r^2)$, $s^2 = 1 - r^2\cos^2\phi$ and $d^2 = 1 + s^2\tan^2\theta - 2r\sin\phi\tan\theta$. For $r = 0$ this reduces to equation AIV.3 (with the addition of the -ve facing cone term) and is replotted for the case $U = 0$ (a stagnation point) in Figure AIV.2. It is more difficult (and physically less meaningful although mathematically interesting) to investigate the limit $r \to 1$, but it can be shown that equation AIV.4 reduces to (for $U = 0$)

$$P_T = \int_0^{2\pi} \frac{\varepsilon\tan^2\theta}{(1 - \sin\phi\tan\theta)^2}\, d\phi$$

where $\varepsilon = 1 - r$. For $\theta < 45^\circ$, $P_T \to 0$ as $\varepsilon \to 0$. This is obvious if one considers that a correlation of 1 between u and v implies that the velocity in the x-y plane is solely along a line at 45° to the x-axis. If the cone semi-angle is less than 45°, at no time can the velocity vector be within this cone. For $\theta > 45^\circ$ the integration has discontinuities at $\sin\phi = 1/\tan\theta$ and there is no analytic solutio- (that the author could find). However by considering the degenerate two-dimensional problem for $r = 1$, it can be shown that

$$P_T = 1 - \frac{2}{\pi}\tan^{-1}\left[1/(\tan^2\theta - 1)^{\frac{1}{2}}\right] \quad \theta > 45^\circ \quad .$$

Figure AIV.2 also shows these results for the limit $r = 1$. In most practical turbulent flows, the correlation coefficient (or turbulent shear stress expressed as $\frac{\overline{uv}}{\sqrt{\overline{u^2}}\sqrt{\overline{v^2}}}$) is always less than about 0.5, and we expect some variation of P_T with θ lying between the two limiting cases described above. The result of a numerical integration of equation AIV.3 for $U = 0$ and $r = 0.5$ is shown in Figure AIV.2 and

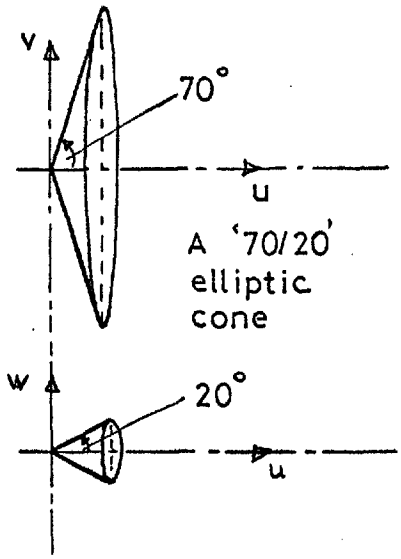
it is clear that the effect of even quite a large correlation on the probability variation with Θ is quite small. It must be remembered however, that this case was for essentially infinite turbulent intensities (e.g. at a free stagnation point) and we would anticipate a somewhat larger effect for more common values of the intensities.

The simplified cases outlined above provided the initial physical insight into the problem, but it was clearly important to obtain results in more meaningful flow situations. Because of the complexity of the integrand in equation AIV.1 it was not expedient, and in fact in most cases quite impossible, to look for more general analytic solutions, so that a numerical program was written to perform the necessary integrations. (This was not too arduous a task as the integral in equation AIV.1 is reducible to a double integral). The following section indicates some of the more general results obtained.

IV.2.2 Results of Numerical Integration of Equation AIV.1

Rather than attempting to vary all the parameters systematically (which would result in a profusion of information) it was thought best at this stage to relate the actual cone-size to the instrument in question, and choose suitable values for the various parameters accordingly. For the present purposes we are interested mainly in the accuracy of hot wire measurements but the principles could be applied to any instrument.

It is usually thought that as long as the velocity vector is not closer than about 20° to the hot-wire axis, the cosine law is a reasonable approximation to the wires actual yaw response. We therefore choose a cone of semi-angle 70° in the x-y plane. There



is however a severer restriction in the x-z plane. Since practically all representations of a hot-wire's response neglect the effect of the w-component of velocity, it is necessary to restrict the semi-angle in this plane to, say, 20°. These restrictions amount to assuming that as long as the instantaneous value of $\frac{w}{U}$ does not exceed ~ 0.35, and $\frac{v}{U}$ does not exceed ~ 2.7, the wire measures the u-component correctly. Many workers would think these rather optimistic values. Figure AIV.3 shows the variation of P for this semi-elliptic cone as the turbulent intensities (assumed equal) vary, for a typical correlation coefficient of 0.300. If a 45° slant wire is used (see Figure AIV.3) the cone of interest should also be inclined at 45° to the u-axis, and Figure AIV.3 shows the results for such a case. The worst case is shown ($\psi = -45^{\circ}$): clearly P would be a little higher for $\psi = +45^{\circ}$ since a positive correlation was used. For turbulent intensities around 30% the results indicate that the velocity vector is only within the cone for about half the time and even for a normal wire P is only 75%. P drops very rapidly between intensities of about 10% and 100%.

If a crossed hot wire is used, errors are likely to occur if the instantaneous velocity vector lies outside a circular cone of semi-angle about 20°, and this case is also shown in Figure AIV.3. This is clearly considerably more restrictive at high intensities than even a single slant wire, as we would expect.

Some workers calibrate their slant, or crossed wires in pitch, as well as in yaw, and then claim more accuracy at high levels of

intensity. Such a calibration could conceivably permit accurate measurements for any velocity vector within (for a crossed wire) an elliptic cone of semi-angle 20° in the x-y plane and, say, 70° in the x-z plane. However, the probability of the vector lying within this cone will be very close to that for the $70^{\circ}/20^{\circ}$ (normal wire) cone of Figure AI.3. In fact for r = 0 the results will be identical. A practical non-zero correlation makes little difference, as is demonstrated in Figure AIV.4. It is clear therefore that at high intensities (greater than 40% say) there will still be significant errors since P is less than 0.5. Indeed, it can be shown that at $\frac{\alpha}{U} = 0.5$, the probability of the velocity vector approaching at least one of the wires in a crossed wire probe from behind is about 20%, and however complex the calibration it can never cover such cases.

IV.3 COMPARISON WITH MEASUREMENTS

With the information provided by the previous sections, it is possible to make some rough estimates of the conditions in which any instrument, in particular the crossed hot wire, is likely to suffer from significant measurement errors caused by inadequate yaw response. For instance, inspection of Figure AIV.3 might suggest that for intensities greater than 20 - 30%, there will be significant errors since, for the crossed hot-wire case, $P < 0.7$. It must be remembered of course that, unlike the pulsed hot-wire, the crossed hot-wire will not measure zero values of velocity for vectors outside the cone of interest; we can imagine some sort of 'sliding scale' operating, so that those vectors that are just outside the cone will only contribute small errors whereas those far outside, or approaching from behind, will contribute larger

errors. This means that P = 0.7 might be a reasonable value, since in only a proportion of the remaining 30% of the time is the vector angle sufficient to cause really large errors.

It would clearly be interesting to compare the experimental vector angle probability distribution with a theoretical one and since digital recordings of crossed-wire data were available this was a fairly simple matter. The crossed wire is really a two-dimensional instrument: only u- and v-component signals are produced and for large intensities these will be in error not only because of inadequate yaw-response, but also because of large w-component fluctuations. We must therefore compare the results with the equivalent two-dimensional theory. Equation AIV.1 reduces to a double integral over x-y space and we effectively allow the w-component to do what it likes. The measured values of $\frac{\alpha_u}{U}$, $\frac{\alpha_v}{U}$, V and r have been used in the numerical integration; in regions of high intensity these will clearly not be correct, but they serve at least as a reasonable first approximation.

The resulting theoretical and experimental variations of P (the probability of lying within a triangle, or wedge, of semi-angle Θ) and of the probability density function F are shown in Figures AIV.5 - AIV.8 for various positions in the plane self-preserving mixing layer (Chapter 4). For low intensities there is no reason why the crossed wire should not be reasonably accurate and we therefore expect differences in theoretical and experimental variations of P and F to be due mainly to fluid mechanic phenomena. Figure AIV.5 shows the results on the high velocity edge (η = - 0.0687) where the flow is very intermittent. The experimental density function differs from the theoretical one (based on normal distributions of the u- and v-components) chiefly in the long 'tail' at the -ve angle

side, and a shorter 'tail' at the +ve side. This was expected for physical reasons. The turbulent bursts in this region of the mixing layer have, on average, high negative v-components and low positive u-components of velocity so the long tail in the density distribution is attributable to these turbulent bursts. On the other hand, the irrotational patches will have, on average, low positive v-components and high positive u-components so that the shorter tail is caused by the irrotational regions.

At the centre of the mixing layer (η = - 0.0144, Figure AIV.6) the flow is almost fully turbulent, but even here the two density functions are not identical. The difference is again attributable to the non-Gaussianity of the velocity distributions, but in this case this cannot be caused by intermittency. The cumulative distribution P, which can be written

$$P = \int_{\Theta=0}^{\pm\Theta} F d\Theta$$

is very close to the Gaussian distribution (integration of course tends to minimise the differences) so that it is reasonable to use the theory based on Gaussian distributions to estimate the probability of obtaining velocity vectors outside the cone of interest.

Further out towards the low velocity edge of the flow we would expect the crossed wire to indicate incorrect distributions of F. Figures AIV.7 and AIV.8 illustrate the effect. The theoretical distributions (which are not exact because measured values of the various parameters were used) have significant regions for which $|\Theta| > 45^{\circ}$. Even if the probe were calibrated so that every angle up to $\pm 45^{\circ}$ is recorded correctly, the measured distribution would be folded back (as shown in dotted lines on Figures AIV.7 and AIV.8).

It seems that the instrument attempts to follow this folded back curve. The particular probe used was calibrated in the standard way as described in Chapter 2, so that only vectors closer than about 15^{o} to the wire axis would not be measured accurately and this appears to be the case. It is difficult to interpret Figures AIV.7 and AIV.8 precisely, since it is not known how much of the difference between experimental and theoretical distributions is caused by the inherent non-Gaussianity of the velocity distributions. We would certainly expect there to be a longer negative tail to the experimental distribution for similar reasons to those given for the high velocity edge of the mixing layer, and it is clear that the instrument error is mostly on the negative side of the density distributions.

Despite the difficulty however, it is possible to make some general remarks.

(i) It would undoubtedly be better to align the probe in the mean streamline direction; for Figure AIV.8 this would be along the $\theta \sim -10^{o}$ line. This would help to equalise the errors on either side caused by the rectifying effect of the wires.

(ii) The crossed-wire measures too low a value of the turbulent intensity. This is obvious even without Figures AIV.7 and AIV.8.

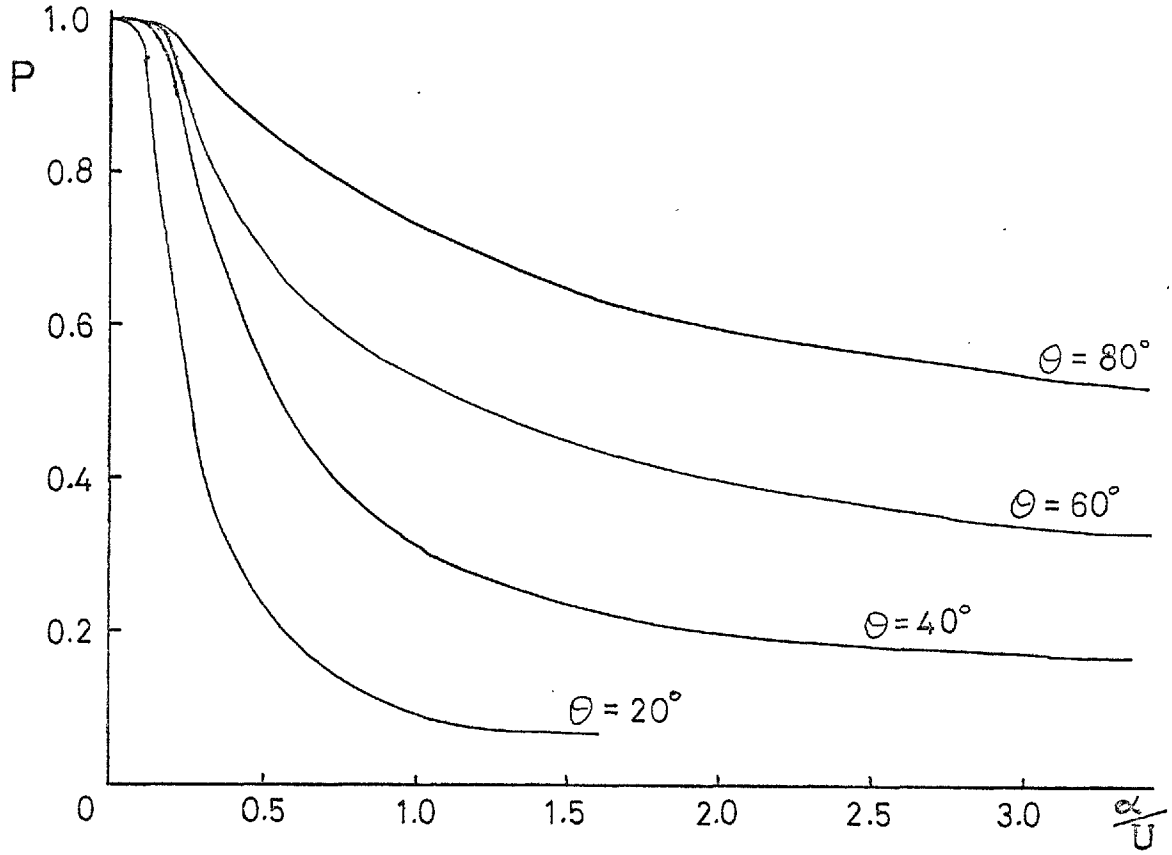
(iii) Even if complex calibrations are made, so that the response is known for flow angles close to the wire axis, there are bound to be significant measurement errors at intensities greater than about 30% (see also Section IV.2.2 and Figure AIV.3).

In order to quantify the actual errors it would be necessary to know the true velocity distributions and it is the author's intention to use

a pulsed hot wire anemometer in an effort to measure these distributions. Unfortunately time has not yet permitted this work.

In view of the findings of this Appendix, the 'effective' cosine law response is used (as described in Section 2.4.2) and it is recognised that there may well be errors in the resulting measurements, particularly at the low velocity edge of the mixing layers.

FIG. A.IV.1 Solution of equation A.IV.3



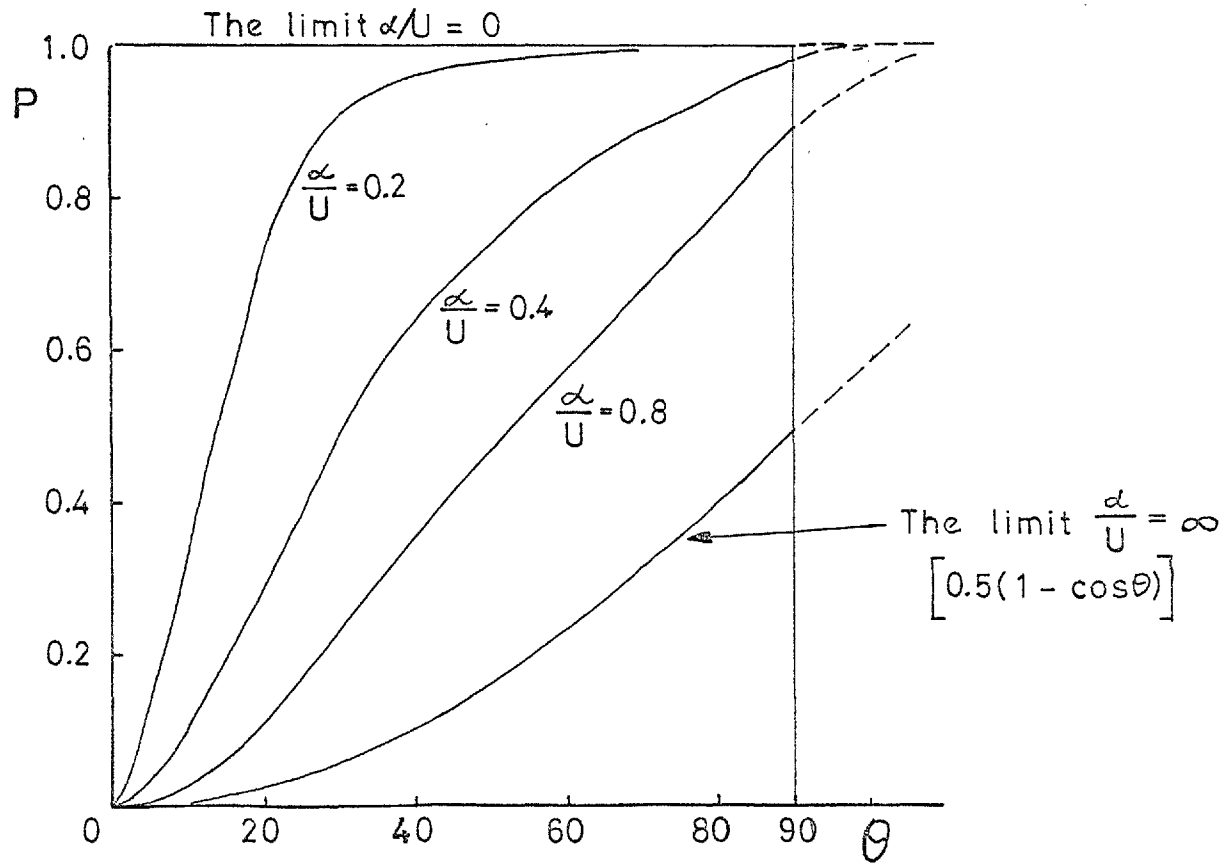
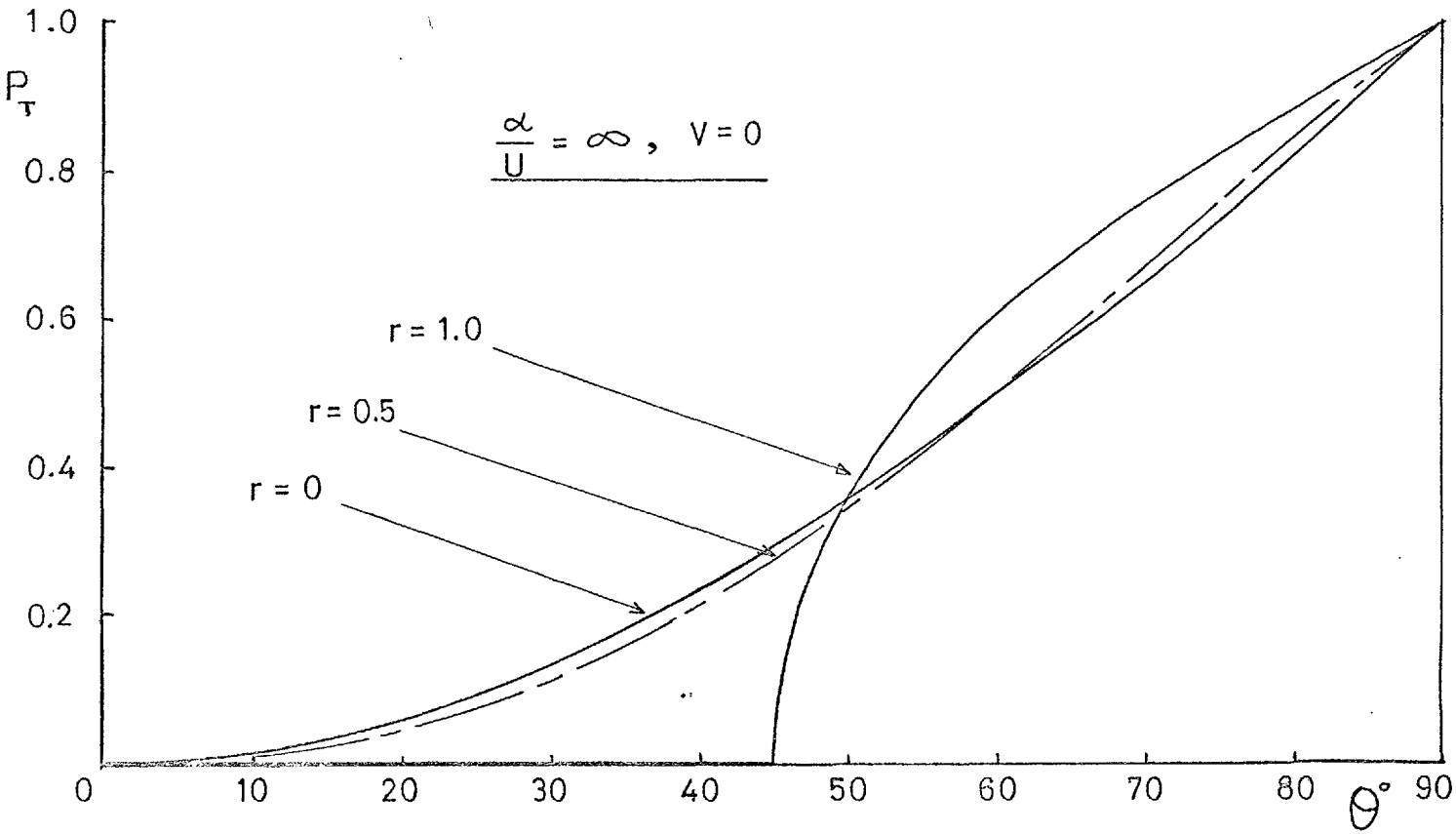
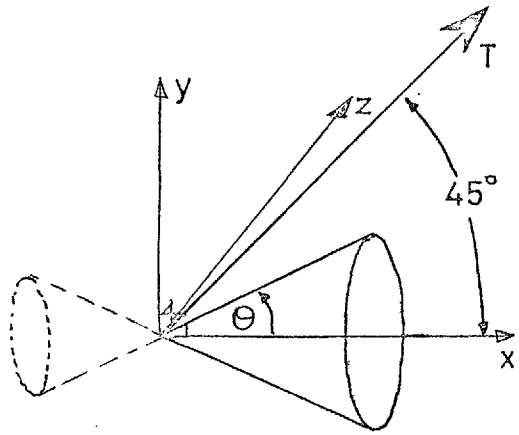


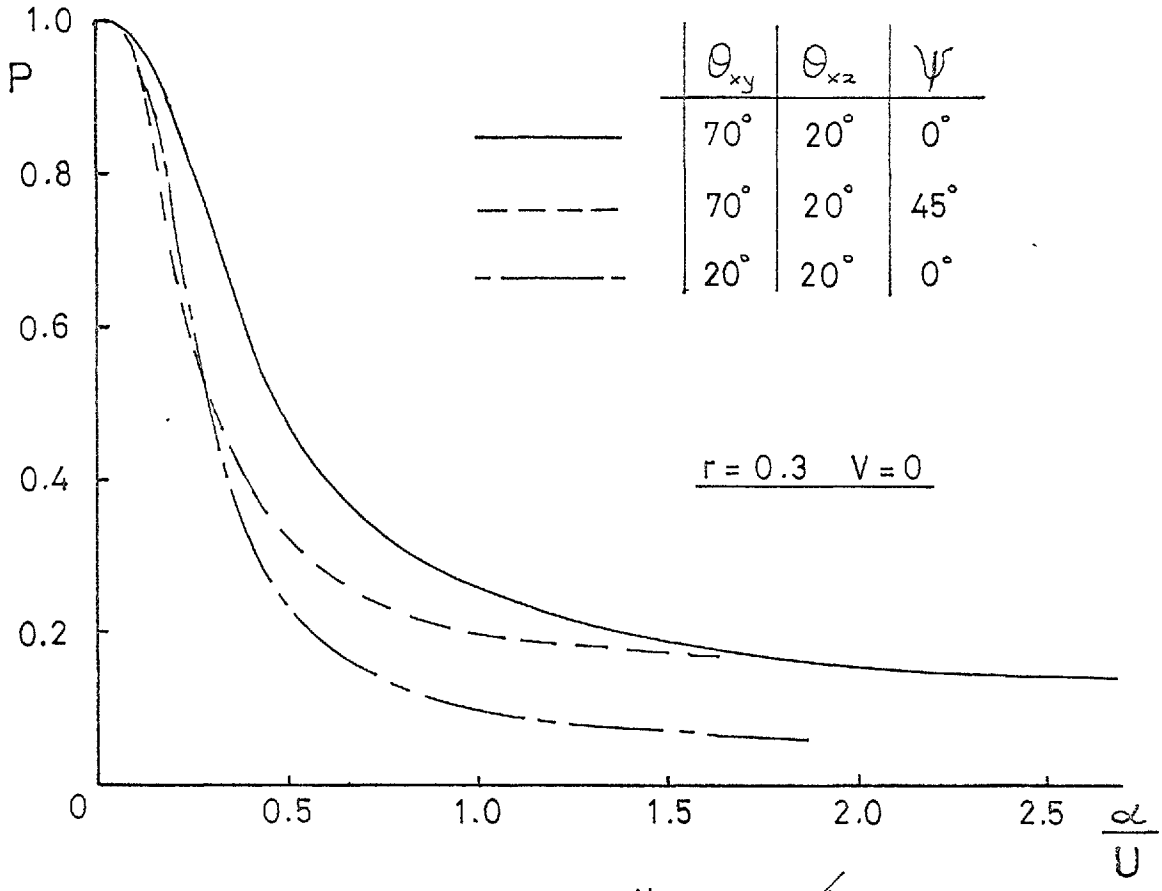
FIG. A.IV.2 Solution of equation A.IV.4



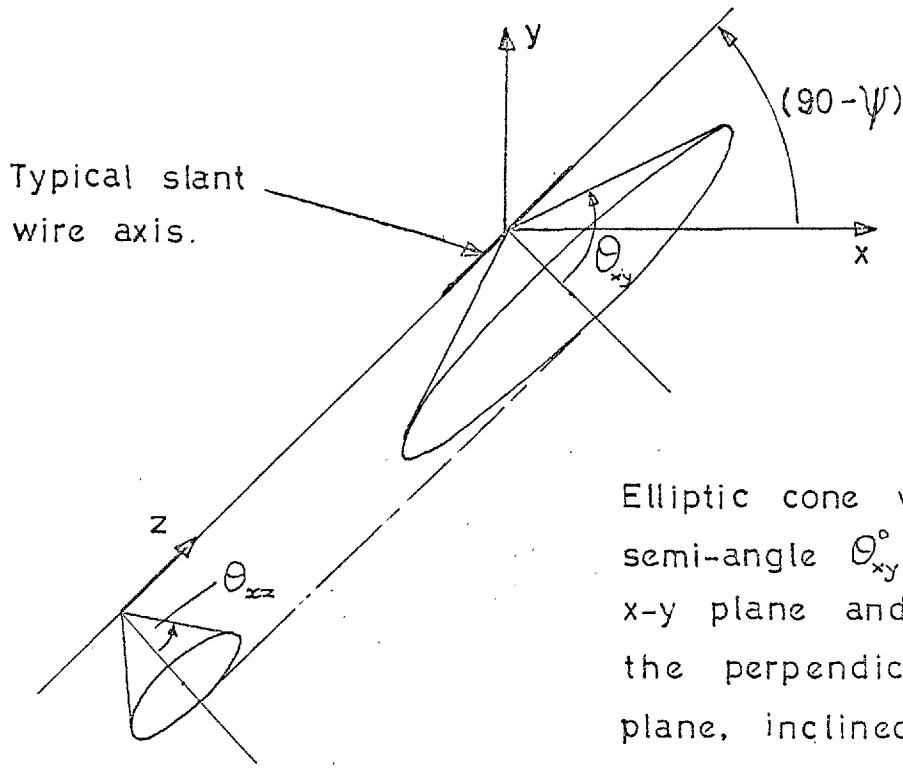


For the limit r=1 the velocity in the x-y plane is along the line

FIG A.IV.3 Results of numerical integration of equation A.IV.1 for typical cases.



	θ_{xy}	θ_{xz}	ψ
———	70°	20°	0°
– – – –	70°	20°	45°
– – ——– –	20°	20°	0°



Elliptic cone with semi-angle θ°_{xy} in the x-y plane and θ°_{xz} in the perpendicular plane, inclined at ψ° to the x-axis.

FIG. A.IV.4

The effect of a non-zero correlation coefficient.

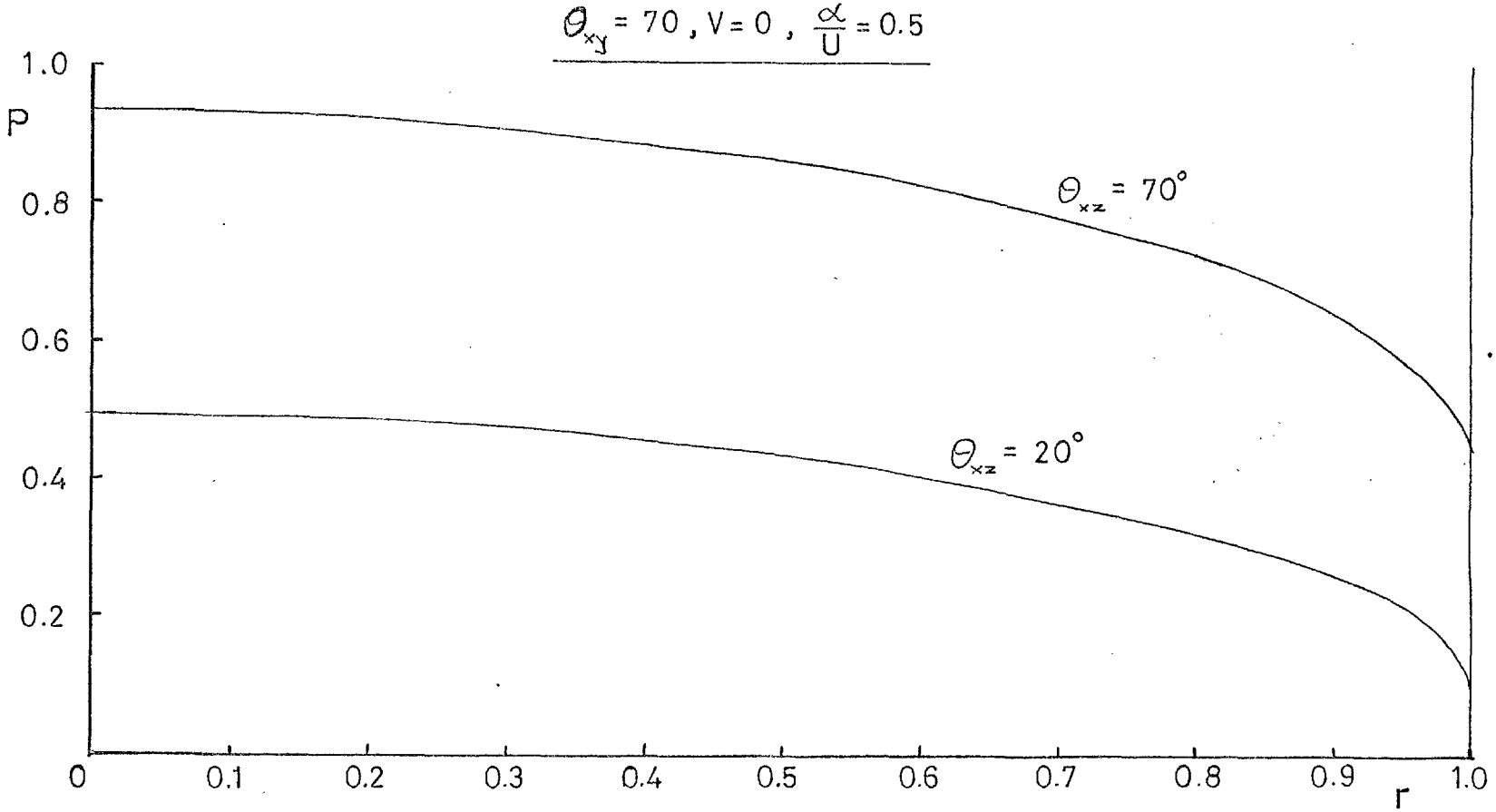
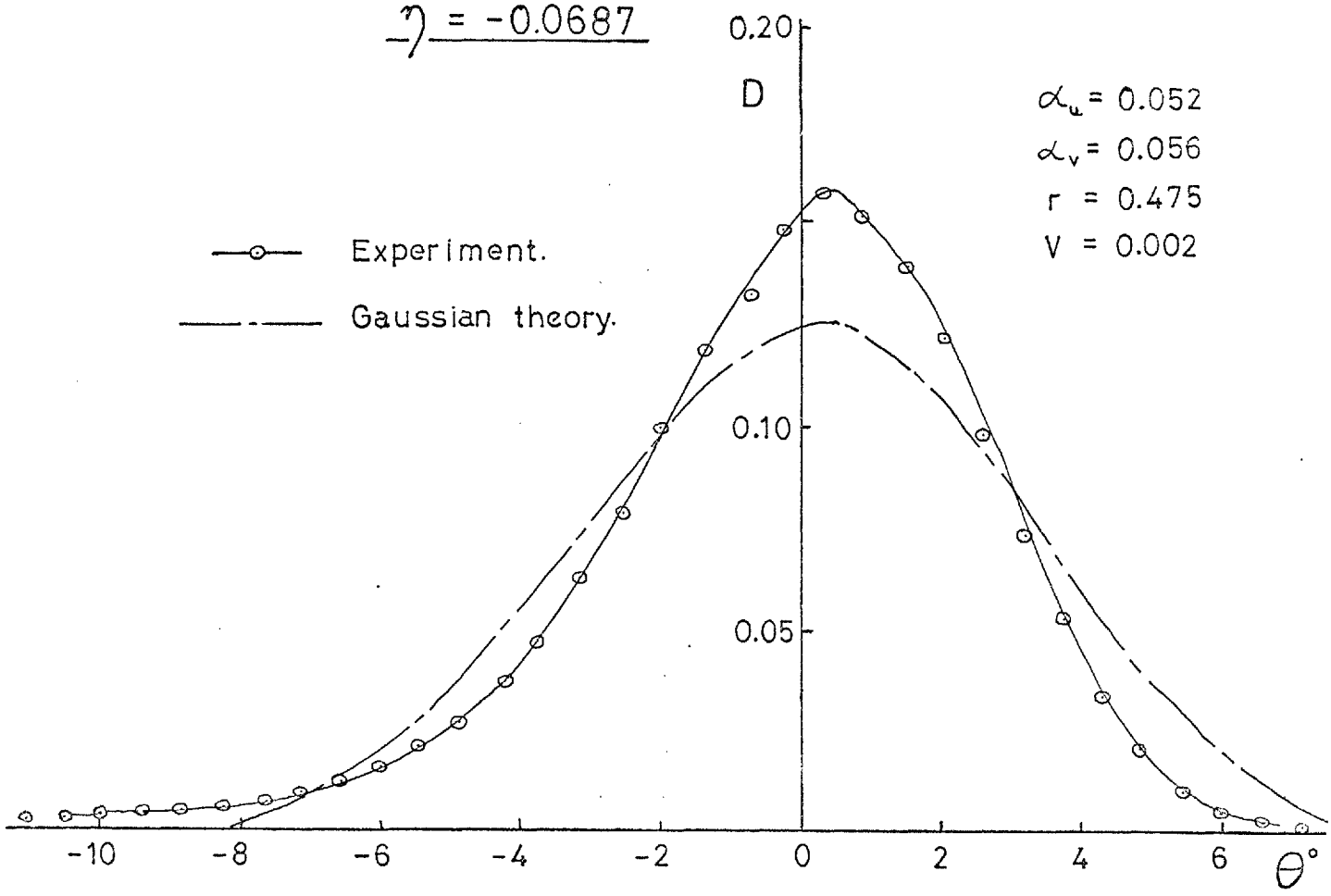


FIG A.IV 5 Probability density of $\mathrm{Tan}^{-1}\left(\frac{V}{U}\right)$



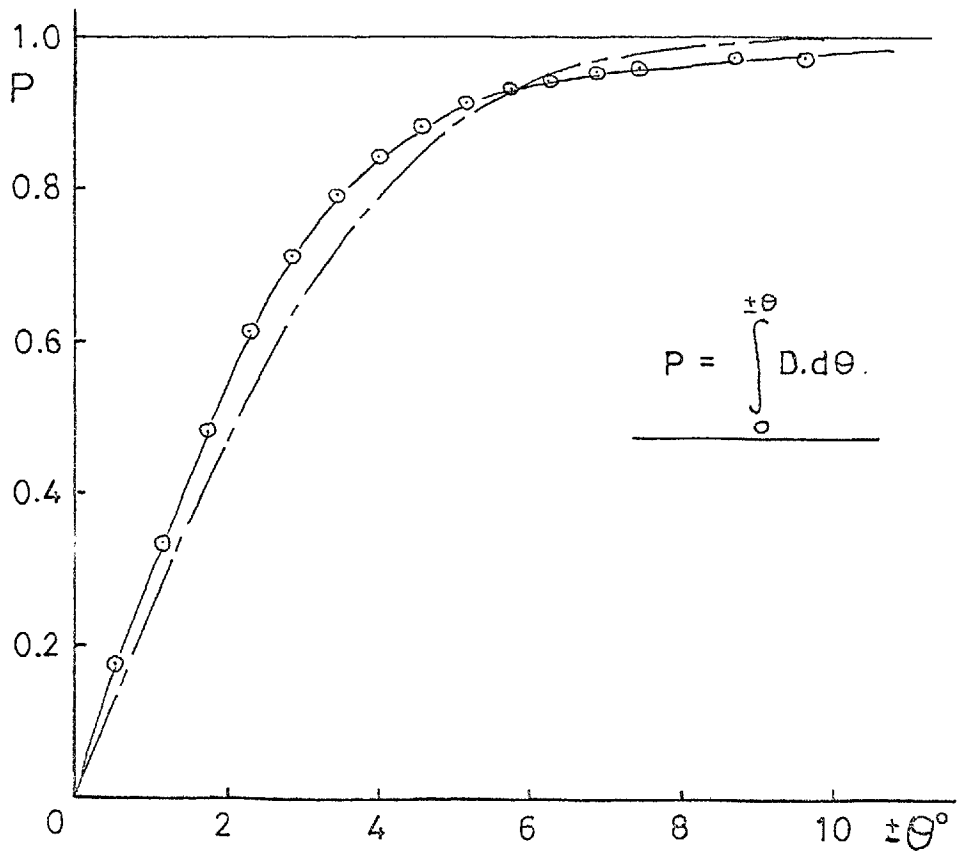


FIG. A.IV.6 Probability density of $\mathrm{Tan}^{-1}(\frac{V}{U})$

$\eta = -0.0144$

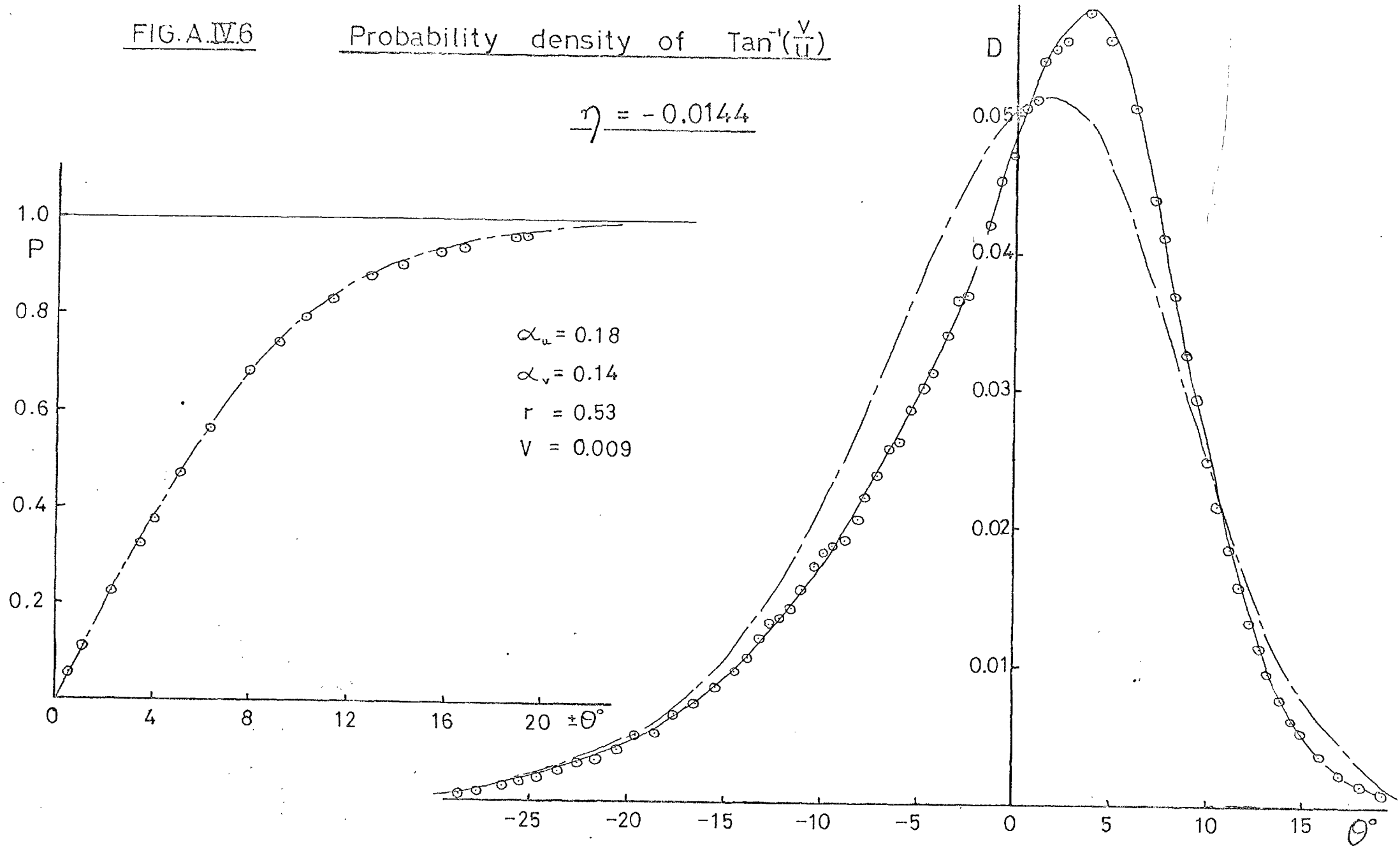


FIG. A.IV.7 Probability density of $\mathrm{Tan}^{-1}(\frac{V}{U})$

$\eta = 0.0757$

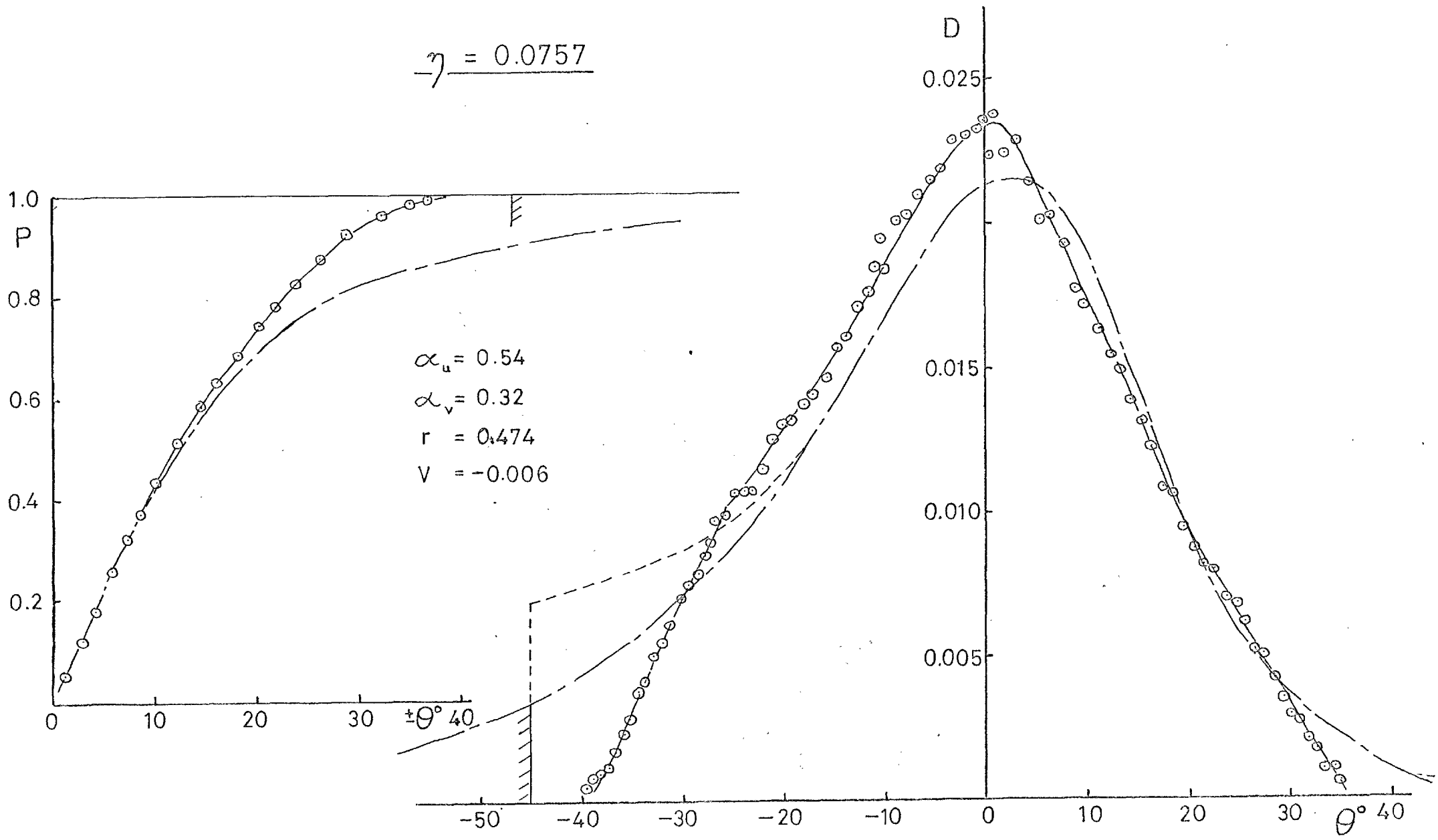
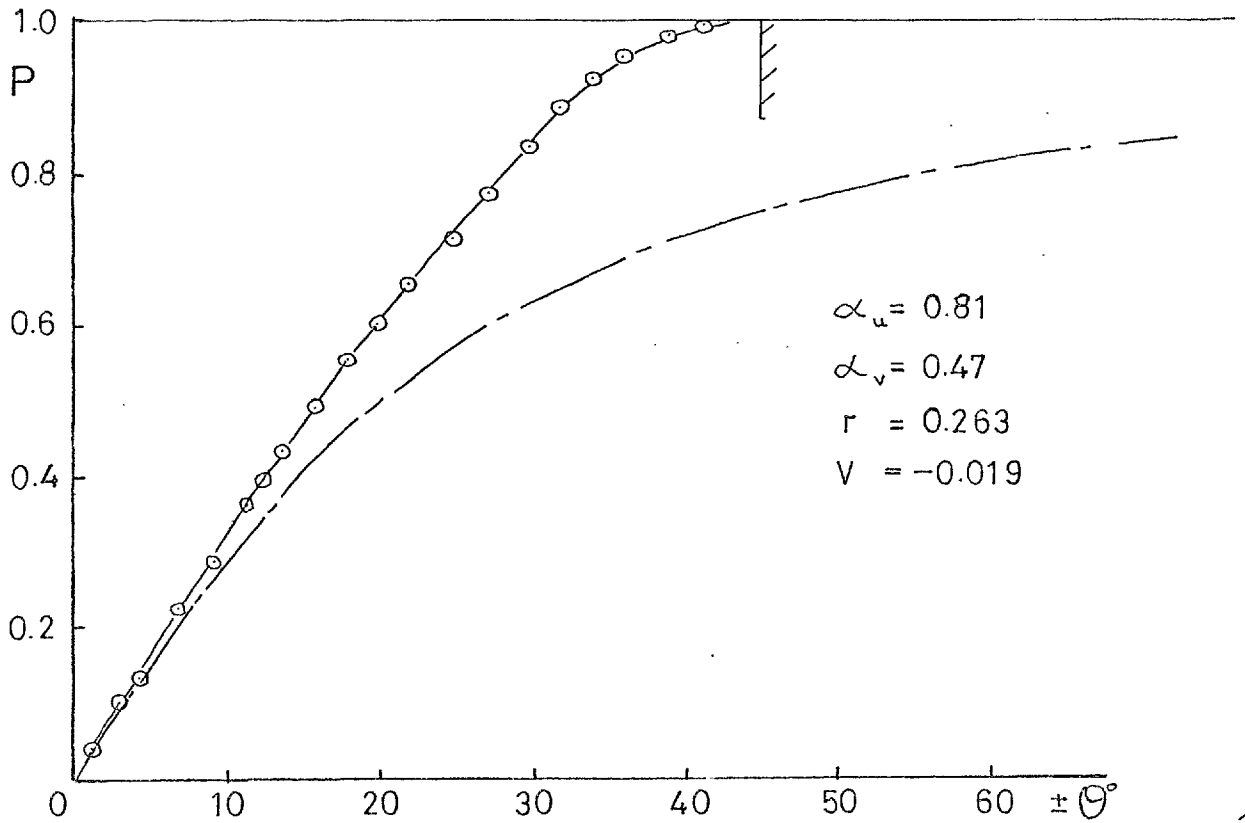
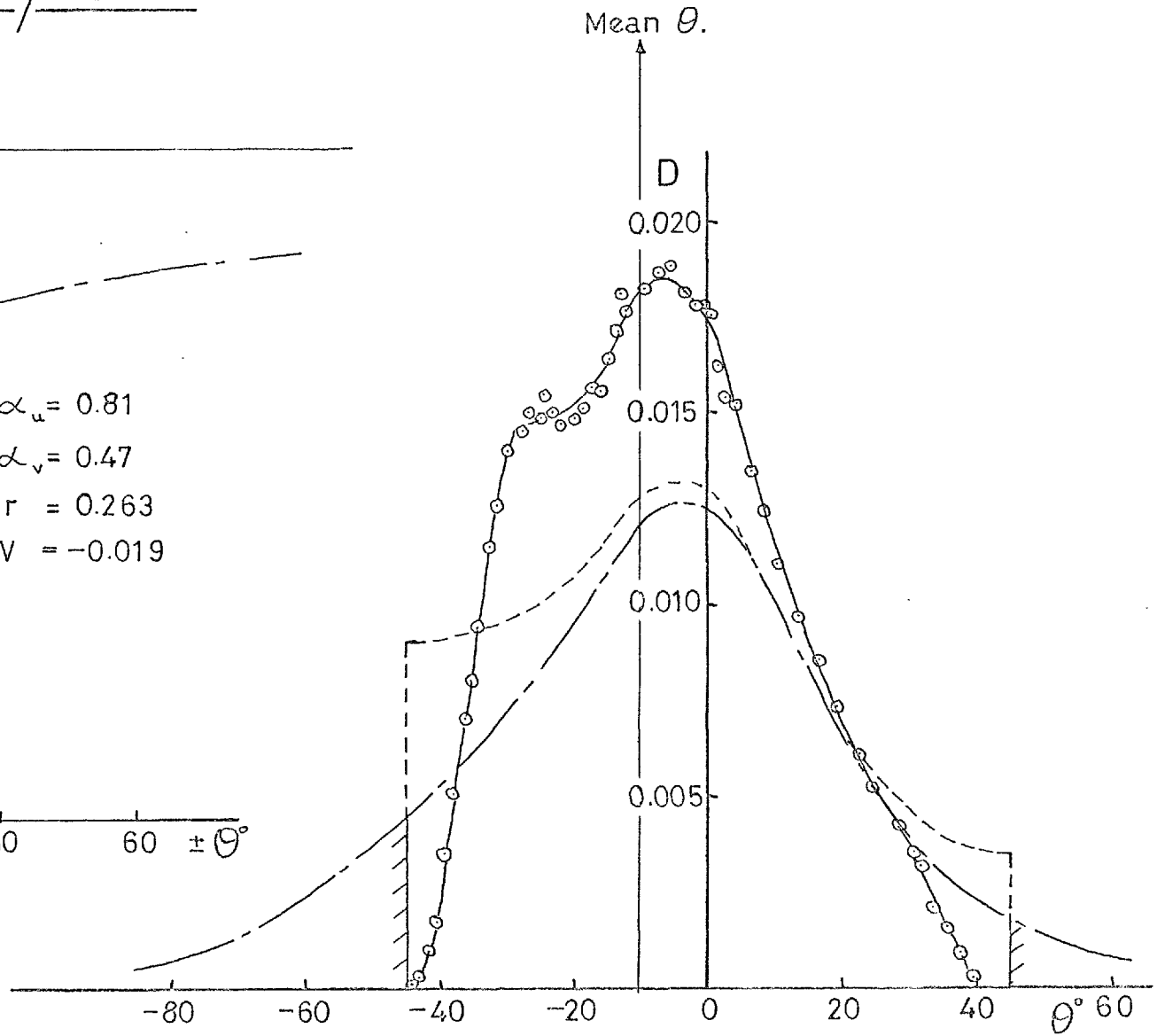


FIG. A.Ⅳ.8 Probability density of $\mathrm{Tan}^{-1}(\frac{V}{U})$

$\eta = 0.112$



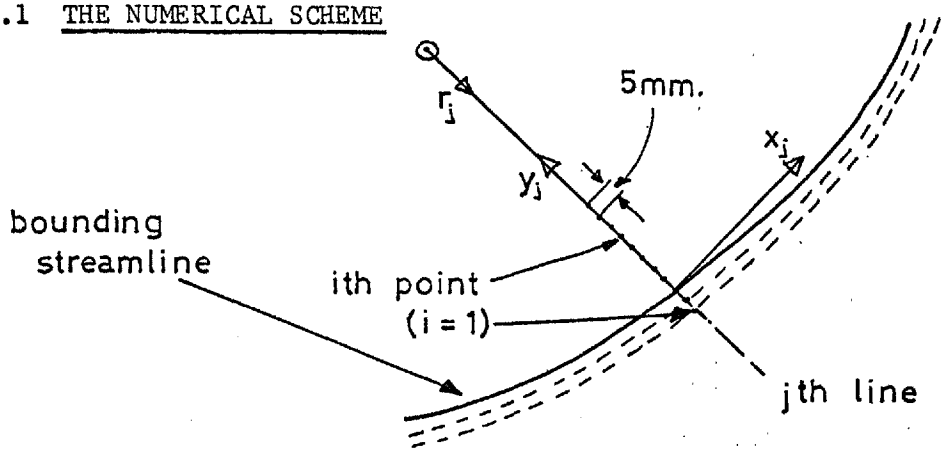


APPENDIX V

THE MEAN FLOW PROGRAMS

As stated in Section 5.1.6, the computation of the mean flow, to derive the transverse and streamwise mean velocities from the measured total velocity profiles using the continuity equation, was split into two parts, one calculating the curved and one the vertical portion of the flow. The former program is described first.

V.1 THE NUMERICAL SCHEME



33 mesh points were spaced along each j-line at intervals of 5 mm (which was found to be quite adequate in the self-preserving flow program) and as a result of the test run described in V.2 the j-lines were spaced at θ-intervals of 5^{o}. Any quantity Q (in particular $\frac{\tilde{U}}{U_r}$) could then be written as $Q_{i,j}$ at each i,j point. Two rows of mesh points outside the bounding streamline were included to aid interpolation at points near this streamline and so the ith point on the jth line corresponded to $y_j' = 5\ (i - 3)$ mm. (See the sketch).

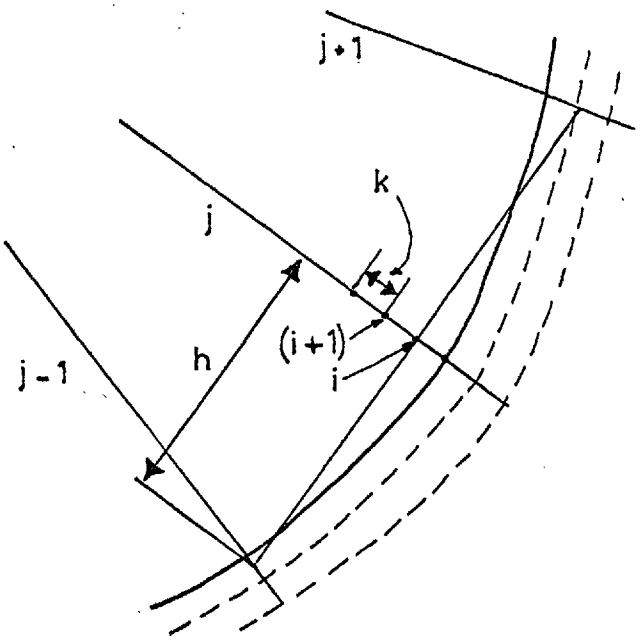
Writing the continuity equation $\frac{\partial U'}{\partial y_j} + \frac{\partial V'}{\partial x_j} = 0$ in finite difference form, and integrating yields

$$V'_{i,j} = V'_{i-1,j} - \frac{k}{2}\left[\left(\frac{\partial U'}{\partial x_j}\right)_{i,j} + \left(\frac{\partial U'}{\partial x_j}\right)_{i-1,j} \right]$$

where

$$\left(\frac{\partial U'}{\partial x_j'}\right)_{i,j} = \frac{U'_{i',j+1} - U'_{i',j-1}}{h} \qquad \text{AV.1}$$

where k, h and i′ are defined in the figure.



In principle the program assumes that $U' = \tilde{U}$ as a first approximation, computes $V'_{i,j}$ everywhere, assigns new values for $U'_{i,j}$ by writing $U'_{i.j} = \left[\tilde{U}'^2_{i.j} - V'^2_{i.j}\right]^{\frac{1}{2}}$ and repeats the procedure until the solution has converged. The program will not be described in detail but the following points should be noted.

(i) The bounding streamline provides the fixed boundary condition so that (for each iteration) the solution starts at j = 1 and i = 4 (i = 3 being on the boundary), setting $\left(\frac{\partial U'}{\partial x_j'}\right)$ and $V'_{3,j}$ as the measured values and marches along each j-line before proceeding downstream to the next.

(ii) Since the mesh is not rectilinear and the bounding streamline is non-circular, the point (i′,j - 1) does not in general coincide with a mesh point on the (j - 1) line so that $U'_{i',j-1}$ and $U'_{i',j+1}$ have to be interpolated. This involves resolving the previously-calculated U′ and V′ on the adjacent mesh lines so that the subsequently interpolated $U'_{i',j+1}$ and $U'_{i',j-1}$ are in the correct co-ordinates with respect to the jth line.

(iii) Near the bounding streamline, where interpolation involves using points outside the boundary (see sketch), fixed values of U′ and V′ have to be used. These are calculated by

assuming that V′ is the same as its measured value on the bounding streamline and using the correct measured $\tilde{U}$ (Figures 4.8 - 4.10) to deduce U′. This is not far from the truth and is certainly better than resorting to a simple forward or backward difference scheme.

(iv) At j = 1 and 19 equation AV.1 is replaced by forward and backward difference schemes respectively. The resulting decrease in accuracy is discussed in Section V.2

(v) At the outer (low velocity) edge of the mixing layer the transverse V′ velocity will exceed the U′ component, so that the finite-difference errors (which will inevitably be greater in this region) may result in the calculated V′ being greater than the measured $\tilde{U}$. This was dealt with by setting V′ equal to $\pm\tilde{U}$ (as appropriate) and U′ = 0 if V′ anywhere exceeded $\tilde{U}$.

V.2 THE TEST CASE

In order to check that the final program worked correctly, and that the mesh size was sufficiently small, a test run was made, using dummy profiles of $\frac{\tilde{U}}{U_r}$. The profile shape was chosen so that analytic calculation of vorticity was possible and the details were as follows:

$$R_j > r_j > 27.0 \qquad \frac{\tilde{U}}{U_r} = 1.0$$

$$27.0 > r_j > 14.5 \qquad \frac{\tilde{U}}{U_r} = \exp\{-(27.0 - r_j)^2/k^2\}$$

$$14.5 > r_j \qquad \frac{\tilde{U}}{U_r} = 0.03$$

and k was chosen as 66.8 so that at $r_j = 14.5$, $\frac{\tilde{U}}{U_r} = 0.03$. Since the hypothetical streamlines were circular the transverse V′ velocity

was zero everywhere. The above profiles have a slight discontinuity in slope at $r_j = 14.5$ but this was sufficiently small and far out at the low velocity edge to be unimportant. One possible disadvantage of this scheme is that the computed V′ values should ideally remain at the initial guess of zero rather than converge to some finite value. However, it turned out that the V′ values actually converged to about 5% of U′ typically if the mesh was too large.

Comparisons were made between the exact rate of strain and vorticity profiles, derivable immediately from the velocity profile and the computed values, and a check on the behaviour of the transverse V′ velocity was made. The former is quite a stringent test since the calculated values are bound to be less accurate than say, the U′ and V′ velocities, since rate of strain and vorticity involve velocity derivatives. Since the experimental profiles had been measured along j-lines 10° apart it was originally hoped that this would provide a sufficiently small mesh. Figure AV.1 shows the error in vorticity along the j = 9 line (chosen as typical over most of the flow) which was clearly unacceptably high for the 10° mesh. A smaller mesh (j-lines every 5°) was therefore used and the resulting error, expressed as a percentage of the correct analytic result, is also plotted in Figure AV.1 and is less than ½% except at the extreme outer (low velocity) edge and in the two regions where there was a discontinuity in the slope of the analytic vorticity profile. Figure AV.1 shows the 'smoothing' of the profiles in these two regions: this was not of course a problem in the real flow.

Because of the forward and backward difference schemes used at j = 1 and 19 respectively, the accuracy was expected to be somewhat less in these regions; this is confirmed by Figure AV.2. Since the numerical program marches along the j-lines starting at the bounding

streamline errors will propagate along the j-lines, so, as Figure AV.2 shows, the errors are worse at the outer (low velocity) edge of the flow. It would be possible to reduce the errors either by increasing the number of mesh lines (which would involve a great deal of extra labour) or by including some 'ghost' lines at $\Theta = 95^{o}$ and -5^{o} and using the central difference scheme on j = 1 and 19. However, Figure AV.2 indicates that it would be necessary to use more than one ghost line at each end to ensure a significant increase in accuracy over the whole of the j = 1 and 19 lines and this was not felt to be worthwhile. It must be remembered that the errors have been expressed as a percentage of the 'local' correct value: if the maximum value of vorticity had been used the errors would be significantly less.

Between j = 3 and 17 the computed V′ velocity (which should be zero everywhere) was found to be less than 1% of U′ everywhere except at the extreme low velocity edge and even on j = 19, V′ only rises to 10% of U′ where U′ is about 22% of its maximum value. Therefore as a result of the test run, the j-line interval used in the main calculation was chosen to be 5^{o}, and the errors were then felt to be sufficiently small over practically all the flow, so that any further attempts to increase the accuracy would not be worthwhile. The one exception was the provision of the two extra 'i-lines' outside the boundary ($r_j > R_j$), mentioned in Section V.1 which were not used in the test programme.

V.3 INPUT DATA FOR THE REAL CASE

The results of the test case investigation showed that the $\tilde{U}$ profiles, measured at 10^{o} intervals of Θ, would not be sufficient for good accuracy of the program. Since it was expected that the

measured profiles would need to be smoothed it seemed unnecessary to make any further measurements, and the required extra data were interpolated manually from smoothed cross-plots of the original data (Figures 4.8 - 4.10). This was done by plotting values of y_j' at constant $\tilde{U}$ against Θ for various values of $\tilde{U}$, smoothing where necessary, and picking off the required values of y_j' for each $\tilde{U}$ and Θ. Very little smoothing was actually necessary but as a final check each interpolated profile was plotted as $\frac{\tilde{U}}{U_r}$ against y_j'. These various cross-plots and extra profiles are not presented; they are all deducible from Figures 4.8 - 4.10 and are available from Mr. P. Bradshaw in the Aeronautics Department.

The only other input requirements were the values of U', V', and $\frac{\partial U'}{\partial x_j'}$ along the bounding streamline. The angle between the streamline and each j-line was first measured from Figure 5.2a and, $\tilde{U}$ being known along this streamline (Figure 5.7), calculation of U', V', and $\frac{V'}{U'}$ followed directly. If s is measured along the streamline,

$$-\int_{j=1}^{j} \frac{V'}{U'}\, ds = dr_j = (R_{j=1} - R_j) = \Delta R \quad .$$

This provided a convenient check of the measured $\frac{V'}{U'}$ values. Figure AV.3 shows $\frac{V'}{U'}$ plotted against s, and the smooth curve gives values of the integral which differ by less than $\frac{1}{2}$ mm from the measured ΔR. Using these smoothed values of $\frac{V'}{U'}$ and the measured $\tilde{U}$, final values of V' and U' were calculated.

$\frac{\partial U'}{\partial x_j'}$ was found by using the relation

$$\frac{\partial \tilde{U}}{\partial s} = \frac{\partial \tilde{U}}{\partial x_j'} \cdot \frac{\partial x_j'}{\partial s} + \frac{\partial \tilde{U}}{\partial y_j'} \cdot \frac{\partial y_j'}{\partial s}$$

writing $\frac{\partial x_j'}{\partial s} = \frac{U'}{\tilde{U}}$ and $\frac{\partial y_j'}{\partial s} = \frac{V'}{\tilde{U}}$. $\frac{\partial \tilde{U}}{\partial x_j'}$ is the only unknown quantity and it was used as an approximation to $\frac{\partial U'}{\partial x_j'}$. Its value was at least

an order of magnitude less than V′ on the boundary streamline, so the inherent inaccuracies were not important.

V.4 THE PROGRAM FOR THE VERTICAL PORTION

For the vertical portion of the mixing layer ($y > 25$) a program similar to that for the ordinary self-preserving mixing layer was used. Since the flow curvature was small in this region a simple rectangular mesh was adequate. The downstream (y) step-length was chosen as 5 cm (this gave good results for the plane layer and no test case was run) and extended over nine of these steps starting at $y = 25.1$ where the measured $\tilde{U}$ profile was identical to the $j = 19$ profile used in the curved portion program. Using the measured velocity profiles (Figures 4.11 and 4.12) profiles at each of the required 5 cm steps were obtained by interpolation in much the same way as for the curved portion. The transverse (x) step length was kept at 5 mm and the boundary streamline was taken as the backplate surface streamline. This amounted to neglecting the effect of the backplate boundary layer which, as Figure 4.10 shows, was less than 1 mm thick at the initial mesh line, $y = 25.1$.

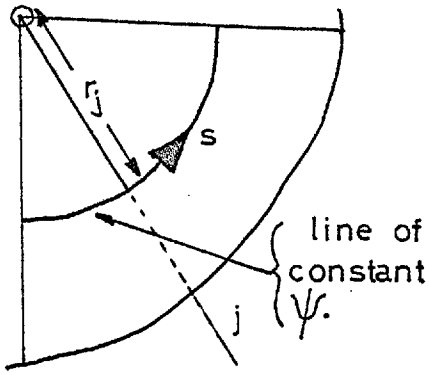
V.5 FURTHER COMMENTS AND CHECKS ON ACCURACY

Both programs calculated the vorticity, rate of strain, V′ and U′ at every point on the mesh and derived the stream function $\psi \equiv \int_{\text{bounding streamline}}^{i} U\,dy$. The integral, ψ, was taken to be zero at the bounding streamline and a simple trapezoidal rule was used to deduce ψ along each mesh line. Even at $j = 1$ where the 5 mm transverse step was relatively coarse ($\delta \approx 25$ mm) ψ (at say $y_j' = 6$ cm) calculated in this way was less than $1\frac{1}{2}\%$ different from a careful hand integration of the velocity profile.

Since different bounding streamlines were used in the two programs the vertical portion program included a routine that found the continuation of the bounding streamline used in the curved portion program, and gave ψ values with respect to this streamline.

As noted in V.3 a convenient check of the calculated $\frac{V'}{U'}$ is to integrate it along a streamline and compare the result with the change in radial position between the two limits of integration. We have

$$\int_{j=k_1}^{j=k_2} \left[\frac{V'}{U'}\right]_\psi ds = (r_{k_2} - r_{k_1}) \quad .$$



The errors will tend to increase towards the outer (low velocity) edge of the flow so $\frac{V'}{U'}$ was plotted against s for three values of ψ in this region of the curved portion. The results are shown in Figure AV.4 and the difference between the integrated values are compared with $r_{k_2} - r_{k_1}$ for various k_1 and k_2 in Table AV.1. Each plot includes the value of U′ at representative points and it is clear that provided U′ is greater than about 0.1, the inaccuracy is equivalent to a spatial error of less than about 1 mm. This was considered very satisfactory particularly as practically all the interesting turbulence phenomena took place at values of U′ higher than 0.1 - as indeed is the case in the self-preserving layer.

FIG. A.V.1 Numerical program test case.

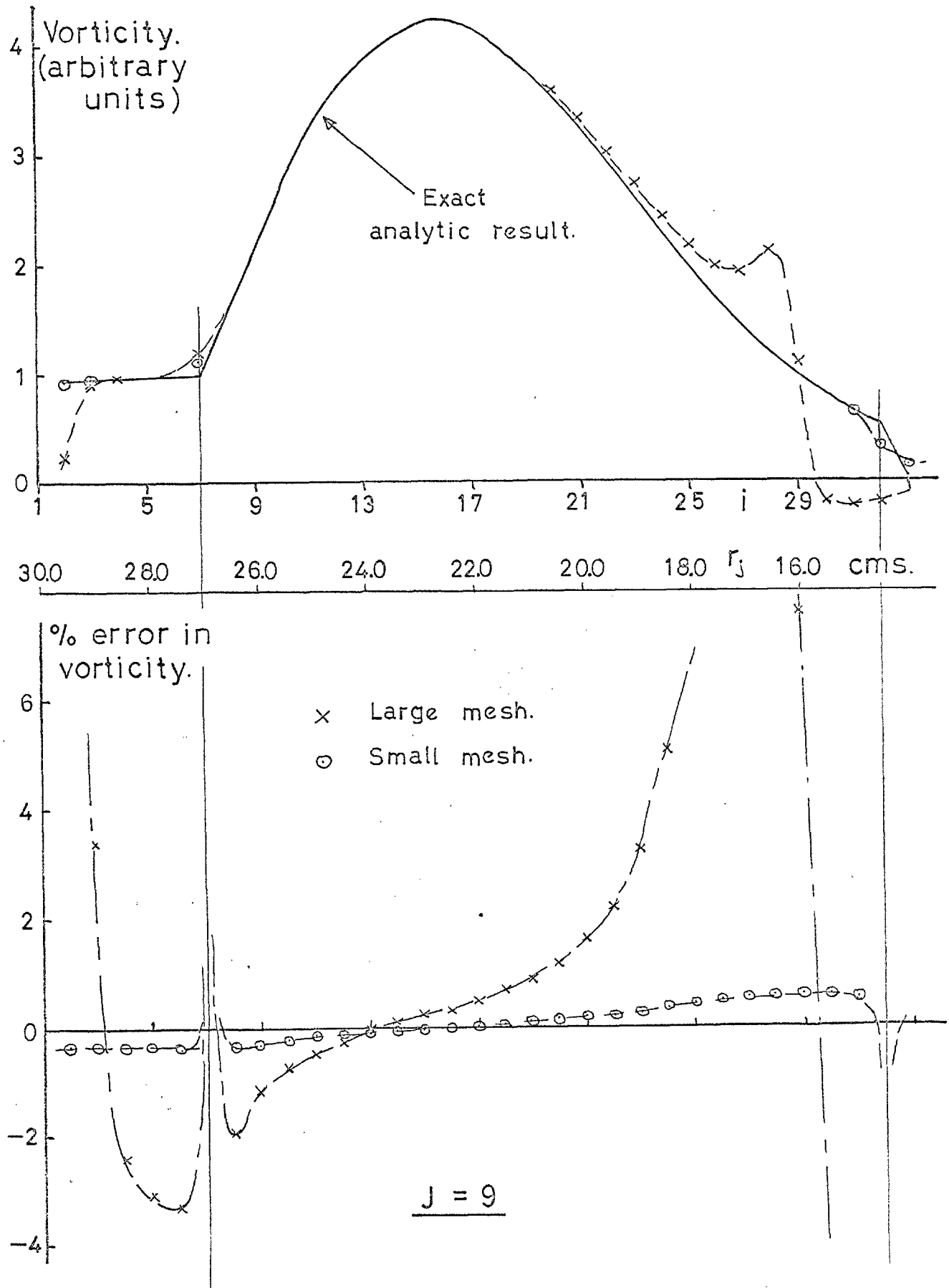


FIG. A.V.2. Test case —— errors in vorticity calculation.

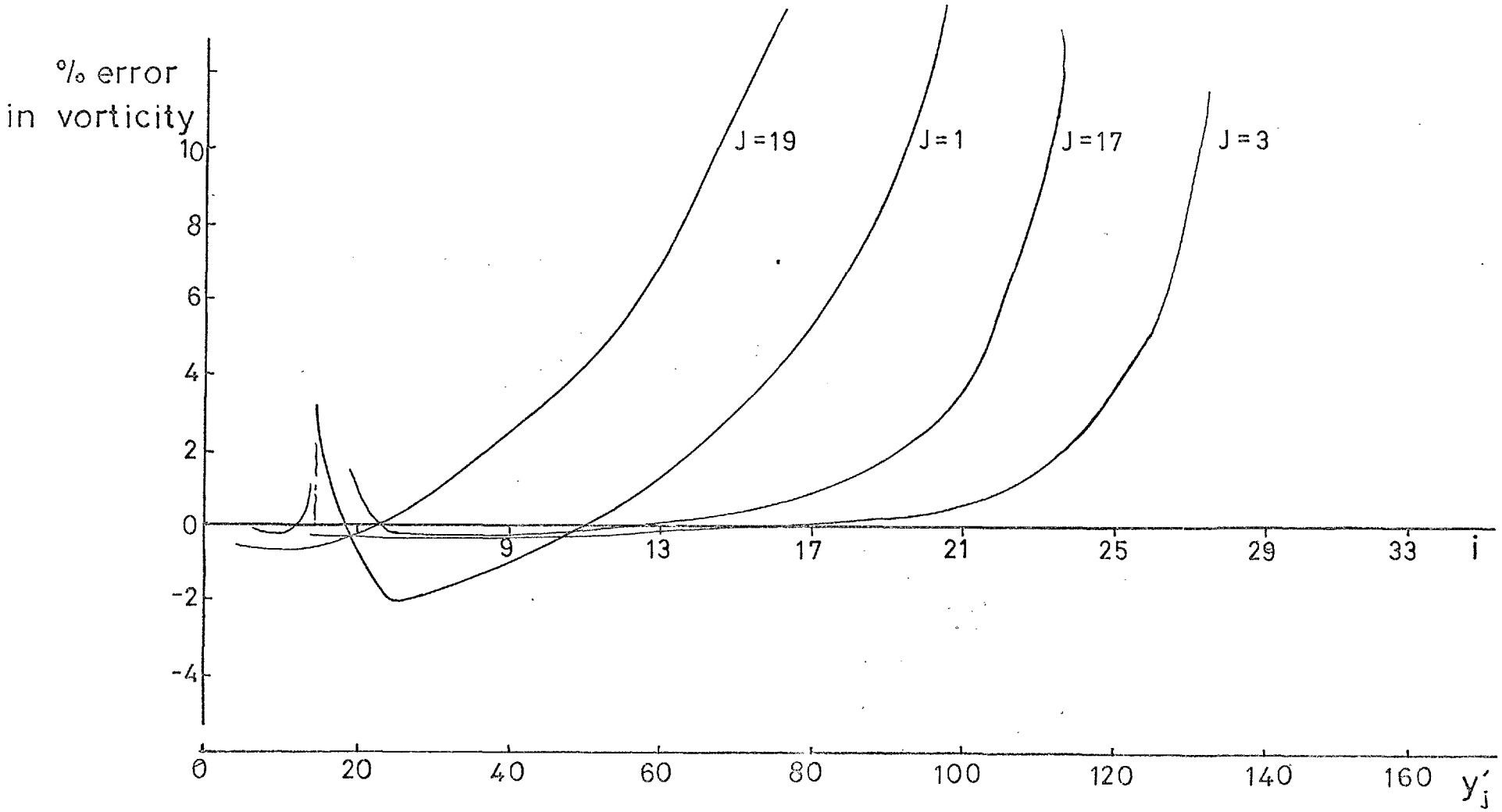


FIG. A.V.3. $\frac{V'}{U'}$ around bounding streamline.

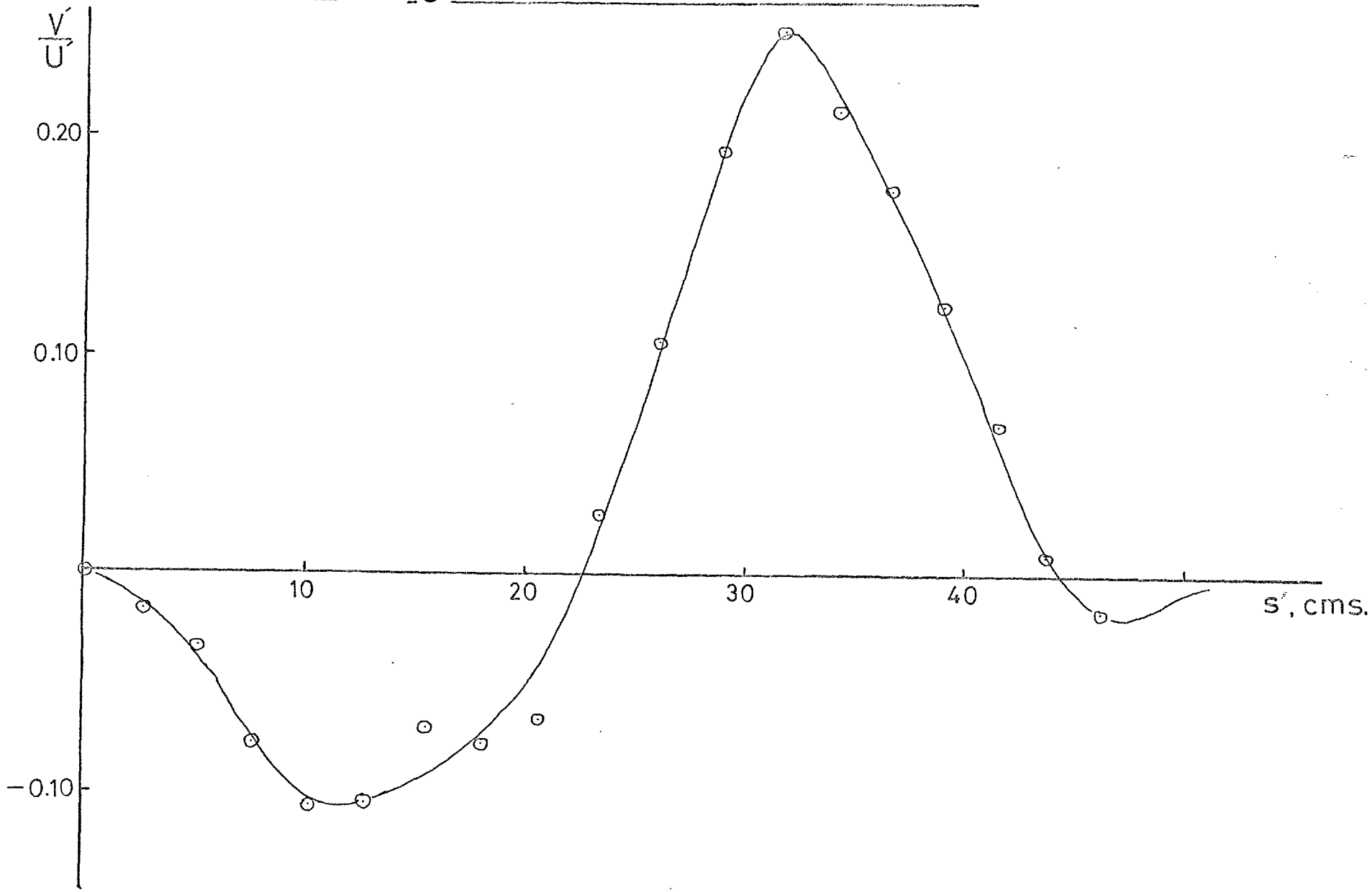


FIG. A.V.4a Accuracy checks (see table AV1).

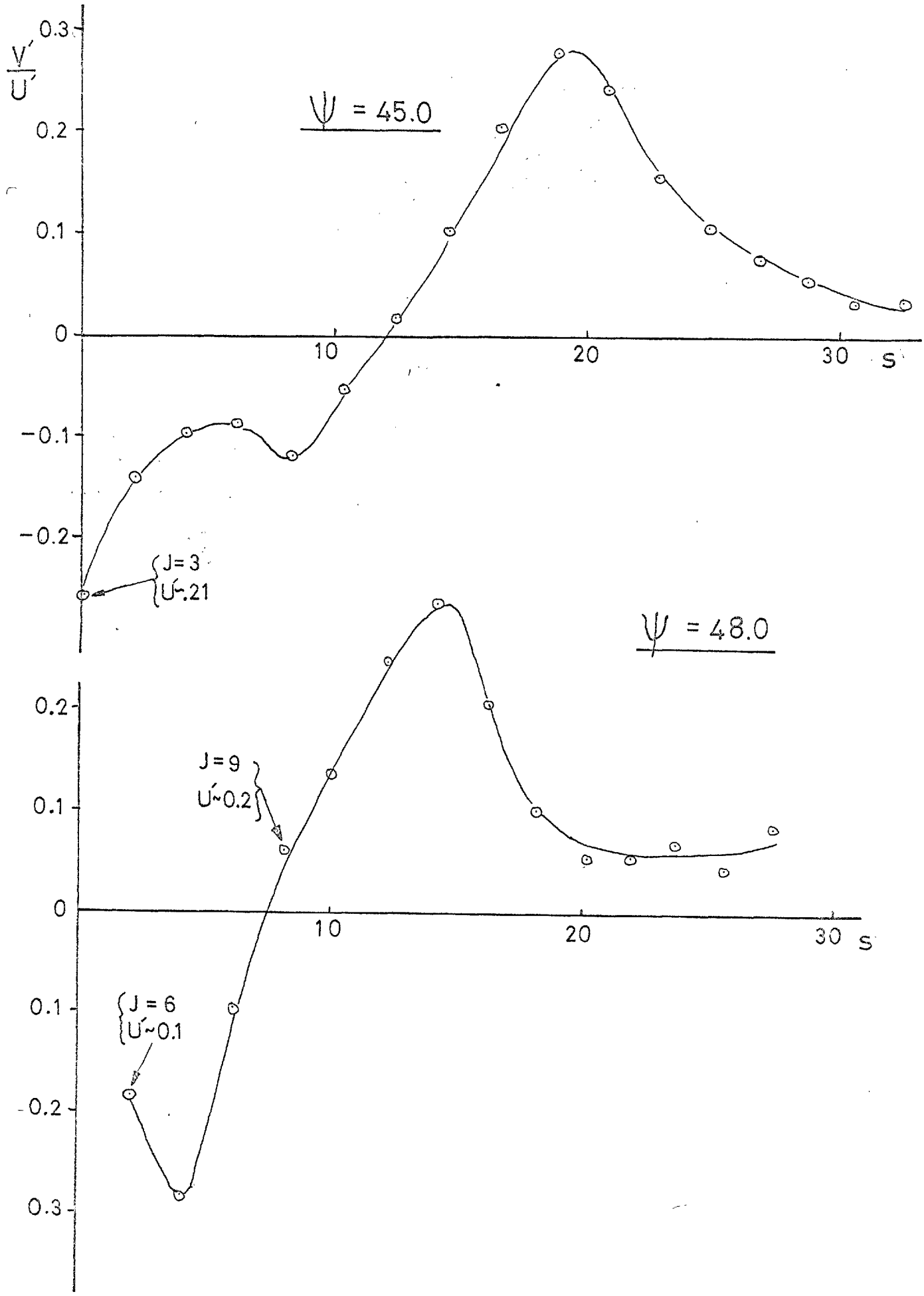


FIG. A.V.4b Accuracy checks.

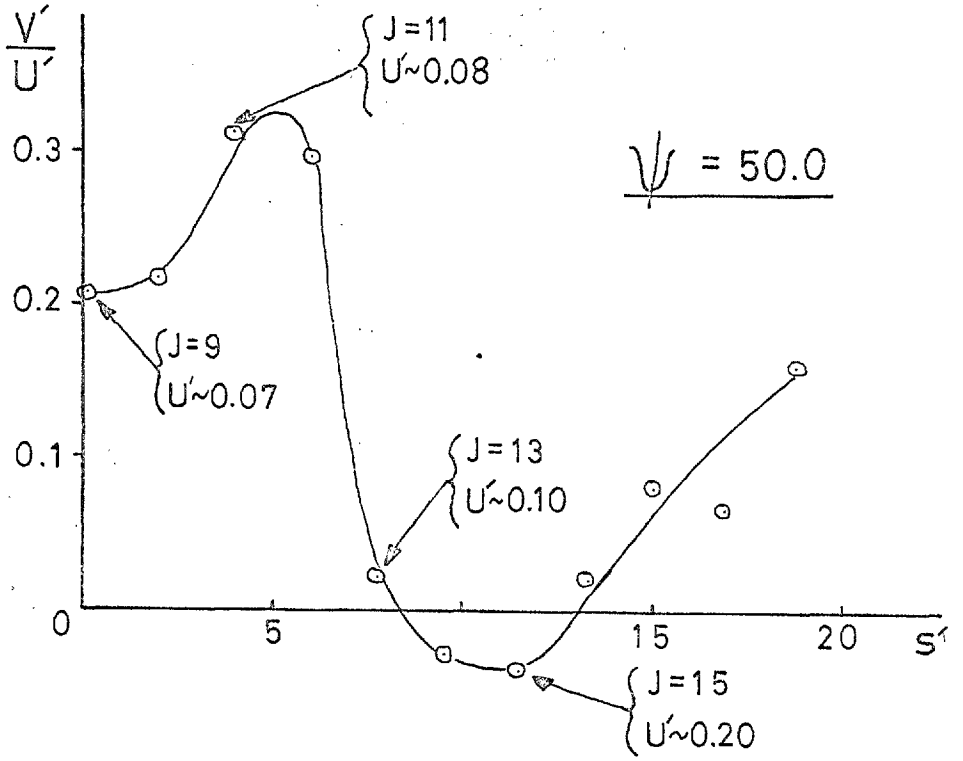


TABLE AV.1. Accuracy checks.

ψ	$(r_{k_1} - r_{k_2})$	$\int_1^2 \frac{V'}{U'} ds'$	k_1	k_2
45	1.56	1.35	3	19
	2.57	2.60	9	19
48	1.54	1.48	6	19
	2.35	2.50	9	19
50	1.54	2.25	9	19
	6.05	4.20	14	19